

Functional Analysis of the Macromolecular Inflammasome Complex

Inauguraldissertation

zur
Erlangung der Würde eines Doktors der Philosophie
vorgelegt der
Philosophisch-Naturwissenschaftlichen Fakultät der Universität Basel
von

Mathias S. Dick

aus Gurbrü/BE, Schweiz

Basel, 2017

Originaldokument gespeichert auf dem Dokumentenserver der Universität Basel
edoc.unibas.ch

Genehmigt von der Philosophisch-Naturwissenschaftlichen Fakultät
auf Antrag von:

Prof. Dr. Petr Broz
Prof. Dr. Sebastian Hiller

Basel, den 13.12.2016

Prof. Dr. Jörg Schibler
Dekan

Abstract

The innate immune system forms the first line of defense against intruding pathogens. A core element of this response is the formation of the inflammasome, a multiprotein complex. This results in the activation of caspase-1 that leads to gasdermin-D-dependent pyroptosis, a pro-inflammatory form of cell death, and the maturation and release of the cytokines IL (interleukin)-1 β and IL-18. Inflammasome formation is initiated by the activation of cytosolic pattern recognition receptors in response to various pathogen-derived stimuli. Most inflammasome-forming receptors contain a PYD (Pyrin domain) through which they recruit an adaptor protein called ASC (apoptosis associated speck like protein containing a CARD). ASC consist of an N-terminal PYD and a C-terminal CARD (caspase recruitment and activation domain) through which it recruits caspase-1. A hallmark of inflammasome activation is the formation of the ASC speck, a micrometer-sized complex formed by ASC. It has been shown that isolated PYDs of human ASC spontaneously form a three-stranded helical filament in which the individual subunits interact with each other via six asymmetric interaction interfaces. Yet, the necessity of oligomeric ASC assemblies for its function has not been shown.

By using a combined solid-state NMR and cryo-electron microscopy approach, we show that also murine ASC^{PYD} filaments display the same three-stranded helical arrangement as human ASC^{PYD} filaments. This indicates that the assembly mechanism of inflammasomes is conserved amongst different species. Furthermore, we provide evidence that, within an ASC speck, filaments of ASC^{PYD} are further condensed via ASC^{CARD}/ASC^{CARD} interactions. Mutations within the ASC^{CARD} that disrupt this interaction lead to the formation of filaments instead of specks. Mutated ASC^{CARDs} are dominant and prevent formation of dense wild type ASC specks in a dose dependent manner when expressed ectopically.

To unravel the biological role of ASC speck formation we used a structure-guided mutagenesis approach targeting all six interaction interfaces based on the murine ASC^{PYD} filament structure. The results suggest that the ASC speck is required for efficient cytokine maturation but dispensable for pyroptosis. Specifically, the mutations E80R and

Y59A in the ASC^{PYD} either completely abrogate or reduce the speed of ASC^{PYD} filament formation *in vitro* and prevent ASC speck formation in cells. These mutants still interact with PYD-containing receptors and are therefore able to support induction of pyroptosis. However, only a small amount of caspase-1 is activated which is not sufficient for efficient cytokine processing. Therefore, we conclude that the ASC speck serves as signal amplification step for inflammasome-dependent cytokine maturation.

Contents

Abstract	3
Contents	5
1 Introduction	7
1.1 Inflammasomes	9
1.2 IL-1 β /IL-18	10
1.3 Pyroptosis	12
1.4 Caspase-1	14
1.5 ASC (apoptosis-associated speck-like protein containing a CARD)	16
1.5.1 Structure of ASC	16
1.5.2 Function of ASC	21
1.5.3 Regulation of ASC	23
1.6 Receptors	28
1.6.1 NLRP3	28
1.6.2 AIM2	31
1.6.3 Pyrin	33
1.6.4 NLRC4	34
1.6.5 Other inflammasome receptors	36
1.6.6 Non-canonical inflammasome: Murine caspase-11 and human caspases-4/-5	38
1.7 Caspase-12	40
1.8 Gasdermin-D	42
1.9 Aim of the thesis	44
2 Results	45
2.1 Research article I	45
2.2 Research article II	62
2.2.1 Additional results related to research article II	95

2.3	Small molecule inhibitor screen for ASC speck formation	97
2.4	Generation and initial characterization of <i>Casp12</i> knock-out mice	102
2.4.1	Materials and methods	102
2.4.2	Results and discussion	104
2.5	Generation of <i>Gsdmd</i> knock-out mice and involvement of gasdermin-D in IL-1 β secretion	107
2.5.1	Materials and methods	107
2.5.2	Results	109
3	Discussion and Outlook	115
4	Acknowledgments	126
5	Bibliography	127
6	Appendix	152
6.1	Research article III	152
6.2	Research article IV	171

1 Introduction

Pathogens are a constant threat to single- and multi-cellular organisms, which over the course of evolution gave rise to the development of different forms of immunity. Even the simplest forms of life, bacteria, have immune system like CRISPR (clustered regularly interspaced palindromic repeats) or restriction enzymes that protect from bacteriophage infections¹. Immunity is more complex in multicellular organisms like vertebrates which evolved the elaborate adaptive immune system. The adaptive immune system allows the formation of an immunological memory after the first contact with a pathogen enabling a very swift elimination of the same pathogen in case of a second infection²⁻⁴. The first line of defense is, however, constituted by the innate immune system. The innate immune system is evolutionary more basal as it is already present in nematodes and insects⁵⁻⁹. It relies on a set of germ-line encoded receptors, PRRs (pattern recognition receptors), that specifically detect conserved molecules of microbial origin, so called PAMPs (pathogen-associated molecular patterns), also referred to as MAMPs (microbe-associated molecular patterns)⁹⁻¹². The PAMPs are essential molecules of pathogens which cannot evolve easily due to their very specific tasks and interactions and are very similar amongst a variety of different pathogens¹³. The prototypic PAMP is LPS (lipopolysaccharide) from the outer membrane of gram negative bacteria. Other examples of PAMPs include peptidoglycan and lipoteichoic acids from gram positive bacteria or double stranded RNA (ribonucleic acid) from viruses¹³. This allows a single PRR to detect multiple different pathogens. Nonetheless, mutations in PAMPs that render them invisible for PRRs occur constantly necessitating the continuous adaption of the innate immune system to changing environments and pathogens¹⁴. A second class of ligands of PRRs are the so called DAMPs (damage-associated molecular patterns). DAMPs are endogenous molecules but they are sensed in places where they are normally not present. For example, detection of intracellular components on the outside of the plasma membrane signifies that non-homeostatic processes are proceeding alerting a cell of impending danger^{15,16}. Multiple different classes of PRRs were described. Examples for PRR-families are the TLRs (Toll-like receptors), the RLRs (RIG-I

[retinoic acid inducible I]-like receptors), ALRs (AIM2 [absent in melanoma 2]-like receptors) and NLRs (NOD [nucleotide-binding and oligomerization domain]-like receptors)¹⁷⁻²². These PRRs differ in their localization, the stimuli leading to their activation but also the responses they elicit. These responses are tailored to the stimulus sensed by the receptor and often result in upregulation of antimicrobial and pro-inflammatory genes¹⁷⁻¹⁹. However, also non-transcriptional responses are known. One example of a non-transcriptional response is the formation of inflammasomes by certain PRRs^{23,24}.

1.1 Inflammasomes

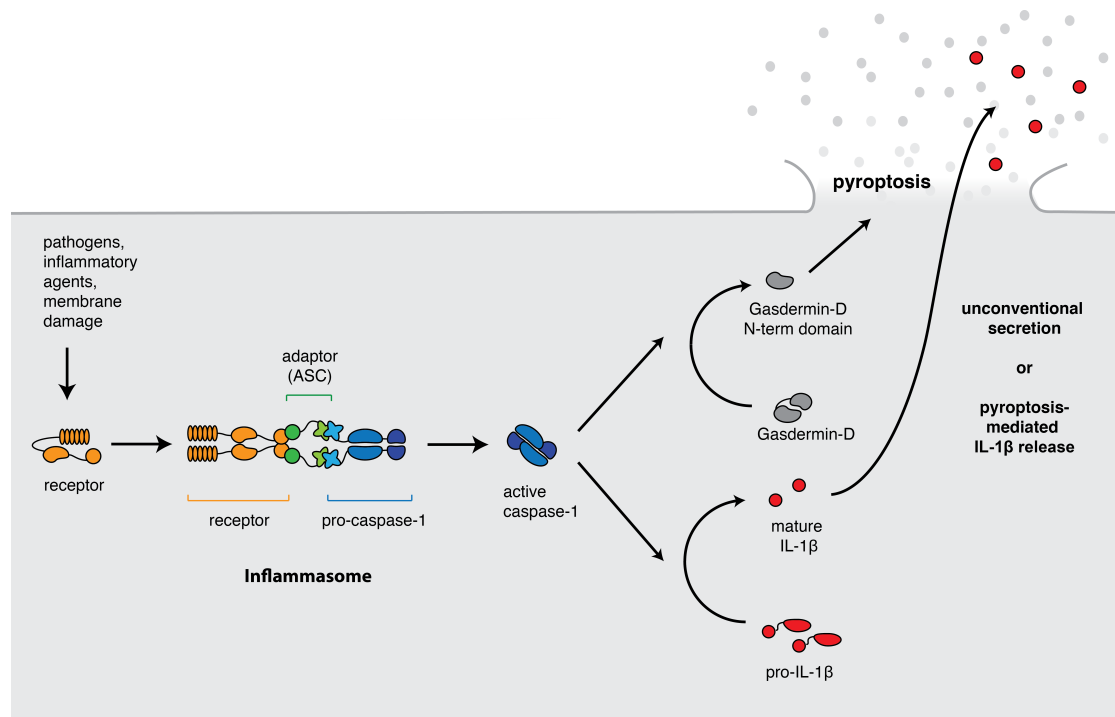


Figure 1.1: **Overview of inflammasome activation.** Adapted from Petr Broz.

Inflammasome receptors are cytosolic soluble PRRs belonging either to the NLRs, ALRs or Pysin^{23,24}. Upon activation, inflammasome receptors oligomerize and recruit the adaptor protein ASC (apoptosis associated speck like protein containing a CARD) (**Fig. 1.1**). Interestingly, usually only one large macromolecular inflammasome complex can be detected per cell. This complex is usually referred to as ASC speck, named after its main constituent^{25,26}. Apart from the receptor and ASC, also the downstream effector pro-caspase-1 is part of the inflammasome^{23,24}. Recruitment of pro-caspase-1 into the inflammasome complex leads to proximity induced auto-proteolytic cleavage and thereby activation of caspase-1^{27,28}. Active caspase-1 cleaves gasdermin-D which induces a pro-inflammatory cell death called pyroptosis^{29–31}. Additionally, caspase-1 is able to cleave the pro-inflammatory cytokines IL-1 β and IL-18. Mature IL-1 β and IL-18 are then released from the cell and can influence the immune system where they act as major drivers of fever and inducers of cytokines³² (**Fig. 1.1**).

1.2 IL-1 β /IL-18

Both, IL (interleukin)-1 β and IL-18 are cytokines belonging to the interleukin-1 family. IL-1 was initially described in 1977³³ while IL-18 was only identified in 1995³⁴. The IL-1 family now consists of 11 members and is closely linked to inflammation³⁵. Most family members are produced as biologically active proteins, but IL-1 β and IL-18 are expressed in an inactive pro-form³⁶. While pro-IL-18 is constitutively expressed, pro-IL-1 β expression requires a signal often referred to as priming. TLR signaling from the cell envelope leads to a NF- κ B (nuclear factor kappa-light-chain-enhancer of activated B cells) dependent upregulation of many pro-inflammatory genes, amongst them pro-IL-1 β . This priming step thereby alerts a cell of impending danger³⁷. After expression, both pro-IL-1 β and pro-IL-18 need to undergo a proteolytic maturation step. This cleavage step separates the N-terminal pro-domain from the protein and renders it signaling competent by allowing it to bind to its receptor³⁵. The main activation pathway is via cleavage of pro-IL-1 β /-18 by the inflammasome-dependent caspase-1 (see below)³². However, alternative pathways exist and most of them are linked to neutrophils. It has been shown that elastase, matrix metalloprotease 9 and granzyme A are able to cleave IL-1 β extracellularly into the biologically active form³⁵. Interestingly, also the apoptotic caspase-8 has been suggested to cleave pro-IL-1 β /-18 in an inflammasome dependent manner further expanding the possibilities for pro-IL-1 β /-18 maturation³⁸.

After processing, IL-1 β and IL-18 need to be released from the cell. As the cytokines lack a classical secretion signal sequence, the export mechanism remained enigmatic and was called unconventional secretion³⁶. Recently, it has been shown that cleavage of gasdermin-D is required for IL-1 β /-18 release but whether the release is unspecific via pyroptosis or via a specific pore is still unknown (see below)^{30,31}. After release, IL-1 β and IL-18 bind to their cognate receptors, IL-1R1 (IL-1 receptor 1) and IL-18R α (IL-18 receptor α), respectively. Receptor binding leads to heterodimerization of IL-1R1 with IL-1RAcP (IL-1R accessory protein) and IL-18R α with IL-18R β . Both receptors contain TIR (Toll/interleukin-1 receptor) homology domains that enable signaling through MyD88 (Myeloid differentiation primary response gene 88) to activate NF- κ B and MAPK (mitogen-activated protein kinases) signaling³⁹. In general, IL-1 β signals the immune system that a threat has been recognized via induction of fever and neutrophil influx³⁹. IL-18 on the other hand does not induce fever but is best known for its ability to induce IFN γ (interferon- γ), another pro-inflammatory cytokine important for innate and adaptive immunity³⁵.

As IL-1 β and IL-18 are such powerful cytokines, not only their maturation and release but also the signaling is tightly regulated. For example, IL-1Ra (IL-1R antagonist) competes with IL-1 β for binding of the IL-1R thereby blocking IL-1R signaling. IL-1R2 on the other hand acts as decoy receptor binding IL-1 β but, in contrast to IL-1R, does not induce the downstream signaling cascade. IL-18BP (IL-18 binding protein) does, as the name suggests, bind to IL-18 with high affinity thereby preventing its interaction with the IL-18 receptor³².

Consequently, elevated IL-1 β /-18 signaling, either through absence of negative regulators or through overproduction of the cytokines themselves, leads to massive systemic inflammation. If the underlying cause is a genetic mutation, the disease is classified as an autoinflammatory disease³⁵. Hyperactivation of caspase-1 by inflammasome receptors harboring gain-of-function mutations (see below) are often the cause of elevated IL-1 β and IL-18 levels³⁵. Therefore, blocking IL-1 β by drugs has proven efficient to ameliorate many autoinflammatory diseases. For example, anakinra (brand name Kineret[®], an IL-1R antagonist), rilonacept (brand name Arcalyst[®], an IL-1 decoy receptor) or canakinumab (brand name Ilaris[®], an anti-IL-1 β antibody) have been used to treat autoinflammatory diseases⁴⁰. A major drawback of these therapies is the high price in the range of 20'000-250'000 US\$ per patient per year⁴¹⁻⁴³. Thus, the need to develop alternative therapies that target IL-1 β maturation or signaling persists.

1.3 Pyroptosis

Besides the maturation of IL-1 β and IL-18, activation of caspase-1 triggers a cell death pathway called pyroptosis. Pyroptosis is a form of programmed cell death but in contrast to apoptosis, and similar to necroptosis, displays a pro-inflammatory rather than an anti-inflammatory phenotype²⁹. Pyroptosis was discovered in *Salmonella* and *Shigella* infected cells but initially described as apoptosis⁴⁴. The term pyroptosis was coined in 2001 when it became clear that the cell death induced by intracellular *Salmonella* was neither apoptosis nor necrosis⁴⁵. Since then, the differences between apoptosis and pyroptosis have been elucidated further⁴⁶.

Even though both types of cell death depend on caspases, apoptotic or inflammatory, and their catalytic activity (see below), the cell fate is fundamentally different. Apoptosis is characterized by nuclear fragmentation and the segmentation of the cell into apoptotic bodies which are then phagocytosed by other cells. Importantly, the integrity of the cell membrane is not compromised and the whole process is inflammatory silent⁴⁷. Pyroptosis on the other hand is characterized by permeabilization of the plasma membrane followed by cell swelling and release of cytosolic contents characterizing pyroptosis as a profoundly pro-inflammatory type of cell death⁴⁷. Pyroptotic cells were described to display multiple bubble-like protrusions similar in size to apoptotic bodies therefore named pyroptotic bodies. Furthermore, it was shown that pyroptotic cells undergo cytoplasmic flattening making them morphologically distinct from necroptotic cells which display cell swelling resulting in an "explosion" of the cell body⁴⁸.

Two functions have been attributed to pyroptosis. The first is to expel intracellular bacteria so they are deprived of their replicative niche⁴⁹. This exposes the bacteria like *Salmonella* to phagocytosis and killing by other immune cells, e.g. neutrophils⁵⁰. For some bacterial pathogens like *Salmonella enterica* serovar Typhimurium, *Legionella pneumophila* or *Burkholderia thailandensis* it was even shown that clearance occurred independently of IL-1 β or IL-18 suggesting that pyroptosis is the main innate immune mechanism against these bacteria⁵⁰.

The second role of pyroptosis is to release further DAMPs, such as ATP (adenosine triphosphate), DNA (deoxyribonucleic acid) or RNA (ribonucleic acid), and alarmins like HMGB1 (high mobility group box 1, also known as amphoterin) or IL-1 α ⁴⁹. The DAMPs can elicit strong pro-inflammatory responses when detected extracellularly by recruiting inflammatory cells and stimulating cytokine secretion⁵⁰. The probably best studied alarmin in the context of pyroptosis is HMGB1⁵¹. HMGB1 is released from

dying cells and can signal through TLR4 (Toll-like receptor 4) to induce TNF (tumor necrosis factor) release and NF- κ B signaling in neighboring cells, thereby further increasing the pro-inflammatory state of the host⁵². Another important group of alarmins are the eicosanoids. These signaling lipids induce vascular leakage and recruitment of immune cells to the inflammatory site⁴⁹. Control of pyroptosis is important as systemic pyroptosis has been linked to the severe outcome of sepsis. If the infection cannot be cleared, prolonged and sustained pyroptosis leads to an often lethal shock due to the massive release of DAMPs⁴⁷. Another case where pyroptosis appears to be detrimental is AIDS (acquired immune deficiency syndrome). One of the hallmarks of developing AIDS is the gradual loss of CD4⁺ T-cells. It was recently shown that the vast majority of CD4⁺ T-cells do not die by apoptosis but rather caspase-1 dependent pyroptosis. Especially cells undergoing an abortive HIV (human immunodeficiency virus) infection die by pyroptosis suggesting caspase-1 as a new target for AIDS medication⁵³.

1.4 Caspase-1

Mammalian genomes encode two groups of caspases (cysteine-dependent aspartate-directed proteases), the apoptotic caspases including caspase-3, caspase-7, caspase-8 and caspase-9, and the inflammatory caspases caspase-1, caspase-12 and caspase-4 and caspase-5 in humans or caspase-11 in rodents⁵⁴. The inflammatory caspases are all present in a single genomic locus. This localization suggests a close evolutionary relationship and possibly the emergence of the different inflammatory caspases by gene duplication^{55,56}.

Caspase-1 was the first inflammatory caspase to be described. It was discovered as protease processing pro-IL-1 β into the mature form and received the name ICE (interleukin-1 converting enzyme)^{27,57–59}. Caspase-1 itself is synthesized as an inactive zymogen called pro-caspase-1²⁷. Pro-caspase-1 is recruited to the inflammasome where it undergoes proximity-induced autocatalytic processing yielding active caspase-1²⁸. While pro-caspase-1 is composed of a N-terminal CARD followed by the catalytic p20 and p10 subunits, all separated by linkers, the active caspase-1 consists of a heterotetramer of two p20 and two p10 subunits²⁷. The active site of caspase-1, cysteine 284 in mice or cysteine 285 in humans, is located in the p20 domain but the p10 is equally essential for the proteolytic activity. Caspase-1 shows a relatively narrow substrate specificity exemplified by the fact that most mutations in the target peptide abrogate its cleavage by caspase-1⁶⁰. Interestingly, the three-dimensional structure of the caspase-1 target seems not to be important as caspase-1 cleaves native and denatured IL-1 β with nearly the same kinetics⁶⁰. Despite the substrate-specificity, many additional caspase-1 substrates have been identified *in vitro*^{55,61}. One of the best substrates of caspase-1 besides IL-1 β and IL-18 is gasdermin-D (see below)^{30,31}. An additional caspase-1 substrate is GAPDH (glyceraldehyde 3-phosphate dehydrogenase) involved in glycolysis, an essential pathway for the generation of ATP. However, the relevance of many of the additional caspase-1 substrates *in vivo* is still unknown, since for example GAPDH cleavage requires a 50 times higher caspase-1 concentration than IL-1 β cleavage. Nonetheless, GAPDH-cleavage has been observed after inflammasome activation⁶².

Clearly, the main functions of caspase-1 are induction of pyroptosis by cleavage of gasdermin-D, and possibly additional yet unknown targets (see below)^{30,31}, and the cleavage and maturation of the pro-inflammatory cytokines pro-IL-1 β and pro-IL-18 (see above)^{55,56,63}. While the catalytic activity of caspase-1 is required for both, py-

roptosis and IL-1 β /-18 secretion, autoproteolytic maturation is not required for pyroptosis. Mutating the various auto-cleavage sites within caspase-1 (D103, D122, D296, D308, D313, D314 in murine caspase-1) rendered cells incapable of IL-1 β secretion after inflammasome activation but pyroptosis was still observed⁶⁴. Additionally, inflammasome-dependent caspase-1 maturation required the adaptor protein ASC. Yet, if the receptor contained a CARD instead of a PYD, absence of ASC did not impair cell death because CARD-containing receptors are able to directly interact with caspase-1 (see below)^{64,65}. Thus, the level of autoprocessing of caspase-1 controls the downstream signaling pathways, although the exact mechanism has remained unclear. Proposed mechanisms include differential substrate specificity or differential levels of activity. Consistent with its role in cell culture, *Casp1* deficient mice display a higher bacterial burden after infection with *S. Typhimurium*, *Francisella tularensis* or *Legionella pneumophila*, reinforcing the importance of the inflammasome during infections⁶⁶⁻⁶⁸.

the death-fold containing proteins are involved in signaling pathways for programmed cell death like apoptosis and pyroptosis. The different subfamilies, DD (death domain), DED (death effector domain), PYD and CARD, all display some specific distinguishing them from each other. DDs have a more exposed H3, DEDs have an additional hydrophobic patch and a RxDL-motif in the H5-H6 loop, PYDs have a short H3 and an extended H2/H3 loop while CARDS have a bent and broken H1 (split into H1a and H1b)⁷⁴. All the death-fold domains are evolutionarily related and the differences are thought to have arisen due to the necessity for binding specificity⁷⁴.

The PYD is the newest member of the death-fold superfamily⁷⁵ and the PYD of human ASC (ASC^{PYD}) was one of the first PYD structures to be solved⁷⁶ (**Fig. 1.3**). The ASC^{PYD} is able to interact with itself as exemplified by the appearance of filamentous structures if the ASC^{PYD} is overexpressed in cells and the aggregation of ASC^{PYD} at neutral pH *in vitro*. At acidic pH, ASC^{PYD} is soluble providing the basis for NMR studies of the domain⁷⁶. Importantly, the structure of monomeric ASC^{PYD} seems to be the same at acidic and neutral pH^{76,77}.

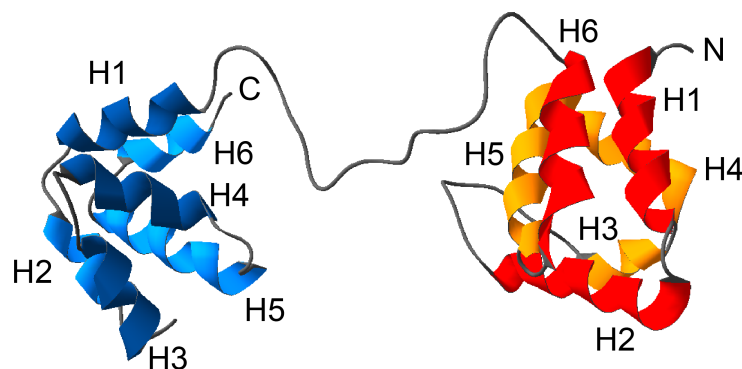


Figure 1.3: **Structure of ASC.** Ribbon representation of the solution structure of monomeric full-length human ASC (PDB 2KN6⁷⁷). CARD colored in dark blue (front) and light blue (back) and PYD colored in red (front) and orange (back). N denotes the N-terminus, C the C-terminus, H1-H6 represent the six characteristic helices of death-fold domains.

As the ASC^{PYD}, the CARD of ASC (ASC^{CARD}) is also able to form filamentous structures in cells^{77,78}. The structure of the ASC^{CARD} shows some peculiarities: While H1 in CARDS is usually fragmented into H1a and H1b, the ASC^{CARD} lacks the H1a fragment and H2 and H3 are in an unusual orientation implying further adaptations towards binding specificity (**Fig. 1.3**)⁷⁷.

ASC^{PYD} and ASC^{CARD} are connected by a relatively long linker of 23 amino acids in humans and 22 amino acids in mice. It displays some residual structure in NMR spectra but overall it is in an extended conformation. This linker flexibility is thought to increase the space being available to be scanned by either domain in order to enhance the chance of protein-protein interactions (**Fig. 1.3**)⁷⁷.

As both domains are involved in protein-protein interactions, extensive mutational analyses of surface exposed residues were conducted. Surface exposed residues of the ASC^{PYD} were mutated to alanine or charge reversals were introduced and the effect on PYD oligomerization was analyzed *in vitro* or in cellular overexpression systems (**Tab. 1.1**). In general, PYD-PYD interactions rely heavily on the opposing charges of two large surfaces. The positively charged surface formed by H2 and H3 interacts with the negatively charged surface formed by H1 and H4 as well as the loop between H3 and H4, referred to as type I interaction^{79,80}. The same interaction interfaces were shown to be important for interactions of ASC^{PYD} with the PYDs of Pyrin, NLRP3 (NLR-family PYD-containing protein 3) and AIM2 (absent in melanoma 2)^{80–83}. Other death-fold domains do not only rely on type I interactions but also employ type II interactions (H4 and loop between H4 and H5 interacting with the H5-H6 loop) and type III interactions (H3 interacting with H1-H2 loop and H3-H4 loop)⁸⁴. Consistently, type II and III interactions were later shown to be involved in ASC^{PYD} oligomerization and interactions with other PYDs^{81,85}.

Table 1.1: **Previously mutated residues in the ASC^{PYD} and their effect on oligomerization.** "Residue" denotes the residues mutated in human ASC^{PYD} while "in mice" denotes the corresponding residues in murine ASC. "Mutation" is the amino acid that was introduced while "effect" describes whether the mutation abrogated (–), diminished (+/–) or did not change (+) interactions of ASC^{PYD} with itself (readout depending on the original study).

residue	mutation	effect	in mice	residue	mutation	effect	in mice
R3	A	+/- ⁸¹ ;+ ^{79,80}	R3	Q		- ⁷⁹	
R5	A	+ ⁷⁹	R5	R41	K	+ ⁷⁹	R41
D6	A	+ ⁷⁹	D6		W	- ⁷⁹	
I8	A	- ⁷⁹	I8	L44	A	+ ⁷⁹	L44

Table 1.1: **Previously mutated residues in the ASC^{PYD}.**

residue	mutation	effect	in mice	residue	mutation	effect	in mice
D10	A	+ ^{79,80}	D10	L45	A	- ⁷⁹	L45
L12	A	- ⁷⁹	L12		I	+ ⁷⁹	
E13	A	- ⁸⁵ ;+/- ⁸⁰ ;+ ⁷⁹	E13		E	+ ⁷⁹	
	R	- ⁸¹		Q	+ ⁷⁹		
L15	A	- ⁷⁹	L15	M47	A	- ⁷⁹	M47
E18	A	+ ^{79,80}	E18		L	+ ⁷⁹	
E19	A	- ^{79,85}	E19		I	+ ⁷⁹	
	Q	+ ⁷⁹			V	+ ⁷⁹	
L20	A	- ⁷⁹	L20	Q	- ⁷⁹		
	A	- ^{79,80,85}		N	- ⁷⁹		
K21	Q	- ^{79,81}	K21	D48	A	- ^{79,80,85}	D48
	R	+ ⁷⁹			N	- ^{79,81}	
	E	- ⁷⁹			E	- ⁷⁹	
K22	A	+ ⁷⁹	K22	R	- ^{79,81}		
F23	A	- ⁷⁹	F23	L50	A	+/- ⁸¹ ;+ ⁷⁹	I50
	L	+ ⁷⁹		A	- ^{79,80,85}		
K24	A	+ ⁷⁹	K24	D51	N	- ⁷⁹	D51
	A	- ^{79,85}			E	+ ⁷⁹	
	M	+ ⁷⁹			R	- ⁸¹	
	I	+ ⁷⁹		K	- ⁷⁹		
	V	+ ⁷⁹		L52	A	- ⁷⁹	L52
L25	F	+ ⁷⁹	L25	D54	A	+ ^{79,80}	D54
	G	- ⁷⁹		K55	A	+ ⁷⁹	K55
	Q	- ⁷⁹		L56	A	- ⁷⁹	L56
	N	- ⁷⁹		V57	A	+ ⁷⁹	V57
	K	- ⁷⁹		F59	A	- ⁸¹ ;+ ⁷⁹	Y59
	E	- ⁷⁹		L61	A	+ ⁷⁹	L61
	A	- ^{79,85}		K26	E62	A	- ⁷⁹ ;+ ⁸⁵
E	- ⁸¹	Q	+ ⁷⁹		E62		
Q	- ⁷⁹	T63	A		+ ⁸⁰	S63	
L27	A	- ⁷⁹	L27	E67	A	- ⁷⁹ ;+ ^{80,85}	E67
	R	+ ⁷⁹			Q	+ ⁷⁹	
L28	A	+ ⁷⁹	L28	L68	A	- ^{79,85}	L68
V30	A	+ ⁷⁹	V30	V72	A	- ⁷⁹	V72
P31	A	+ ⁷⁹	Q31	L73	A	- ⁸⁵ ;+ ⁷⁹	L73
L32	A	+ ⁷⁹	L32	R74	A	+ ^{79,80}	R74

Table 1.1: **Previously mutated residues in the ASC^{PYD}.**

residue	mutation	effect	in mice	residue	mutation	effect	in mice
R33	A	+ ⁷⁹	R33	D75	A	+ ⁷⁹	D75
E34	A	+ ^{79,80}	E34	M76	A	- ⁷⁹	M76
Y36	A	+/- ⁸¹	Y36	L78	A	+ ⁷⁹	L78
R38	A	+ ^{79,80}	R38	E80	A	- ⁷⁹ ;+ ⁸⁰	E80
I39	A	+ ⁷⁹	I39	R		+/- ⁸¹	
R40	A	- ⁷⁹	P40	M81	A	+ ⁷⁹	L81
R41	A	- ^{79,80,85}	R41	Q84	A	- ⁸⁰	Q84
	E	- ⁸¹		L85	A	+ ⁷⁹	L85

A similar mutational approach for surface exposed residues was taken for ASC^{CARD} probing their involvement in interactions with itself and the CARD of caspase-1 (caspase-1^{CARD}, **Tab. 1.2**)^{85,86}. Again, type I interactions have proven to be crucial for both, ASC^{CARD} oligomerization and its interaction with caspase-1^{CARD}⁸⁶.

Regarding oligomeric ASC, the structure of the filament formed by human ASC^{PYD} was solved using cryo-electron microscopy⁸¹. The ASC^{PYD} filament is a 3 start helix with an inner diameter of 20 Å and outer diameter of 90 Å displaying a 53° right-handed rotation and 14.0 Å axial rise per subunit⁸¹. In this filament, the extensive (880 Å²) type I interactions connect the subunits of a strand while the less extensive type II (540 Å²) and type III (360 Å²) interactions connect the different strands. There are some differences between the structure of the soluble ASC^{PYD} and the ASC^{PYD} in the filament, especially in the long H2-H3 loop and the short H3, but overall the two structures overlap quite well⁸¹.

In accordance with the function of ASC as inflammasome adaptor (see below), ASC^{PYD} filament formation can be nucleated by the PYDs of AIM2 and NLRP3 which is shown by an enhanced oligomerization speed of ASC^{PYD} in presence of either AIM2^{PYD} or NLRP3^{PYD} *in vitro*. Additionally, substoichiometric amounts of AIM2^{PYD} and NLRP3^{PYD} are located at one end of ASC^{PYD} filaments⁸¹. Furthermore, it has been shown that the ASC^{PYD} has prion like properties. After filament nucleation, the ASC^{PYD} undergoes a slight structural rearrangement which is then propagated to further ASC^{PYD} subunits during filament formation. This suggests that ASC^{PYD} filament formation is an all-or-nothing, irreversible process^{87,88}.

No similar oligomeric structure is known for the ASC^{CARD} so far but the oligomeric state of full length ASC, the ASC speck, has been investigated using high-resolution fluo-

rescence microscopy and electron microscopy. The analysis revealed that ASC speck has an irregular, filamentous structure with a denser core^{88,89} but in-depth structural analyses of the ASC speck are missing.

Table 1.2: **Previously mutated residues in the ASC^{CARD} and their effect on oligomerization.** "Residue" denotes the residues mutated in human ASC^{CARD} while "in mice" denotes the corresponding residues in murine ASC. "Mutation" is the amino acid that was introduced while "effect" describes whether the mutation abrogated (-), diminished (+/-) or did not change (+) interactions of ASC^{CARD} with itself⁸⁵ or caspase-1⁸⁶ (readout depending on the original study).

residue	mutation	effect	in mice
R125	D	- ⁸⁶	R123
E130	R	- ⁸⁶	D128
D134	R	- ⁸⁶	D132
Y137	E	- ⁸⁶	H135
D143	A	+ ⁸⁶	E141
E144	R	- ⁸⁶	G142
Q145	A	+ ⁸⁶	Q143
Y146	E	+ ⁸⁶	Y144
R150	E	+ ⁸⁶	R148
M159	A	- ⁸⁵	M157
R160	E	- ⁸⁶	R158
	A	- ⁸⁵	
D191	R	- ⁸⁶	D189

1.5.2 Function of ASC

ASC was initially identified in cancer cell lines where it aggregated into speck-like, macromolecular complexes in the cellular periphery of apoptotic cells. Furthermore, its expression correlated with increased sensitivity to apoptotic stimuli²⁵. Apart from being involved in apoptosis, ASC was initially implied in NF- κ B signaling. Conflicting reports emerged whether ASC enhances or impairs NF- κ B signaling, but later studies suggested that ASC is not involved in NF- κ B signaling at all⁹⁰⁻⁹³.

Besides, it was described that the promoter of ASC is a target of hyper-methylation thereby silencing ASC expression. This was observed in various cancer cell lines and primary isolates of breast cancers leading to the alternative name TMS-1 (target of

methylation-induced gene silencing). Mechanistically, loss of ASC expression was proposed to provide cancer cells with the ability to escape cell death thereby enhancing proliferation^{92,94}. Methylation-induced silencing of ASC has since also been associated with additional types of cancers like prostate and colorectal cancer^{95–97}.

With the emergence of the inflammasome as important step in caspase-1 activation, the role of ASC became better defined²⁸. After activation (and oligomerization) of PYD-containing inflammasome receptors (see below), ASC is recruited via PYD-PYD interactions. This interaction serves as nucleation point for ASC oligomerization and speck formation. The ASC speck is the large, macromolecular form of the inflammasome with a size of approximately 1-2 μm ^{25,98}. Aggregation of the ASC speck was reported to be a quick process with all soluble ASC incorporated into the speck in less than three minutes^{98,99}. The ASC speck is largely insoluble and its formation is independent of caspase-1, although pro-caspase-1 is recruited to it^{64,98}. ASC specks can be released by pyroptosis and might be taken up by phagocytic cells where they initiate further pro-inflammatory signaling events. Moreover, ASC specks were detected in extracellular fluids of patients with CAPS (cryopyrin associated periodic syndrome), an auto-inflammatory disease characterized by constitutive inflammasome activation due to mutations in NLRP3 (see below)^{88,89}.

It was proposed that after recruitment to the ASC speck, caspase-1 forms filaments on its own via its CARD^{81,100}. However, the physiological role of caspase-1^{CARD} filaments was not determined yet. Nonetheless, recruitment of pro-caspase-1 leads to its activation by proximity-induced auto-processing into the active caspase-1 p10/p20 heterotetramer. Active caspase-1 in turn cleaves the pro-inflammatory cytokines pro-IL-1 β and pro-IL-18 into their bioactive forms which are then released (see above)^{27,81}.

Consistent with its role as adaptor, ASC deficient cells fail to induce pyroptosis and cytokine secretion after stimulation of PYD-containing receptors like NLRP3, AIM2 or Pyrin^{23,24}. Furthermore, ASC also plays an important role *in vivo*. *Asc* knock-out mice, similarly to *Casp1* knock-out mice, have a significantly higher bacterial burden and mortality after infection with *Francisella tularensis* compared with wild type⁶⁸.

In the case of the NLRC4 (NLR-family CARD-containing protein 4) inflammasome (see below), the role of ASC is different. NLRC4 has a CARD instead of a PYD and is able to directly interact with the caspase-1^{CARD}, thereby seemingly bypassing the requirement of ASC⁶⁵. Consistently, cell death after NLRC4 activation in cells is independent of ASC. Nonetheless, if present, ASC forms a speck after NLRC4 activation and the amount of secreted cytokines is markedly enhanced^{64,67,91,101}. In an *in vivo* model of

S. Typhimurium infection, a potent activator of NLRC4, ASC has only a limited effect. Even though cytokine levels were markedly reduced in *Asc* deficient mice, the disease outcome was similar to wild type mice indicating that pyroptosis is the main innate immune response against *S. Typhimurium*¹⁰².

Collectively, ASC plays an important role in innate immunity as an adaptor for inflammasomes. Despite the fact that ASC speck formation is observed after activation of all known inflammasome receptors, it was not directly shown that the ASC speck or ASC filaments are indeed required for inflammasome signaling¹⁰³. Furthermore, it is not clear how CARD-containing receptors like NLRC4 recruit ASC to form the ASC speck.

1.5.3 Regulation of inflammasomes on the level of ASC

As inflammasomes are important and potent signaling complexes, they need to be tightly regulated. The most studied regulation step is the activation of the different receptors, which will be discussed below for the different receptors individually. But also ASC itself and its oligomerization are regulated in multiple ways. The first mechanism is to control the expression of ASC. Hypermethylation of the CpG-island in the ASC promoter leads to transcriptional repression and thereby blocks the expression of ASC, as observed in many cancer cells, thereby efficiently blocking pyroptosis⁹⁴.

But also the localization of ASC is crucial for inflammasome activation and signaling. While in resting cells ASC is primarily localized in the nucleus, ASC needs to relocate into the cytosol for inflammasome assembly. This happens during the priming phase of the cells and retaining ASC in the nucleus by using a fusion protein with a nuclear localization sequence prevents IL-1 β release after NLRP3 stimulation¹⁰⁴. It was proposed that ASC is associated with IKK α (I κ B kinase α) in the nucleus in resting cells. The priming signal then enables translocation of the ASC/IKK α complex out of the nucleus which requires the kinase activity of IKKi (IKK related kinase). Once in the cytoplasm, the second signal leads to the dissociation of the ASC/IKK α complex enabling interaction of ASC with the receptor and the formation of the speck¹⁰⁵.

Post translational modifications were shown to be involved in multiple innate immune signaling pathways and also in inflammasome signaling¹⁰⁶. Phosphorylation of human ASC on residues Y146 and Y187 (or the corresponding murine ASC residue Y144) located in the ASC^{CARD} in a Syk (spleen tyrosine kinase) and / or JNK (c-Jun N-terminal kinase) dependent way was reported. In absence of ASC phosphorylation the formation of ASC specks is reduced and less IL-1 β is secreted after NLRP3 and AIM2 but

not NLRC4 activation^{107,108}. These findings are, however, complicated by the fact that Syk is a negative regulator of pro-IL-1 β and NLRP3 expression after TLR stimulation by extracellular PAMPs¹⁰⁸. Recently, it was shown that, downstream of Syk, Pyk2 (proline-rich tyrosine kinase 2) directly interacts with ASC after NLRP3 activation and phosphorylates the human ASC^{CARD} on residue Y146. This phosphorylation enables the formation of ASC specks. On the other hand, ASC speck formation after AIM2 activation is not dependent on Pyk2 but another kinase called FAK (focal adhesion kinase)¹⁰⁹. A kinase related to Syk called BTK (Bruton's tyrosine kinase) was also proposed to modulate ASC activity. BTK associates with ASC and possibly phosphorylates human ASC on Y146 and helps to form the interaction with NLRP3 but BTK is not involved in the AIM2 inflammasome¹¹⁰. Why different kinases are required for ASC^{CARD} phosphorylation after AIM2 and NLRP3 activation and why ASC^{CARD} phosphorylation is not involved in NLRC4 signaling¹¹¹, even though all inflammasome receptors initiate ASC speck formation, is not clear yet. Furthermore, why multiple kinases that phosphorylate the same residues in the ASC^{CARD} exist and how exactly they regulate inflammasome assembly remains to be addressed experimentally.

An additional form of post-translational modification of ASC to regulate inflammasome activity is ubiquitination. It was reported that the linear ubiquitin assembly complex (LUBAC), consisting of HOIL-1L (heme-oxidized IRP2 [iron regulated protein 2] ubiquitin ligase 1L), HOIP (HOIL-1L interacting protein) and SHARPIN (Shank-associated RH [regulator of G-protein signaling homology] domain-interacting protein), directly ubiquitinates ASC *in vitro*. Furthermore, macrophages deficient in HOIL-1L failed to release IL-1 β after NLRP3 stimulation and displayed reduced IL-1 β release after AIM2 activation. Therefore, linear ubiquitination of ASC seems to promote inflammasome function¹¹². Conversely, ASC was shown to display K63-linked ubiquitination after AIM2 activation directing it to autophagy dependent degradation and decreasing inflammasome signaling¹¹³. Furthermore, viral infections were shown to cause K63-linked ubiquitination of ASC on residue K174 by TRAF3 (TNFR [tumor necrosis factor receptor]-associated factor 3). This K63-linked ubiquitination seemed to enhance NLRP3 inflammasome activation¹¹⁴. However, how these contradictory reports of the role of ubiquitination of ASC can be reconciled and why no involvement of ubiquitination was observed after NLRC4 activation^{112,114} remains to be determined.

Furthermore, a set of proteins only consisting of a CARD or a PYD, termed COPs (CARD only proteins) and POPs (Pyrin only proteins), respectively, thought to be involved in inflammasome regulation exists in humans and related primates but not in

rodents. Additionally, some viruses encode viral POPs (vPOPs)^{115,116}. Humans express 3 COPs called CARD16 (COP/Pseudo-ICE), CARD17 (INCA, inhibitory CARD) and CARD18 (ICEBERG). They are all encoded in the same gene cluster as the pro-inflammatory caspases-1, -4, -5, and -12 and are thought to have arisen from gene duplications of caspase-1, with which they share the highest homology. Nonetheless, different functions were attributed the COPs^{115,116}. CARD16 has the highest homology to caspase-1^{CARD} and exists in two isoforms, a long and a short one. While nothing is known about the long isoform, the short isoform was initially described to interact with the caspase-1^{CARD} and to block IL-1 β release^{117,118}. A more recent study found that CARD16 not only interacts with caspase-1 but also with ASC and thereby promotes the formation of caspase-1^{CARD} filaments and subsequently enhances IL-1 β release¹¹⁹. But the mechanism of this enhanced caspase-1 oligomerization is yet unknown. Also CARD17 was first described to interact with caspase-1^{CARD}¹²⁰. Conflicting reports exist concerning the interaction between CARD17 and ASC^{CARD}, but the possible interaction between CARD17 and ASC^{CARD} seems not have any consequences on ASC oligomerization or speck formation^{100,119}. Yet, CARD17 blocks the oligomerization of caspase-1 by capping growing caspase-1^{CARD} filaments *in vitro* and efficiently blocks caspase-1 activation and cytokine release¹⁰⁰. CARD18 was described as yet another inhibitor of IL-1 β production by binding to caspase-1^{CARD}^{117,121}. It has since been suggested that CARD18 associates with caspase-1^{CARD} filaments but its overexpression does not change IL-1 β levels therefore questioning the role as caspase-1 inhibitor¹⁰⁰.

In contrast to the COPs, that all arose from caspase-1 gene duplications, the three POPs arose from different gene duplications. The most interesting POP regarding ASC is POP1 that originated from a duplication of exon 1 of ASC coding for the ASC^{PYD} and displays 64% identity to the ASC^{PYD}^{115,116}. POP1 can interact with ASC^{PYD} and as the structure of POP1 is highly similar to ASC^{PYD}, ASC^{PYD}/POP1 interactions are very similar to ASC^{PYD}/ASC^{PYD} interactions^{122,123}. The effect of this ASC^{PYD}/POP1 interaction was first reported to promote IL-1 β release¹²², but further analysis showed an opposite phenotype¹²⁴. Stable knock-down of POP1 increases IL-1 β release while overexpression decreases IL-1 β release in the human monocytic cell line THP-1. Furthermore, transgenic mice expressing human POP1 in the macrophage / dendritic cell lineage have lower levels of IL-1 β after systemic NLRP3 challenge¹²⁴. Mechanistically, POP1 binds to ASC^{PYD} and thereby blocks the interaction of ASC with a PYD-containing receptor^{123,125}. The exact effect of POP1 on inflammasome signaling via CARD-containing receptors warrants further investigation, although experimental evi-

dence suggest a similar function than for PYD-containing receptors¹²⁴. POP2 shows the highest similarity to the PYD of NLRP2 (69% amino acid similarity) and it is able to interact with ASC, NLRP1, NLRP3 and NLRP12. Consequently, it blocks IL-1 β release after activation of NLRP1 and NLRP3 inflammasomes. The mechanism is suggested to be either binding to ASC^{PYD} and preventing interaction with the receptor or binding to the PYD of the receptor and thereby blocking recruitment of ASC^{115,116,126}. POP3 seems to have arisen from a partial gene duplication of AIM2, with whose PYD (AIM2^{PYD}) it shares 61% sequence identity. POP3 does not interact with ASC^{PYD} but only with AIM2^{PYD}, thereby blocking ASC recruitment and blocking inflammasome signaling after AIM2 activation¹²⁷. Interestingly, some poxviruses have acquired vPOPs via horizontal gene transfer and employ them in their immune evasion strategies. Myxoma and Shope Fibroma virus encode a POP1/ASC^{PYD} homologue each, called ML013L and gp013L, respectively. Both proteins co-localize with the ASC speck and interact with ASC. Moreover they inhibit IL-1 β release thereby facilitating the host colonization by the virus^{128,129}.

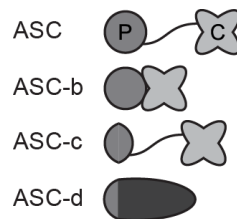


Figure 1.4: **ASC isoforms.** P, PYD; C, CARD. Adapted from Bryan *et al.*¹³⁰

Lastly, alternative splicing variant of ASC were discovered in both humans and mice (**Fig. 1.4**). ASC-b consists of the ASC^{PYD} and the ASC^{CARD} without the flexible linker, ASC-c lacks H3-H6 of ASC^{PYD} but retains the linker and the ASC^{CARD} and ASC-d consists of ASC^{PYD} H1 and H2 and a novel 69-amino acid peptide without homology to any known domain. While ASC and ASC-b are able to interact and co-localize with NLRP3, ASC-c and ASC-d do not. On the other hand, co-localization with caspase-1 was observed for ASC, ASC-b and ASC-d, all containing a complete CARD^{130,131}. Functionally, some discrepancies were reported. While one group reported that inflammasome reconstitution with ASC-b leads to higher IL-1 β levels than reconstitution with ASC¹³¹, the second group reported that co-expression of ASC-b with ASC reduces IL-1 β levels below the level of ASC expression alone¹³⁰. ASC-c inhibits IL-1 β secretion

and as it mainly consists of a CARD it might be regarded as another COP while ASC-d does not have any influence on IL-1 β secretion¹³⁰.

Collectively, many regulatory mechanisms were described controlling inflammasomes on the level of ASC but vastly diverging outcomes were reported for some mechanisms. This might be due to the experimental settings as most studies were done in overexpression systems or *in vitro* calling for better characterization in more realistic conditions, for example by generation of knock-out cell lines and the expression of physiological levels of the different proteins.

1.6 Receptors

All known inflammasome receptors belong either to the ALR (AIM2 like receptors) family, to the NLR (Nod-like receptor) family, or Pyrin. However, not all of the receptors directly bind to a ligand but some rather act as adaptor molecules.

1.6.1 NLRP3

In 2004, NLRP3 (NLR-family PYD-containing protein 3, also called Cryopyrin or Nalp3) was for the first time described to be able to initiate inflammasome formation¹³². Even though NLRP3 is the most extensively studied inflammasome receptor so far, the exact mechanisms and signals leading to its activation are still unclear and its physiological role is debated¹³³. Interestingly, basal expression of NLRP3 is not sufficient for inflammasome activation which therefore relies on a two-step activation mechanism. A first priming step upregulates NLRP3 expression in a NF- κ B dependent manner downstream of TLR signaling, a pathway also leading to pro-IL-1 β expression^{134,135}. Furthermore, also post-translational modifications like deubiquitination of NLRP3 by BRCC3 (BRAC1/BRAC2-containing complex) are part of the priming process¹³⁶⁻¹³⁸. A second activation step is then required to initiate inflammasome formation. This second signal can be one of a large group of chemically different substances including crystalline and particulate matters (monosodium urate [MSU] crystals, silica, asbestos and alum), pore-forming toxins and ionophores, extracellular ATP and several substances of pathogenic origin (viral, bacterial, fungal and protozoan)³⁷. As these stimuli are chemically diverse they probably do not directly bind to NLRP3 but rather converge on a common signal¹³⁹. Multiple mechanisms have been proposed to take over this function: The production of ROS (reactive oxygen species), mitochondrial damage and lysosomal rupture¹⁴⁰. The best candidate as a common trigger for NLRP3 activation is, however, the efflux of K⁺ and a concomitant drop of intracellular K⁺ concentrations¹⁴¹. While depletion of intracellular K⁺ is sufficient to trigger NLRP3 inflammasome activation acting either on or upstream of NLRP3, the exact mechanisms of NLRP3 activation are still unknown¹⁴¹. On the other hand, mitochondrial perturbation and ROS production were not required for NLRP3 activation, although both is frequently observed with stimuli activating NLRP3¹⁴¹.

The main groups of NLRP3 activators are K⁺ ionophores, extracellular ATP and crystalline / particulate substrates¹⁴². The discovery that extracellular ATP leads to secretion of mature IL-1 β and that it leads to a drop in intracellular K⁺ concentration predates

the discovery of inflammasomes by nearly a decade^{28,143}. Millimolar concentrations of extracellular ATP activate NLRP3 by inducing K⁺ efflux via P2X₇R (P2X₇ receptor)¹⁴⁴. P2X₇R is an ion channel which opens after ATP binding and facilitates the exchange of intracellular K⁺ for extracellular Na⁺ and Ca²⁺ efficiently decreasing intracellular K⁺ concentrations¹⁴⁵. Also nigericin was known as IL-1 β trigger before the discovery of the inflammasome^{28,143}. Nigericin is one of the most commonly used triggers for NLRP3 activation¹⁴⁴. It can either exist in a free, membrane-impermeant anionic form or as neutral, membrane-permeant form when bound to either K⁺ or H⁺. In one cycle, protonated, extracellular nigericin enters the cells where the proton is released and exchanged with a potassium ion. The potassium-bound nigericin then crosses the plasma membrane once more thereby dissipating the K⁺ gradient without changing the charge of the cell¹⁴⁶. There are also other ionophores that are able to induce NLRP3 activation like gramicidin¹⁴⁷. Gramicidin is a peptide inserting into the plasma membrane and facilitates K⁺ efflux balanced by Na⁺ influx leading to NLRP3 activation¹⁴⁸.

The mechanism of NLRP3 activation by crystalline and particulate stimuli is less clear. These stimuli including monosodium urate crystals (MSU)¹⁴⁹, which is associated with gout, and alum^{150,151}, an adjuvant approved for use in humans, are taken up by phagocytes. However, at one point along the phagocytosis pathway, lysosomal rupture is observed leading to K⁺ efflux in an unknown fashion resulting in NLRP3 activation¹⁴². Recently, a new mechanism was proposed to detect intracellular gram-positive bacteria. *N*-acetylglucosamine originating from the gram-positive cell wall binds to the glycolytic enzyme hexokinase. This leads to the inactivation of hexokinase and its dissociation from its usual binding partner VDAC (voltage-dependent anion channel) in the mitochondrial outer membrane. This results in NLRP3 activation in a yet unresolved manner. Interestingly, while NLRP3 dependent IL-1 β release was observed, the cells did not display any signs of pyroptosis. Furthermore, the process is seemingly independent of K⁺ efflux, questioning the role of K⁺ efflux as general NLRP3 activation mechanism¹⁵². Furthermore, another K⁺-independent pathway of NLRP3 activation has been reported¹⁵³. The authors found that imiquimod and the related molecule CL097 inhibited the quinone oxidoreductases NQO2 (NAD(P)H [nicotinamide adenine dinucleotide phosphate] quinone dehydrogenase 2) and the mitochondrial complex I, thus inducing a burst of mitochondrial ROS production and thiol oxidation that led to NLRP3 activation¹⁵³.

As with all inflammasome components, NLRP3 needs to be tightly regulated. To achieve this, several regulatory mechanisms were proposed to control NLRP3 inflammasome

activation. The most important steps are the above mentioned priming step upregulating NLRP3 expression and the activation of NLRP3^{134,135}. But multiple other, modulatory, mechanisms were described. Recently, NEK7 (NIMA [never in mitosis A] related kinase 7) was discovered by three groups independently to be a new, essential component of the NLRP3 inflammasome. NEK7 associates with NLRP3 using its kinase domain but independently of its kinase activity. The NEK7-NLRP3 association is downstream of K⁺ efflux as high extracellular K⁺ levels efficiently blocked the interaction. Interestingly, NEK7 is also involved in mitosis and therefore it was postulated that during mitosis NEK7 is not sufficiently available to interact with NLRP3 thereby blocking simultaneous activation of inflammasomes and mitosis^{154–156}.

But also multiple post-translational mechanisms are acting on NLRP3¹⁰⁶. For example, multiple kinases were shown to enhance NLRP3 signaling including Syk (spleen tyrosine kinase), DAPK (death associated protein kinase), TAK1 (transforming growth factor beta-activated kinase 1), ERK (extracellular signal-regulated kinase) and BTK (Bruton's tyrosine kinase)^{110,111,157–162}. Additionally, ubiquitination of NLRP3 by ubiquitin ligases FBXL2 (F-box/LRR-repeat protein 2) and MARCH7 (membrane associated ring-CH-type finger 7) was shown to downregulate NLRP3 activation^{163,164}. Conversely, deubiquitination of the LRR of NLRP3 by murine BRCC3 or human BRCC36 leads to enhanced NLRP3 activation^{137,138}. Furthermore, S-nitrosylation and ADP-ribosylation were also implicated in NLRP3 regulation^{165–169}. But also proteinaceous components are known to regulate NLRP3 directly. An example is the orphan receptor SHP (small heterodimer partner) that directly binds to and inhibits NLRP3¹⁷⁰. Lastly, also an NLRP3 intrinsic regulatory mechanism was described. The central NOD (nucleotide binding and oligomerization domain) of NLRP3 is able to bind and hydrolyze ATP. Mutations in the NOD abrogating ATP binding also blocked NLRP3 oligomerization and ASC recruitment indicating that ATP binding is required for NLRP3 signaling¹⁷¹.

The importance of NLRP3 regulation is corroborated by the involvement of faulty NLRP3 activation in autoinflammatory diseases^{172,173}. A variety of gain-of-function mutations were discovered in the NOD of NLRP3 leading to enhanced inflammasome activation. These mutations result in autoinflammatory diseases which are collectively referred to as CAPS (cryopyrin-associated periodic syndromes). Depending on the exact mutation as well as additional factors the disease severity varies from FCAS (familial cold autoinflammatory syndrome), as the mildest form, to MWS (Muckle-Wells syndrome) and the most debilitating form, NOMID (neonatal-onset multisystem inflammatory disease) also called CINCA (chronic infantile neurological, cutaneous and articular syndrome)^{174–178}.

The typical symptoms of FCAS are rash, fever and joint pain after cold exposure, while MWS presents with recurrent rashes, hearing loss and amyloidosis. NOMID/CINCA is characterized by the above mentioned symptoms accompanied by mental retardation, meningitis and bone deformities^{172,178}. Treatment of these diseases using IL-1 β blocking agents was shown to be effective in several studies where either the recombinant IL-1 receptor antagonist anakinra, the IL-1 trap rilonacept or the anti-IL-1 β antibody cankinumab were used^{179–181}. Consequently, these drugs were approved for use in CAPS patients by authorities¹⁷².

Besides the mutations of NLRP3 and the resulting autoinflammatory diseases, NLRP3 was also shown to be involved in the pathogenesis of other diseases in mostly age-related conditions. During aging, a progressive, low-grade but chronic inflammatory state is developing. NLRP3 is associated with many chronic inflammatory diseases as it can be triggered by many of the metabolic byproducts. These include MSU crystals in gout, β -amyloid plaques in Alzheimer's disease, free fatty acids and islet amyloid polypeptide in type 2 diabetes and cholesterol crystals in atherosclerosis^{149,182–184}. Also in these diseases, preliminary studies targeting IL-1 β downstream of NLRP3 showed promising results¹⁸⁵.

1.6.2 AIM2

AIM2 (absent in melanoma 2) was initially discovered as a tumor-suppression gene¹⁸⁶. Further studies then correlated AIM2 expression with cancer outcome, i.e. patients without AIM2 expression in cancers cells have a worse prognosis. It is thought that AIM2 has an inhibitory role in cell proliferation thereby reducing cancer growth. Interestingly, the anti-cancer effects of AIM2 are independent of inflammasomes¹⁸⁷.

Only later, a inflammasome complex sensing double stranded DNA (dsDNA) in the cytosol was discovered¹⁸⁸ and the receptor for this complex was identified as AIM2^{189–192}. AIM2 consists of two domains, a PYD (AIM2^{PYD}) required for interaction with ASC^{PYD} and a HIN-200 (hematopoietic interferon-inducible nuclear proteins with a 200-amino-acid repeat) domain required for dsDNA binding. AIM2 seems to recognize any dsDNA, either of bacterial, viral, synthetic origin or even host-derived dsDNA, provided it resides in the cytosol and has a length of at least 80 bases¹⁹³. Structurally, a concave, positive surface of the HIN-200 domain binds the sugar-phosphate backbone of dsDNA creating an interaction surface of 1'000-1'200 Å² resulting in a high binding affinity of the HIN-200 domain to dsDNA¹⁹³. The interaction between AIM2 and dsDNA is highly flexible

allowing multiple AIM2 monomers to closely bind to a stretch of dsDNA which serves as oligomerization hub, a function that is taken over by the NOD (nucleotide binding and oligomerization domain) in NLRs (**Fig. 1.5**)¹⁹³.

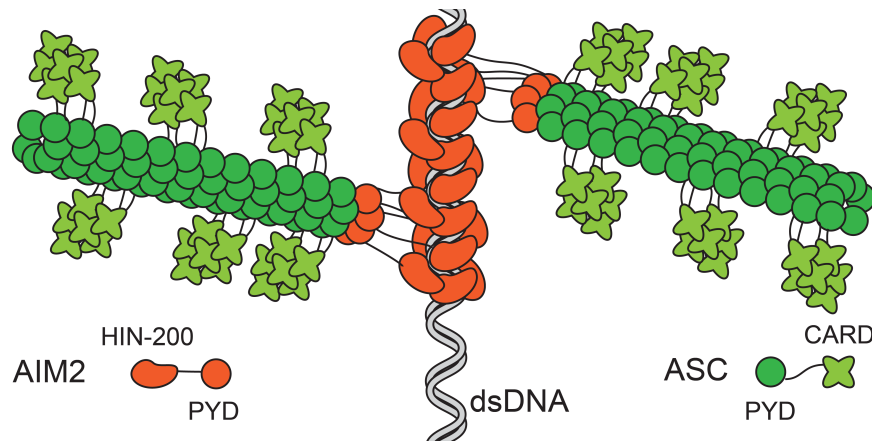


Figure 1.5: **Model of the AIM2 inflammasome.** Adapted from Lu and colleagues¹⁹⁴.

In the resting state, the AIM2^{PYD} binds to the HIN-200 domain thereby keeping it inactive. Similar to the binding of dsDNA, the AIM2^{PYD} binds to the concave, positive surface of the HIN-200 domain. Only dsDNA recognition relieves this auto-inhibition and allows signaling¹⁹⁵. Multiple AIM2 monomers wrap around a stretch of dsDNA in a filament-like fashion bringing their PYDs into close proximity. The relatively long linker between the HIN-200 and the PYD of approximately 50 amino acids stretching a distance of up to 19 nm enables even relatively distant AIM2^{PYDs} to interact. The AIM2^{PYDs} then form short helical arrangements which serve as nucleation platforms for the ASC^{PYD} filaments (**Fig. 1.5**)¹⁹⁴. Consistently, activation of AIM2 in macrophages can be either achieved by sterile delivery (transfection, electroporation) of dsDNA or synthetic dsDNA analogues like poly(dA:dT) (poly [deoxyadenylic-deoxythymidylic] acid). But also infections with certain bacteria like *Francisella tularensis* subspecies *novicida*^{196–201}, *Mycobacterium tuberculosis*^{202,203}, *Listeria monocytogenes*^{204–206} or *Brucella abortus*²⁰⁷ activate AIM2 and in absence of AIM2 reduced caspase-1 activation and IL-1 β release can be observed. While most bacteria also engage other inflammasome receptors, *Francisella* is the only known bacterium that solely activates AIM2. Mice deficient in *Aim2* are generally more susceptible to infections with reduced cytokine serum levels and increased bacterial burdens after *Francisella*^{197–199}, *M. tuberculosis*²⁰⁸, *B. abortus*²⁰⁷ but also *Staphylococcus aureus* challenge²⁰⁹.

Additionally, cell culture experiments also established a role for AIM2 in recognition of certain viruses like MCMV (mouse cytomegalovirus), *Vaccinia virus*, Human papillomaviruses or Hepatitis B virus. But apart from MCMV, where *Aim2* deficiency lead to increased viral titers after infection, the significance of the AIM2 inflammasome during viral infections *in vivo* is unknown^{199,201,210,211}.

Furthermore, the AIM2 inflammasome does not only participate in host defense but aberrant AIM2 activation by host DNA is responsible for elevated IL-1 β levels in patients with acute or chronic skin conditions like psoriasis or arthritis¹⁸⁷. However, mechanisms are in place to prevent auto-activation. Among these are, in humans and other primates, the POPs. Especially POP3, binding to the AIM2^{PYD} thereby blocking ASC recruitment¹²⁷, and POP1, binding to the ASC^{PYD} thereby modulating IL-1 β release, are relevant in the context of the AIM2 inflammasome (see above)^{123–125}. Another modulatory protein of the AIM2 inflammasome is p202. p202 contains tandem HIN-200 domains and is also able to bind to dsDNA in a similar fashion as AIM2. Expression of p202 blocks ASC recruitment to AIM2 as it leads to a separation of AIM2 on the dsDNA placing the AIM2^{PYDs} to far apart to be able to initiate ASC^{PYD} oligomerization. This efficiently blocks inflammasome assembly^{192,212,213}.

1.6.3 Pyrin

Pyrin is encoded by the gene *MEFV* (Mediterranean fever). It was identified to harbor point mutations associated with the autoinflammatory disease FMF (familial Mediterranean fever)^{214,215}. The severity of FMF is varying from patient to patient but it is generally characterized by recurrent episodes of fever and polyserositis¹⁷². The disease is, as the name suggests, mainly confined to the Mediterranean. In some populations up to one third of the people are heterozygous carriers of a mutation suggesting a selective advantage conferred by some mutations. But the selective pressure and why it is confined to the Mediterranean is not known²¹⁶. Most of the known FMF-associated mutations of Pyrin map to the C-terminal B30.2 domain²¹⁶. B30.2 domains were described to be involved in protein-protein interactions²¹⁷ and specifically the Pyrin B30.2 was described to interact with caspase-1²¹⁸. The effect of this interaction is, however, not fully clear and conflicting reports regarding its effect on IL-1 β secretion exist^{219–221}. Interestingly, murine Pyrin lacks the C-terminal B30.2 domain. Knock-ins of human Pyrin B30.2 mutants associated with FMF lead to an FMF-like phenotype in mice. Furthermore, high levels of IL-1 β can be detected in these mice independent of NLRP3

but dependent on ASC suggesting that the FMF-associated mutations lead to the constitutive formation of a Pyrin inflammasome²²². This is consistent with the fact that Pyrin harbors an N-terminal PYD and interacts with ASC^{PYD83,221}. However, the signal leading to Pyrin inflammasome formation, in absence of FMF-associated mutations, was only described recently to be inactivation of Rho (Ras homology gene family) GTPases, specifically RhoA, but not Cdc42 (cell division control protein 42 homolog) and Rac1 (Ras-related C3 botulinum toxin substrate 1)²²³. Rho GTPases are crucial for cell homeostasis and cytoskeleton function²²⁴. They are therefore often targeted and inactivated by pathogens to control host cell behavior. Examples for this are the glucosylation of RhoA by the *Clostridium difficile* toxin B (TcdB), the adenylylation by *Histophilus somni* effector protein IbpA and *Vibrio parahaemolyticus* effector protein VopS, the ADP-ribosylation by *Clostridium difficile* C3 toxin or the deamination by *Burkholderia cenocepacia* in a type VI secretion system dependent manner^{223,225}. Additionally, Pyrin must be dephosphorylated to be activated²²⁶ and this can be exploited by pathogens. For example *Yersinia* prevents Pyrin activation by induction of Pyrin phosphorylation therefore keeping it in an inactive state despite modifications of Rho GTPases²²⁷. Thus, Pyrin is activated by disturbances of cell homeostasis during infections and not by sensing the pathogens themselves²²³.

So far, however, the relevance for the Pyrin inflammasome in fighting bacterial infections has only been shown for *B. cenocepacia*²²³. Furthermore, the role of Pyrin might be even more complex. It was recently suggested that Pyrin directs NLRP3 but also NLRP1 and pro-caspase-1 to autophagy-dependent degradation thereby decreasing inflammasome activation and that this function is affected by FMF-associated mutations²²⁸. Collectively, additional work needs to be conducted to elucidate the physiological role of Pyrin, especially *in vivo*, and to address the exact mechanisms by which the FMF-associated Pyrin mutations cause disease in order to specifically treat patients. The standard treatment for FMF is a daily dose of colchicine^{229–232}, an inhibitor of microtubule polymerization which is toxic at higher doses²³³. Recently, targeting IL-1 β with anakinra or canakinumab showed promising results in some patients¹⁷². However, the need for safe and less expensive drugs still persists.

1.6.4 NLRC4

The NLRC4 (NLR-family CARD-containing protein 4) inflammasome was shown to be activated in response to bacteria in the cytosol by detecting T3SS (type III secretion sys-

tem) components and flagella^{91,234–236}. A group of other NLR proteins, known as NAIPs (NLR family, apoptosis-inhibitory protein), act as co-receptors for NLRC4 by directly binding these ligands and initiating NLRC4 oligomerization. NAIPs have a tri-partite domain organization containing an N-terminal BIR-domain (Baculovirus inhibitor of apoptosis protein repeat), a central NOD (nucleotide binding and oligomerization domain) and C-terminal LLRs (leucine rich repeats). While the human genome only encodes a single NAIP, the murine genome encodes seven NAIPs probably originating from gene duplications^{237,238}. Using the central NOD, the NAIPs bind to different components from T3SS or flagella. Specifically, murine NAIP1 binds to the T3SS needle subunit, murine NAIP2 to the T3SS rod subunit and murine NAIP5 or NAIP6 to flagellin²³⁹. As humans only encode a single NAIP, it is assumed that different splice variants show different binding specificities and take over the roles of the different mouse orthologues²⁴⁰. Once bound to their ligand, NAIPs are relieved from their auto-inhibited state and are able to recruit NLRC4. NLRC4 is another member of the NLR-family consisting of C-terminal LRRs, a central NOD and an N-terminal CARD. Also NLRC4 is present in an auto-inhibited state where the LRRs prevent protein-protein interactions via the CARD of NLRC4²⁴¹. Ligand-activated NAIPs interact with inactive NLRC4 and induce structural rearrangements in NLRC4 that relieve its auto-inhibitory state and exposing a so-called "activating" surface. This then enables sequential recruitment of further NLRC4 monomers, concomitantly relieving auto-inhibition. Finally, one active NAIP recruits 9–11 NLRC4 monomers into a wheel-like structure. This wheel-like structure then recruits ASC and caspase-1 leading to caspase-1 activation and finally cytokine secretion and pyroptosis^{242–245}. Therefore, minute amounts of cytosolic, bacterial PAMPs can lead to a massive immune response. However, how the CARD-containing NLRC4 recruits ASC is not known.

To control and prevent aberrant NLRC4 activation, it was suggested that NLRC4 activation requires phosphorylation of S533 by PKC γ (protein kinase C delta type). Absence of S533 phosphorylation correlated with decreased IL-1 β levels after NLRC4 activation^{246,247}.

As NLRC4 contains a CARD, it was shown that it is able to directly interact with caspase-1 in absence of ASC^{65,248}. This interaction leads to an active form of caspase-1 and results in pyroptosis. However, caspase-1 is not auto-processed and no IL-1 β release can be observed in absence of ASC. As only pyroptosis can be observed, this putative, small complex consisting of NAIP, NLRC4 and caspase-1 was termed "death complex"⁶⁴.

Functionally, the NLRC4 inflammasome is best studied in the case of *S. Typhimurium* infections. But also other T3SS expressing bacteria like *Pseudomonas aeruginosa* and flagellated bacteria like *Legionella pneumophila* are potent activators of the NLRC4 inflammasome. Therefore, NLRC4 deficient macrophages fail to induce pyroptosis and cytokine secretion upon challenge with these bacteria^{66,91,234–236}. Consistently, NLRC4 deficient mice succumb faster and display higher bacterial burdens than wild type controls after infection with gram-negative bacteria like *S. Typhimurium*, *Legionella pneumophila* or *Klebsiella pneumoniae*^{234,249–252}.

Similar to NLRP3, gain-of-function mutations were found in human NLRC4. These single amino acid substitutions (T337S, V341A, and H443P) map to the central NOD and result in the release of the auto-inhibitory state and thereby constitutive NLRC4 inflammasome activation. This is accompanied by a general, systemic inflammatory state characterized by elevated cytokine levels and recurrent MAS (macrophage activation syndrome). Pathologically, patients with the NLRC4 gain-of-function mutations display episodes of fever, often cold induced, and rashes. Similar phenotypes could be recapitulated in murine models and treatment with an IL-1 receptor antagonist (anakinra) clearly improved the conditions^{253–255}.

1.6.5 Other inflammasome receptors

Apart from the widely studied and well understood inflammasome receptors NLRP3, AIM2, Pypin and NLRC4 also other inflammasome receptors were proposed. However, the degree of study and how well they are established varies²⁴.

NLRP1

NLRP1 was the first inflammasome receptor to be described²⁸. NLRP1 belongs to the NLR-family but has a more complicated domain architecture than for example NLRP3 or NLRC4. Human NLRP1 has an C-terminal PYD, followed by an NOD, LRRs, a FIIND (function-to-find domain) and a C-terminal CARD^{256,257}. Interestingly, rodents have 3 paralogs called NLRP1A, NLRP1B and NLRP1C but all of them lack the PYD²⁵⁸. Functionally, NLRP1B was shown to be cleaved and activated by lethal toxin of *Bacillus anthracis*²⁵⁹. Lethal toxin is an A/B toxin consisting of the lethal factor and the protective antigen binding to the cell²⁶⁰. Yet, several murine *Nlrp1b* alleles exist with some being lethal toxin responsive and some unresponsive. Surprisingly, both responsive and non-responsive NLRP1B variants are cleaved by lethal toxin suggesting that NLRP1 inflam-

masome activation is a multistep process²⁶¹. Consistently, a processing event within the FIIND was observed to be required for activation in lethal toxin responsive NLRP1B variants²⁶². Thus, the current model suggests that NLRP1B acts as a decoy target for lethal toxin during *B. anthracis* infection thereby protecting the host²⁴. Gain-of-function mutations in human NLRP1 have recently been identified, showing that human NLRP1 also signals through its CARD, while the PYD serves a regulatory function. However the endogenous ligand that activates NLRP1 in humans is unknown so far²⁶³.

NLRP6

NLRP6 is mainly expressed in the intestines²⁶⁴. Deficiency in *Nlrp6* leads to increased susceptibility to chemically induced colitis and colitis induced tumors in mice and correlates with a decrease in IL-18 secretion. This observation and the described interaction of NLRP6 with ASC suggest the existence of an NLRP6 inflammasome^{264,265}. It was further shown that NLRP6 also regulates the microbiota as *Nlrp6* deficient mice show a dysbiotic microbiota^{266,267}. Furthermore, NLRP6 was also implicated in intestinal antiviral immunity²⁶⁸. However, the signals recognized by NLRP6 and whether NLRP6 is a *bona fide* inflammasome receptor remain unknown^{24,269}.

NLRP7

NLRP7 is only present in humans but not mice. Initial structure determinations of the PYD of NLRP7 suggested that it will not be able to interact with the ASC^{PYD}²⁷⁰. Yet, it was later shown that NLRP7 can assemble an ASC-dependent inflammasome in response to microbial acylated lipoproteins from *Mycoplasma* sp. in human macrophages²⁷¹. Furthermore, also *Mycobacteria* are able to activate NLRP7²⁷². Similar to NLRP3, NLRP7 requires ATP binding by its NOD to initiate signaling²⁷³. However, the extent and relevance of the NLRP7 inflammasome remains to be shown.

NLRP12

NLRP12 was discovered to be recruited to ASC in an overexpression system²⁷⁴. Subsequently, NLRP12 was postulated as a negative regulator of NF- κ B signaling²⁷⁵, a function which requires ATP binding to its central NOD²⁷⁶. Additionally, NLRP12 is also implicated in controlling migration of dendritic cells and neutrophils²⁷⁷. Furthermore, NLRP12 was suggested to initiate inflammasome formation in response to *Yersinia*

pestis and *Plasmodium* infections^{278,279}. Moreover, rare gain-of-function mutations in NLRP12 exist leading to an autoinflammatory disease characterized by recurrent fever and cold sensitivity. The identified mutations result in increased speck formation and elevated IL-1 β levels^{280–282}. Thus, an initial study using the IL-1 receptor antagonist anakinra to treat patients with *Nlrp12* mutations showed a positive effect on disease manifestation²⁸³.

IFI16

Human IFI16 and the murine orthologue IFI204 are DNA sensors regulating interferon production during viral and bacterial infections^{284,285}. However, IFI16 interacts with ASC in the nucleus upon infection with Kaposi's sarcoma-associated herpesvirus and initiates an inflammasome complex²⁸⁶. Furthermore, IFI16 is associated with inflammasome activation upon HIV infections^{53,287}. IFI16 recognizes dsDNA and binds to it in a sequence-independent manner similarly to AIM2 (see above)²⁸⁸. But for both, IFI16 and IFI204, the physiological relevance as inflammasome receptor remains unknown.

1.6.6 Non-canonical inflammasome: Murine caspase-11 and human caspases-4 and -5

Initial studies with *Casp1* and *Casp11* deficient mice suggested that the two inflammatory caspases have redundant roles regarding septic shock^{289,290}. However, it was discovered that *Casp1* knock-out mice were also deficient for *Casp11*²⁹¹. While *Casp1*^{-/-}/*Casp11*^{+/+} mice were susceptible to lethal sepsis, *Casp11*^{-/-}/*Casp1*^{+/+} mice were resistant showing that caspase-1 and caspase-11 have non-redundant roles and that caspase-11 is responsible for the severe outcome of sepsis²⁹¹.

Caspase-11 is a cytosolic protein that requires an activation step^{290,292}. Activation of caspase-11 leads to pyroptotic cell death. Caspase-11 dependent pyroptosis is morphologically indistinguishable from caspase-1 dependent pyroptosis and it is also dependent on cleavage of gasdermin-D^{30,31} (see below). Additionally, release of IL-1 β and IL-18 can be observed after caspase-11 activation, hence the name non-canonical inflammasome as opposed to the canonical caspase-1 inflammasome. However, maturation of IL-1 β /-18 requires the formation of a canonical NLRP3 inflammasome^{291,293}. NLRP3 activation after non-canonical inflammasome activation is a cell intrinsic process and requires the efflux of K⁺²⁹⁴.

Consistent with its role in sepsis, it was shown that caspase-11 is activated in response

to cytosolic LPS²⁹⁵, specifically the lipid A moiety of LPS. Caspase-11 activation requires hexa-acylated LPS, and bacteria that feature modified versions of LPS do not activate this pathway, such as *Francisella novicida* that has a tetra-acylated LPS^{293,295}. Surprisingly, LPS binds directly to the CARD of caspase-11 and activates it without the requirement of any further receptors. Also the CARDS of human caspase-4 and caspase-5 can directly bind to LPS²⁹⁶. Consistently, bacteria like *Burkholderia* that reside in the cytosol are potent triggers of caspase-11²⁹⁷. But also *S. Typhimurium* or *L. monocytogenes* mutants (*sifA* and *sdhA*, respectively), that lead to a cytosolic localization of these usually vacuolar bacteria, activate caspase-11²⁹⁷. Furthermore, in absence of caspase-1, also wild type *S. Typhimurium* can activate caspase-11²⁹⁸.

1.7 Caspase-12

Murine caspase-12 is an additional inflammatory caspase displaying high homology to murine caspase-1 (39% identity), murine caspase-11 (38% identity), human caspase-4 (48% identity) and human caspase-5 (45% identity) placing it in the group of the pro-inflammatory caspases^{299,300}. While the *Casp12* gene is intact in rodents as well as non-human primates, two different alleles exist in the human population. The short form CASP12S, which is fixed in the Caucasian population as well as most other non-African populations, contains a premature stop codon at position 125 instead of an arginine³⁰¹. The CASP12S allele therefore only consists of the CARD of caspase-12. The CASP12L allele on the other hand can nearly exclusively be found in populations of sub-Saharan African descent and contains the full open reading frame. While also in these populations many people are homozygous for the CASP12S allele, a large fraction of the people are heterozygous and some even homozygous for the CASP12L allele. In sub-Saharan African populations the average frequency of CASP12L allele was estimated to be approximately 28%^{302,303}. As the CASP12S alleles seem to have a common origin, it has been suggested that the pseudogenization of CASP12L to CASP12S predates the out-of-Africa migration of *Homo sapiens* (approximately 40'000-60'000 years ago)^{303,304}. This quick fixation of the CASP12S allele in the Caucasian and other non-African populations is a clear indication of a positive selection pressure on the CASP12S allele. Indeed, the selective advantage was estimated to be approximately 0.5-1% and started 60'000-100'000 years ago^{303,304}. However, the origin of this selective pressure is not known so far.

Initially, the CASP12L allele has been described to protect patients from severe sepsis in a small cohort of African-Americans³⁰¹. However, this has since been questioned by a larger study with Malian volunteers that found no difference in secretion of pro-inflammatory cytokines in whole blood after challenge with LPS or different *Yersinia* strains (*Y. pestis*, *Y. pseudotuberculosis*, *Y. enterocolitica*) in people carrying both *Casp-12* alleles compared to homozygous carrier of the CASP12S allele³⁰². Furthermore, another study could not find any correlation between the presence of the CASP12L allele and spontaneous clearance of hepatitis C virus, which happens in a small fraction of people whereas most develop a chronic infection³⁰⁵.

There has also been some considerable effort to elucidate the function of the rodent caspase-12 homologue. So far, no caspase-12 targets besides itself are known and the catalytic activity of caspase-12 is the lowest amongst the characterized caspases³⁰⁶.

Additionally, caspase-12 is only able to cleave itself (in *cis* and *trans*) between the large (p20) and small (p10) subunits but not between the pro-domain (CARD) and the large subunit which further differentiates caspase-12 from other caspases³⁰⁶. Nonetheless, caspase-12 has been linked to the ER (endoplasmic reticulum) stress response where it has been shown to be upregulated³⁰⁷. Furthermore, it has been proposed to be essential for ER stress-dependent apoptosis but not for the extrinsic or intrinsic apoptosis pathways³⁰⁰. Even though additional factors like TRAF2 (TNF [tumor necrosis factor] receptor-associated factor 2) have been implicated as well³⁰⁷ the exact mechanism how caspase-12 should be involved in apoptosis is unclear and its role in ER stress has also been contested³⁰⁸.

On the other hand, it was reported that in mice caspase-12 should act as dominant negative regulator of caspase-1³⁰⁸. With the aid of *Casp12* knock-out mice, it was reported that caspase-12 deficient cells display increased caspase-1 activity and therefore release more IL-1 β and IL-18 but also interferon- γ ³⁰⁸. Furthermore, caspase-12 was reported to dampen the immune response to *Plasmodium* infection thereby amelioration the outcome of cerebral malaria in an inflammasome independent but NF- κ B dependent manner³⁰⁹ and it was reported that caspase-12 modulates NOD (nucleotide-binding and oligomerization domain-containing protein) signaling by interacting with RIP2 (receptor interacting serine/threonine kinase 2)³¹⁰. Finally, caspase-12 was described to restrict West Nile virus infections in a caspase-1 and RIG-I dependent manner³¹¹. However, the original *Casp12* knock-out mice created by Saleh and colleagues³⁰⁸ are also deficient for *Casp11*^{312,313} therefore questioning which of the observed phenotypes could be assigned to caspase-11 and which to caspase-12. Recently, however *Casp11* proficient *Casp12* knock-out mice were generated^{312,313} and the results show that caspase-12 inhibits diet induced obesity and insulin resistance³¹². Importantly however, no effect of caspase-12 on canonical and non-canonical inflammasome signaling could be detected *in vivo* after LPS injection or *Listeria monocytogenes* infection or *ex vivo* in BMDMs incubated with ATP or nigericin, infected with *E. coli*, *Citrobacter rodentium* or *S. Typhimurium* or transfected with dsDNA³¹³ thereby further questioning the physiological role of caspase-12.

1.8 Gasdermin-D

Recently, two independent approaches identified gasdermin-D as an important executioner of pyroptotic cell death. The first group employed a forward genetic screen using ENU (*N*-ethyl-*N*-nitrosourea) induced mutagenesis in mice for mediators of non-canonical inflammasome signaling (LPS injection)³⁰ while the second group used a CRISPR-Cas9 genome wide knock-out screen for both caspase-11 and NAIP/NLRC4 mediated pyroptosis³¹. A third report later announced the identification of gasdermin-D in the NLRP3 complex by a mass spectrometry approach³¹⁴. Gasdermin-D is part of the gasdermin family of proteins consisting of gasdermin-A, -B, -C, DFNA5 and DFNB59 in humans and gasdermin-A1–A3, -C1–C4, DFNA5 and DFNB59 in mice³¹⁵. Gasdermins were identified to be expressed in the gastrointestinal tract as well as the skin and derive their name thereof³¹⁶. Importantly, all gasdermins, except DFNB59, display a conserved two-domain architecture³¹⁷.

Upon inflammasome activation, gasdermin-D is cleaved into an N-terminal (p30) and a C-terminal (p20) fragment whereby the N-terminal fragment is sufficient to induce pyroptosis³¹. The C-terminal domain of gasdermin-D functions as auto-inhibitory domain as well as solubility tag and after cleavage of gasdermin-D the C-terminal fragment stays soluble while the N-terminal fragment precipitates *in vitro*³¹⁸. In cells, the released N-terminal gasdermin-D fragment associates with the plasma membrane and can bind to phosphatidylinositol (4)-phosphate, (4,5)-bisphosphate and (3,4,5)-triphosphate^{48,319}. This is supported by the fact that a reduction of phosphatidylinositol phosphate concentrations in the plasma membrane by chemical means is able to block pyroptosis⁴⁸. After membrane association, the N-terminal fragment of gasdermin-D can insert into the membrane and form a pore. It was estimated that 16-24 monomers of the gasdermin-D N-terminal domain participate in one pore^{317,320}. The size of the pore has an inner diameter of approximately 15 nm and an outer diameter of approximately 23 nm³¹⁷⁻³¹⁹. This pore size would theoretically be large enough to let pass both IL-1 β -18 (4.5 nm diameter) as well as caspase-1 (7.5 nm diameter)³¹⁷. However, it was not shown so far whether IL-1 β and IL-18 are indeed released through the gasdermin-D pore.

Interestingly, after caspase-11 activation gasdermin-D is essential for both, pyroptosis and NLRP3 dependent caspase-1 and IL-1 β maturation and secretion. On the other hand, gasdermin-D is not required for canonical caspase-1 and IL-1 β processing and at later time points even pyroptosis is independent of gasdermin-D³⁰. This difference

between the absolute requirement for caspase-11 mediated pyroptosis and relative requirement for caspase-1 mediated pyroptosis is mirrored in their evolutionary relationships. While all vertebrates display caspase-1 dependent cell death, only mammals express caspase-11 and gasdermin-D indicating a possible co-evolution of caspase-11 and gasdermin-D³⁰.

1.9 Aim of the thesis

The ability of ASC to form speck-like aggregates, so-called ASC specks, was known even before the inflammasome emerged as important pathway in innate immunity. Yet, the structure and the organization of these ASC specks has remained enigmatic, although it had been observed that ASC has the ability to oligomerize into filaments by its death-fold domains, namely the ASC^{PYD} or ASC^{CARD}. The aim of the first part of my thesis was to aid in elucidation of the structure of the murine ASC^{PYD} filament by a novel combined NMR and electron microscopy approach. The aim of the main part of my thesis was to clarify the roles of the two domains of ASC in speck formation, determine how CARD-containing receptors initiate speck formation and clarify whether the ASC speck has indeed a role in inflammasome signaling.

2 Results

2.1 Research article I

Structure and assembly of the mouse ASC inflammasome by combined NMR spectroscopy and cryo-electron microscopy

L. Sborgi*, F. Ravotti*, V. P. Dandey*, **M. S. Dick**, A. Mazur, S. Reckel, M. Chami, S. Scherer, M. Huber, A. Böckmann, E. H. Egelman, H. Stahlberg, P. Broz, B. H. Meier and S. Hiller.

* denotes equal contribution.

Proceedings of the National Academy of Science of the United States of America
2015 October 27; 112(43):13237-42. doi: 10.1073/pnas.1507579112.³²¹

Statement of contribution

I performed all experiments in cells, i.e. generated the cell lines and performed inflammasome activation, cell death and IL-1 β release measurements as well as the fluorescence microscopy and speck quantification. These data were included in Fig. 1b, Fig. 5 and Fig. S6. Additionally, I performed some of the ASC^{FL} and ASC^{PYD} purifications for electron microscopy and was involved in writing of the manuscript.

Structure and assembly of the mouse ASC inflammasome by combined NMR spectroscopy and cryo-electron microscopy

Lorenzo Sborgi^{a,1}, Francesco Ravotti^{b,1}, Venkata P. Dandey^{c,1}, Mathias S. Dick^a, Adam Mazur^{a,d}, Sina Reckel^{a,2}, Mohamed Cham^c, Sebastian Scherer^c, Matthias Huber^b, Anja Böckmann^e, Edward H. Egelman^f, Henning Stahlberg^c, Petr Broz^{a,3}, Beat H. Meier^{b,3}, and Sebastian Hiller^{a,3}

^aBiozentrum, University of Basel, 4056 Basel, Switzerland; ^bPhysical Chemistry, Swiss Federal Institute of Technology in Zurich, 8093 Zurich, Switzerland; ^cCenter for Cellular Imaging and NanoAnalytics, Biozentrum, University of Basel, 4058 Basel, Switzerland; ^dResearch IT, Biozentrum, University of Basel, 4056 Basel, Switzerland; ^eInstitute for the Biology and Chemistry of Proteins, 69367 Lyon, France; and ^fDepartment of Biochemistry and Molecular Genetics, University of Virginia, Charlottesville, VA 22908

Edited by Gerhard Wagner, Harvard Medical School, Boston, MA, and approved September 24, 2015 (received for review April 17, 2015)

Inflammasomes are multiprotein complexes that control the innate immune response by activating caspase-1, thus promoting the secretion of cytokines in response to invading pathogens and endogenous triggers. Assembly of inflammasomes is induced by activation of a receptor protein. Many inflammasome receptors require the adapter protein ASC [apoptosis-associated speck-like protein containing a caspase-recruitment domain (CARD)], which consists of two domains, the N-terminal pyrin domain (PYD) and the C-terminal CARD. Upon activation, ASC forms large oligomeric filaments, which facilitate procaspase-1 recruitment. Here, we characterize the structure and filament formation of mouse ASC *in vitro* at atomic resolution. Information from cryo-electron microscopy and solid-state NMR spectroscopy is combined in a single structure calculation to obtain the atomic-resolution structure of the ASC filament. Perturbations of NMR resonances upon filament formation monitor the specific binding interfaces of ASC-PYD association. Importantly, NMR experiments show the rigidity of the PYD forming the core of the filament as well as the high mobility of the CARD relative to this core. The findings are validated by structure-based mutagenesis experiments in cultured macrophages. The 3D structure of the mouse ASC-PYD filament is highly similar to the recently determined human ASC-PYD filament, suggesting evolutionary conservation of ASC-dependent inflammasome mechanisms.

inflammation | protein structure | protein filament | ASC speck | innate immune response

The innate immune system rapidly detects and responds to different types of pathogen- and danger-associated molecular patterns (PAMPs and DAMPs, respectively) at minimal concentrations via specific, germline-encoded pattern-recognition receptors (PRRs) (1–3). A subset of cytosolic PRRs respond to PAMPs and DAMPs by initiating the assembly of cytosolic macromolecular inflammasome complexes (4–6). Inflammasome assembly leads to the activation of caspase-1, the proteolytic maturation of interleukins, and the induction of pyroptosis. The correct assembly of inflammasome complexes is critical, and malfunctions are related to major human diseases including cancer and autoimmune syndromes (4, 7). Inflammasome signaling initiates with the activation of dedicated sensor proteins, such as the NOD-like receptor (NLR) family, through mechanisms that still are poorly understood (2, 4). The typical domain architecture of NLRs is tripartite, including an N-terminal effector domain (8). Based on the type of effector domain, which can be pyrin domains (PYDs), caspase-recruitment domains (CARDs), or baculovirus inhibitor of apoptosis (IAP) repeat (BIR) domains, NLRs are classified as NLRPs, NLRCs, or NLRBs, respectively (9). In the initial reaction step upon recognition of the specific molecular pattern, the receptor self-associates (Fig. 1*A*). Because death domains interact in a homotypic fashion, NLRCs can activate procaspase-1, which

features a CARD, directly. In contrast, NLRPs require the recruitment of the bipartite adaptor protein ASC (apoptosis-associated speck-like protein containing a CARD) as an intermediate signaling step. ASC interacts with the receptor via its N-terminal PYD and activates procaspase-1 with its C-terminal CARD. Importantly, the interaction with the receptor is not stoichiometric, but ASC oligomerizes *in vivo* to a micrometer-sized assembly, the ASC speck (Fig. 1*A* and *B*) (10). Procaspase-1 is recruited to the speck, resulting in its autoproteolysis and the formation of the catalytically active heterotetramer of cleaved p10 and p20 subunits.

Given its central role in NLRP inflammasomes, a description of ASC structure and dynamics in its soluble and filamentous form is crucial to understand inflammation processes at the atomic level. NMR spectroscopy is the method of choice for the structural and functional characterization of PYDs that are

Significance

Invading pathogens and other danger-associated signals are recognized by the innate immune system. Subsequently, the eukaryotic protein ASC [apoptosis-associated speck-like protein containing a caspase-recruitment domain (CARD)] assembles to long filaments, which might serve to amplify the signal and activate an inflammatory response. We have determined the structure of the mouse ASC filament at atomic resolution. The pyrin domain of ASC forms the helical filament core, and the CARD, thus far elusive to experimental observation, is flexibly unfolded on the filament periphery. The integration of data from two structural methods, cryo-electron microscopy and solid-state NMR spectroscopy, opens perspectives for structural studies of inflammasomes and related molecular assemblies.

Author contributions: L.S., F.R., A.M., A.B., H.S., P.B., B.H.M., and S.H. designed research; L.S., F.R., V.P.D., M.S.D., A.M., S.R., M.C., S.S., and M.H. performed research; L.S., F.R., V.P.D., M.S.D., A.M., S.R., M.C., S.S., A.B., E.H.E., H.S., P.B., B.H.M., and S.H. analyzed data; and L.S., F.R., M.S.D., A.M., A.B., E.H.E., H.S., P.B., B.H.M., and S.H. wrote the paper.

The authors declare no conflict of interest.

This article is a PNAS Direct Submission.

Freely available online through the PNAS open access option.

Data deposition: The density map from cryo-EM data was deposited in the Electron Microscopy Data Bank (accession code EMD-2971). The atomic coordinates of the ASC PYD filament (model 3) were deposited in the Protein Data Bank (PDB ID code 2N1F). Chemical shifts of the soluble and filament form of mouse ASC-PYD were submitted to the Biological Magnetic Resonance Bank (accession codes 25561 and 26550, respectively).

¹L.S., F.R., and V.P.D. contributed equally to this work.

²Present address: School of Life Sciences, Swiss Federal Institute of Technology in Lausanne, 1015 Lausanne, Switzerland.

³To whom correspondence may be addressed. Email: petr.broz@unibas.ch, beme@ethz.ch, or sebastian.hiller@unibas.ch.

This article contains supporting information online at www.pnas.org/lookup/suppl/doi:10.1073/pnas.1507579112/-DCSupplemental.

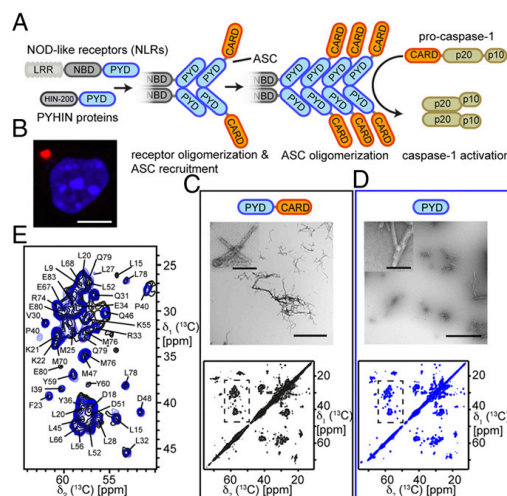


Fig. 1. Structural determinants of ASC filament formation. (A) Schematic representation of ASC-mediated inflammasome assembly and caspase-1 activation. Detection of specific molecular patterns by NLR or pyrin and HIN domain-containing protein (PYHIN) family members results in their activation and oligomerization. Activated receptors recruit the inflammasome adaptor ASC, which in turn oligomerizes to ASC filaments. The effector protease caspase-1 is activated by this complex. LRR, leucine-rich repeat. (B) Endogenous ASC specks in immortalized murine macrophages stained with antibodies for ASC (red) appear as large, macromolecular complexes. Nuclei are stained blue. (Scale bar, 5 μm .) (C and D) Characterization of filaments from ASC-FL (C, black) and ASC-PYD (D, blue) reconstituted *in vitro*. (Upper) EM images of negatively stained preparations of ASC filaments. (Scale bars, 1 μm ; 100 nm in Insets). (Lower) 2D ^{13}C -DARR solid-state NMR spectra of $[\text{U-}^{13}\text{C}]$ -labeled filaments (mixing time 20 ms). The spectra were recorded on an 850-MHz spectrometer at 17 kHz MAS. (E) Superimposition of a selected region of the 2D ^{13}C -DARR spectra shown in C and D. Sequence-specific resonance assignments are indicated.

difficult to crystallize (11–13). In particular, the solution structures of isolated human ASC pyrin domain (ASC-PYD) and ASC full-length protein (ASC-FL) have been determined, showing that the PYD and the CARD, connected by a flexible linker, tumble independently in solution (14, 15). A suitable method for the structural characterization of the insoluble ASC aggregates that form at physiological pH conditions is cryo-EM, which recently has provided the first structure of an ASC-PYD filament at near-atomic resolution (16). Filaments of human ASC-PYD feature a helical arrangement along well-defined molecular interfaces, in agreement with other molecular assemblies of death domains (16–18). An alternative method to determine structures of insoluble protein assemblies at atomic resolution is solid-state NMR spectroscopy under magic-angle-spinning (MAS) conditions (19–22). Cryo-EM density maps do not recover disordered or dynamic polypeptide segments, but solid-state NMR spectroscopy renders data from both the rigid and dynamic parts of a molecular assembly. The two techniques thus can provide complementary information. Structural studies of inflammasomes from different vertebrates remain of great interest because of the extensive diversification of inflammasome signaling pathways among species.

Here, we combine data from solid-state NMR spectroscopy and cryo-EM to determine the atomic-resolution structure of mouse ASC filaments formed by the PYDs via helical stacking along well-defined interfaces. Additional solid-state NMR measurements address the dynamic CARD as part of the ASC-FL filament. A comparison of chemical shifts reveals conformational changes upon filament formation. Structure-guided mutagenesis

in living cells confirms the network of interactions that are essential for the integrity of the filament and thus ASC-dependent inflammasome signaling.

Results

Reconstitution and Characterization of ASC Filaments *In Vitro*. These mouse ASC-FL and ASC-PYD were soluble at low pH or in chaotropic solution and showed a high propensity for assembling into filaments at physiological pH conditions. Negatively stained preparations visualized by EM showed that oligomerization led to the formation of long, well-defined filaments, with typical lengths in the range of 500–2,000 nm (Fig. 1 C and D). The filaments were organized in larger aggregates of variable size with the ASC-FL filaments branching more frequently than the ASC-PYD filaments. In general, the atomic structure of filament depends on the assembly conditions *in vivo* and *in vitro*, and polymorphism is common in some systems (23, 24). To characterize the sample homogeneity in our preparations, we used solid state NMR spectroscopy, which is highly sensitive to even small changes in the local molecular conformation (23). A 2D dipolar assisted rotational resonance (DARR) ^{13}C - ^{13}C -correlation spectrum as well as an NCA correlation spectrum of the filament of the isolated PYD showed narrow cross-peaks, with typical carbon linewidths of about 0.5 ppm (Fig. 1 D and E and Fig. S1). The observation of a single set of peaks—one per carbon or nitrogen atom—is a strong indication of a homogeneous preparation and the absence of polymorphism. Notably, the observation of a single set of resonances also indicates that all monomers in the filament are symmetry-equivalent. We repeated the same experiments on the filament of ASC-FL under the same conditions and observed highly similar DARR and NCA spectra (Fig. 1 C and E and Fig. S1). The two pairs of spectra feature a complete set of correlation cross-peaks at the same positions, indicating that the CARD is essentially invisible in the spectrum of ASC-FL and that the observable PYD adopts the same structure in both types of filament. The ASC-PYD alone thus forms the scaffold of the ASC-FL filament whereas the CARD is not strictly required for the filament core and does not perturb the PYD filament conformation. The absence of additional strong signals in the full-length protein relative to the PYD shows that the CARD is flexible relative to the filament core. Consistently, although mouse ASC-PYD filaments feature a smooth surface in negative-stained EM, filaments formed by mouse ASC-FL have a rough surface, possibly because the ASC CARD is exposed outside the ASC filament (Fig. 1 C and D). These data directly indicate that the two domains of mouse ASC which in human ASC have been shown to tumble independently in solution (14), also are independent in the filament form.

Cryo-EM of the ASC-PYD Filament. Based on the observation that the ASC-PYD is the minimal structural requirement for filament formation, we studied the structure of filaments of the mouse ASC PYD without the CARD. Optimization of the filament formation protocol by observation with cryo-EM showed that these filaments are well-ordered (Fig. S2). Image collection was done manually on an FEI Titan Krios transmission electron microscope using a Gatan K2 Summit direct electron detector. Recorded image series were automatically drift-corrected and averaged using the 2dx_automato (25), employing MOTIONCORR (26). The averaged power spectrum of multiple individual segments of filaments from these cryo EM images shows a clear meridional reflection at $1/14.2 \text{ \AA}^{-1}$, corresponding to the reciprocal of the axial rise. Image processing with the Iterative Helical Real Space Reconstruction (IHRSR) method (27) yielded a final electron density map at a resolution of ~ 4.0 – 4.5 \AA (Fig. 2A). The ASC-PYD filament is a hollow helical fiber with inner and outer diameters of 20 \AA and 90 \AA , respectively. The polar filament has C3 point group symmetry with 53° right-handed rotation and a 14.2- \AA axial rise per subunit.

Solid-State NMR of the Mouse ASC-PYD Filament. For the resonance assignment, we recorded a set of correlation experiments on uniformly ^{13}C - and ^{15}N -labeled filaments under MAS condition

(28). The spectra were well resolved and allowed sequence-specific resonance assignments of the backbone and amino acid side chains, as detailed in ref. 29 (Fig. 2 *B* and *C*). The backbone assignment was complete for residues 4–84, and in this segment most of the side-chain carbon atoms were assigned also. The secondary chemical shifts allowed a direct determination of the location of secondary-structure elements. Mouse ASC-PYD in its filament form features six α -helices at positions 3–14, 17–29, 41–46, 49–59, 62–76, and 80–84 (Fig. 2*D*). The last helix presumably extends until residue 89, but resonances that could correspond to the segment 85–89 were not found in any of the spectra. Because an INEPT (insensitive nuclei enhanced by polarized transfer)-based spectrum of the ASC-PYD filaments did not show resonances, we assume that these four residues feature millisecond dynamics, leading to line broadening below the level of detection, a common feature of terminal residues even in microcrystalline proteins (30).

Calculation of the Structure of the Mouse ASC-PYD Filament. The cryo-EM density map of the ASC-PYD filament was combined with solid-state NMR data toward a joined structure calculation, which proceeded in three steps (Fig. 2*E*). Model 1 of the ASC-PYD filament monomer is based on the EM electron density map and on the location of the six α -helical segments in the amino acid sequence, as determined from solid-state NMR secondary chemical shifts. It was built by placing the helices interactively into the cryo-EM density map using Coot (31) and connecting them as indicated by electron density. Because some of the side chains were well resolved in the electron density map, matching them allowed a tentative rotational orientation. The full-filament coordinates were created from this monomer by application of the helical symmetry (C3, 53° rotation, 14.2-Å rise). The resulting model 1 was refined further using the X-PLOR-NIH program (32) under continuous symmetry enforcement, using the cryo-EM structure factors (the Fourier transform of the density

map) as restraints, as well as the TALOS+ dihedral angles from solid-state NMR chemical shifts for a total of 70 residues and $i,i+4$ backbone hydrogen-bond restraints for residues in α -helical secondary structure (see above). The resulting model 2 shows a well-defined backbone structure, as indicated by a backbone rmsd of 0.23 Å and an overall heavy atom rmsd of 0.94 Å for the conformer bundle. Model 2 is cross-validated by a set of spectrally unambiguous cross-peaks in 2D [^{13}C , ^{13}C]-CHHC and [^{13}C , ^{13}C]-proton assisted recoupling (PAR) solid-state NMR experiments, which are all in agreement with the 3D structure (Fig. S3*A* and Table S1).

In an attempt to improve side-chain orientations, we used further NMR distance restraints from 2D [^{13}C , ^{13}C]-CHHC and [^{13}C , ^{13}C]-PAR spectra. The spectra were peak-picked automatically by Sparky (33) and assigned to 674 atom pairs with the CANDID algorithm (34) using the 3D structure information of model 2 as input (Fig. S3*B*). A structure calculation with X-PLOR-NIH (32) under symmetry enforcement yielded model 3, using as input the cryo-EM-derived structure factors, TALOS+-derived dihedral angle restraints, and the 674 ambiguous NMR distance restraints but no hydrogen-bond restraints. In model 3, the ensemble of the 10 lowest energy conformers of the ASC-PYD filament featured a backbone rmsd of 0.17 Å and an overall heavy atom rmsd of 0.63 Å (Fig. 2 *F–I*, Table S2, and Movies S1 and S2). Because all data, including the EM map, were treated with strict symmetry enforcement, these values are equally representative for the individual monomer subunits.

A comparison of model 3 with model 1 showed significant improvements. The models differ by backbone and all heavy atom rmsds of 0.84 Å and 1.04 Å, respectively. The comparison of model 3 with model 2 showed only small differences overall (backbone and all heavy atom rmsds of 0.27 Å and 0.33 Å, respectively). Visual inspection showed that the improvement is not uniform but that a number of side-chain orientations were

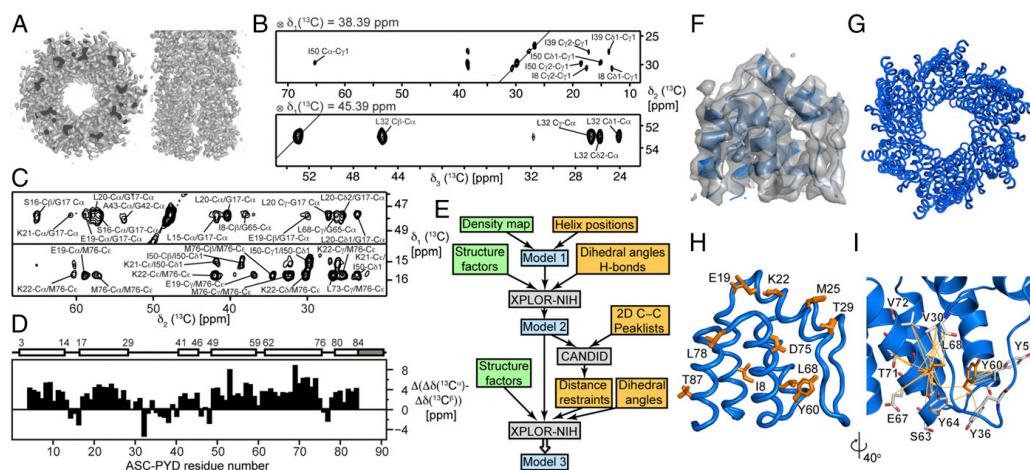


Fig. 2. Structure determination of the ASC-PYD filament by the combination of cryo-EM and solid-state NMR data. (A) Electron density map of the ASC-PYD filament obtained by cryo-EM and image processing. Darker segments are the inner bulk volume of the density map. (B) Strips from a 3D ^{13}C -correlation spectrum of a [^{13}C]-labeled ASC-PYD filament. The strips were taken at the ^{13}C positions of residues Ile-50 and Leu-32, respectively. (C) Strips from a 2D [^{13}C , ^{13}C]-DARR (Upper) and a CHHC (Lower) spectrum. Pairwise ^{13}C - ^{13}C contacts as identified by CANDID are shown using the one-letter amino acid code and residue number. (D) Secondary chemical shifts of ASC-PYD in the filament from solid-state NMR experiments. The data identify six α -helices, as indicated above the panel with the starting and ending residue numbers. (E) Flowchart of the ab initio structure determination of the ASC-PYD filament. The data contributions from solid-state NMR spectroscopy and cryo-EM are indicated by yellow and green rectangles, respectively. The individual structural models 1–3 are shown in light blue. Software packages are identified in gray rectangles. See *S1 Materials and Methods* for details. (F) Cryo-EM density reconstruction superimposed with the single-subunit ASC-PYD structure. (G and H) Backbone superposition of the 20 lowest-energy conformers of the ASC-PYD filament (G) and a single monomer within the assembled filament (H). The conformational ensemble of 10 arbitrarily selected side chains is shown as stick models in orange. (I) Structural features of a single ASC-PYD monomer as part of the filament. The spectrally ambiguous distance constraints between Tyr60 and Leu68 (orange) and the neighboring residues (gray), obtained from solid-state NMR experiments are shown as orange lines.

better defined in model 3 through the integration of the distance restraints. Therefore, we conclude that the resolution of the EM map was high enough so that, in combination with NMR-derived secondary structure information, a high-resolution structure can be obtained de novo, without the requirement of prior knowledge of the protein monomer structure (model 2). Because this procedure requires only NMR chemical-shift assignments for the protein backbone, this approach is accessible for even larger proteins with contemporary technology (35). Additionally, the fact that CANDID interprets 91% of all observed cross-peaks using the narrow tolerance of 0.2 ppm for ^{13}C chemical shifts is an important cross-validation of models 2 and 3. Finally, the Fourier shell correlation (FSC) between the final structural model and the density map showed a resolution of 4.3 Å (Fig. S2E).

Structure of the Mouse ASC-PYD Filament. Mouse ASC-PYD forms a triple-stranded, right-handed helical filament in which each PYD interacts with six adjacent subunits through three asymmetric interfaces, types I–III (Fig. 3A–F and Movies S3 and S4). Interface type I is formed by amino acid residues belonging to helices 1 and 4 on one subunit and helix 3 in the adjacent subunit, defining helical PYD strands winding around the helix axis (Fig. 3D). It involves interactions between residues of opposite charges that contribute to the filament stabilization. The solvent-exposed positively charged side chains of Lys22, Lys26, and Lys21 from helix 2 and Arg41 from helix 3 are involved in electrostatic interactions with the negatively charged side chain of residues Glu13 and Asp6 from helix 1 and residues Asp48 and Asp54 from helix 4 of the neighboring subunit. In addition, a network of hydrophobic interactions is formed by Leu9, Met25, Val30, and Ile50. The lateral contact of strands parallel to the filament axis emerges from interface type II (Fig. 3E). Residues in helices 4 and 5 and in the central part of the loop between helices 2 and 3 on one subunit interact with residues at the corner of helices 5 and 6 of the next subunit by specific hydrophobic

interactions. The interactions of Tyr59 and Tyr60 from the loop between helices 4 and 5 and Gly77 and Leu78 from the loop between helices 5 and 6 of the neighboring subunit define the contact surface between two helical layers. In addition, the contribution of further charged and uncharged side chains suggests a more heterogeneous interaction network. The type II interface is formed by residues from the end of helix 1 and the sequential short loop on one subunit with helix 3 on the adjacent subunit, mediating the contact of a helical strand with an adjacent helical layer (Fig. 3F). It is defined by interactions involving both polar and hydrophobic side chains. The charged residue Glu13, Glu19, and Arg41 are located close to this interface but do not form specific salt-bridge interactions.

The Monomer Structure Is Maintained in the Filament. Mouse ASC-PYD is soluble at low pH conditions, leading to well-folded monomeric species as indicated by the signal dispersion and narrow line widths of the 2D $[^{15}\text{N}, ^1\text{H}]$ -heteronuclear single quantum coherence (HSQC) spectrum (Fig. S4A). Analysis of the backbone secondary chemical shifts confirmed the position of the six α -helices at positions 3–14, 17–29, 41–46, 49–59, 62–76 and 80–84 as the secondary structure elements of mouse ASC-PYD in solution. Thus these helices are located at the same positions in the dissolved monomer as in the filament form. Furthermore, a comparison of backbone dihedral angles ϕ and ψ as predicted by TALOS+ (36) from the backbone chemical shift confirms that all secondary structure elements are equally retained in the solution and filament forms of mouse ASC-PYD thus explaining the absence of major structural rearrangement upon filament formation. A direct comparison of the backbone chemical shifts of the monomer form of ASC-PYD in solution with the filament form reveals a largely identical conformation with chemical-shift differences mostly smaller than 0.6 ppm. Notable exceptions can be found; these exceptions point directly to residues located at the subunit interfaces, where slight

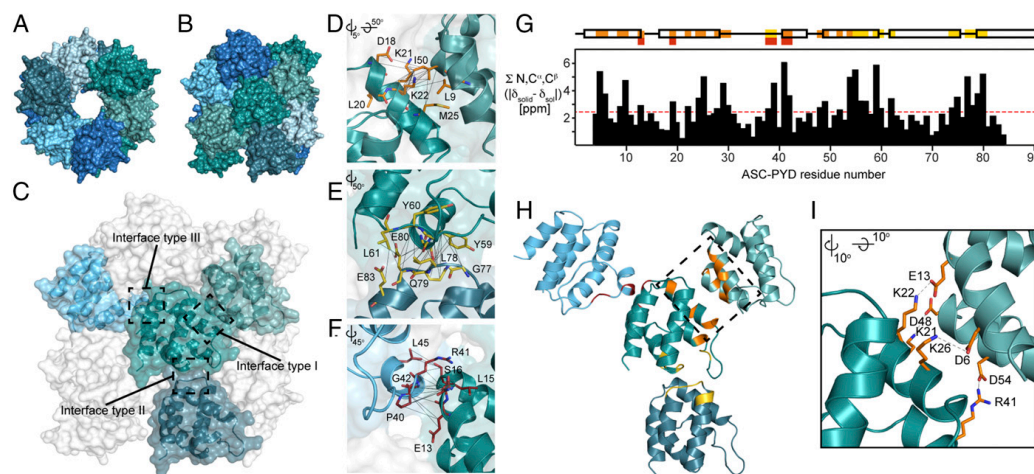


Fig. 3. 3D arrangement of the ASC-PYD filament. (A and B) Top (A) and side (B) views of the ASC-PYD filament in surface representation. The three helical oligomer strands are colored blue, teal, and dark blue, and individual ASC-PYD subunits have alternating darker and lighter shades. (C) Four ASC-PYD monomers are shown in surface representation as part of the filament using the color code in A and B. Three interaction interfaces I–III are indicated by dashed square rectangles. (D–F) Detailed view of interaction interfaces I–III, respectively. Intermolecular atom-pair contacts observed as ambiguous peaks by solid-state NMR spectroscopy and identified by CANDID are indicated by solid black lines. The residues defining interfaces I, II, and III are labeled and colored orange, yellow, and red, respectively. (G) Chemical-shift difference between solution- and solid-state chemical shifts for the nucleus ^{15}N , $^{13}\text{C}_\alpha$, and $^{13}\text{C}_\beta$. Chemical-shift variations larger than the mean value are marked with different color codes on the secondary structure elements. Residues that belong to the type I, II, and III interfaces are marked in orange, yellow, and red, respectively. (H) Structural location of the residues with significant chemical-shift differences between the monomeric and filament forms, as identified and using the color code in G. (I) Structural details of interface type I as indicated by the dashed square rectangle in H. Side chains involved in intersubunit salt bridges are shown as stick models and with their sequence label.

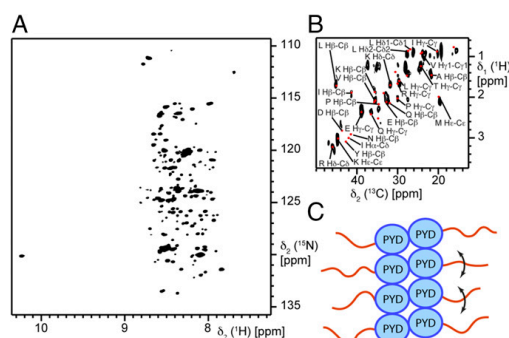


Fig. 4. The CARD in the mouse ASC-FL filament is flexibly unfolded. (A) Solid-state 2D [^{15}N , ^1H]-HSQC spectrum of [^{13}C , ^{15}N]-labeled ASC-FL. (B) Carbon-detected refocused INEPT spectrum of [^{13}C , ^{15}N]-labeled mouse ASC-FL. Random-coil chemical-shift positions for the 20 common amino acids are reported as red dots. (C) Model of the ASC-FL filament. Multiple ASC-PYDs (blue) provide the structural scaffold for the filament formation; the ASC-CARDs (orange) remain flexible relative to the ordered filament core and probably exist in random-coil form.

conformational changes are induced by the packing effects upon filament formation (Fig. 3 *G–I* and Fig. *S4B–E*). Thus these chemical-shift data independently confirm the three asymmetric interfaces that are characteristic of the filament architecture.

Conservation of the ASC-PYD Filament Architecture. A comparison of the mouse ASC-PYD filament structure with the human ASC-PYD filament (PDB ID code 3J63) (16) shows that the spatial assemblies and the structures of the monomer subunits are highly similar (Fig. *S5*). The structures of monomeric subunits of human and mouse ASC-PYD from the respective filament structures overlay with a backbone rmsd of 1.1 Å. Also the 3D arrangement of the subunits toward the filament structure shows the same overall arrangement (helical parameters: 53° rotation, 14.2-Å rise for mouse versus 52.9° rotation, 13.9-Å rise for human). Although an agreement in the tertiary structure between mouse and human ASC is expected, because they differ in only 20 of the 93 residues, the identity in the quaternary structure is noteworthy. This finding suggests functional conservation of the ASC polymerization mechanism as part of the innate immune response system in mouse, human, and possibly other species.

Dynamics and Flexibility of the CARD. MAS solid-state NMR spectra can be recorded with different polarization-transfer schemes. Experiments based on cross-polarization (CP) techniques filter for rigid parts of the assemblies, whereas INEPT-based experiments monitor flexible parts of the molecular assemblies. Our initial CP-based experiments of ASC-FL filaments have established that the rigid parts of the filament are formed entirely by the PYD and that

the CARD is a flexible part of the filament arrangement (Fig. 1). Consequently, INEPT-based experiments (37) were used to obtain spectral information on the conformation and dynamics of this domain. The 2D [^{15}N , ^1H]-INEPT spectrum of mouse ASC-FL filaments shows a set of ~105 strong and multiple additional weak backbone amide correlation cross-peaks, with chemical-shift values in the random-coil region and the small dispersion typical of flexible polypeptide chains (Fig. 4*A*). These signals must arise from the 14-residue linker and/or the 89-residue CARD, because a corresponding INEPT spectrum of mouse ASC-PYD filaments did not contain any peaks. Furthermore, the narrow dispersion of amide proton chemical shifts indicates that the linker and probably a major part of or all the CARD populates a conformational ensemble of flexibly unfolded structures in fast equilibrium, similar to a random-coil ensemble. Consistently, 2D INEPT-based [^1H , ^{13}C]-correlation spectra of the mouse ASC-FL filament also feature no significant chemical-shift dispersion, resulting in the observation of few resonance correlations at the random-coil chemical-shift position (Fig. 4*B*). In our preparations of the mouse ASC filament, the CARD thus is flexible while attached to the well-folded, rigid filament core (Fig. 4*C*).

Robustness of the ASC Inflammasome Architecture. To test the physiological effects of ASC mutations on inflammasome signaling and to avoid overexpression artifacts, we reconstituted immortalized mouse *Asc*^{-/-} macrophages with endogenous levels of WT and mutant versions of N-terminally mCherry-tagged ASC-FL. Based on the mouse ASC-PYD structure and previously reported studies (38), mutations K21A and K26A in interface I were selected (Fig. 5 and Fig. *S6*). As expected, the induction of cell death and IL-1 β secretion upon activation of the PYD-containing inflammasome sensors NLRP3 and absent in melanoma 2 (AIM2) was abrogated by each of these mutations. Consistent with the deficiency in signaling, no ASC specks could be detected in macrophages expressing these two single-amino acid mutants. Furthermore, the induction of cell death upon stimulation of the receptors NLRC4, which is ASC independent (39, 40), is not affected by the K21A and K26A mutations (Fig. *S6D*). However, the mutations significantly reduced IL-1 β release and completely abolished ASC speck formation during *Salmonella* infection (Fig. *S6D*). In line with previous reports that show the importance of functional ASC for these aspects of NLRC4 biology (40, 41). These data show that mutations in the type I interface can prevent ASC speck formation and inflammasome signaling during activation of the three best-studied inflammasome receptors, NLRP3, AIM2, and NLRC4. The disruption of filament formation upon mutation of lysine 21 or 26 to alanine confirms the importance of the precise balance of charged residues in interface I and suggests that the mechanism of filament assembly proposed for the in vitro reconstruction is extendable to cell cultures. This finding indicates that, independently of which ligand and receptor induce inflammasome activation, the architecture of the filaments in the ASC speck remains conserved.

Discussion

The integration of solid-state NMR data with a cryo-EM density map used here toward a joint determination of structure is one of

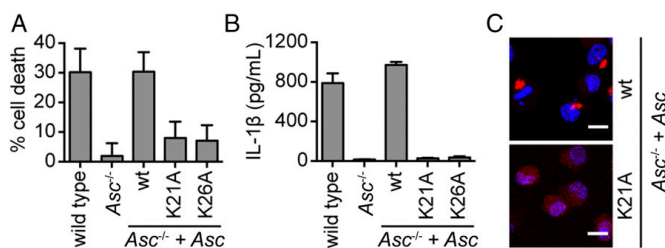


Fig. 5. Effect of single point mutations on ASC-dependent signaling. (A and B) Cell death as measured by lactate dehydrogenase (LDH) release (A) and IL-1 β secretion (B). (C) Overview images showing DNA in blue and ASC in red in LPS-primed immortalized mouse macrophages from the indicated genotypes: wild-type (wt), *Asc*^{-/-}, or *Asc*^{-/-} expressing endogenous levels of wild-type (wt) or ASC-mCherry K21A and K26A. Macrophages were stimulated with 5 mM ATP. (Scale bars, 10 μm .)

very few recent examples of this emerging approach. The other published example comprises structural studies of the type III secretion needle, also a helical arrangement (20, 42). Importantly, the two techniques provide complementary information, leading to an overall comprehensive description extending beyond the power and resolution of cryo-EM or solid-state NMR alone. The EM density map in combination with the identification of helix location and the use of individual dihedral backbone angle restraints from solid-state NMR data allow unambiguous determination of the backbone structure de novo. Thereby, the amount of information for solid-state NMR experiments can be increased gradually from backbones to side chains to intermonomer correlations by recording and analyzing additional experiments. This feature allows a convergence of the structure-determination procedure, as demonstrated here in the stepwise protocol from models 1–3. The measurement of NMR distance restraints, considerably more laborious than the determination of backbone angles, was shown to be consistent with, but not necessary for, backbone localization. It did lead to a significant, albeit relatively minor, improvement of side-chain conformations.

The mouse ASC filament is a helical arrangement of individual PYDs mediated by electrostatic and hydrophobic intermolecular contacts along specific interfaces. The comparison with the previously established human ASC-PYD filament (16) shows that the molecular architecture is strongly conserved between the two species. The filament architecture thus is encoded in the amino acid sequence of ASC and determines the correct quaternary assembly upon inflammatory stimulation. This observation suggests that the molecular mechanism of the ASC-dependent innate immune response is conserved and follows the same biophysical principles in both species, implicating a

biological role for the filament structure. Thereby, the helical arrangement and the interfaces I–III are in full agreement with other reported helical arrangements of death domains (17, 43). The CARD in ASC-FL filaments was found to be dynamic and a least partially unfolded in our experimental conditions. Low thermodynamic stability of a CARD has been reported before [e.g., in the procaspase-1 CARD (44)], and a population shift toward unfolded conformations upon filament formation might constitute a general functional element of ASC. For example the dynamic nature of ASC-CARD could be required for the interaction with downstream caspase-1, or it may reduce the amount of CARD–CARD-mediated filament branching and thus control the protein density in the 3D ASC speck in vivo. The structure of mouse ASC filament provides an ideal basis for structure-based mutagenesis, as demonstrated with our single point mutation experiments in cultured macrophages. This approach allows experiments at native expression levels of ASC, avoiding artifactual induction of ASC filament formation.

Materials and Methods

Experimental details of sample preparation, cryo-electron microscopy, NMR spectroscopy and the cell culture experiments are given in *SI Materials and Methods*.

ACKNOWLEDGMENTS. We thank Vesna Oliveri, Janine Zankl, and Timr Maier for experimental help and discussions. This work was supported by NIH Grant EB001567 (to E.H.E.), by Swiss National Science Foundation (SNSF) Grants 200020_146757 (to B.H.M.), ANR-12-BS08-0013-01 (to A.B.), and ANR 11-BSV8-021-01 (to A.B.), and by the Swiss Initiative in Systems Biology SytemsX.ch (Research, Technology and Development Project Cellular Imaging and Nanoanalytics).

- Franchi L, Muñoz-Planillo R, Núñez G (2012) Sensing and reacting to microbes through the inflammasomes. *Nat Immunol* 13(4):325–332.
- Lamkanfi M, Dixit VM (2014) Mechanisms and functions of inflammasomes. *Cell* 157(5):1013–1022.
- Vamaja SK, Rathinam VA, Fitzgerald KA (2015) Mechanisms of inflammasome activation: Recent advances and novel insights. *Trends Cell Biol* 25(5):308–315.
- Schroeder K, Tschopp J (2010) The inflammasomes. *Cell* 140(6):821–832.
- Walsh JG, Muruve DA, Power C (2014) Inflammasomes in the CNS. *Nat Rev Neurosci* 15(2):84–97.
- Strowig T, Henao-Mejia J, Elinav E, Flavell R (2012) Inflammasomes in health and disease. *Nature* 481(7381):278–286.
- Lamkanfi M, Dixit VM (2012) Inflammasomes and their roles in health and disease. *Annu Rev Cell Dev Biol* 28:137–161.
- Hu Z, et al. (2013) Crystal structure of NLR4 reveals its autoinhibition mechanism. *Science* 341(6142):172–175.
- Lu A, Wu H (2015) Structural mechanisms of inflammasome assembly. *FEBS J* 282(3):435–444.
- Masumoto J, et al. (1999) ASC, a novel 22-kDa protein, aggregates during apoptosis of human promyelocytic leukemia HL-60 cells. *J Biol Chem* 274(48):33835–33838.
- Srimathi T, et al. (2008) Mapping of POP1-binding site on pyrin domain of ASC. *J Biol Chem* 283(22):15390–15398.
- Hillier S, et al. (2003) NMR structure of the apoptosis- and inflammation-related NALP1 pyrin domain. *Structure* 11(10):1199–1205.
- Vajihala PR, et al. (2014) Identification of multifaceted binding modes for pyrin and ASC pyrin domains gives insights into pyrin inflammasome assembly. *J Biol Chem* 289(34):23504–23519.
- de Alba E (2009) Structure and interdomain dynamics of apoptosis-associated speck-like protein containing a CARD (ASC). *J Biol Chem* 284(47):32932–32941.
- Liepinsh E, et al. (2003) The death-domain fold of the ASC PYRIN domain, presenting a basis for PYRIN/PYRIN recognition. *J Mol Biol* 332(5):1155–1163.
- Lu A, et al. (2014) Unified polymerization mechanism for the assembly of ASC-dependent inflammasomes. *Cell* 156(6):1193–1206.
- Qiao Q, et al. (2013) Structural architecture of the CARMA1/Bcl10/MALT1 signalosome: Nucleation-induced filamentous assembly. *Mol Cell* 51(6):766–779.
- Park HH, et al. (2007) Death domain assembly mechanism revealed by crystal structure of the oligomeric PIDosome core complex. *Cell* 128(3):533–546.
- Wasmer C, et al. (2008) Amyloid fibrils of the HET-s(218–289) prion form a beta solenoid with a triangular hydrophobic core. *Science* 319(5869):1523–1526.
- Loquet A, et al. (2012) Atomic model of the type III secretion system needle. *Nature* 486(7402):276–279.
- Debelouchina GT, Platt GW, Bayro MJ, Radford SE, Griffin RG (2010) Intermolecular alignment in β 2-microglobulin amyloid fibrils. *J Am Chem Soc* 132(48):17077–17079.
- Petkova AT, et al. (2002) A structural model for Alzheimer's beta-amyloid fibrils based on experimental constraints from solid state NMR. *Proc Natl Acad Sci USA* 99(26):16742–16747.
- Meier BH, Böckmann A (2015) The structure of fibrils from 'misfolded' proteins. *Curr Opin Struct Biol* 30:43–49.
- Lu JX, et al. (2013) Molecular structure of β -amyloid fibrils in Alzheimer's disease brain tissue. *Cell* 154(6):1257–1268.
- Scherer S, et al. (2014) 2dx_automator: Implementation of a semiautomatic high-throughput high-resolution cryo-electron crystallography pipeline. *J Struct Biol* 186(2):302–307.
- Li X, et al. (2013) Electron counting and beam-induced motion correction enable near atomic-resolution single-particle cryo-EM. *Nat Methods* 10(6):584–590.
- Egelman EH (2000) A robust algorithm for the reconstruction of helical filament using single-particle methods. *Ultramicroscopy* 85(4):225–234.
- Schuetz A, et al. (2010) Protocols for the sequential solid-state NMR spectroscopic assignment of a uniformly labeled 25 kDa protein: HET-s(1–227). *ChemBioChem* 11(11):1543–1557.
- Ravotti F, et al. (September 24, 2015) Sequence-specific solid-state NMR assignment of the mouse ASC PYRIN domain in its filament form. *Biomol NMR Assign*, 10:100: s12104-015-9647-6.
- Igumenova TI, et al. (2004) Assignments of carbon NMR resonances for microcytalline ubiquitin. *J Am Chem Soc* 126(21):6720–6727.
- Emsley P, Cowtan K (2004) Coot: Model-building tools for molecular graphics. *Acta Crystallogr D Biol Crystallogr* 60(Pt 12 Pt 1):2126–2132.
- Schwieters CD, Kuszewski JJ, Tjandra N, Clore GM (2003) The Xplor-NIH NMR molecular structure determination package. *J Magn Reson* 160(1):65–73.
- Kneller DG, Kuntz ID (1993) UCSF Sparky – an NMR display, annotation and assignment tool. *J Cell Biochem* 53(S17C):254–254.
- Herrmann T, Güntert P, Wüthrich K (2002) Protein NMR structure determination with automated NOE assignment using the new software CANDID and the torsion angle dynamics algorithm DYANA. *J Mol Biol* 319(1):209–227.
- Habenstein B, et al. (2011) Extensive de novo solid-state NMR assignments of the 33 kDa C-terminal domain of the Ure2 prion. *J Biomol NMR* 51(3):235–243.
- Shen Y, Delaglio F, Cornilescu G, Bax A (2009) TALOS+: A hybrid method for predicting protein backbone torsion angles from NMR chemical shifts. *J Biomol NMR* 44(4):213–222.
- Morris GA, Freeman R (1979) Enhancement of nuclear magnetic resonance signals by polarization transfer. *J Am Chem Soc* 101(3):760–762.
- Moriya M, et al. (2005) Role of charged and hydrophobic residues in the oligomerization of the PYRIN domain of ASC. *Biochemistry* 44(2):575–583.
- Mariathasan S, Monack DM (2007) Inflammasome adaptors and sensors: Intracellular regulators of infection and inflammation. *Nat Rev Immunol* 7(1):31–40.
- Broz P, von Moltke J, Jones JW, Vance RE, Monack DM (2010) Differential requirement for Caspase-1 autoproteolysis in pathogen-induced cell death and cytokin processing. *Cell Host Microbe* 8(6):471–483.
- Van Opendenbosch N, et al. (2014) Activation of the NLRP1b inflammasome independent of ASC-mediated caspase-1 autoproteolysis and speck formation. *Nat Commun* 5:3209.
- Demers JP, et al. (2014) High-resolution structure of the Shigella type-III secretion needle by solid-state NMR and cryo-electron microscopy. *Nat Commun* 5:4976.
- Lin SC, Lo YC, Wu H (2010) Helical assembly in the MyD88-IRAK4-IRAK2 complex I TLR/IL-1R signalling. *Nature* 465(7300):885–890.
- Chen YR, Clark AC (2004) Kinetic traps in the folding/unfolding of procaspase-1 CARD domain. *Protein Sci* 13(8):2196–2206.
- Güntert P, Döttsch V, Wider G, Wüthrich K (1992) Processing of multi-dimensional NMR data with the new software PROSA. *J Biomol NMR* 2(6):619–629.

Supporting Information

Sborgi et al. 10.1073/pnas.1507579112

SI Materials and Methods

Cloning, Expression, and Purification of ASC-FL and ASC-PYD. cDNA coding for the mouse ASC-FL protein (residues 1–193) and for the PYD (residues 1–91) were cloned with a C-terminal six-histidine tag into a pET28a vector under the control of a T7 promoter. A GSGSLE linker was introduced at the C terminus to minimize the His-tag effect on protein structures. Both protein constructs were transformed in BL21(DE3) *Escherichia coli* strains, and the proteins were expressed by growing the cultures at 37 °C to an OD₆₀₀ of 0.8 and by induction with 1 mM isopropyl β-D-1-thiogalactopyranoside for 4 h. ASC-FL and ASC-PYD [¹⁵N]- and [¹⁵N,¹³C]-labeled, were produced using ¹³C-glucose and ¹⁵NH₄Cl as the sole carbon and nitrogen sources. The cells were harvested by centrifugation, and the pellet was resuspended in 50 mM phosphate buffer (pH 7.5), 300 mM NaCl, 0.1 mM protease inhibitor.

The resuspended cells were incubated for 1 h at room temperature with DNase I and then were sonicated on ice and centrifuged at 20,000 × g at 4 °C for 30 min. The inclusion body pellet was resuspended in 50 mM phosphate buffer (pH 7.5), 300 mM NaCl, 6 M guanidinium hydrochloride and was centrifuged at 20,000 × g at 4 °C for 30 min. The supernatant was incubated for 2 h at room temperature with preequilibrated Ni-NTA affinity resin (Thermo Scientific) and then was passed through a column for gravity flow purification. The column was washed with 20 column volumes of resuspension buffer containing 20 mM imidazole, and the fusion protein was eluted with three column volumes of the same buffer with 500 mM imidazole. To avoid aggregation, all the purification steps were carried out at 4 °C, and 2 mM DTT was added to all buffers used for the ASC-FL purification. An additional purification step was used to obtain the monomeric soluble form of ASC-PYD. ASC precipitates at physiological pH conditions; thus the pH of the elution fraction from the Ni column was decreased to 3.8 and dialyzed against 50 mM glycine buffer (pH 3.8), 150 mM NaCl. The protein was purified further on a preequilibrated Superdex 75 gel filtration column (GE Healthcare) and was used immediately or frozen in small aliquots in liquid N₂.

ASC-FL and ASC-PYD Filament Formation *In Vitro*. Two protocols for ASC-FL and ASC-PYD filament formation based on a pH or dialysis step were used, leading to identical filament structures as determined by negative-stain EM and solid-state NMR spectroscopy. For the method based on the pH step, the elution fraction from the Ni column was concentrated to half of the volume (~5 mL) using Vivaspin and then was diluted with 150 mM acetic acid (pH 2.5) in a 1:9 ratio (vol/vol). The neutral pH condition was achieved by the addition of 3 M Tris buffer (pH 8) in a 1:5 ratio (vol/vol). The solution was incubated overnight at room temperature with continuous stirring to facilitate filament formation. The solution was centrifuged at 20,000 × g at 4 °C for 30 min, yielding a gel-like pellet of ASC filaments that was resuspended in water and then was transferred into the rotor by centrifugation or stored at 4 °C. For the dialysis-based filament formation method, the elution fraction of NiNTA purification was dialyzed overnight against 25 mM phosphate buffer (pH 7.5), 100 mM NaCl. The ASC filaments were centrifuged, washed, and stored as described above.

Solution NMR Spectroscopy. NMR samples were prepared at 0.3 mM [¹⁵N,¹³C]-labeled ASC-PYD in 20 mM glycine buffer (pH 3.7), 150 mM NaCl, 0.1 mM NaN₃, 5% D₂O/H₂O. Under these

conditions the ASC-PYD remains soluble and monomeric according to NMR line-width values. NMR experiments were acquired at 298 K in Bruker 600, 700, and 800 MHz spectrometer equipped with room-temperature and cryogenic triple-resonance probes. Sequence-specific backbone chemical-shift assignments were obtained from the experiments [¹⁵N-¹H]-HSQC, 3D HNCACB, and 3D C(CO)NH-TOCSY. All NMR data were processed using the software PROSA (45) and analyzed with CARA.

Solid-State NMR Spectroscopy. Protein filaments were packed into 3.2-mm ZrO₂ rotors (Bruker Biospin) using ultracentrifugation and a custom-made filling device in a SW41-T1 swing-out rotor spinning at 25,000 rpm for 12 h in an Optima L90-K ultracentrifuge (Beckmann). The spectra used for the assignment and for the distance restraints were recorded on a Bruker Avance II spectrometer operating at 850 MHz ¹H Larmor frequency with a sample temperature of 288 K. For the backbone assignment, a standard set of experiments, NCOCA, NCACO, NCACB, and CANCO, were recorded at 17 kHz MAS frequency. A second set of experiments, N(CO)CACB, and CAN(CO)CA, was used to complete the assignment in regions of spectral overlap. The side-chain assignment was achieved using 3D CCC and N(CA)CBCX and 2D DARR experiments. The spectra were processed with Topspin (Bruker Biospin), using a shifted cosine square as apodization function and were analyzed with CCPN. Long-range spin contacts were obtained from 2D DARR, CHHC, and PAI experiments, recorded at 15 kHz MAS to avoid overlap with the sideband in the region of the aromatic carbons. See ref. 29 for further details of the assignment procedure.

Cryo-EM Microscopy and Image Reconstruction. ASC-PYD filament polymerized by dilution with buffer solution were applied to glow discharged thin carbon film-coated copper EM grids. The grid were blotted for 1 s and vitrified by being plunged into liquid nitrogen-cooled liquid ethane, using an FEI Vitrobot MK4. Grid containing ASC-PYD filaments were imaged using an FEI Titan Krios electron microscope operated at an acceleration voltage of 300 keV. Images were recorded using a 4k × 4k K2 Summit direct electron detector with a back thinned CMOS chip, operated in electron-counting mode. Images were recorded in movie-mode format and were automatically drift corrected and averaged using a 2dx_automator (25), employing MOTIONCORR (26). In total, 150 images were recorded by operating the microscope in low-dose mode at a nominal magnification of 22,500× with a cumulated dose below ~20 e⁻/Å² distributed over 30 frames recorded over 5 s. The effective pixel size of the images was 1.34 Å on the sample level.

The defocus was determined using CTFFIND3, and the contrast transfer function (CTF) of the microscope was corrected by multiplying the images with the theoretical CTF (a Wiener filter in the limit of a low signal-to-noise ratio). Long filament sections were cut from the images using the e2helixboxer routine within EMAN2. The SPIDER software package was used for most of the image processing and for the calculation of the FSC plot. Then a total of 21,138 overlapping 320-pixel-long boxes, with 1.34 Å per pixel, were cut from the long filament boxes, using a shift of 1 pixel (95% overlap). These segments initially were decimated by a factor of three (to 4.02 Å per pixel) and were centered. Subsequent processing involved the IHRSR algorithm (27) implemented within SPIDER, with the imposition of a C3 rotational symmetry about the helical axis. A negative B-factor of 150 was

used. The defocus range was -1.0 microns to -3.5 microns. The final reconstruction was corrected for the CTF (which had been imposed twice, once by the microscope and once during image processing) by dividing by the sum of the CTFs squared. A reconstruction was tried using a 384-pixel box length but suffered from worse resolution, reflecting the limited long-range order in these filaments.

Procedure for Structure Calculation. In the first step of calculation, a single ASC-PYD subunit was constructed de novo using the program Coot (31). Thereby, the ASC-PYD polypeptide chain was placed into the cryo-EM density, and helical regions were defined interactively according to secondary chemical shifts from the solid-state NMR assignments. Well-defined side-chain electron densities for residues F23, R38, Y59, Y60, and Y64 facilitated the correct positioning of the polypeptide chain into the density map. The structure of the single monomer then was translated into all symmetrically identical positions of the electron density map. The resulting model was refined locally to match the electron density map. The model then was refined using X-PLOR-NIH under continuous symmetry enforcement, using as constraints the cryo-EM density map, TALOS+-determined dihedral angle constraints, and hydrogen-bond constraints (32, 36). These $i, j+4$ backbone hydrogen-bond constraints for residues 4–10, 17–24, 41–42, 49–55, 62–71, and 79–90 were based on the secondary structure prediction from solid-state NMR chemical shifts by TALOS+. Only constraints for residues with good TALOS+ prediction quality were kept. For use in X-PLOR-NIH, the cryo-EM map was placed into an artificial crystal lattice environment and transformed to reciprocal space representation to calculate structure factors. The amplitudes and phases of the structure factors were used as experimental diffraction data for model refinement by crystallographic conjugate gradient minimization, B-factor optimization, and simulated annealing refinement. This conversion from the real-space cryo-EM map to reciprocal-space structure factors, fully preserving the information content of the data, is necessary for the simultaneous refinement with NMR data. The X-PLOR-NIH structure calculation protocol was repeated 100 times, and the 20 structures with the lowest energy were selected. The resulting structural ensemble was used as input for the automatic assignment of the solid-state 2D $[^{13}\text{C}, ^{13}\text{C}]$ -CHHC and $[^{13}\text{C}, ^{13}\text{C}]$ -PAR spectra. The spectra were automatically peak-picked, and the peak lists were interpreted using the CANDID algorithm in the structure calculation program CYANA (34). Chemical-shift tolerances for CANDID were set at 0.2 ppm for ^{13}C , and only the last cycle (cycle 7) of the CYANA automatic protocol was applied. The peak lists were converted to upper limit distance restraints assuming a uniform distance limit of 7 Å for every peak. A final round of X-PLOR-NIH structure calculation was performed under symmetry enforcement with the cryo-EM-derived struc-

ture factors, the dihedral angle restraints from TALOS+, but no the H-bond restraints, and the distance restraints from CANDID. The $R_{\text{work}}/R_{\text{free}}$ ratio was obtained from a randomly selected 95%/5% work/free dataset. The 10 lowest-energy structures from were selected from a total of 100 structures and were subjected to local real-space refinement against the cryo-EM map. The N- and C-terminal residues M1 and E91 were removed because of the absence of any experimental data for these residues.

Cell Culture Experiments. WT and *Asc*^{-/-} immortalized murine bone marrow-derived macrophages (40) were cultured in DMEM (Sigma) supplemented with 10% 3T3 macrophage-colony stimulating factor (M-CSF) supernatant and 10% FCS (Bio Concept). Genes encoding *mCherry* and murine *Asc* were cloned into a replication-defective mouse stem cell retroviral construct (pMSCV2.2). Site-directed mutagenesis was performed with QuikChange (Stratagene). Retroviral transduction of immortalized bone marrow-derived macrophages (iBMDMs) with ASC *mCherry* and the K21A and K26A mutations was done as previously described (40), and monoclonal cell lines were generated by limiting dilution. ASC protein levels were estimated by Western blot using anti-ASC (Genentech) and anti- β -actin (Sigma) antibodies, and clones expressing levels of ASC comparable to the levels in WT cells were selected. iBMDMs were prestimulated for 4 h with 100 ng/mL LPS O55:B5 (Invivogen). NLRP3 was triggered by 5 mM ATP (Sigma) for 90 min, AIM2 by transfection of 1 $\mu\text{g}/\text{ml}$ poly(deoxyadenylic-deoxythymidylic acid [poly(dA:dT)]) (Invivogen) in OptiMEM (Gibco) using Lipofectamine 2000 (Invitrogen) for 2.5 h, and NLRC4 by infection with log-phase *Salmonella enterica* serovar Typhimurium SL1344 WT at a multiplicity of infection (MOI) of 10 for 60 min. Cell death was measured by LDH release (Clontech LDH Cytotoxicity Detection Kit) and IL-1 β by ELISA (eBioscience).

Confocal Microscopy. To assess the formation of ASC-mCherry specks, the cells were seeded on glass coverslips, and inflammation activation was triggered as described above. To prevent cell death and subsequent detachment from the coverslips, the cells were treated with 25 μM Z-Val-Ala-DL-Asp-fluoromethylketone (ZVAD; Bachem) to inhibit caspase activation at the time of inflammasome activation. iBMDMs were fixed with 4% paraformaldehyde, mounted with VECTASHIELD containing DAPI and imaged using a Leica Point Scanning Confocal “SP8” with either an HC PL APO CS 40 \times objective for speck quantification or an HC PL APO CS2 63 \times objective for overview images. Images were acquired using the Leica LAS AF software (version 3) and analyzed using Fiji. For speck quantifications, Z-stacks of five arbitrarily chosen regions per condition and replicate were acquired, and the number of cells with specks was determined manually.

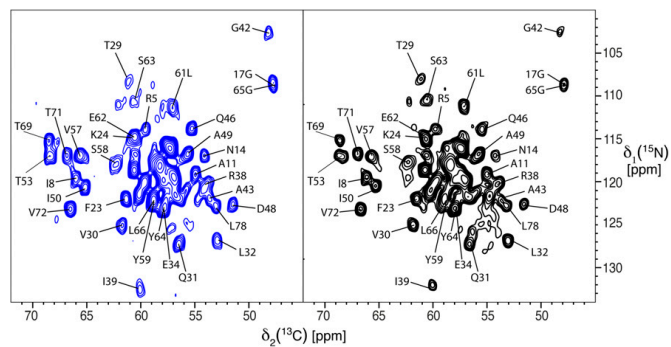


Fig. S1. Backbone correlation spectra of ASC-PYI and ASC-FL filaments are highly similar. Solid-state 2D NCA correlation spectra of filaments of ASC-PYI (blue) and ASC-FL (black), recorded under MAS conditions. Sequence-specific assignments are shown for signals in the less crowded regions of the spectra.

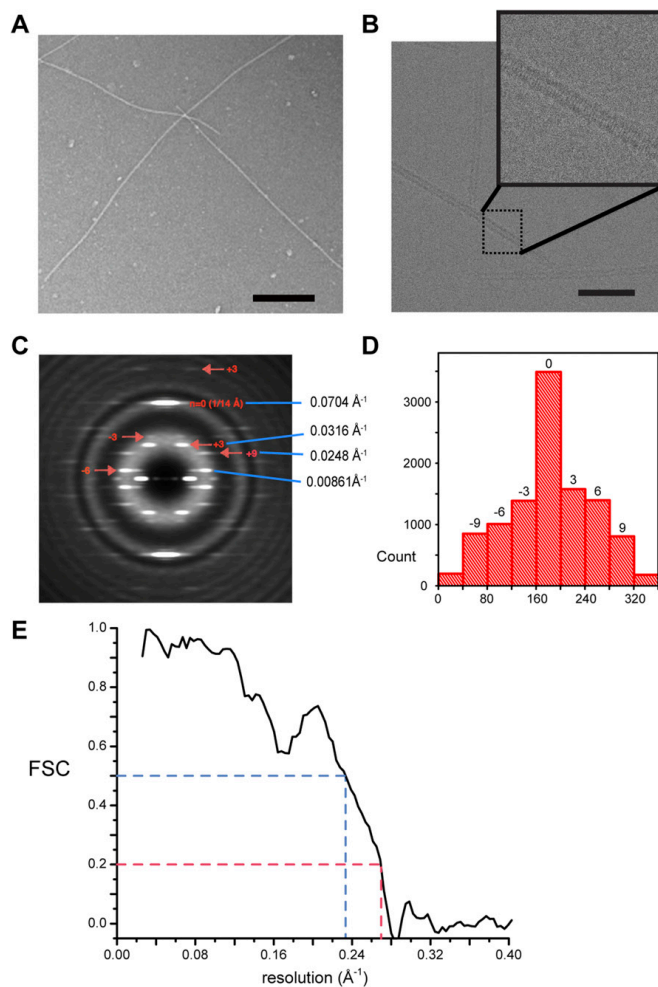


Fig. S2. Cryo-EM with the ASC-PYD filament. (A) Filaments of the ASC-PYD obtained by dilution of denatured protein with phosphate buffer are well-ordered and separated. (Scale bar, 100 nm.) (B) Cryo-EM image of ASC-PYD filaments. (Scale bar, 50 nm.) (C) Layer-line analysis of average power spectra of ASC-PYD filaments, showing the axial rise per subunit of 14.2 Å ($n = 0$ layer line). Because of the well-ordered nature of the filaments, there is no variable twist feature (D) Statistics of filament segments divided into separate bins according to out-of-plane tilts of -12° to $+12^\circ$. (E) FSC between the NMR-refined model and the cryo-EM map. FSCs of 0.2 and 0.5 are reached to resolutions of 3.7 Å (red line) and 4.3 Å (blue line), respectively.

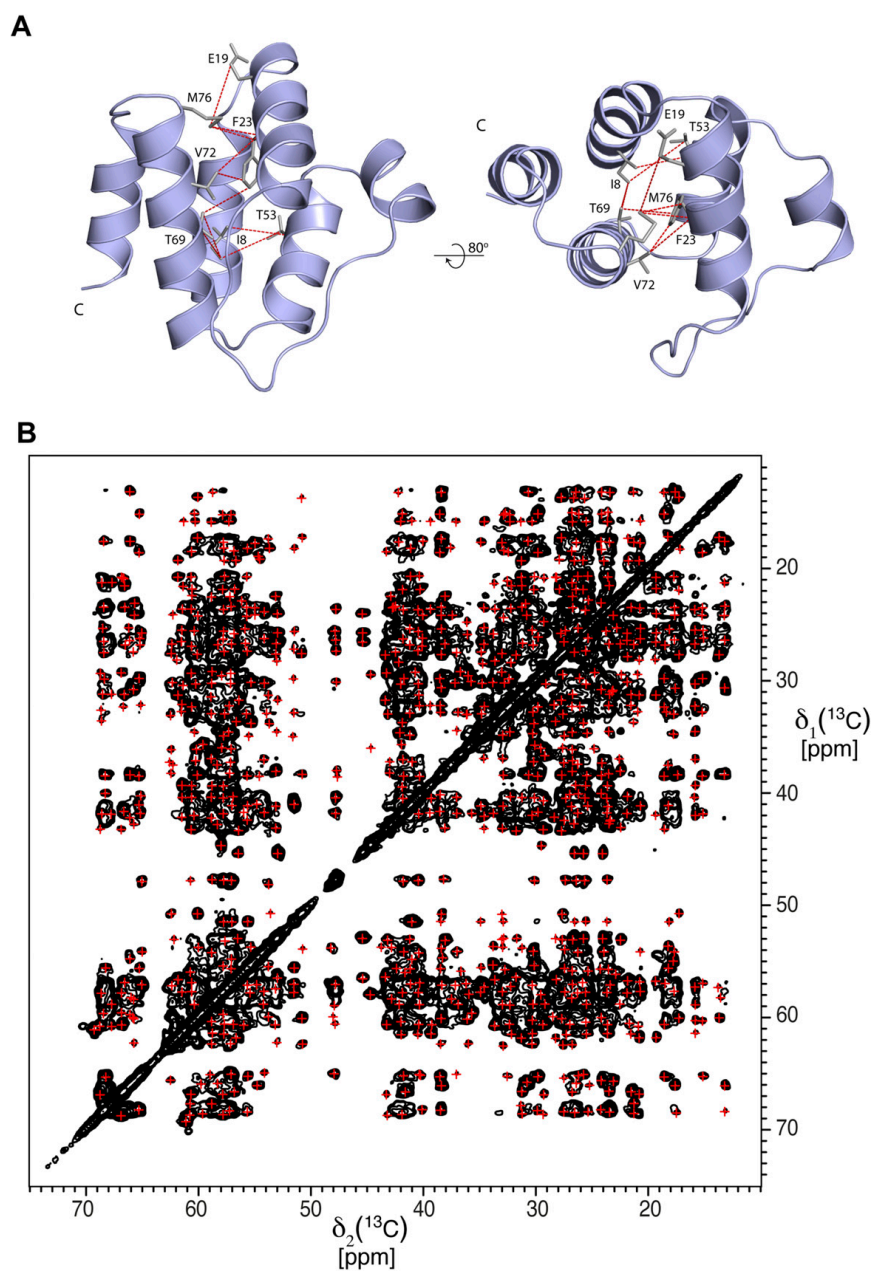


Fig. S3. Distance restraints from solid-state NMR experiments. (A) Structure of an ASC-PYD monomer from the filament. All unambiguous distance restraint from 2D solid-state NMR experiments (Table S1) are indicated by red dashed lines. (B) Aliphatic region of a 2D ^{13}C - ^{13}C -PAR spectrum acquired on a $[\text{U-}^{13}\text{C}]$ labeled ASC-PYD filament. The spectra were recorded on an 850-MHz spectrometer at 15 kHz MAS conditions. Red crosses show site-specific cross-peak assignments determined using the CANDID algorithm.

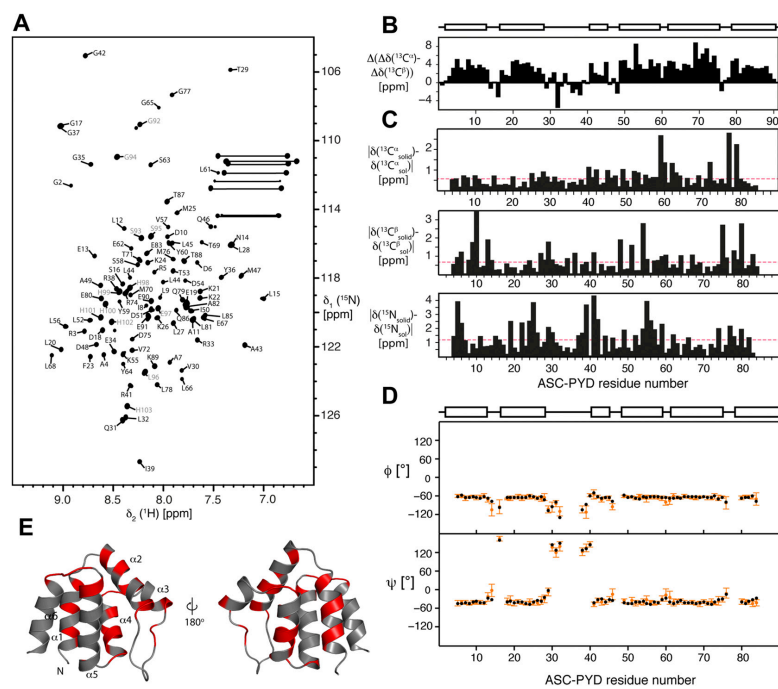


Fig. 54. Solution NMR spectroscopy of monomeric ASC-PYD and its comparison with the filament form. (A) 2D [^{15}N , ^1H]HSQC spectrum of monomeric [^{15}N] labeled ASC-PYD recorded in 50 mM glycine buffer and 150 mM NaCl (pH 3.7) at 25 °C. Sequence-specific resonance assignments obtained from 3D triple-resonance solution NMR experiments are shown using the one-letter amino acid code and residue number. Correlations of NH α moieties of Gln and Asn side chains are connected by solid lines. Cross-peaks that belong to the C-terminal tag are labeled in gray. (B) Secondary chemical shifts of monomeric ASC-PYD in solution. (C) Comparison of isotropic chemical shift of monomeric ASC-PYD in solution versus the oligomerized solid-state form computed as the absolute values of the differences (solid – solution). The mean values for $^{13}\text{C}\alpha$ (0.56 ppm), $^{13}\text{C}\beta$ (0.68 ppm), and ^{15}N (1.18 ppm) are indicated by red dashed lines. (D) Comparison of backbone dihedral angles predicted by TALOS+ for monomeric ASC-PYD in solution (black dots) versus ASC-PYD filament (orange dots). Data are shown for all statistically significant predictions. Error bars for solid-state values are based on the 10 best database matches. (E) Structure of the ASC-PYD monomer as part of the filament. All residues with a combined chemical-shift difference for ^{15}N , $^{13}\text{C}\alpha$, and $^{13}\text{C}\beta$ larger than the average value (Fig. 4C) are shown in red. All other residues are shown gray.

Table S1. Spectrally unambiguous distance restraints from 2D solid-state NMR experiments and their distance in model 2

Experiment	Nucleus 1	Nucleus 2	Distance restraint r , Å*	Intramolecular distance d in model 2, Å
CHHC	23 Phe C β	76 Met C ϵ	7.0	4.1
	69 Thr C β	8 Ile C δ 1	7.0	5.6
	19 Glu C γ	76 Met C ϵ	7.0	6.7
PAR	23 Phe C α	76 Met C ϵ	7.0	4.5
	23 Phe C β	76 Met C ϵ	7.0	4.1
	19 Glu C γ	76 Met C ϵ	7.0	6.7
	23 Phe C α	72 Val C γ 1	7.0	5.2
	23 Phe C α	76 Met C ϵ	7.0	4.5
	8 Ile C δ 1	53 Thr C β	7.0	6.8
	8 Ile C γ 2	53 Thr C α	7.0	5.7
	23 Phe C ζ	69 Thr C γ 2	7.0	5.2
	23 Phe C ϵ	72 Val C γ 1	7.0	3.4
	8 Ile C δ 1	69 Thr C γ 2	7.0	6.0

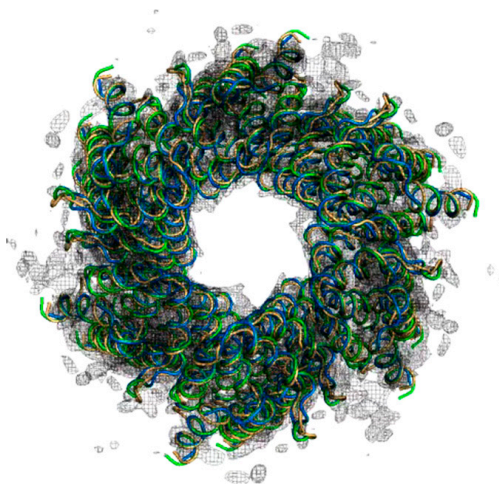
*All these distance restraints are fulfilled intramolecularly by model 2, because $d < r$. Note that the restraints are spectrally unambiguous (only one assignment possibility in each dimension) but are not necessarily unambiguous with respect to their intra-/intermolecularly.

Table S2. Structural statistics for the mouse ASC PYD filament

NMR distance and dihedral constraints	
Distance constraints*	
Total	674
Intraresidue	19
Interresidue	655
Sequential, $ i - j = 1$	89
Medium range, $ i - j < 4$	209
Long-range, $ i - j > 5$	179
Intermolecular	65
Hydrogen bonds	0
Total dihedral angle restraints	140
ϕ	70
ψ	70
Cryo-EM	
Resolution, Å	3.7
No. reflections	50,317 (work: 48,264; test: 2,572)
R_{work}/R_{free}	0.32/0.33
Structure statistics	
Violations (mean and SD)	
Distance constraints, Å	0
Dihedral angle constraints, °	2 (0)
Max. dihedral angle violation, °	10.5 (0.3)
Max. distance constraint violation, Å	0.0
Deviations from idealized geometry	
Bond lengths, Å	0.0028
Bond angles, °	0.51
Impropers, °	0.46
Ramachandran analysis	
Most favored regions, %	99.0
Disallowed regions, %	0.0
Average pairwise rmsd [†] , Å	
Heavy	0.48
Backbone	0.14

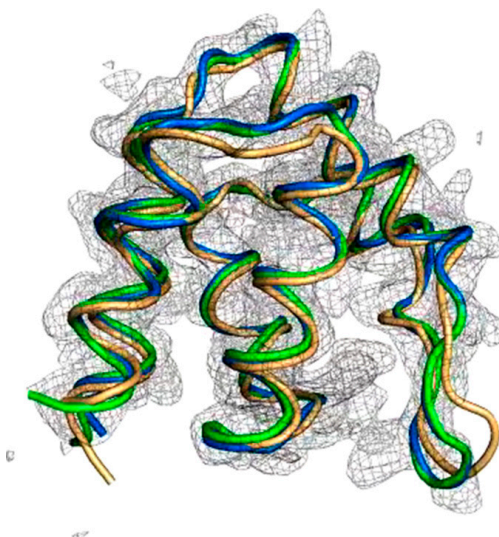
*Obtained from 2D [¹³C,¹³C]-CHHC and 2D [¹³C,¹³C]-PAR, interpreted by CANDID.

[†]Pairwise rmsd was calculated among 10 refined structures.



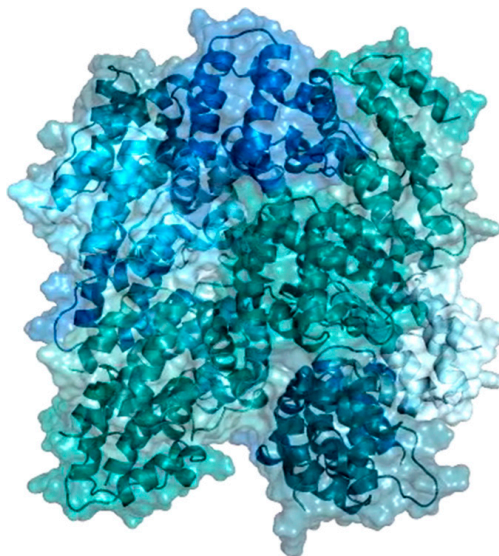
Movie S1. Electron density and structure of the mouse ASC-PYD filament. Top and side views of the filament are shown. The electron density from cryo-EM is shown at the 3σ level as a shaded gray surface. Structural models 1, 2, and 3 are shown in backbone representation (beige, green, and blue, respectively).

[Movie S1](#)



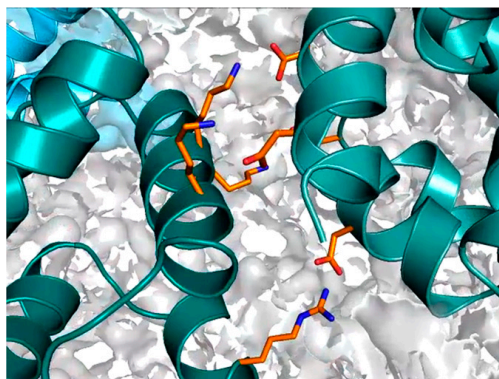
Movie S2. Electron density and structure of the mouse ASC-PYD filament. Density and structural models for a single ASC-PYD monomer are shown in the same representation as in Movie S1. Residues E34, Q31, Q79 and Y59 are shown in side-chain representation (in order of appearance). Note the improved fitting of model 3 (blue) to the electron density compared with model 1 (beige).

[Movie S2](#)



Movie S3. Structure of the mouse ASC-PYD filament. Top and side views of a rotating 15-subunit segment of the ASC-PYD filament are shown in surface representation. The three helical oligomer strands are colored blue, teal, and dark blue, and individual ASC-PYD units within each strand are reported with alternating darker and lighter shades.

[Movie S3](#)



Movie S4. Structure of the mouse ASC-PYD filament. Structural details of interfaces I (orange), II (yellow), and III (red), including side-chain positions, are shown.

[Movie S4](#)

2.2 Research article II

ASC filament formation serves as a signal amplification mechanism for inflammasomes

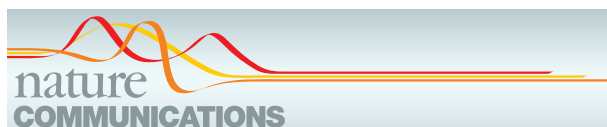
M. S. Dick, L. Sborgi, S. Rühl, S. Hiller and P. Broz.

Nature Communications

2016 June 22; 7:11929. doi: 10.1038/ncomms11929.³²²

Statement of contribution

I generated the ASC^{PYD} mutants and all cell lines. Subsequently, I performed all inflammasome stimulation experiments and conducted all cell death and IL-1 β release measurements, fluorescence microscopy and speck quantifications. Furthermore, I performed all Western blots including co-immunoprecipitations and was involved in co-expression of ASC^{FL} and ASC^{CARD} mutants in primary macrophages. Finally, I wrote the manuscript together with Petr Broz and the help of Lorenzo Sborgi and Sebastian Hiller.



ARTICLE

Received 23 Nov 2015 | Accepted 11 May 2016 | Published 22 Jun 2016

DOI: 10.1038/ncomms11929

OPEN

ASC filament formation serves as a signal amplification mechanism for inflammasomes

Mathias S. Dick¹, Lorenzo Sborgi², Sebastian Rühl¹, Sebastian Hiller² & Petr Broz¹

A hallmark of inflammasome activation is the ASC speck, a micrometre-sized structure formed by the inflammasome adaptor protein ASC (apoptosis-associated speck-like protein containing a CARD), which consists of a pyrin domain (PYD) and a caspase recruitment domain (CARD). Here we show that assembly of the ASC speck involves oligomerization of ASC^{PYD} into filaments and cross-linking of these filaments by ASC^{CARD}. ASC mutants with a non-functional CARD only assemble filaments but not specks, and moreover disrupt endogenous specks in primary macrophages. Systematic site-directed mutagenesis of ASC^{PYD} is used to identify oligomerization-deficient ASC mutants and demonstrate that ASC speck formation is required for efficient processing of IL-1 β , but dispensable for gasdermin-D cleavage and pyroptosis induction. Our results suggest that the oligomerization of ASC creates a multitude of potential caspase-1 activation sites, thus serving as a signal amplification mechanism for inflammasome-mediated cytokine production.

¹Focal Area Infection Biology, Biozentrum, University of Basel, Klingelbergstrasse 50/70, 4056 Basel, Switzerland. ²Focal Area Structural Biology, Biozentrum, University of Basel, Klingelbergstrasse 50/70, 4056 Basel, Switzerland. Correspondence and requests for materials should be addressed to P.B. (email: petr.broz@unibas.ch).

Detection of pathogens by the innate immune system relies on germline-encoded pattern recognition receptors (PRRs), which recognize a variety of pathogen-derived molecules, known as pathogen-associated molecular patterns (PAMPs), and host-derived danger signals, known as danger-associated molecular patterns¹. Although most PRRs initiate transcriptional responses, such as the expression of cytokines^{2,3}, a subset of cytosolic PRRs promote the assembly of inflammasome complexes and subsequent activation of the cysteine protease caspase-1 (refs 4,5). To date, only members of the NOD-like receptor (NLR) family, the PYHIN protein family and PYRIN were shown to assemble inflammasomes in response to different cytosolic PAMPs or danger-associated molecular patterns^{5,6}. A unifying feature of all these receptors is either a pyrin domain (PYD) or a caspase recruitment domain (CARD), both of which belong to the death-fold domain superfamily. On the basis of the presence of these domains, the receptors can be classified as PYD-containing receptors (NLRP3: NLR family, PYD containing 3; AIM2: absent in myeloma 2; pyrin) or CARD-containing receptors (NLRC4: NLR family, CARD containing 4; NLRP1: NLR family, PYD containing 1). After receptor activation and oligomerization, these domains recruit the adaptor protein ASC (apoptosis-associated speck-like protein containing a CARD) and pro-caspase-1 into the complex through homotypic domain-domain interactions. Within the inflammasome, pro-caspase-1 is activated by dimerization and auto-proteolysis, and the proteolytically active hetero-tetramer is released⁷. Several substrates of caspase-1 have been identified, among them the pro-forms of the cytokines interleukin (IL)-1 β and IL-18 (refs 7–9). Another consequence of inflammasome activation is the induction of a pro-inflammatory cell death called pyroptosis¹⁰. Pyroptosis is driven by the amino-terminal cleavage fragment of gasdermin-D, a protein cleaved by caspase-1, and results in the lysis of the host cell and subsequent release of cytoplasmic content, among them processed IL-1 β and IL-18 (refs 11,12).

Recent studies have started to elucidate the role of the inflammasome adaptor protein ASC^{13–15}, a bipartite protein composed of a PYD and a CARD, also known as PYCARD^{16,17}. ASC has previously been regarded as a simple adaptor protein that links PYD-containing receptors to the CARD-containing caspase-1, via homotypic PYD–PYD and CARD–CARD interactions¹⁸. However, its role appears to be more complex, as on receptor activation ASC also forms the so-called ASC speck, a macromolecular form of the inflammasome with a diameter of $\sim 1\text{--}2\ \mu\text{m}$ ^{19,20}. Formation of the ASC speck is independent of caspase-1 activity, but requires the oligomerization of ASC into large insoluble aggregates^{20,21}. These ASC aggregates are stable and have even been shown to be released into the extracellular space, after pyroptosis induction, where they can trigger prolonged inflammasome activation in phagocytic cells^{22,23}. Analyses of stimulated emission depletion microscopy images and electron micrographs suggest an irregular, filamentous shape^{22,23}. Consistently, we and others have shown that ASC oligomerizes into long helical filaments via its PYD^{13–15}. Despite the advances regarding the atomic structure of the ASC filament, whether the ASC speck is the functional unit of the inflammasome is unclear. Several inflammasome receptors (for example, NLRC4 and mouse Nlrp1b) contain a CARD instead of a PYD and are able to recruit caspase-1 even in the absence of ASC. Indeed, we and others have shown that ASC is not required for cell death induction by these receptors^{24–28}. Nonetheless, activation of CARD-containing receptors results in ASC speck formation in wild-type (WT) cells, but how their CARD initiates ASC filaments is unknown. Furthermore, it is unclear whether ASC oligomerization itself is required for inflammasome

signalling. Previous mutagenesis studies of ASC could not address the role of ASC oligomerization in signalling, as they were based on overexpression of ASC mutants in HEK293 cells, which is prone to artefact generation and lacks the means to study the effects on downstream signalling^{13,29,30}.

Here we use retroviral expression of ASC mutants in ASC-deficient immortalized mouse macrophages, to address the mechanism of ASC speck formation and the functional relevance of ASC filament formation for inflammasome signalling. Our results reveal an architectural role for the ASC^{CARD}, showing that it is required to link individual ASC filaments towards forming the dense ASC speck. Furthermore, we show that ASC bridging molecules are necessary to allow CARD-containing receptors the initiation of ASC filament formation. Finally, we use site-directed mutagenesis of the ASC^{PYD}–ASC^{PYD} interaction interfaces to identify mutations that disrupt ASC filament formation without affecting the interaction to receptor PYDs. Surprisingly, such ASC mutants are still able to initiate caspase-1-dependent gasdermin-D maturation and subsequent cell death, but lack the ability to form filaments, to assemble ASC specks and to process IL-1 β , thus uncoupling the two major downstream signalling pathways. In conclusion, our data show that the ASC speck has a function in inflammasome signalling and support a model in which the rapid oligomerization of ASC via its PYD creates a multitude of potential caspase-1 activation sites, thus serving as a signal amplification mechanism for inflammasome signalling.

Results

Distinct roles for the ASC^{PYD} and ASC^{CARD} in speck assembly. Although ASC is the main structural component of the ASC speck^{20,24}, conflicting reports have implicated either the ASC^{PYD} or the ASC^{CARD} in speck assembly^{13,31,32}. To address the role of the ASC^{PYD} and the ASC^{CARD} in speck formation and downstream signalling, we transduced immortalized *Asc*^{-/-} murine bone marrow-derived macrophages (BMDMs) with fluorescently tagged full-length ASC (ASC^{FL}) or ASC^{PYD} and ASC^{CARD} alone (Fig. 1a). As overexpression of ASC^{FL} can result in aggregation even in the absence of activated receptor¹⁹, we selected individual clonal lines that did not display any autoactivation when unstimulated (Supplementary Fig. 1a). To test the functionality of these constructs, cells were primed with lipopolysaccharide (LPS) and transfected with the synthetic DNA analogue poly(deoxyadenylic-deoxythymidylic) acid (poly(dA:dT)), an activator of AIM2 (refs 33,34). mCherry-tagged ASC^{FL}, expressed in *Asc*^{-/-} cells, promoted pyroptosis (as measured by the release of lactate dehydrogenase (LDH)) and IL-1 β release (measured by enzyme-linked immunosorbent assay (ELISA)), to levels seen in immortalized WT macrophage controls (Fig. 1b). We also observed comparable levels of IL-1 β /-18 and caspase-1 processing and release by western blotting (Supplementary Fig. 1b). In contrast, neither the ASC^{PYD} nor ASC^{CARD} restored cell death, IL-1 β /-18 secretion or caspase-1 cleavage on AIM2 activation (Fig. 1b and Supplementary Fig. 1b). Similarly, expression of the individual domains did not restore inflammasome signalling in response to extracellular ATP, an NLRP3 activator³⁵ (Supplementary Fig. 1c,d).

Heterologous expression of ASC^{PYD} and ASC^{CARD} or CARDs of mitochondrial antiviral-signalling protein (MAVS), retinoic acid-inducible gene 1 (RIG-I) and pro-caspase-1 results in the formation of filaments of varying length in different cell types and *in vitro*^{13,36–40}. However, it is possible that such ASC^{PYD} or ASC^{CARD} filaments are overexpression artefacts, as ASC^{FL} normally forms a distinct dense speck structure²⁰. To assess the ability of ASC^{PYD} and ASC^{CARD} to form macromolecular assemblies, we examined the above described cell lines by

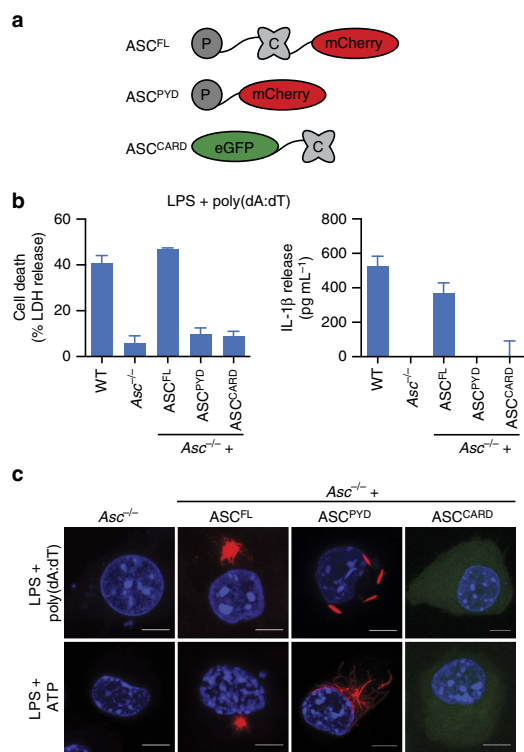


Figure 1 | Both domains of ASC are required for signalling. (a) Schematic representation of the domain organization of fluorophore-tagged (mCherry or enhanced GFP (eGFP)) WT ASC (ASC^{FL}), ASC^{PYD} and ASC^{CARD} constructs. (b) Release of LDH (assessing cell death) and IL-1 β from LPS-primed immortalized WT, Asc^{-/-} or Asc^{-/-} BMDMs expressing ASC^{FL}, ASC^{PYD} or ASC^{CARD} 3 h after poly(dA:dT) transfection (1 $\mu\text{g ml}^{-1}$). (c) Representative images of cell lines from (b) 3 h after poly(dA:dT) transfection (1 $\mu\text{g ml}^{-1}$) or 1 h after ATP treatment (5 mM). DNA (blue, Hoechst), ASC^{FL} or ASC^{PYD} (red) and ASC^{CARD} (green). Scale bars, 10 μm . Data (b,c) are representative of three independent experiments. Graphs show the mean and s.d. from quadruplicate wells. See also Supplementary Fig. 1.

microscopy, following inflammasome stimulation. As expected, activation of AIM2 or NLRP3 induced the formation of perinuclear specks in cells expressing mCherry-tagged ASC^{FL} (Fig. 1c and Supplementary Fig. 1e,f). In line with the reported ability of ASC to form filaments^{13,15}, specks formed by ASC^{FL} had a dense core with emanating filaments (Fig. 1c). Instead of forming similarly dense specks, the ASC^{PYD} assembled into filaments on the engagement of NLRP3 or AIM2 (Fig. 1c). Of note, filaments formed after NLRP3 or AIM2 activation differed in their appearance, possibly due to distinct modes of how NLR and PYHIN family members assemble complexes and initiate ASC filaments^{13,41}. Remarkably, these filaments had varying lengths and widths, with some appearing clearly thicker than 90 Å, the reported diameter of an ASC^{PYD} filament^{13,15}. Unlike reported before, we observed that the ASC^{CARD} was not able to form macromolecular assemblies (Fig. 1c and Supplementary Fig. 1e,f). Taken together, these data suggest that although both domains of ASC are necessary for signalling, only the

ASC^{PYD} forms filaments on inflammasome activation. This is consistent with reports by us and others showing that full-length ASC forms helical filaments *in vitro* via the ASC^{PYD} (refs 13,15), whereas the ASC^{CARD} is exposed on the surface and not involved in ASC filament formation¹⁵. As straight filaments are formed by ASC^{PYD} and compact specks are formed by ASC^{FL}, our data also suggest that the ASC^{CARD} must contribute significantly to the macroscopic structure of the ASC speck.

ASC^{CARD}s condense ASC^{PYD} filaments into ASC specks. To test whether ASC^{CARD} is required to form ASC specks, we generated immortalized Asc^{-/-} macrophage lines expressing ASC^{D130R} or ASC^{D134R} (Fig. 2a and Supplementary Fig. 2a), two mutations in surface-exposed residues of the ASC^{CARD} that abrogate interaction of the ASC^{CARD} with the pro-caspase-1^{CARD} (ref. 31). As expected, Asc^{-/-} macrophages expressing ASC^{D130R} or ASC^{D134R} did not activate caspase-1, release mature IL-1 β or undergo pyroptosis in response to DNA transfection or ATP treatment (Fig. 2b and Supplementary Fig. 2b–d). ASC^{D130R} and ASC^{D134R} formed long filaments rather than dense ASC specks in response to AIM2 and NLRP3 activation (Fig. 2c,d and Supplementary Fig. 2e,f), similar to the ASC^{PYD} alone, thus supporting our hypothesis that a functional ASC^{CARD} is required to assemble ASC^{PYD} filaments into a speck. To confirm that these mutations not only disrupt ASC^{CARD}–pro-caspase-1^{CARD} interactions but also ASC^{CARD}–ASC^{CARD} interactions, we expressed enhanced green fluorescent protein (eGFP)-tagged ASC^{CARD} in the presence of reconstituted inflammasomes, formed by co-transfection of AIM2 with mCherry-tagged ASC^{FL}, ASC^{PYD}, ASC^{D130R} or ASC^{D134R} in HEK293T cells. Co-localization and co-immunoprecipitation assays demonstrated that GFP-ASC^{CARD} was only able to interact with WT ASC and not with ASC^{D130R} or ASC^{D134R}, confirming that the two mutations blocked ASC^{CARD}–ASC^{CARD} interaction (Supplementary Fig. 2g,h).

If the ASC^{CARD} organizes ASC filaments into dense specks, we speculated that increasing levels of ASC^{CARD} mutants would disrupt specks formed by WT ASC, resulting in larger but less dense ASC specks. Therefore, we retrovirally transduced various ratios of mCherry-tagged WT and mCherry-tagged ASC^{D130R} into primary WT C57BL/6 macrophages (containing endogenous ASC) and measured median speck size on the activation of AIM2 by poly(dA:dT) transfection or NLRP3 by Nigericin, a pore-forming toxin³⁵. Indeed, increasing levels of ASC^{D130R} resulted in a significant increase in ASC speck size (Fig. 2e,f). As expected, microscopy analysis of these large ASC specks showed that they were also less dense and had a filamentous nature (Fig. 2g). Taken together, these results support a model in which the ASC speck observed in WT cells is composed of individual ASC filaments that are formed via their PYDs and cross-linked to each other via their CARDs (Supplementary Fig. 3a).

NLR4 oligomerizes ASC via a bridging ASC molecule. Most inflammasome-forming receptors contain a PYD and initiate ASC filaments directly by homotypic PYD–PYD interactions. Notable exceptions are NLR4 and mouse Nlrp1b, which contain a CARD and thus might recruit and activate caspase-1 directly^{42,43}. Nevertheless, ASC promotes caspase-1 processing and efficient IL-1 β /-18 release after NLR4 and Nlrp1b activation^{26,44}. ASC specks can be observed after NLR4 activation, but how CARD-containing receptors initiate oligomerization of ASC is unknown. Theoretically, NLR4 could initiate ASC oligomerization either by (i) NLR4^{CARD}–ASC^{CARD} interaction and ASC^{CARD} oligomerization, (ii) heterotypic interaction between related death-fold domains, that is,

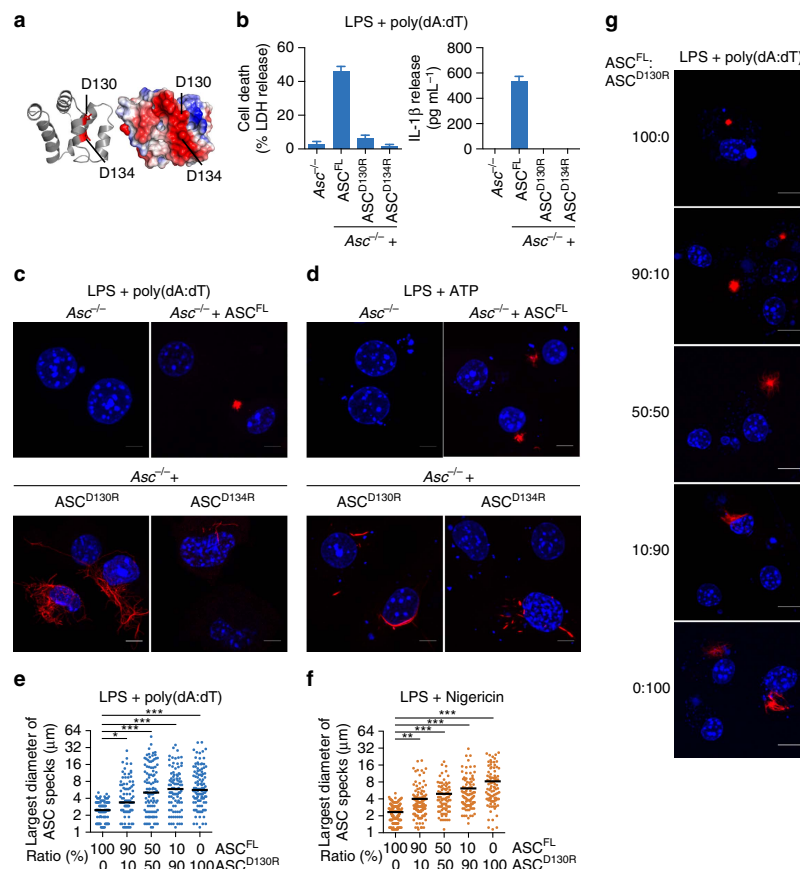


Figure 2 | The CARD of ASC condenses PYD filaments into the speck. (a) Structural model of the mouse ASC^{CARD} based on the human homologue (PDB 2KN6 (ref. 67)). The structure is shown in ribbon (left) and electrostatic surface representation (right, blue, positive charge; red, negative charge). Residues D130 and D134, involved in the interaction with pro-caspase-1, are highlighted³¹. (b) Release of LDH and IL-1 β from LPS-primed immortalized *Asc*^{-/-} BMDMs and *Asc*^{-/-} BMDMs expressing ASC^{FL}, ASC^{D130R} or ASC^{D134R} 3 h after poly(dA:dT) transfection (1 $\mu\text{g ml}^{-1}$). (c,d) Representative images of cell lines from (b) 3 h after poly(dA:dT) transfection (1 $\mu\text{g ml}^{-1}$) (c) or 1 h after ATP treatment (5 mM) (d). DNA was stained with Hoechst (blue) and ASC (red). Scale bars, 10 μm . (e,f) Measurement of the ASC speck diameter in primary C57BL/6 BMDMs transduced with the indicated ratio of mCherry-tagged ASC^{FL} or ASC^{D130R} and transfected with poly(dA:dT) (3 h at 1 $\mu\text{g ml}^{-1}$) (e) or treated with nigericin (1 h, 20 μM) (f) after LPS priming. (g) Representative images from e. DNA was stained with Hoechst (blue) and ASC (red). Scale bars, 5 μm . Data are representative of three (b-d) independent experiments. Graphs show the mean and s.d. from quadruplicate wells (b) or triplicate coverslips (e,f). The numbers of specks measured were 99, 92, 104, 94 and 108 in (e) and 149, 134, 85, 98 and 95 in (f). * $P < 0.05$, ** $P < 0.01$ and *** $P < 0.001$ (one-way analysis of variance). See also Supplementary Figs 2 and 3.

by a non-canonical NLRC4^{CARD}-ASC^{PYD} interaction or (iii) via bridging ASC molecules that would be linked with NLRC4 via CARD-CARD interactions and provide their free PYDs as seeds for ASC^{PYD} filament formation. To determine which domain of ASC was necessary for ASC speck formation after NLRC4 activation, we infected the above described cell lines harbouring the single domains of ASC with log-phase *Salmonella enterica* serovar Typhimurium SL1344 (*Salmonella* Typhimurium), a robust activator of NLRC4 (refs 45,46). Consistent with published reports^{24,27,47}, immortalized *Asc*^{-/-} BMDMs still induced cell death, whereas efficient IL-1 β processing and release required ASC (Fig. 3a). Expression of ASC^{FL} in *Asc*^{-/-} cells restored IL-1 β release, but neither the ASC^{PYD} nor ASC^{CARD} alone were able to functionally restore inflammasome activation

(Fig. 3a). We next analysed whether the ASC^{PYD} or ASC^{CARD} would form specks or filaments after NLRC4 activation by microscopy. Although ASC^{FL} formed specks, ASC^{PYD} alone did not initiate filaments following activation of NLRC4 (Fig. 3b,c), which was in contrast to what we had observed for PYD-containing receptors (Fig. 1c). In addition, cells expressing ASC^{CARD} alone did not form any specks or macromolecular filaments, again suggesting that the ASC^{CARD} in the endogenous setting is not able to form filaments (Fig. 3b,c). These results exclude the possibilities that ASC specks form via CARD oligomerization after NLRC4 activation, or that a heterotypic NLRC4^{CARD}-ASC^{PYD} interaction initiates ASC filament formation. Instead, they suggest that one or several bridging molecules of ASC are required to initiate ASC filament formation

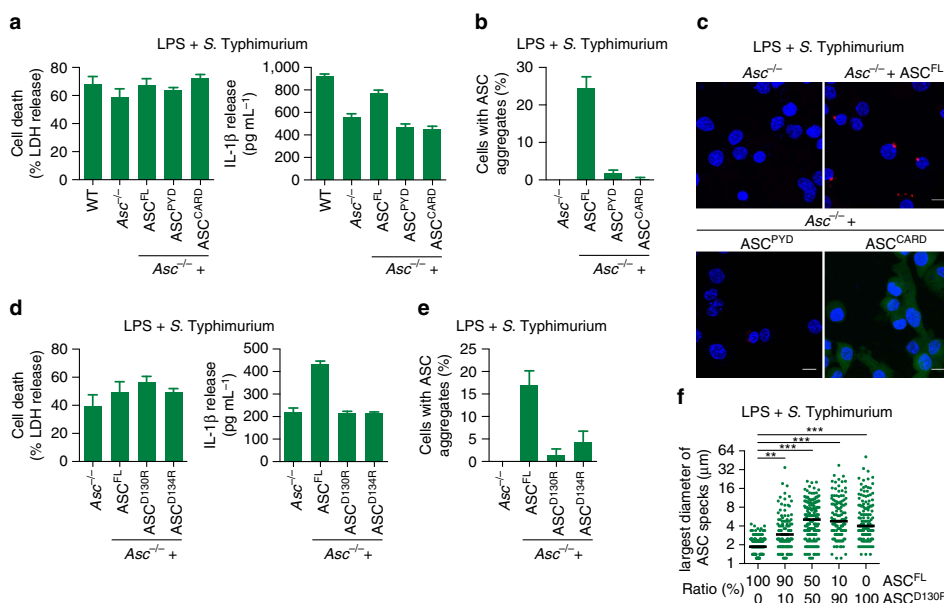


Figure 3 | A bridging ASC molecule is required for ASC speck formation after NLR4 activation. (a) Release of LDH and IL-1 β from LPS-primed immortalized WT, $Asc^{-/-}$ or $Asc^{-/-}$ BMDMs expressing ASC^{FL}, ASC^{PYD} or ASC^{CARD} after infection with log-phase WT *S. Typhimurium* SL1344 (multiplicity of infection (MOI) 10 for 1 h). (b) Quantification of the percentage of cells from a with ASC specks or filaments (collectively referred to as ASC aggregates). (c) Representative images of cell lines from b. DNA (blue, Hoechst) and ASC (red). Scale bars, 10 μ m. (d) Release of LDH and IL-1 β from LPS-primed $Asc^{-/-}$ BMDMs and $Asc^{-/-}$ BMDMs expressing ASC^{FL}, ASC^{D130R} or ASC^{D134R} after infection with log-phase WT *S. Typhimurium* SL1344 (MOI 10 for 1 h). (e) Quantification of the percentage of cells with ASC aggregates from d. (f) Measurement of the ASC speck diameter in primary C57BL/6 BMDMs transduced with the indicated ratio of mCherry-tagged ASC^{FL} or ASC^{D130R} and infected with log-phase WT *S. Typhimurium* SL1344 (MOI 10 for 1 h) after LPS priming. Data are representative of three (a–e) independent experiments. Graphs show the mean and s.d. from quadruplicate wells in (a,c,e) and triplicate coverslips in f. The numbers of specks measured were 194, 134, 184, 128 and 141 in f. * $P < 0.05$, ** $P < 0.01$ and *** $P < 0.001$ (one-way analysis of variance). See also Supplementary Fig. 3.

after NLR4 activation, and that in these conditions ASC oligomerization into filaments and specks also proceeds via the ASC^{PYD}.

We also examined cells expressing ASC^{D130R} and ASC^{D134R} mutants, which are defective for CARD–CARD interactions (Supplementary Fig. 2g,h (ref. 31)). As expected, expression of these mutants in $Asc^{-/-}$ macrophages did not complement the release of mature IL-1 β after NLR4 activation (Fig. 3d). Furthermore, we did not observe the formation of filaments or specks in cells expressing ASC^{D130R} or ASC^{D134R} (Fig. 3e), confirming the requirement for a functional ASC^{CARD} for ASC oligomerization by NLR4. Finally, we also tested our notion that the ASC^{CARD} is required to condense ASC filaments into a speck in the context of NLR4 activation. Primary WT C57BL/6 BMDMs (containing endogenous ASC, thus enabling initiation of ASC oligomerization) were retrovirally transduced with varying ratios of mCherry-tagged ASC^{FL} or ASC^{D130R} and the speck diameter was measured on *S. Typhimurium* infection (Fig. 3f). The increase in speck size concurring with increasing concentrations of the ASC^{D130R} mutant indicated that also in the NLR4 inflammasome the ASC^{CARD} condenses the ASC filaments into the speck. In conclusion, our results suggested a triple functional role for ASC^{CARD} in the NLR4 inflammasome: (1) mediating the interaction with pro-caspase-1 (refs 17,31), (2) condensing ASC^{PYD} filaments into the speck and (3) initiating ASC oligomerization through bridging ASC molecules (Supplementary Fig. 3b).

Pyroptosis induction is independent of ASC oligomerization.

Having elucidated the general architecture of the ASC speck, we next investigated whether the ASC speck constitutes the active, signalling-competent inflammasome. Higher-order signalosomes were reported for other innate immune signalling pathways (Toll-like receptors, receptor-interacting serine/threonine-protein kinase 2 (RIP2K) and MAVS) and could promote signal amplification and digital all-or-nothing responses⁴⁸, leading us to hypothesize that ASC oligomerization and filament formation might have a similar function for inflammasome signalling.

Within the ASC^{PYD} filaments that form the backbone of ASC specks in human and murine cells (Supplementary Fig. 4a (refs 13,15)), individual ASC^{PYD}s interact with other six adjacent ASC^{PYD}s through three asymmetric interfaces, types I–III (Fig. 4a). Mutations targeting these interfaces can abrogate ASC filament formation *in vitro* or in cell overexpression systems^{13,29,49}. As these mutations also most probably abrogate the interaction between the receptor^{PYD} and ASC^{PYD}, and/or were only tested in an artificial overexpression system, a definite confirmation that ASC filament formation is required for inflammasome signalling is still missing⁵⁰. Identification of mutations that abrogate ASC oligomerization but leave ASC–receptor interaction intact allowed us to characterize the role of ASC filaments in inflammasome signalling. Therefore, we generated a number of clonal immortalized $Asc^{-/-}$ macrophage lines expressing different mCherry-tagged ASC mutants targeting all three interaction interfaces (Fig. 4a and Supplementary

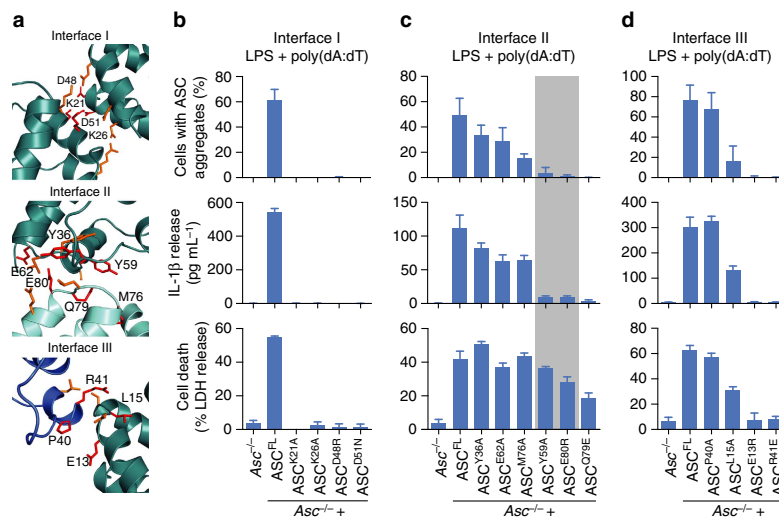


Figure 4 | Mutations in interface II uncouple speck formation and IL-1 β release from cell death. (a) Detailed view of the three interaction interfaces forming the ASC^{PYD} filament (PDB 2N1F (ref. 15), shown in Supplementary Fig. 4a). The polypeptide backbones are shown in ribbon representation. All amino acid side chains involved in intersubunit contacts are shown as stick models. Residues mutated in this study are coloured red with their sequence label. (b–d) Quantification of ASC aggregates or the release of LDH and IL-1 β from LPS-primed immortalized Asc^{-/-} BMDMs and Asc^{-/-} BMDMs expressing ASC^{FL} or the indicated ASC mutants 3 h after poly(dA:dT) transfection (1 μ g ml⁻¹). ASC^{Y59A} and ASC^{E80R} are highlighted in grey. Graphs show means and s.d. from quadruplicate wells or ten random fields of view. Data are representative of at least three independent experiments. See also Supplementary Figs 4 and 6.

Fig. 4b–d). Next, we assessed the effects of these mutations on ASC speck/filament formation on AIM2 activation by poly(dA:dT) transfection. Mutations targeting interface I (that is, K21A, K26A, D48N and D51R) completely abrogated the filament formation as determined by microscopy (Fig. 4b upper panel and Supplementary Fig. 4e). This is consistent with interface I being the most extensive interface and required for the propagation of single layers of the filament^{13,15}. In contrast, mutations in interfaces II and III displayed a larger variability, ranging from no defect in ASC speck formation (Y36A, E62A (interface II) or P40A (interface III)), intermediate phenotypes (M76A (interface II) or L15A (interface III)) to complete abrogation in ASC speck formation (Y59A, Q79E, E80R (interface II) or E13R and R41E (interface III)) (Fig. 4c,d upper panels and Supplementary Fig. 4e). Taken together, these data suggest that the formation of ASC specks requires all three interfaces of ASC^{PYD}.

We next tested how these mutations affect downstream inflammasome signalling by measuring IL-1 β secretion (Fig. 4b–d middle panels) and pyroptosis (Fig. 4b–d lower panels). In line with the loss of ASC speck formation, interface I proved to be essential for induction of downstream inflammasome signalling (Fig. 4b). Macrophages expressing mutants in interface III of ASC^{PYD} displayed similar phenotypes as interface I mutations: the ability to form ASC specks correlated with both IL-1 β secretion and pyroptosis, that is, mutants either lost all inflammasome signalling (E13R and R41E), were partially affected (L15A) or not affected at all (P40A) (Fig. 4d). These results show that interface III is important for induction of downstream inflammasome signalling, albeit some mutations are tolerated.

Mutants in interface II displayed a differential signalling phenotype (Fig. 4c). Although some mutations had no or only a very small effect on inflammasome signalling (Y36A, E62A and M76A) or abrogated inflammasome signalling altogether (Q79E),

we identified two mutations (Y59A and E80R) that retained the ability to induce cell death, while losing the ability to release mature IL-1 β and to form ASC specks in response to AIM2 stimulation (Fig. 4c middle and lower panels, highlighted in grey). Of note, the ELISA assay displays a higher sensitivity for the mature form of IL-1 β than the pro-form, thus pro-IL-1 β , which is potentially released into the supernatant by pyroptosis, is poorly detected (Supplementary Fig. 5). To test whether the phenotype of the different mutants is specific to the AIM2 inflammasome, we analysed ASC speck formation, secretion of mature IL-1 β and pyroptosis in response to NLRP3 stimulation by ATP treatment. Asc^{-/-} macrophages expressing the ASC interface I, II and III mutants showed the same phenotype for NLRP3 stimulation as for AIM2 stimulation (Supplementary Fig. 6a–c). Importantly, also ASC^{Y59A} and ASC^{E80R} mutations abrogated speck formation and IL-1 β secretion but still promoted pyroptosis on NLRP3 stimulation (Supplementary Fig. 6b, highlighted in grey). Finally, we also examined IL-1 β release and pyroptosis of macrophages expressing interface II mutants treated with *Clostridium difficile* Toxin B (TcdB). TcdB was recently described to activate the pyrin inflammasome, which senses modifications of Rho GTPases⁶. Again, Asc^{-/-} macrophages expressing ASC^{Y59A} or ASC^{E80R} were competent for cell death induction but could not efficiently release IL-1 β (Supplementary Fig. 6d, highlighted in grey). In conclusion, our site-directed mutagenesis approach identified two mutations, Y59A and E80R, in the inflammasome adaptor ASC that uncouple pyroptosis from ASC speck formation and cytokine secretion.

ASC oligomerization mutants maintain receptor interaction. As cell death was still observed in cells expressing ASC^{Y59A} and ASC^{E80R}, we speculated that the mutant proteins retained the ability to interact with the PYD of the receptor, but lost the

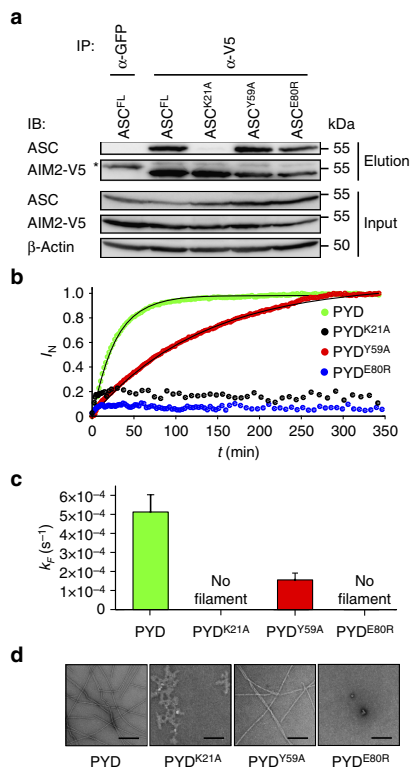


Figure 5 | ASC-receptor interaction and ASC filament formation can be uncoupled genetically. (a) Western blot analysis of the interaction of AIM2 with ASC^{FL} or the indicated ASC mutants. AIM2-V5 was immunoprecipitated from lysates of HEK293T cells co-transfected with AIM2-V5 and the indicated ASC mutants. Co-immunoprecipitating proteins were identified using anti-ASC and anti-V5. *Immunoglobulin heavy chain. Results shown are representative from two independent experiments. (b) Filament formation of WT ASC^{PYD} and its single amino-acid variants K21A, Y59A and E80R *in vitro* monitored by dynamic light scattering. Normalized growth signals (I_n) are reported as a function of time for one representative experiment for each variant (dots). Best fits to single exponential functions are shown with solid lines. (c) Kinetic rate constants k_f of filament formation obtained from three independent experiments. (d) Representative negative-stained TEM micrographs of filament formed by ASC^{PYD} and its variants after 350 min of incubation at physiological pH condition. Scale bars, 200 nm. See also Supplementary Figs 7 and 9.

ability to oligomerize into ASC filaments. To investigate this, we reconstituted the AIM2 inflammasome by co-expressing V5-tagged AIM2 with ASC^{FL} or the ASC^{K21A}, ASC^{Y59A} or ASC^{E80R} mutants in HEK293T cells. AIM2 interactors were then immunoprecipitated using an anti-V5 antibody and analysed by western blotting (Fig. 5a). Consistent with our notion, ASC^{Y59A} and ASC^{E80R} retained the ability to interact with AIM2, similar to WT ASC. In contrast, ASC^{K21A} did not interact with AIM2, possibly explaining the clear-cut phenotypes of interface 1 mutants (Fig. 4b and Supplementary Fig. 6b).

Given that ASC^{Y59A} and ASC^{E80R} mutants still interacted with the receptor (Fig. 5a), but did not form any ASC filaments/specks (Fig. 4c and Supplementary Fig. 4e), we speculated that the mutations abolished or reduced the ability of ASC to organize

itself into filaments following the recruitment to the activated receptor. Based on our previous observation that purified ASC^{PYD} or ASC^{FL} form filaments *in vitro*¹⁵, we established an assay to monitor the kinetics of this oligomerization process by dynamic light scattering and analysed the kinetics of filament formation for WT ASC^{PYD} and the above-mentioned mutants (Fig. 5b,c and Supplementary Fig. 7a,b). Although WT PYD rapidly formed well-structured filaments, the K21A mutant was no longer able to oligomerize correctly and formed unspecific aggregates (Fig. 5d). Interestingly, E80R also lost the ability to oligomerize into ordered filaments, whereas the Y59A mutant formed well-ordered filaments, but at a much slower rate than the WT protein (Fig. 5b–d and Supplementary Fig. 7a,b). Thus, these results confirmed that the ASC–receptor interaction and the ASC filament formation can be uncoupled, and that the ability to rapidly form filaments/specks strongly correlates with the levels of cytokine production but not cell death.

Gasdermin-D cleavage is independent of ASC oligomerization.

The observation that even in the absence of ASC oligomerization inflammasome activation still promotes cell death but not cytokine release (Fig. 4c, Supplementary Fig. 4e) was reminiscent of NLRC4 activation in *Asc*^{-/-} macrophages²⁴. In the absence of ASC, NLRC4 interacts with pro-caspase-1 to initiate cell death but not efficient caspase-1 autoprocessing and cytokine secretion. We therefore examined to what level ASC^{Y59A} and ASC^{E80R} were able to promote caspase-1 autoprocessing on activation of the AIM2 inflammasome. In contrast to cells expressing ASC^{FL}, macrophages expressing the mutant proteins displayed significantly reduced levels of caspase-1 processing, as determined by western blotting for the released p20 subunit (Fig. 6a). Furthermore, caspase-1 autoprocessing correlated with the amount of released bioactive IL-1 β (Figs 4c and 6a), but not with the induction of cell death (Fig. 4c) and the release of the danger signal high mobility group box 1 (HMGB1) into the cell supernatants (Fig. 6a), an alternative marker for cell lysis during inflammasome activation⁵¹. Similarly, results were obtained on activation of the NLRP3 inflammasome (Supplementary Fig. 8a). To exclude the possibility that the observed cell death is induced through caspase-1-independent pathways, we knocked out *Casp1* by CRISPR-Cas9-mediated gene targeting^{52,53} in the cell lines expressing ASC^{FL}, ASC^{Y59A} or ASC^{E80R}. Western blotting for pro-caspase-1 confirmed successful targeting (Supplementary Fig. 8b). *Casp1* deficiency significantly abrogated pyroptosis induction in cells expressing ASC^{FL}, ASC^{Y59A} or ASC^{E80R} (Fig. 6b), thus confirming that the cell death observed in the parental cell lines was caspase-1 dependent. Taken together, these data confirm that caspase-1 processing is not a prerequisite for induction of cell death, expanding previous findings from CARD-containing inflammasome receptors²⁴ to PYD-containing receptors.

Recent reports showed that a major substrate of caspase-1 responsible for pyroptosis is gasdermin-D, and that *Gsdmd*-deficiency abrogates pyroptosis^{11,12}. Caspase-1 cleaves full-length gasdermin-D, whereby the active N-terminal fragment (gasdermin-D^{Nterm}) is generated (Supplementary Fig. 8c,d), which induces pyroptotic cell death^{11,12}. Consistently, CRISPR-Casp9-mediated *Gsdmd* knockout (Supplementary Fig. 8e) reduced cell death significantly in response to AIM2 and NLRP3 activation (Supplementary Fig. 8f,g). As ASC^{Y59A} and ASC^{E80R} mutants induced cell death, we speculated that gasdermin-D is still processed in cells expressing these mutant forms of ASC. Indeed, although gasdermin-D was not processed in *Asc*^{-/-} macrophages on stimulation of AIM2 or NLRP3, we observed gasdermin-D processing to its 30 kDa gasdermin-D^{Nterm} fragment in *Asc*^{-/-}

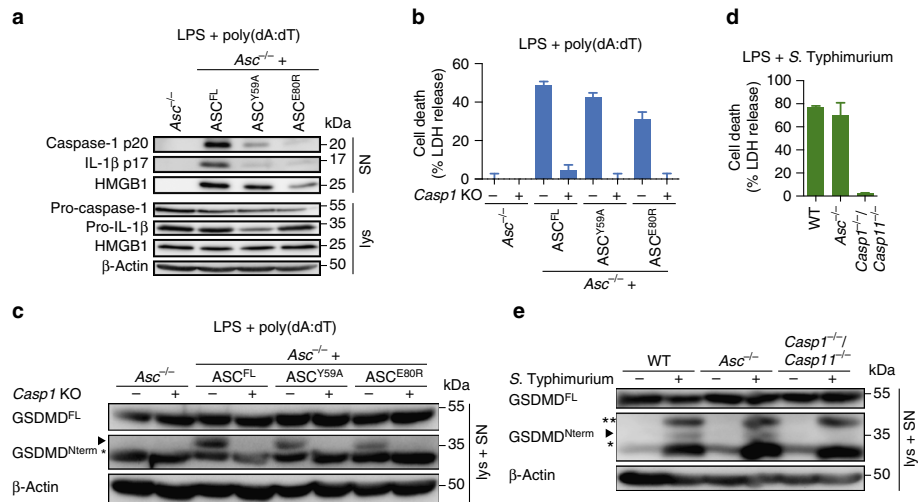


Figure 6 | Caspase-1 but not gasdermin-D processing depends on ASC oligomerization. (a) Western blot analysis for cleaved caspase-1 p20, IL-1 β p17, and HMGB1 in cell supernatants (SN) and pro-caspase-1, pro-IL-1 β and HMGB1 in cell lysates (lys) of LPS-primed immortalized *Asc*^{-/-} BMDMs or *Asc*^{-/-} BMDMs expressing ASC^{FL}, ASC^{Y59A} or ASC^{E80R} 3 h after poly(dA:dT) transfection (1 μ g ml⁻¹). (b) Release of LDH from LPS-primed immortalized *Asc*^{-/-} BMDMs or *Asc*^{-/-} BMDMs expressing ASC^{FL}, ASC^{Y59A} or ASC^{E80R}, or derived *Casp1* knockouts 3 h after poly(dA:dT) transfection (1 μ g ml⁻¹). (c) Western blot analysis for processing of full-length gasdermin-D (GSDMD^{FL}) into the active N-terminal fragment (GSDMD^{N-term}) in combined lysates and supernatants (lys + SN) of LPS-primed immortalized *Asc*^{-/-} BMDMs expressing ASC^{FL}, ASC^{Y59A} or ASC^{E80R}, or derived *Casp1* knockouts 3 h after poly(dA:dT) transfection (1 μ g ml⁻¹). Arrowhead, gasdermin-D^{N-term} p30; *a cross-reacting band. (d) Release of LDH from LPS-primed primary C57BL/6 WT (WT), *Casp1*^{-/-}/*Casp11*^{-/-} or *Asc*^{-/-} BMDMs infected with *S. Typhimurium* (multiplicity of infection (MOI) = 10, 1 h). (e) Western blot analysis for processing of full-length gasdermin-D (GSDMD^{FL}) into the active N-terminal fragment (GSDMD^{N-term}) in combined lysates and supernatants (lys + SN) of LPS-primed primary C57BL/6 WT (WT), *Casp1*^{-/-}/*Casp11*^{-/-} or *Asc*^{-/-} BMDMs infected with *S. Typhimurium* (MOI = 10, 1 h) or left uninfected. Arrowhead, gasdermin-D^{N-term} p30; *a cross-reacting band; ** a *S. Typhimurium*-specific cross-reactive band. See also Supplementary Figs 8 and 9.

macrophages expressing ASC^{FL}, ASC^{Y59A} and ASC^{E80R} (Fig. 6c and Supplementary Fig. 8h). Furthermore, processing of gasdermin-D on AIM2 stimulation is dependent on caspase-1 in cells harbouring oligomerization-deficient ASC mutants, as *Casp1* deficiency abrogated gasdermin-D cleavage (Fig. 6c). These results indicated that gasdermin-D^{N-term} causes the cell death observed in these mutations. As significant levels of cell death can be observed in *Asc*-deficient macrophages after NLR4 activation²⁴, but caspase-1 processing is reduced below detection levels, we next determined whether gasdermin-D is processed under these conditions. Indeed, we found that the induction of cell death in *S. Typhimurium*-infected WT, *Asc*^{-/-} and *Casp1*^{-/-}/*Casp11*^{-/-} macrophages (Fig. 6d) correlated with detectable levels of processed gasdermin-D (Fig. 6e). Furthermore, CRISPR-Cas9-mediated *Gsdmd* knockout confirmed that gasdermin-D played an essential role in inducing pyroptosis during *S. Typhimurium* infections (Supplementary Fig. 8i). Taken together, these results confirm that even the smallest amounts of active caspase-1, as judged by the amount of processed caspase-1 p20 subunits, are sufficient to efficiently process gasdermin-D and trigger gasdermin-D-induced cell death. On the other hand, large amounts of processed, active caspase-1 are required to produce detectable amounts of mature, bioactive IL-1 β as seen by the direct correlation of the level of caspase-1 processing with the levels of cytokine release. Importantly, the ability of ASC to form filaments and ASC specks correlates with caspase-1 activation and cytokine processing, thus supporting a model in which the rapid formation of ASC filaments acts as a signal amplification mechanism for inflammasomes, generating a multitude of

caspase-1 activation sites and thus enabling the cells to rapidly mature IL-1 β before the onset of pyroptosis.

Discussion

The formation of higher-order signalling machineries, signalosomes, for transmission of receptor activation information to cellular responses is an emerging theme in signal transduction⁴⁸. It is particularly important in innate immune signalling, where the signal generated by a few ligand-receptor interactions needs to trigger an appropriate cellular response. Formation of oligomers has been reported for different signalling adaptors, for example, B-cell lymphoma/leukemia 10 (Bcl10) or MAVS filaments, the Myddosome^{36,54,55} and others. However, the archetypical supramolecular assembly formed during inflammasome activation, the ASC speck, has remained relatively poorly understood. Here we present evidence that the formation of ASC speck by oligomerization of the inflammasome adaptor protein ASC acts as a signal amplification mechanism for inflammasomes (Fig. 7), as the rapid formation of ASC^{PYD} filaments that expose ASC^{CARD} on their surface creates a multitude of pro-caspase-1 recruitment and activation sites. We speculate that such a system might therefore be able to detect the smallest amounts of PAMPs in the host cell cytosol, as recent reports have shown that a single ligand molecule (flagellin, PrgI) is sufficient to initiate assembly of a NLR family, apoptosis inhibitory protein (NAIP) and 10-12 NLR4 proteins into a wheel-shaped receptor oligomer that acts as seed for ASC oligomerization^{39,56}.

Our result reveals that this signal amplification mechanism only applies to cytokine maturation, whereas gasdermin-D-

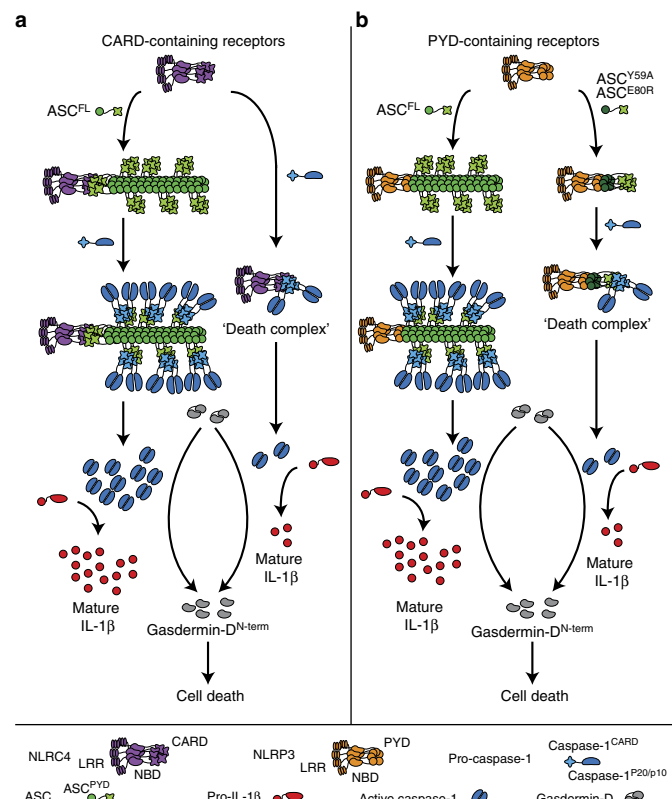


Figure 7 | Model of signal amplification by ASC filaments. (a) CARD-containing receptors recruit the adaptor protein ASC via homotypic CARD-CARD interactions, that is, a bridging ASC molecule. This step nucleates the ASC^{PYD} of several bridging ASC molecules, leading to the formation of an ASC^{PYD} filament, which is condensed into the ASC speck by the ASC^{CARD}. Filament formation promotes the activation of large quantities of caspase-1, thus promoting the proteolytic maturation of large amounts of cytokines (pro-IL-1 β). In the absence of ASC, CARD-containing receptors directly interact with pro-caspase-1, leading to the formation of so-called 'death complexes'. In these small complexes, only few molecules of caspase-1 are activated and pro-caspase-1 processing might not happen. The few molecules of caspase-1 are sufficient to effectively induce pyroptosis, but cytokine processing is reduced. (b) PYD-containing receptors can directly interact with ASC via homotypic PYD-PYD interactions, leading to ASC^{PYD} filaments and finally the ASC speck. As for CARD-containing receptors, this leads to caspase-1 activation and subsequent cytokine processing and pyroptosis. Mutations blocking or slowing ASC filament formation (for example, ASC^{E80R} or ASC^{Y59A}) only allow for few molecules of caspase-1 being activated. This is sufficient to induce pyroptosis, but insufficient to produce large amounts of mature cytokines before the cell lyses.

induced pyroptotic cell death could be observed even in the absence of ASC oligomerization. Why would cells need to amplify the receptor-generated signal to process IL-1 β /-18? We speculate that a cell will inevitably progress towards pyroptosis, once a few molecules of caspase-1 have been activated, given the rapid kinetics by which gasdermin-D is processed⁵⁷ and the strong toxicity of the gasdermin-D^{N-term} fragment^{11,12}. This fate leaves a limited time window to mature the pro-forms of IL-1 β /-18 to their bioactive form. As processing of IL-1 β /-18 occurs with slow kinetics, increasing the amount of active caspase-1 is a means to generate large amounts of bioactive IL-1 β /-18 in the available time window. Consistent with this notion we have observed that gasdermin-D processing does not correlate with the overall level of active caspase-1. Furthermore, pyroptosis has been observed to occur within 30–60 min in stimulated cells, whereas ASC speck formation was reported to proceed much faster^{23,58}, with all cytosolic ASC being incorporated into a speck in <3 min^{20,59}. Thus, ASC speck formation might serve to activate sufficient

amounts of caspase-1 to generate enough bioactive cytokines before the cell lyses and releases its intracellular content, including proteolytically matured cytokines.

Although recent studies revealed that ASC specks are filamentous in nature^{22,23}, consistent with recently reported structures of human and murine ASC^{PYD} filaments^{13,15}, it was so far unknown how these filaments assemble into a speck. Our mutagenesis studies indicates that the clustering of ASC^{PYD} filaments and finally their condensation into a dense ASC speck structure is mediated by the ASC^{CARD}, which, as we have shown¹⁵, is exposed on the surface of the ASC^{PYD} filament. These results have uncovered a function for the ASC^{CARD} in ASC speck formation, beyond its role as adaptor domain between receptor and caspase-1. How ASC^{CARDs} condense ASC^{PYD} filaments is unknown, but it can be assumed that either dimeric interactions between ASC^{CARDs} or limited oligomerization of ASC^{CARD} from different filaments could build lattices interconnecting the ASC^{PYD} filaments. Interestingly, the same residues in ASC^{CARD}

that are required for ASC–pro-caspase-1 interaction are also needed for ASC speck formation. Notably, it has previously been shown that phosphorylation of the ASC^{CARD} at Y144/Y146 is not only required for caspase-1 activation, but also for ASC speck formation^{60,61}. Our model of the ASC speck, which includes interactions between the ASC^{CARD} domains, now provides a structural rationale for these data. To which extent ASC filaments are still formed in the absence of ASC^{CARD} phosphorylation remains to be determined.

Recently, a unified assembly mechanism was proposed for the PYD-containing receptors AIM2 and NLRP3: the receptors nucleate clusters of ASC through PYD–PYD interactions, which in turn nucleate caspase-1 filaments¹³. In analogy, it was proposed that the CARD-containing receptor NLR4 directly nucleates caspase-1 filaments^{13,39}, as in theory CARD-containing receptors do not require ASC for caspase-1 recruitment. Although direct recruitment of pro-caspase-1 to NLR4 might indeed happen in *Asc*-deficient cells as we hypothesized before²⁴, it does not seem to efficiently activate caspase-1, because we and others have reported that caspase-1 processing into its p20/p10 subunits and the levels of released mature cytokines are reduced. Furthermore, a large number of ASC specks can be observed in WT cells on NLR4 activation^{24–28}, indicating that ASC nevertheless plays an important role in NLR4 signalling. Our results now indicate that the ASC^{CARD} lacks the ability to form higher-order oligomers at physiological concentrations, and that even on NLR4 activation ASC speck formation relies on the ASC^{PYD}. Our data thus support a model in which CARD-containing receptors initiate ASC speck formation with the help of ASC bridging molecules, and that the PYDs of these ASC molecules nucleates an ASC^{PYD} filament. Thus, the ASC^{CARD} can have a triple function in inflammasome signalling on CARD-receptor activation.

In conclusion, our study gives insights into the architecture of the ASC speck and the mechanism by which ASC filaments assemble this structure. Furthermore, we provide experimental evidence that ASC filament formation serves as an amplification mechanism in inflammasome signalling, and that this amplification serves to generate sufficient mature cytokines before the onset of pyroptotic cell death. Nevertheless, important questions remain; the higher-resolution structure of the activated NLR4 receptor has been recently reported^{39,56}, yet how exactly such receptor complexes with C₁₀–C₁₂ stoichiometry initiate the 3-start ASC^{PYD} filaments is still unknown. Furthermore, the structure of the whole ASC speck assembly, including receptor, ASC and caspase-1, is still lacking and it remains unknown whether other proteins participate in its formation. Finally, additional theoretical and experimental approaches will be necessary to understand if and how ASC speck formation might impart threshold responses, reduce biological noise and control temporal and spatial control of inflammasome signalling.

Methods

Cell culture. Immortalized BMDM cell lines were generated from bone marrow using infection with a v-myc/v-raf-expressing J2 retrovirus^{24,62}. WT and *Asc*^{-/-} immortalized murine BMDMs were cultured in DMEM (Sigma) supplemented with 10% FCS (Biocconcept) and 10% 3T3-MCSF supernatant, and incubated at 37 °C with 5% CO₂.

Generation of monoclonal cell lines with mutations in ASC. Murine *Asc*^{FL} and *Asc*^{PYD} were cloned with a carboxy-terminal mCherry tag and *Asc*^{CARD} with an N-terminal enhanced GFP tag into V48, a derivative of the replication-defective murine stem cell retroviral construct pMSCV2.2 (excision of the IRES-GFP by EcoRI digestion, gift from Thomas Henry). Mutations were introduced by SOE PCR using appropriate oligonucleotides (Supplementary Table 1) and cloned into V48. GP2 packaging cells were transfected with the individual vectors (9 µg per 1.5 × 10⁶ cells) and the lentiviral envelope vector VSV-G (Addgene, 6 µg per 1.5 × 10⁶ cells), and the retroviral particles were used to transduce *Asc*^{-/-}

iBMDMs (10⁶ cells). Seven days later, the transduced iBMDMs were sorted into single cells based on the mCherry or enhanced GFP expression (FACS) and grown up to clonal cell lines. Up to ten clones of each cell line were tested for inflammasome activation and the level of ASC expression was assessed by western blotting and a representative clone was selected for further analysis.

Retroviral transduction of primary BMDMs. For transduction of primary bone marrow cells, retroviral particles were generated in Phoenix-Eco packaging cells and used to transduce WT C57BL/6 bone marrow cells after 48 and 72 h of culture in medium with 10% 3T3-MCSF supernatant. Inflammasome stimulation was performed 4 days after the first transduction²⁴.

Inflammasome stimulation. Immortalized BMDMs (seeded at 250 000 cells per ml in 96-well plates) were primed for 4 h with 100 ng ml⁻¹ LPS O55:B5 (Invivogen). The NLRP3 inflammasome was triggered by addition of 5 mM extracellular ATP (Sigma-Aldrich) for 60 min. The AIM2 inflammasome was triggered by transfection of 1 µg ml⁻¹ of the synthetic DNA analogue poly(dA:dT) (Invivogen) using Lipofectamine 2000 (Invitrogen), according to the manufacturer's protocol, in OptiMEM (Gibco) for 3 h. The NLR4 inflammasome was triggered by infection of the cells with *S. enterica* serovar Typhimurium SL1344 at a multiplicity of infection of 10. The infection was synchronized by centrifugation and continued for 60 min. The pyrin inflammasome was triggered by addition of 1 µg ml⁻¹ (final concentration) of *C. difficile* toxin B (CdtB, Enzo Biotech) for 2.5 h.

Cell death and IL-1β release measurements. IL-1β release was measured by ELISA (eBiosciences). Cell death was quantified by measuring LDH release using the LDH Cytotoxicity detection kit (TaKaRa Clontech). To normalize for spontaneous cell lysis, the percentage of cell death was calculated as follows: [(LDH sample) – (LDH negative control)] / [(LDH positive control) – (LDH negative control)] × 100.

Imaging and quantification of ASC speck formation. Cells were seeded on coverslips (150 000 cells per coverslip) and treated as described above with the addition of 25 µM Z-VAD-fmk (Bachem) to prevent detachment of pyroptotic cells and therefore loss of cells with ASC specks. Coverslips were fixed with 4% paraformaldehyde (PFA) (15 min, 37 °C, Alfa Aesar) and washed with PBS. Nuclei were stained with Hoechst 33342 (Life Technologies) for 10 min and the slides mounted using Vectashield (Vector Laboratories). For quantifications of ASC aggregates (specks or filaments), ten random regions of interest were imaged at ×20 magnification (Leica DMI3000B inverted fluorescence microscope, HCX PL FLUOTAR objective, Leica DFC3000G camera and LAS AF Version 3 software) and the number of ASC aggregates and cells were counted. For representative images, the slides were imaged at ×63 magnification (Leica point scanning confocal 'SP8', HC PL APO CS2 ×63 objective, Leica AF software version 3). For measurements of speck sizes, random regions of interest were imaged at ×63 magnification (Leica point scanning confocal 'SP8') and the largest diameters of individual specks were measured using Fiji⁶³.

Western blotting. For western blotting of supernatant and lysate samples, cells were seeded at 10⁶ cells per well in six-well plates and treated as described above. Supernatants were precipitated with 10% trichloroacetic acid, precipitates washed with acetone and resuspended in 40 µl 1 × SDS-PAGE sample buffer and boiled at 95 °C for 10 min. Cells were lysed with 200 µl 1 × RIPA (50 mM Tris-HCl pH 7.5, 150 mM NaCl, 0.1% SDS, 0.5% sodium deoxycholate, 1% NP-40, 1 × protease inhibitor cocktail (Roche)) for 30 min on ice. Lysates were re-suspended in 5 × SDS-PAGE sample buffer and boiled at 95 °C for 10 min⁶⁴. For combined supernatant and lysates, samples were prepared as above, but supernatant precipitates were resuspended in lysate samples. Samples were run on 14% (supernatants or lysates) or 12% (combined SN + lysates) acrylamide gels (1 h, 170 V, 40 mA per gel), transferred to polyvinylidene difluoride membranes (1 h, 100 V constant), blocked in 5% milk in Tris-buffered saline + Tween-20 (TBS-T) and incubated with primary antibodies in 5% BSA–TBS-T for 16 h at 4 °C or 2 h at room temperature with agitation. Secondary antibodies were diluted 1:5,000 in 5% milk–TBS-T and incubated for 1 h at room temperature. The membranes were developed using either LumiGLO (KPL) or LumiGLO Reserve (KPL). The following antibodies and dilutions were used: rat anti-Caspase-1 p20 (Genentech, 1:1,000; Supplementary Figs 1b,d and 2c,d) or mouse anti-Caspase 1 p20 (1:4,000, AG20B-0042, AdipoGen; Fig. 6a and Supplementary Fig. 8a), rat anti-ASC (Genentech, 1:2,000; Fig. 5a and Supplementary Fig. 2a,h) or rabbit anti-ASC (1:1,000, AG25B-006, AdipoGen, all other figures), rabbit anti-IL-18 (5180R-100, Biovision, 1:1,000), goat anti-IL-1β (AF-401-NA, R&D, 1:1,000), mouse anti-GFP (632381, Clontech, 1:1,000), mouse anti-mCherry (ab125096, Abcam, 1:1,000), mouse anti-V5 (R960-25, Invitrogen, 1:1,000), rabbit anti-HMGB1 (GTX-101277, Genetex, 1:1,000), mouse anti-gasdermin-D (GSDMDCl (A-7), Santa Cruz Biotechnology, 1:1,000; Supplementary Fig. 7), rabbit anti-gasdermin-D (1:2,000, G7422, Sigma, all other figures) and mouse anti-β-actin (A1987, Sigma, 1:1,000).

Co-immunoprecipitation. Co-immunoprecipitation was done according to a modified protocol published previously¹⁹. For assessment of ASC/AIM2 interactions, $3 \times 800,000$ HEK293T cells were transfected with 2 μg per well AIM2-V5 and ASC-mCherry (ASC^{FL}, ASC^{K21A}, ASC^{Y59A} or ASC^{E80R}) encoding plasmids at a ratio of 1:4 using linear polyethylenimine (PEI, Polysciences) at a ratio DNA:PEI of 1:4 (refs 65,66). Twenty-four hours after transfection, the cells were washed twice with ice-cold $1 \times$ PBS and lysed using HEK lysis buffer (20 mM HEPES pH 7.4, 10 mM KCl, 1 mM EDTA, 0.1 mM phenylmethylsulfonyl fluoride, 1 mM Na₃VO₄, 5 mM NaF, 0.5 % Nonidet P-40 and $1 \times$ protease inhibitor cocktail (Roche)). Lysates were sonicated for 5×7 s before removing debris and non-lysed cells by centrifugation (10,000 g, 15 min, 4 °C). The samples were incubated with 1 μg mouse anti-V5 antibody (R960-25, Invitrogen) or a control antibody (mouse anti-GFP, 632381, Clontech) with agitation for 16 h at 4 °C. For assessment of ASC^{CARD}/ASC^{CARD} interactions, $3 \times 800,000$ HEK293T cells were transfected with 1 μg per well ASC-mCherry (ASC^{FL}, ASC^{PYD}, ASC^{D130R} or ASC^{D134B}), 1 μg per well ASC^{CARD}-GFP and 0.2 μg AIM2-V5, to initiate ASC/ASC interactions using linear PEI. Forty hours after transfection, the cells were washed, lysed and sonicated as described above. The samples were then incubated with 1 μg mouse anti-mCherry antibody (ab125096, Abcam) or a control antibody (mouse anti-HA, MMS-101R-200, Covance). The samples were then incubated with agitation for 2 h at 4 °C with 25 μl Pierce Protein A Plus Agarose bead slurry (22810, Thermo Scientific). Beads were washed three times with lysis buffer (centrifugation 1 min 1,000 g, 4 °C), resuspended in $2 \times$ SDS-PAGE sample buffer (30 μl) and boiled at 95 °C, before analysing the eluted proteins by western blotting as described above.

CRISPR-Cas9-mediated Caspase1 and Gasdermin-D knockout. Two guide RNAs⁵² targeting exon 4 of *Casp1* (5'-gagggcaagcgtctacgag-3' and 5'-cgagtggtttgattcattat-3') and one guide RNA targeting exon 2 of *Gsdmd* (5'-ggctcaagaatgtgatacagg-3') were cloned into lentiCRISPRv2 harbouring a puromycin resistance cassette (Addgene⁵³). These constructs were transfected into HEK293T cells using PEI (as described above) together with the lentiviral packaging vector PsPax2 (Addgene) and the lentiviral envelope vector VSV-G (Addgene). Sixteen hours after transfection, medium was exchanged with macrophage medium and incubated at 37 °C for 2 days to produce lentiviral particles. The lentiviral particles were used to transfect the immortalized macrophage cell lines (800,000 cells per well in 6-well plates) using polybrene (Merck) to favour virus attachment. Two days after viral transduction, the macrophages were expanded. Attached macrophages were then treated with $10 \mu\text{g ml}^{-1}$ puromycin (Gibco) for 6 days to select for successful lentiviral transduction. After puromycin selection, the cells were tested for successful knockout by western blotting.

Expression and purification of ASC^{PYD}. The ASC^{PYD} (residues 1–91) was cloned with a C-terminal His₆ tag into the pET28a vector under the control of a T7 promoter. Protein expression was induced by isopropyl- β -D-thiogalactopyranosid addition in BL21(DE3) *Escherichia coli* at an OD₆₀₀ of 0.8 for 4 h at 37 °C. Bacteria were harvested by centrifugation and resuspended in 50 mM phosphate buffer pH 7.5, 300 mM NaCl, with Complete protease inhibitor (Roche). Resuspended bacteria were incubated for 1 h at room temperature with DNase I, sonicated on ice and centrifuged at 20,000 g at 4 °C for 30 min. The pellet, including ASC^{PYD}-containing inclusion bodies, was solubilized in 50 mM phosphate buffer pH 7.5, 300 mM NaCl, 6 M guanidinium hydrochloride and centrifuged at 20,000 g at 4 °C for 30 min. The supernatant was incubated for 2 h at room temperature with pre-equilibrated Ni-NTA affinity resin (Thermo Scientific) and then passed through a plastic body column for gravity flow purification. The column was washed with 20 column volumes of solubilization buffer containing 20 mM imidazole and eluted with 3 column volumes of solubilization buffer with 500 mM imidazole. The pH of the elution fraction was decreased to 3.8 and dialysed against 50 mM glycine buffer pH 3.8, 150 mM NaCl. The protein was further purified on a pre-equilibrated Superdex 75 gel filtration column (GE Healthcare). This gel-filtration step removed traces of pre-existing aggregates and yielded highly pure, monomeric soluble form of ASC^{PYD}. Samples were either used immediately or stored after flash-freezing in small aliquots in liquid N₂.

Measurements of ASC^{PYD} filament formation kinetics *in vitro*. Immediately before the experiments, samples of monomeric soluble ASC^{PYD} were centrifuged at 20,000 g at 4 °C for 30 min and filtered with 0.1 μm filter (Millipore). The protein concentration was adjusted to 25 μM by dilution from a higher-concentrated stock solution. Filament formation was triggered by rapid dilution to neutral pH. Thereby, 70 μl of monomeric ASC^{PYD} was mixed with 0.45 μl of 2.75 M NaOH solution to reach the pH of 7.5. The solution was mixed at room temperature by careful pipetting, to avoid introduction of air bubbles, and immediately transferred to a quartz cuvette with 1 cm path length. Between runs, cuvettes were carefully cleaned with 1 M Hellmanex solution (Sigma-Aldrich) to avoid cross-seeding effects between sequential measurements. Filament growth was monitored by dynamic light scattering with a Malvern Zetasizer Nano ZS series instrument. The laser focal spot was positioned in the middle of the cuvette and maintained fixed for all the measurements. To maximize the intensity of the scattered light, the minimal attenuation level was used. Data were acquired in 60 s intervals by averaging three runs of 20 s, until a total time of 350 min. Afterwards, the protein

solution was blotted on EM grids, negatively stained and imaged with transmission electron microscopy to visualize filament formation.

Data analysis. Filament growth was modelled assuming pseudo-first-order kinetics where the filament propagation step occurs by the addition of monomers to the initial growth centre. The time-dependent growth signal I was fitted independently for each measurement by a single exponential function,

$$I(t) = I_{\infty} \left(1 - e^{-k_F t}\right)$$

where I_{∞} corresponds to the signal at time t and at infinite time, respectively, and k_F is the first-order rate constant. Fits were done with nonlinear least-square minimization.

Data availability. The data that support the findings of this study are available from the corresponding author upon request.

References

1. von Moltke, J., Ayres, J. S., Kofoed, E. M., Chavarría-Smith, J. & Vance, R. E. Recognition of bacteria by inflammasomes. *Annu. Rev. Immunol.* **31**, 73–106 (2013).
2. Philpott, D. J., Sorbara, M. T., Robertson, S. J., Croitoru, K. & Girardin, S. E. NOD proteins: regulators of inflammation in health and disease. *Nat. Rev. Immunol.* **14**, 9–23 (2014).
3. Franchi, L., Warner, N., Viani, K. & Nuñez, G. Function of Nod-like receptors in microbial recognition and host defense. *Immunol. Rev.* **227**, 106–128 (2009).
4. Martinon, F., Burns, K. & Tschopp, J. The inflammasome: a molecular platform triggering activation of inflammatory caspases and processing of proIL-beta. *Mol. Cell* **10**, 417–426 (2002).
5. Schroder, K. & Tschopp, J. The inflammasomes. *Cell* **140**, 821–832 (2010).
6. Xu, H. et al. Innate immune sensing of bacterial modifications of Rho GTPases by the Pyrin inflammasome. *Nature* **513**, 237–241 (2014).
7. Thornberry, N. A. et al. A novel heterodimeric cysteine protease is required for interleukin-1 β processing in monocytes. *Nature* **356**, 768–774 (1992).
8. Gu, Y. et al. Activation of interferon-gamma inducing factor mediated by interleukin-1beta converting enzyme. *Science* **275**, 206–209 (1997).
9. Ghayur, T. et al. Caspase-1 processes IFN- γ -inducing factor and regulates LPS-induced IFN- γ production. *Nature* **386**, 619–623 (1997).
10. Fink, S. L. & Cookson, B. T. Apoptosis, pyroptosis, and necrosis: mechanistic description of dead and dying eukaryotic cells. *Infect. Immun.* **73**, 1907–1916 (2005).
11. Kayagaki, N. et al. Caspase-11 cleaves gasdermin D for non-canonical inflammasome signaling. *Nature* **526**, 666–671 (2015).
12. Shi, J. et al. Cleavage of GSDMD by inflammatory caspases determines pyroptotic cell death. *Nature* **526**, 660–665 (2015).
13. Lu, A. et al. Unified polymerization mechanism for the assembly of ASC-dependent inflammasomes. *Cell* **156**, 1193–1206 (2014).
14. Cai, X. et al. Prion-like polymerization underlies signal transduction in antiviral immune defense and inflammasome activation. *Cell* **156**, 1207–1222 (2014).
15. Sborgi, L. et al. Structure and assembly of the mouse ASC inflammasome by combined NMR spectroscopy and cryo-electron microscopy. *Proc. Natl. Acad. Sci. USA* **112**, 13237–13242 (2015).
16. Martinon, F., Burns, K. & Tschopp, J. The inflammasome: a molecular platform triggering activation of inflammatory caspases and processing of proIL-beta. *Mol. Cell* **10**, 417–426 (2002).
17. Srinivasula, S. M. et al. The PYRIN-CARD protein ASC is an activating adaptor for caspase-1. *J. Biol. Chem.* **277**, 21119–21122 (2002).
18. Stehlik, C. et al. Apoptosis-associated speck-like protein containing a caspase recruitment domain is a regulator of procaspase-1 activation. *J. Immunol.* **171**, 6154–6163 (2003).
19. Masumoto, J. et al. ASC, a novel 22-kDa protein, aggregates during apoptosis of human promyelocytic leukemia HL-60 cells. *J. Biol. Chem.* **274**, 33835–33838 (1999).
20. Fernandes-Alnemri, T. et al. The pyroptosome: a supramolecular assembly of ASC dimers mediating inflammatory cell death via caspase-1 activation. *Cell Death Differ.* **14**, 1590–1604 (2007).
21. Broz, P. et al. Redundant roles for inflammasome receptors NLRP3 and NLRCA in host defense against *Salmonella*. *J. Exp. Med.* **207**, 1745–1755 (2010).
22. Franklin, B. S. et al. The adaptor ASC has extracellular and 'prionoid' activities that propagate inflammation. *Nat. Immunol.* **15**, 727–737 (2014).
23. Baroja-Mazo, A. et al. The NLRP3 inflammasome is released as a particulate danger signal that amplifies the inflammatory response. *Nat. Immunol.* **15**, 738–748 (2014).
24. Broz, P., von Moltke, J., Jones, J. W., Vance, R. E. & Monack, D. M. Differential requirement for Caspase-1 autoproteolysis in pathogen-induced cell death and cytokine processing. *Cell Host Microbe* **8**, 471–483 (2010).

25. Case, C. L., Shin, S. & Roy, C. R. Asc and Ipaf Inflammasomes direct distinct pathways for caspase-1 activation in response to *Legionella pneumophila*. *Infect. Immun.* **77**, 1981–1991 (2009).
26. Mariathasan, S. *et al.* Differential activation of the inflammasome by caspase-1 adaptors ASC and Ipaf. *Nature* **430**, 213–218 (2004).
27. Suzuki, T. *et al.* Differential regulation of caspase-1 activation, pyroptosis, and autophagy via Ipaf and ASC in *Shigella*-infected macrophages. *PLoS Pathog.* **3**, e111 (2007).
28. Guey, B., Bodnar, M., Manié, S. N., Tardivel, A. & Pettrilli, V. Caspase-1 autoproteolysis is differentially required for NLRP1b and NLRP3 inflammasome function. *Proc. Natl. Acad. Sci. USA* **111**, 17254–17259 (2014).
29. Moriya, M. *et al.* Role of charged and hydrophobic residues in the oligomerization of the PYRIN domain of ASC. *Biochemistry* **44**, 575–583 (2005).
30. Sahillioglu, A. C., Sumbul, F., Ozoren, N. & Haliloglu, T. Structural and dynamics aspects of ASC speck assembly. *Structure* **22**, 1–13 (2014).
31. Proell, M., Gerlic, M., Mace, P. D., Reed, J. C. & Riedl, S. J. The CARD plays a critical role in ASC foci formation and inflammasome signalling. *Biochem. J.* **449**, 613–621 (2013).
32. Masumoto, J., Taniguchi, S. & Sagara, J. Pyrin N-terminal homology domain- and caspase recruitment domain-dependent oligomerization of ASC. *Biochem. Biophys. Res. Commun.* **280**, 652–655 (2001).
33. Hornung, V. *et al.* AIM2 recognizes cytosolic dsDNA and forms a caspase-1-activating inflammasome with ASC. *Nature* **458**, 514–518 (2009).
34. Fernandes-Alnemri, T., Yu, J.-W., Datta, P., Wu, J. & Alnemri, E. S. AIM2 activates the inflammasome and cell death in response to cytoplasmic DNA. *Nature* **458**, 509–513 (2009).
35. Mariathasan, S. *et al.* Cryopyrin activates the inflammasome in response to toxins and ATP. *Nature* **440**, 228–232 (2006).
36. Xu, H. *et al.* Structural basis for the prion-like MAVS filaments in antiviral innate immunity. *Elife* **2014**, 1–25 (2014).
37. Peisley, A., Wu, B., Xu, H., Chen, Z. J. & Hur, S. Structural basis for ubiquitin-mediated antiviral signal activation by RIG-I. *Nature* **509**, 110–114 (2014).
38. Hou, F. *et al.* MAVS forms functional prion-like aggregates to activate and propagate antiviral innate immune response. *Cell* **146**, 448–461 (2011).
39. Zhang, L. *et al.* Cryo-EM structure of the activated NAIP2- NLR4 inflammasome reveals nucleated polymerization. *Science* **4**, 12–14 (2015).
40. Vajjhala, P. R. *et al.* The inflammasome adaptor ASC induces procaspase-8 death effector domain filaments. *J. Biol. Chem.* **290**, 687731 (2015).
41. Lu, A. *et al.* Plasticity in PYD assembly revealed by cryo-EM structure of the PYD filament of AIM2. *Cell Discov.* **1**, 15013 (2015).
42. Nour, A. M. *et al.* Anthrax lethal toxin triggers the formation of a membrane-associated inflammasome complex in murine macrophages. *Infect. Immun.* **77**, 1262–1271 (2009).
43. Poyet, J. L. *et al.* Identification of Ipaf, a human caspase-1-activating protein related to Apaf-1. *J. Biol. Chem.* **276**, 28309–28313 (2001).
44. Faustin, B. *et al.* Reconstituted NALP1 inflammasome reveals two-step mechanism of caspase-1 activation. *Mol. Cell* **25**, 713–724 (2007).
45. Franchi, L. *et al.* Cytosolic flagellin requires Ipaf for activation of caspase-1 and interleukin 1beta in salmonella-infected macrophages. *Nat. Immunol.* **7**, 576–582 (2006).
46. Miao, E. A. *et al.* Cytoplasmic flagellin activates caspase-1 and secretion of interleukin 1beta via Ipaf. *Nat. Immunol.* **7**, 569–575 (2006).
47. Miao, E. A. *et al.* Caspase-1-induced pyroptosis is an innate immune effector mechanism against intracellular bacteria. *Nat. Immunol.* **11**, 1136–1142 (2010).
48. Kagan, J. C., Magupalli, V. G. & Wu, H. SMOCs: supramolecular organizing centres that control innate immunity. *Nat. Rev. Immunol.* **14**, 821–826 (2014).
49. Vajjhala, P. R., Mirams, R. E. & Hill, J. M. Multiple binding sites on the pyrin domain of ASC protein allow self-association and interaction with NLRP3 protein. *J. Biol. Chem.* **287**, 41732–41743 (2012).
50. Elliott, E. I. & Sutterwala, F. S. Initiation and perpetuation of NLRP3 inflammasome activation and assembly. *Immunol. Rev.* **265**, 35–52 (2015).
51. Lamkanfi, M. *et al.* Inflammasome-dependent release of the alarmin HMGB1 in endotoxemia. *J. Immunol.* **185**, 4385–4392 (2010).
52. Cong, L. *et al.* Multiplex genome engineering using CRISPR/Cas systems. *Science* **339**, 819–823 (2013).
53. Sanjana, N. E., Shalem, O. & Zhang, F. Improved vectors and genome-wide libraries for CRISPR screening. *Nat. Methods* **11**, 783–784 (2014).
54. Qiao, Q. *et al.* Structural architecture of the CARMA1/Bcl10/MALT1 signalosome: nucleation-induced filamentous assembly. *Mol. Cell* **51**, 766–779 (2013).
55. Lin, S.-C., Lo, Y.-C. & Wu, H. Helical assembly in the MyD88-IRAK4-IRAK2 complex in TLR/IL-1R signalling. *Nature* **465**, 885–890 (2010).
56. Hu, Z. *et al.* Structural and biochemical basis for induced self-propagation of NLRCA. *Science* **350**, 1–11 (2015).
57. Agard, N. J., Maltby, D. & Wells, J. A. Inflammatory stimuli regulate caspase substrate profiles. *Mol. Cell. Proteomics* **9**, 880–893 (2010).
58. Sagoo, P. *et al.* *In vivo* imaging of inflammasome activation reveals a subcapsular macrophage burst response that mobilizes innate and adaptive immunity. *Nat. Med.* **22**, 64–71 (2015).
59. Cheng, J. *et al.* Kinetic properties of ASC protein aggregation in epithelial cells. *J. Cell. Physiol.* **222**, 738–747 (2010).
60. Hara, H. *et al.* Phosphorylation of the adaptor ASC acts as a molecular switch that controls the formation of speck-like aggregates and inflammasome activity. *Nat. Immunol.* **14**, 1247–1255 (2013).
61. Lin, Y.-C. *et al.* Syk is involved in NLRP3 inflammasome-mediated caspase-1 activation through adaptor ASC phosphorylation and enhanced oligomerization. *J. Leukoc. Biol.* **97**, 1–11 (2015).
62. Blasi, E. *et al.* Selective immortalization of murine macrophages from fresh bone marrow by a raf/myc recombinant murine retrovirus. *Nature* **318**, 667–670 (1985).
63. Schindelin, J. *et al.* Fiji: an open-source platform for biological-image analysis. *Nat. Methods* **9**, 676–682 (2012).
64. Broz, P. & Monack, D. M. Measuring inflammasome activation in response to bacterial infection. *Methods Mol. Biol.* **1040**, 65–84 (2013).
65. Reed, S. E., Staley, E. M., Mayginnnes, J. P., Pintel, D. J. & Tullis, G. E. Transfection of mammalian cells using linear polyethylenimine is a simple and effective means of producing recombinant adeno-associated virus vectors. *J. Virol. Methods* **138**, 85–98 (2006).
66. Tang, Y., Garson, K., Li, L. & Vanderhyden, B. Optimization of lentiviral vector production using polyethylenimine-mediated transfection. *Oncol. Lett.* **9**, 55–62 (2014).
67. de Alba, E. Structure and interdomain dynamics of apoptosis-associated speck-like protein containing a CARD (ASC). *J. Biol. Chem.* **284**, 32932–32941 (2009).

Acknowledgements

We thank V. Dixit (Genentech) for the rat antibody to ASC and rat antibody to caspase-1 p20; Vesna Oliveri, Tim Sharpe, the Imaging Core Facility, FACS Core Facility, Biophysics Core Facility and the Microscopy Center of the Biozentrum, University of Basel, for technical assistance. Work was supported by the Swiss National Science Foundation (PP00P3_139120/1 to P.B.).

Author contributions

M.S.D., L.S., S.H. and P.B. designed research. M.S.D., L.S., S.R. and P.B. performed experiments. M.S.D., L.S., S.H. and P.B. analysed data and wrote the manuscript.

Additional information

Supplementary Information accompanies this paper at <http://www.nature.com/naturecommunications>

Competing financial interests: The authors declare no competing financial interests.

Reprints and permission information is available online at <http://npg.nature.com/reprintsandpermissions/>

How to cite this article: Dick, M. S. *et al.* ASC filament formation serves as a signal amplification mechanism for inflammasomes. *Nat. Commun.* **7**:11929 doi: 10.1038/ncomms11929 (2016).



This work is licensed under a Creative Commons Attribution 4.0 International License. The images or other third party material in this article are included in the article's Creative Commons license, unless indicated otherwise in the credit line; if the material is not included under the Creative Commons license, users will need to obtain permission from the license holder to reproduce the material. To view a copy of this license, visit <http://creativecommons.org/licenses/by/4.0/>



DOI: 10.1038/ncomms15030 OPEN

Corrigendum: ASC filament formation serves as a signal amplification mechanism for inflammasomes

Mathias S. Dick, Lorenzo Sborgi, Sebastian Rühl, Sebastian Hiller & Petr Broz

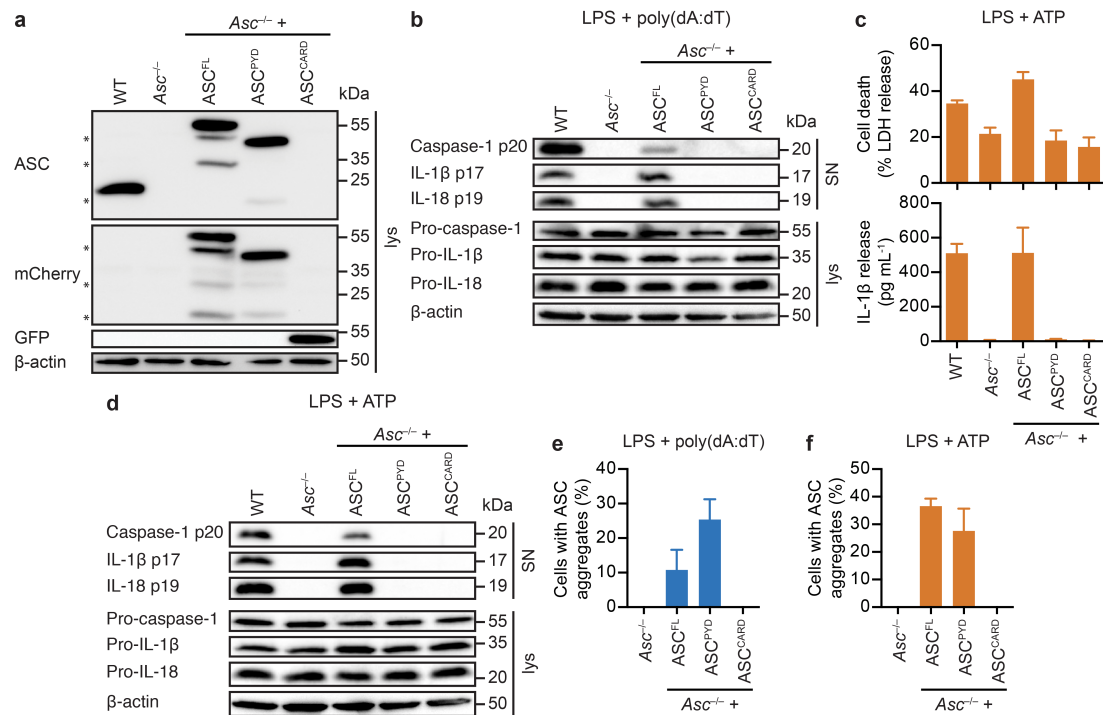
Nature Communications 7:11929 doi: 10.1038/ncomms11929 (2016); Published 22 Jun 2016; Updated 17 Mar 2017

In this Article, residues D128 and D132 of ASC are consistently referred to incorrectly as D130 and D134, respectively. These errors appear in the Results, Methods, Fig. 2, Fig. 3 and Supplementary Fig. 1.



This work is licensed under a Creative Commons Attribution 4.0 International License. The images or other third party material in this article are included in the article's Creative Commons license, unless indicated otherwise in the credit line; if the material is not included under the Creative Commons license, users will need to obtain permission from the license holder to reproduce the material. To view a copy of this license, visit <http://creativecommons.org/licenses/by/4.0/>

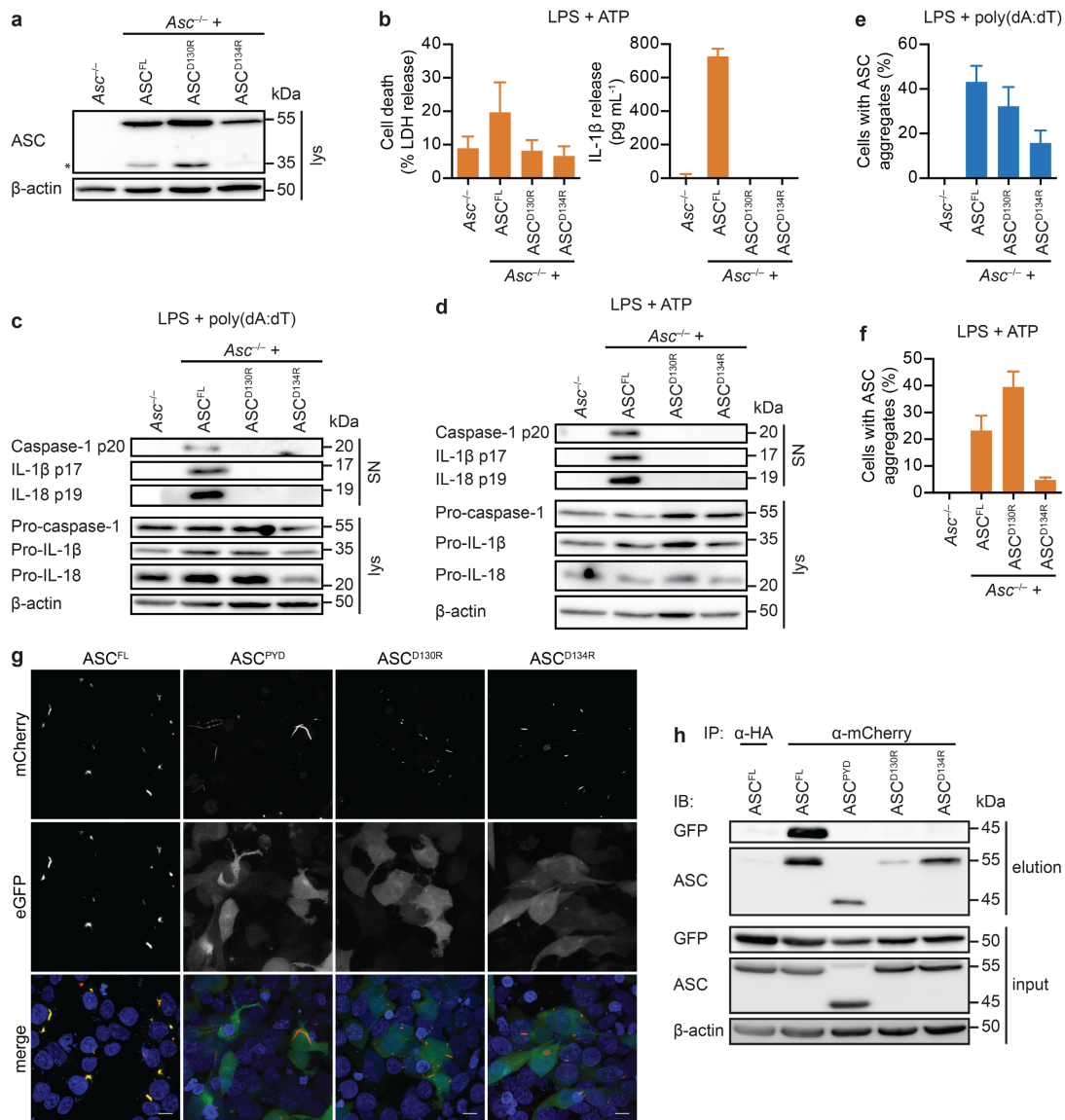
© The Author(s) 2017



Supplementary Figure 1 (Related to Fig. 1)

(a) Expression of the ASC constructs in immortalized *Asc*^{-/-} BMDM cell lysates (lys) as assessed by immunoblotting against eGFP, mCherry, ASC and β-actin. * denotes degradation bands resulting from a degraded mCherry, but with intact ASC. (b) Immunoblot analysis for cleaved caspase-1 p20, IL-1β p17 and IL-18 p19 in cell supernatants (SN) and pro-caspase-1, pro-IL-1β, pro-IL-18 and β-actin in lysates (lys) of LPS-primed immortalized wildtype (WT), *Asc*^{-/-} or *Asc*^{-/-} BMDMs expressing wildtype ASC (ASC^{FL}), ASC^{PYD} or ASC^{CARD} 3 h after poly(dA:dT) transfection (1 μg ml⁻¹). (c) Release of LDH and IL-1β from LPS-primed immortalized wildtype, *Asc*^{-/-} or *Asc*^{-/-} BMDMs expressing ASC^{FL}, ASC^{PYD} or ASC^{CARD} 1 h after ATP treatment (5 mM). (d) Immunoblots analysis for cleaved caspase-1 p20, IL-1β p17 and IL-18 p19 in cell supernatants (SN) and pro-caspase-1, pro-IL-1β, pro-IL-18 and β-actin in lysates (lys) of LPS-primed immortalized wildtype, *Asc*^{-/-} or *Asc*^{-/-} BMDMs expressing ASC^{FL}, ASC^{PYD} or ASC^{CARD} 1 h after 5 mM ATP treatment. (e-f) Quantification of ASC aggregates (specks and filaments) in LPS-primed immortalized *Asc*^{-/-} BMDMs

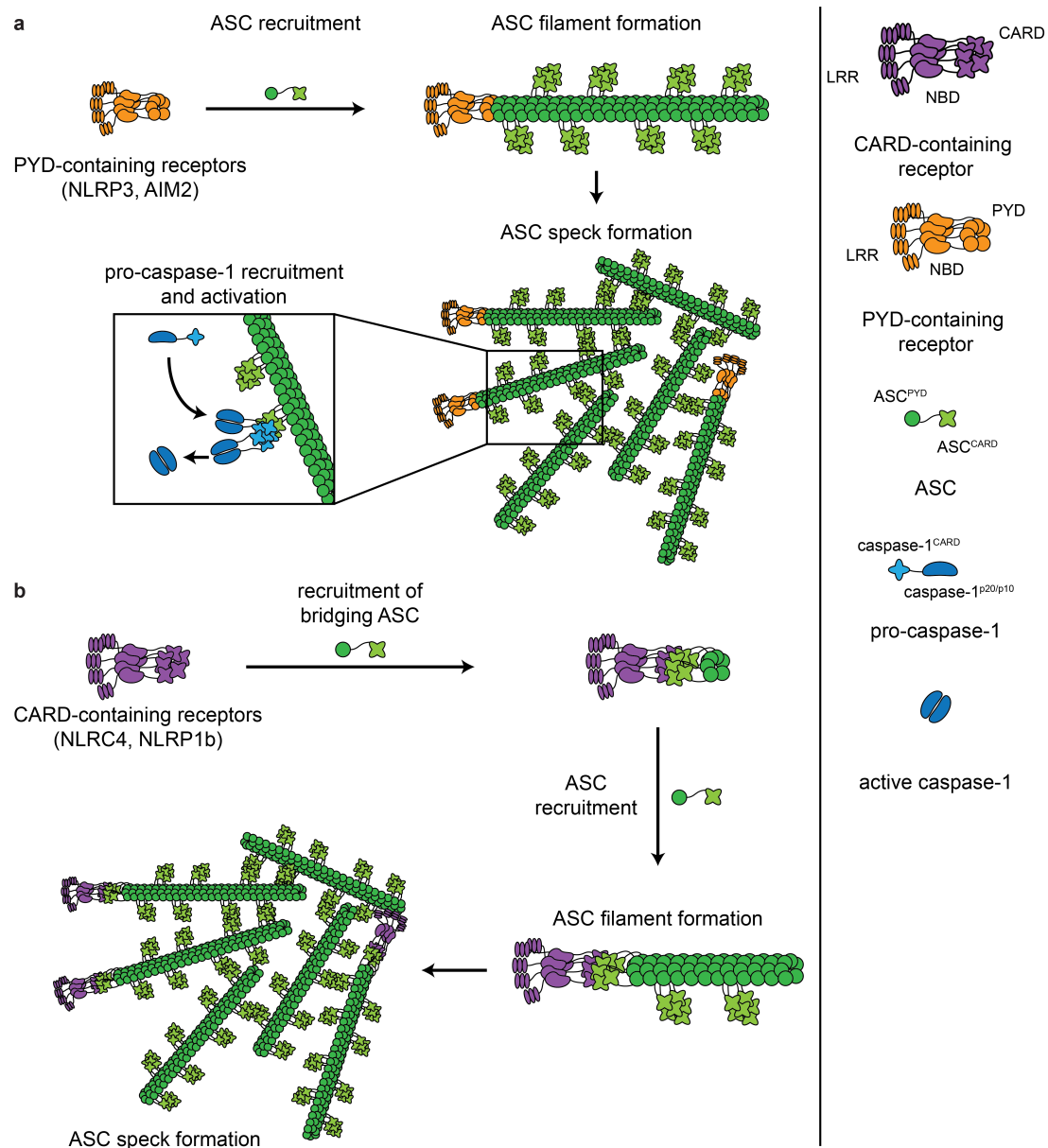
expressing ASC^{FL}, ASC^{PYD} or ASC^{CARD} 3 h after poly(dA:dT) transfection (1 $\mu\text{g ml}^{-1}$) (e) or 1 h after ATP treatment (5 mM) (f). Graphs show the mean and s.d. of quadruplicate wells or ten random fields of view. Results shown are representative of at least three (a, c, e-f) or two independent experiments (b, d). See also Supplementary Figure 9.



Supplementary Figure 2 (Related to Fig. 2)

(a) Equal expression of ASC^{CARD} mutants (ASC^{D130R} and ASC^{D134R}) in immortalized *Asc*^{-/-} BMDM cell lysates (*lys*) as assessed by immunoblotting against ASC and β -actin. * denotes a degradation band. (b) Release of LDH and IL-1 β from LPS-primed immortalized *Asc*^{-/-} BMDMs and *Asc*^{-/-} BMDMs expressing ASC^{FL}, ASC^{D130R} or ASC^{D134R} 1 h after ATP treatment (5 mM). (c-d) Immunoblots analysis for cleaved caspase-1 p20, IL-1 β p17 and IL-18 p19 in cell supernatants (SN) and pro-caspase-1, pro-IL-1 β , pro-IL-18 and β -actin in lysates

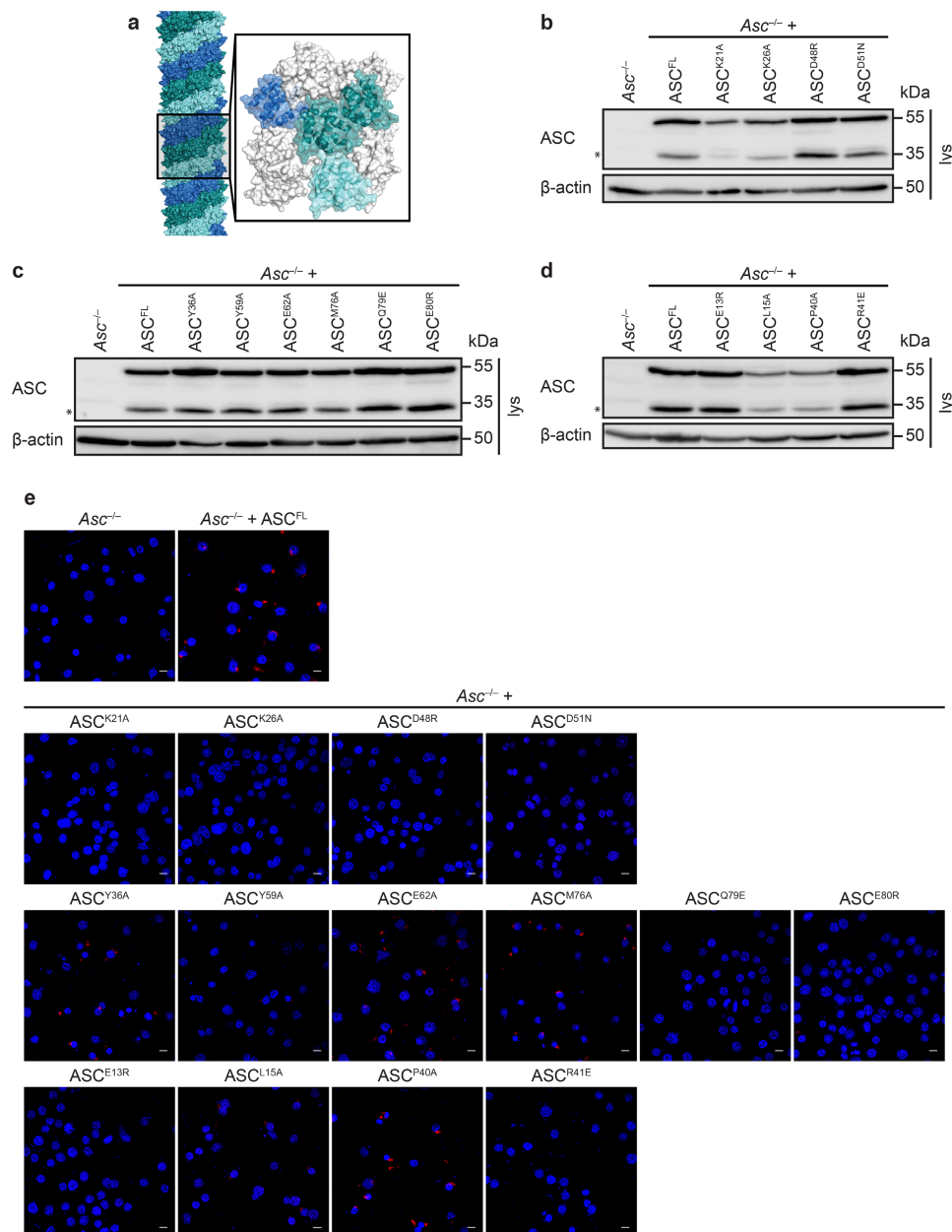
(lys) of LPS-primed immortalized *Asc*^{-/-} BMDMs and *Asc*^{-/-} BMDMs expressing ASC^{FL}, ASC^{D130R} or ASC^{D134R} 3 h after poly(dA:dT) transfection (1 µg ml⁻¹) (c) or 1 h after 5 mM ATP treatment (5 mM) (d). (e-f) Quantification of ASC aggregates (specks and filaments) from LPS-primed immortalized *Asc*^{-/-} BMDMs and *Asc*^{-/-} BMDMs expressing ASC^{FL}, ASC^{D130R} or ASC^{D134R} 3 h after poly(dA:dT) transfection (e) or 1 h after ATP treatment (5 mM) (f). (g) Co-localization of mCherry-tagged ASC^{FL}, ASC^{PYD}, ASC^{D130R} and ASC^{D134R} (red) with GFP-tagged ASC^{CARD} (green) overexpressed in HEK293T cells together with AIM2-V5 (to induce inflammasome assembly, not shown). DNA was stained with Hoechst (blue). Scale bars 10 µm. (h) Immunoblot analysis of the interaction of ASC^{CARD} with ASC^{FL}, ASC^{PYD}, ASC^{D130R} or ASC^{D134R}. ASC-mCherry was immunoprecipitated from lysates of HEK293T cells co-transfected with AIM2-V5, ASC^{CARD}-GFP and the indicated ASC-mCherry constructs. Co-immunoprecipitating proteins were identified using anti-GFP, anti-ASC and anti-β-actin antibodies. Graphs show the mean and s.d. of quadruplicate wells or ten random fields of view. Results shown are representative of at least two (a, c-d, g-h) or three (b, e-f) independent experiments. See also Supplementary Figure 9.



Supplementary Figure 3. Model describing ASC filament initiation and ASC speck assembly. (Related to Fig. 2 and Fig. 3)

(a) Activation of PYD-containing inflammasome receptors leads to the recruitment of ASC by homotypic receptor^{PYD}-ASC^{PYD} interaction and nucleation of ASC^{PYD} filaments. ASC^{CARDs} are exposed on the surface of ASC^{PYD} filaments. CARD-CARD interactions between ASC^{CARDs} of different filaments connect the different ASC^{PYD} filaments and condense them into the dense ASC speck

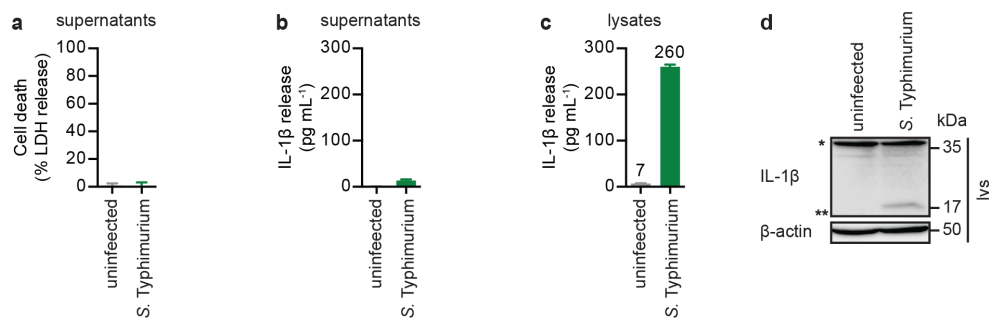
structure. At the same time surface exposed ASC^{CARD} serves as the recruitment and activation point for pro-caspase-1. (b) CARD-containing receptors recruit ASC bridging molecules by homotypic receptor^{CARD}-ASC^{CARD} interactions. The PYDs of the ASC bridging molecules act as a nucleation point for ASC^{PYD} filaments, a function that is otherwise executed by the receptor^{PYD}, as described in (a). The different ASC^{PYD} filaments are then condensed into the ASC speck by the ASC^{CARD}.



Supplementary Figure 4 (Related to Fig. 4)

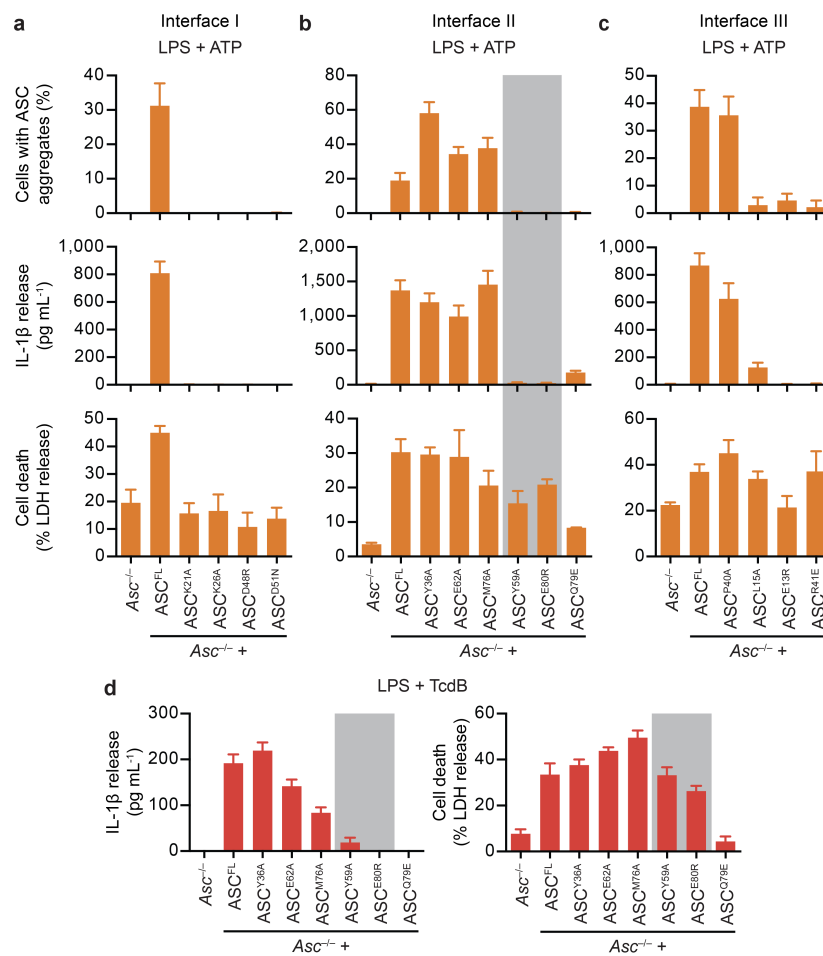
a) Structure of the mouse ASC^{PYD} filament [PDB 2N1F¹]. The three helical layers are colored blue, teal and light blue. A zoom up view shows the surface representation of ASC^{PYD} monomers as part of the filament. (b-d) Equal expression of wildtype ASC (ASC^{FL}) and ASC interaction interface I (b), interface II (c) and interface III (d) mutants in immortalized *Asc*^{-/-} BMDM cell lysates (lys) as assessed by immunoblotting using anti-ASC and anti-β-actin antibodies. *

denotes a degradation band. (e) Representative images from LPS-primed immortalized *Asc*^{-/-} BMDMs expressing mCherry-tagged ASC^{FL} or the indicated ASC interaction interface mutants after 3 h of poly(dA:dT) transfection (1 $\mu\text{g ml}^{-1}$). DNA was stained with Hoechst (blue), ASC (red). Scale bars 10 μM . Results shown are representative of two (b-d) or three (e) independent experiments. See also Supplementary Figure 9.



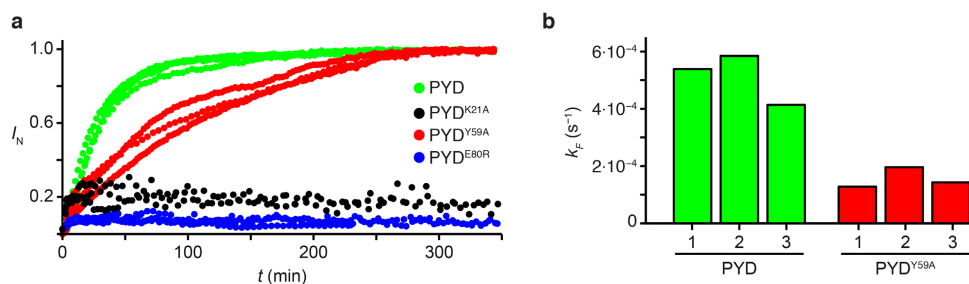
Supplementary Figure 5. The IL-1 β ELISA kit is more specific for the cleaved IL-1 β p17.

(a-b) Release of LDH (a) and IL-1 β from LPS-primed immortalized *Gsdmd*^{-/-} BMDMs left uninfected or infected with log phase *S. Typhimurium* SL1344 (MOI 10 for 1 h). (c) Release of IL-1 β as detected by the ELISA kit used for this study (Mouse IL-1 beta ELISA Ready-SET-Go!® from eBiosciences, CatNo. 88-7013) from the cells in (a) and lysed by freezing and thawing in water. Numbers above bars indicate the average values. (d) Immunoblot analysis for pro-IL-1 β (*) and bioactive IL-1 β p17 (**) in lysates of the cells as in (c). Graphs show the mean and s.d. of quadruplicate wells and results shown are representative of at least three independent experiments. See also Supplementary Figure 9.



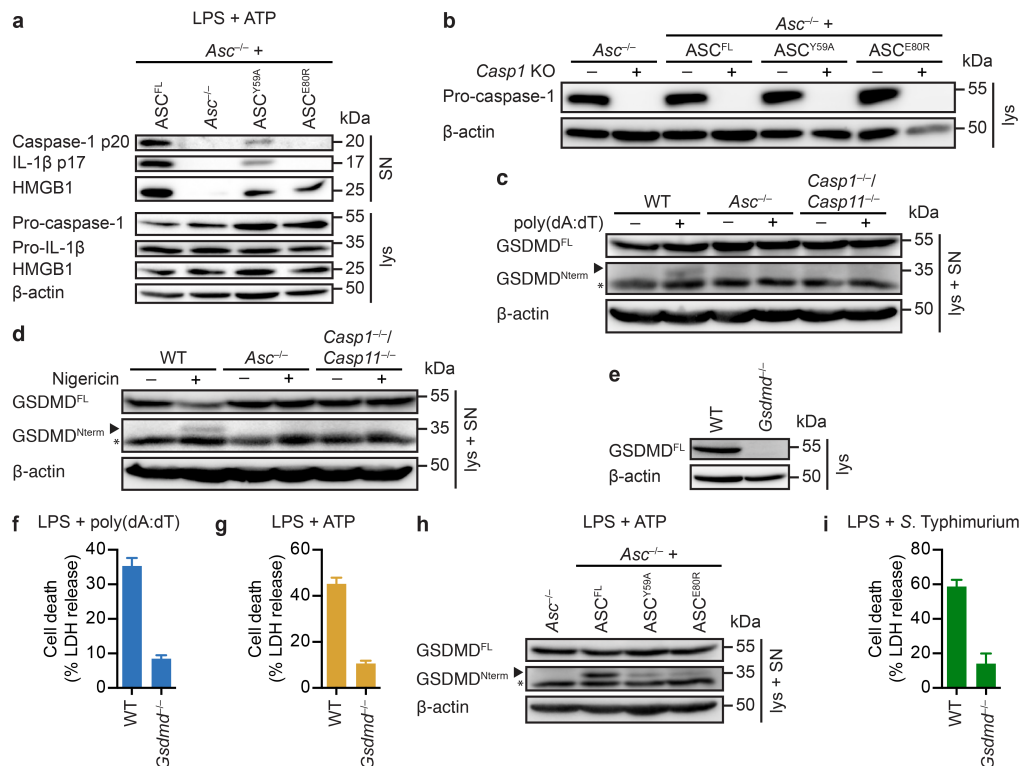
Supplementary Figure 6. Cell death is uncoupled from IL-1 β release in NLRP3 and PYRIN inflammasomes (Related to Fig. 4)

(a-c) Quantification of ASC aggregates or the release of LDH and IL-1 β from LPS-primed immortalized Asc^{-/-} BMDMs and Asc^{-/-} BMDMs expressing ASC^{FL} or the indicated ASC mutants 1 h after ATP treatment (5 mM). (d) Release of LDH and IL-1 β from LPS-primed immortalized Asc^{-/-} BMDMs and Asc^{-/-} BMDMs expressing ASC^{FL} or the indicated ASC interface type II mutants 2.5 h after treatment with *Clostridium difficile* toxin B (TcdB, 1 μ g ml⁻¹). ASC^{Y59A} and ASC^{E80R} are highlighted in grey. Graphs show mean and s.d. from quadruplicate wells or ten random fields of view. Data are representative of at least three independent experiments.



Supplementary Figure 7. Measurement of filament formation kinetics *in vitro* (Related to Fig. 5)

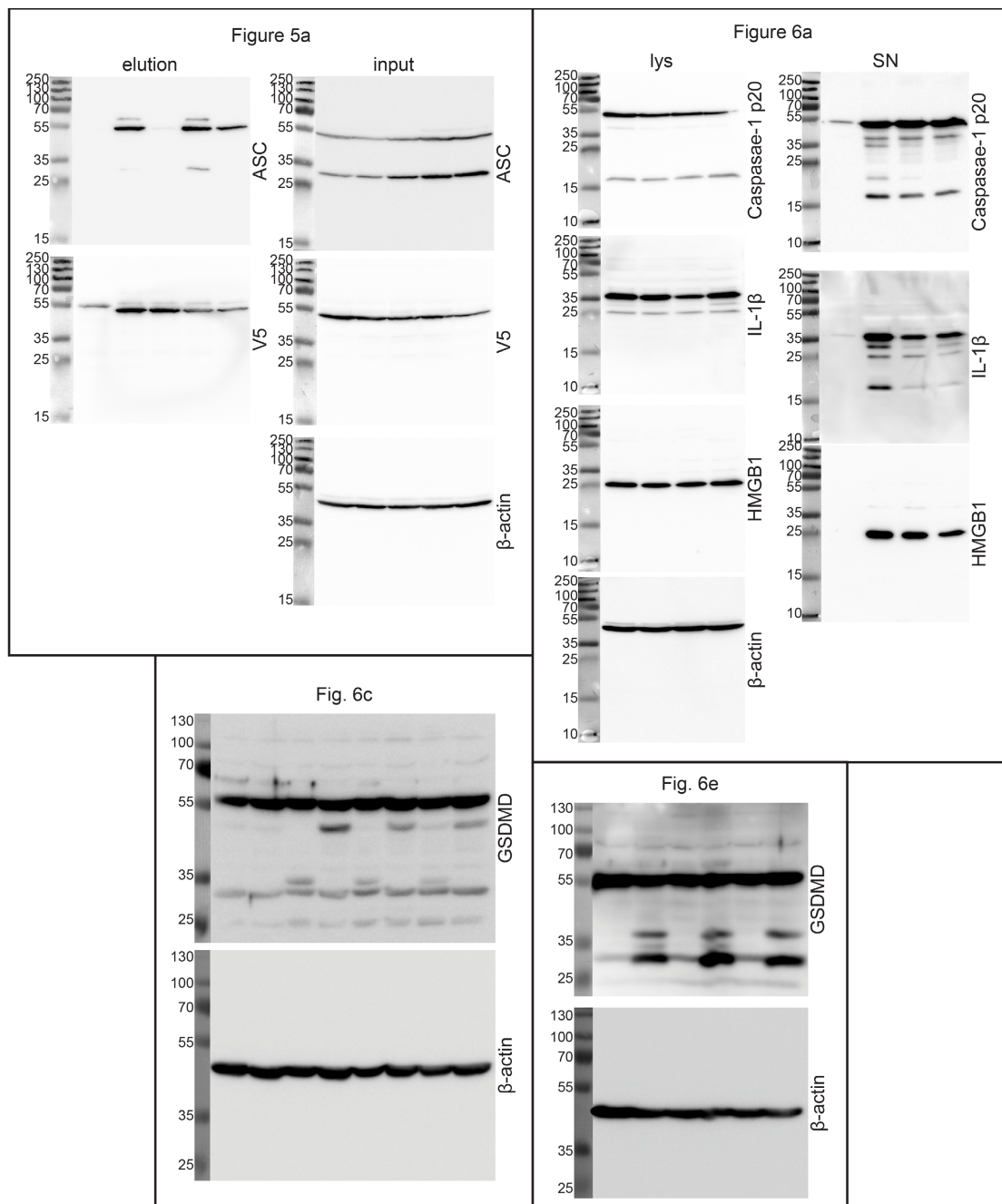
(a) Filament formation of wild-type ASC^{PYD} and its single amino-acid variants Y59A, K21A and E80R *in vitro* monitored by dynamic light scattering. Normalized growth signals (I_N) are reported as a function of time for three independent replicates of each variant (dotted lines). Three independent replicates are shown for each protein variant. Figure 5b displays one of these replicates. (b) Kinetic rate constants k_F of filament formation obtained from fitting the data in A with single exponential functions. Figure 5c displays the average and standard deviation of these data.

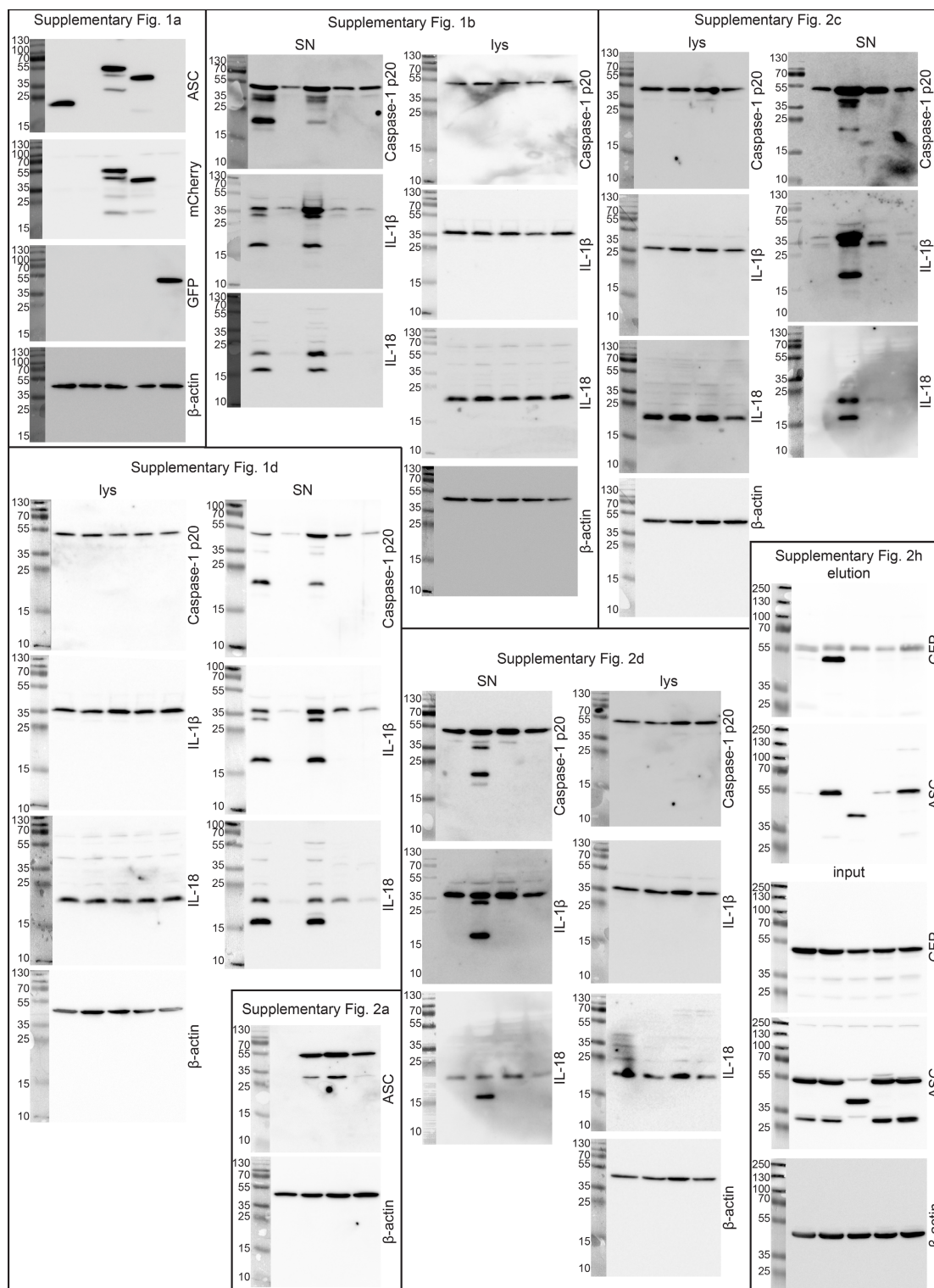


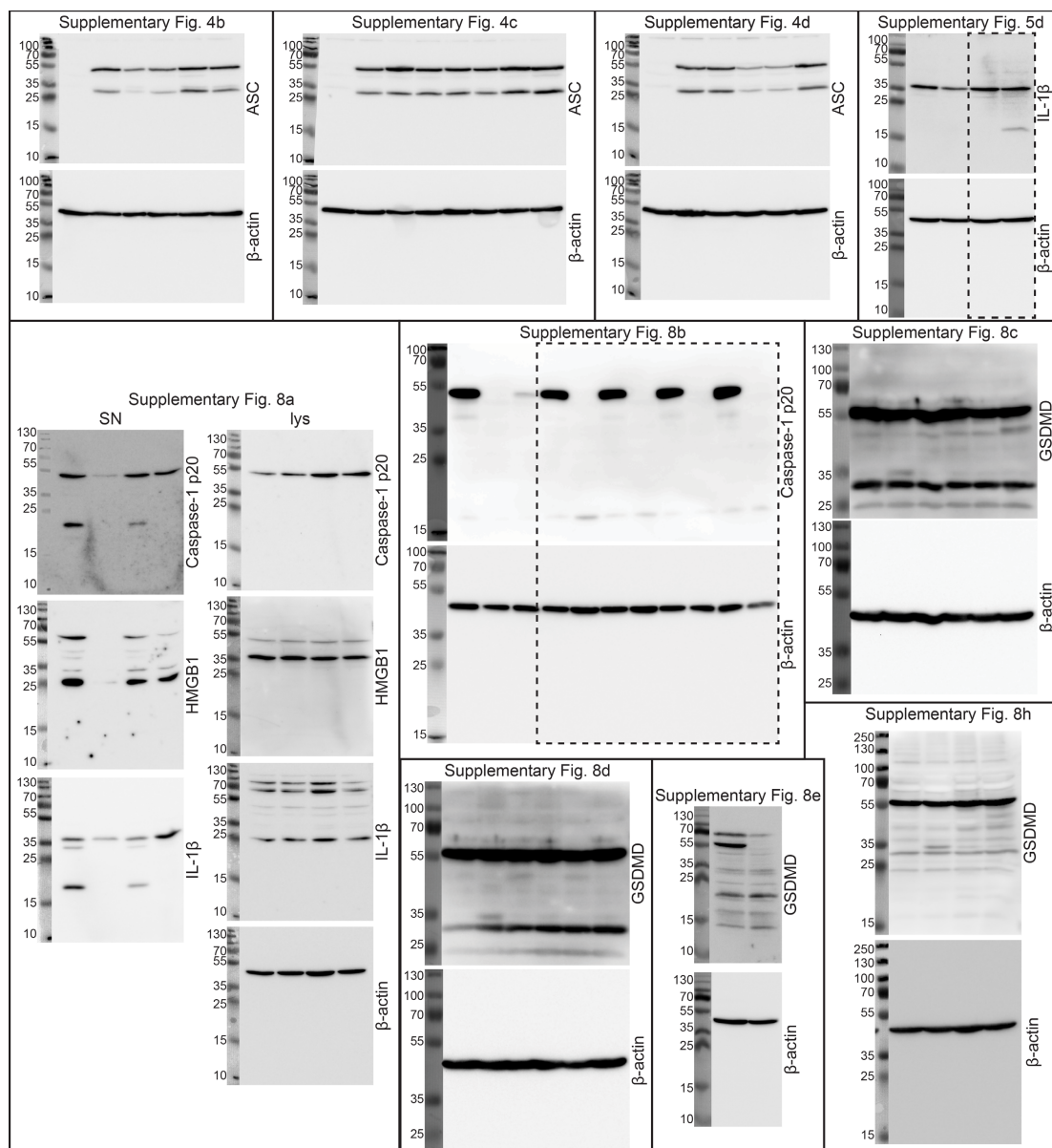
Supplementary Figure 8 (Related to Fig. 6)

(a) Immunoblot analysis for cleaved caspase-1 p20, IL-1β p17, and HMGB-1 in cell supernatants (SN) and pro-caspase-1, pro-IL-1β, and HMGB-1 in cell lysates (lys) of LPS-primed immortalized *Asc*^{-/-} BMDMs or *Asc*^{-/-} BMDMs expressing ASC^{FL}, ASC^{Y59A} or ASC^{E80R} after ATP treatment (5 mM, 1 h). (b) Confirmation of CRISPR-Cas9 mediated *Casp1* knock-out in immortalized *Asc*^{-/-} BMDMs expressing ASC^{FL}, ASC^{Y59A} or ASC^{E80R} by immunoblotting. (c-d) Immunoblot analysis for processing of GSDMD into the active N-terminal fragment in combined lysates (lys) and supernatants (SN) of LPS-primed primary C57BL/6 WT (WT), *Casp1*^{-/-}/*Casp11*^{-/-} or *Asc*^{-/-} BMDMs transfected with 1 μg ml⁻¹ poly(dA:dT) for 3 h (c), treated with 5 mM ATP for 1 h (d) or left untreated. (e) Confirmation of CRISPR-Cas9 mediated *Gsdmd* knock-out in immortalized WT BMDMs. (f-g) LDH release from immortalized WT or *Gsdmd*^{-/-} BMDMs primed with LPS and then transfected with poly(dA:dT) (1 μg ml⁻¹, 3 h [f]) or treated with ATP (5 mM, 1 h [g]).

(h) Immunoblot analysis for processing of GSDMD into the active N-terminal fragment in combined lysates and supernatants (lys + SN) of LPS-primed immortalized *Asc*^{-/-} BMDMs expressing ASC^{FL}, ASC^{Y59A} or ASC^{E80R} 1 h after ATP treatment (5 mM). (i) LDH release from immortalized WT or *Gsdmd*^{-/-} BMDMs, primed with LPS and then infected with *S. Typhimurium* (MOI = 10, for 1 h). Arrowheads indicate the GSDMD^{Nterm} p30, * indicate a cross-reacting band. β -actin immunoblots serve as loading controls. Graphs show mean and s.d. from quadruplicate wells. Results shown are representative of two (a-b) or three (c-i) independent experiments. See also Supplementary Figure 9.







Supplementary Figure 9

Full images of blots shown in the main text and supplementary figures.

SUPPLEMENTARY TABLE

Supplementary Table 1. Oligonucleotides used for plasmid construction

Name	No.	Sequence	Restricti on Site	Description
ASC_D48R_fw	O94	GCCCTGCTGCAGATGcgcG CCATAgatCTCACTGACAAA C		site directed mutagenesis, ASC ^{D48R}
ASC_D48R_rv	O95	GTTTGTCTCAGTGAgatcTATG GCgcgCATCTGCAGCAGGG C		site directed mutagenesis, ASC ^{D48R}
ASC_D51N_fw	O104	CTGCAGATGGACGCCATAa acCTCACTGACAAACTTGTG AGC		site directed mutagenesis, ASC ^{D51N}
ASC_D51N_rv	O105	GCTGACAAGTTTGTCTCAGTG AGgttTATGGCGTCCATCTGC AG		site directed mutagenesis, ASC ^{D51N}
ASC_Y59A_fw	O108	CACTGACAAACTTGTCTCAGCg ccTATCTGGAGTCGTATGGC TTG		site directed mutagenesis, ASC ^{Y59A}
ASC_Y59A_rv	O109	CAAGCCATACGACTCCAGA TAggcGCTGACAAGTTTGTG AGTG		site directed mutagenesis, ASC ^{Y59A}
ASC_Y36A_fw	O155	gcaactgcgagaaggcgccggg atccac		site directed mutagenesis, ASC ^{Y36A}
ASC_Y36A_rv	O156	gtgggatgcgcccggcgcttctc gtgcag		site directed mutagenesis, ASC ^{Y36A}
ASC_E62A_fw	O159	gacaaactgtcagctactatctg GCct cgtaggcttgagctc		site directed mutagenesis, ASC ^{E62A}
ASC_E62A_rv	O160	gagctccaagccatacgaGGC cagagtagtagctgacaagttt gtc		site directed mutagenesis, ASC ^{E62A}
ASC_M76A_fw	O161	caatgactgtgcttagagacGCC ggcttacaggagctgg		site directed mutagenesis, ASC ^{M76A}
ASC_M76A_rv	O162	ccagctcctgtaagccGGCgt ctctaacgacagctattg		site directed mutagenesis, ASC ^{M76A}
ASC_Q79E_fw	O163	gtgcttagagacatgggctta GAAgagctggctgagcag		site directed mutagenesis, ASC ^{Q79E}
ASC_Q79E_rv	O164	ctgctcagccagctcTTCTa agcccatgtcttaagcac		site directed mutagenesis, ASC ^{Q79E}
ASC_E80R_fw	O165	cttagagacatgggcttacag CGCctggctgagcagctg		site directed mutagenesis, ASC ^{E80R}
ASC_E80R_rv	O166	cagctgctcagccagGCGct gtaagccatgtcttaag		site directed mutagenesis, ASC ^{E80R}
ASC_E13R_fw_XhoI	O243	GATCctcgagCCACCatggg ggcgagatgccatcctggacg ctcttCGCaactgtcag	XhoI	site directed mutagenesis, ASC ^{E13R}
ASC_R41E_fw	O244	gggcgcatcccaGAAggggcc ctgc		site directed mutagenesis, ASC ^{R41E}
ASC_R41E_rv	O245	gcagggcccccTTctgggatg cgccc		site directed mutagenesis, ASC ^{R41E}
ASC_L15A_fw_XhoI	O246	GATCctcgagCCACCatggg ggcgagatgccatcctggacg ctctt	XhoI	site directed mutagenesis, ASC ^{L15A}

		gaaaacGCctcaggggatg		
ASC_P40A_fw	O247	gctatgggcgcatcGCCcgggggc cc		site directed mutagenesis, ASC ^{P40A}
ASC_P40A_rv	O248	gggccccgCGGCgatgcgccata gc		site directed mutagenesis, ASC ^{P40A}
ASCfwXhoI	O7	GATCctcgagCCACCatggggcg ggcacgagatgc	XhoI	cloning of ASC into V48, forward
ASC1-92rvEcoRI	O4	GATCgaattcGctcttcttagctgttg cagct	EcoRI	cloning of ASC ^{P40A} into V48, reverse
ASC-CARD-GFPprimer A	O21	GATCGCGGCCCGCCACCATG GGAGCTGTGGCAGCTGCA G	NotI	cloning of ASC ^{CARD} - GFP into V48 by SOE PCR
ASC-CARD-GFPprimer B	O22	GATCCACCGGTGCGCCACCA TGTTGAGCAAGGGCGAGG		cloning of ASC ^{CARD} - GFP into V48 by SOE PCR
ASC-CARD-GFPprimer C	O23	CCTCGCCCTTGCTCACCAT GGTGGCGACCGGTGGATC		cloning of ASC ^{CARD} - GFP into V48 by SOE PCR
ASC-CARD-GFPprimer D	O24	GATCGTTTAACTTATCTAG ATCCGGTGGATCCC	PmeI	cloning of ASC ^{CARD} - GFP into V48 by SOE PCR
RV_ascfl_EcoRI	O59	GATCgaattcggctctgctccagggtc atca	EcoRI	cloning of ASC ^{FL} into V48, reverse
FWascD13 0R	O13	CACAGAAGTGAGGGGAGTG CTG		site directed mutagenesis, ASC ^{D130R}
RVascD13 0R	O14	CAGCACTCCCCTCACTTCT GTG		site directed mutagenesis, ASC ^{D130R}
FWascD13 4R	O15	CGGAGTGCTGAGGGCTTTG CATG		site directed mutagenesis, ASC ^{D134R}
RVascD13 4R	O16	CATGCAAAGCCCTCAGCAC TCCG		site directed mutagenesis, ASC ^{D134R}

SUPPLEMENTARY REFERENCES

1. Sborgi, L. *et al.* Structure and assembly of the mouse ASC inflammasome by combined NMR spectroscopy and cryo-electron microscopy. *Proc. Natl. Acad. Sci.* (2015). doi:10.1073/pnas.1507579112

2.2.1 Additional results related to research article II

Apart from the *Casp1* CRISPR-Cas9 knock-outs in immortalized BMDMs (bone marrow derived macrophages) expressing ASC-mCherry mutants (*Asc*^{-/-}, *Asc*^{-/-} + ASC^{FL}, *Asc*^{-/-} + ASC^{Y59A}, *Asc*^{-/-} + ASC^{E80R}) and the *Gsdmd* KO in wild type immortalized BMDMs, I knocked out *Gsdmd* in immortalized *Asc*^{-/-} BMDMs or immortalized *Asc*^{-/-} BMDMs expressing ASC^{FL}, ASC^{Y59A}, or ASC^{E80R} (for materials and methods see research article II³²²). The goal was to show that gasdermin-D is indeed responsible for cell death in absence of ASC oligomerization.

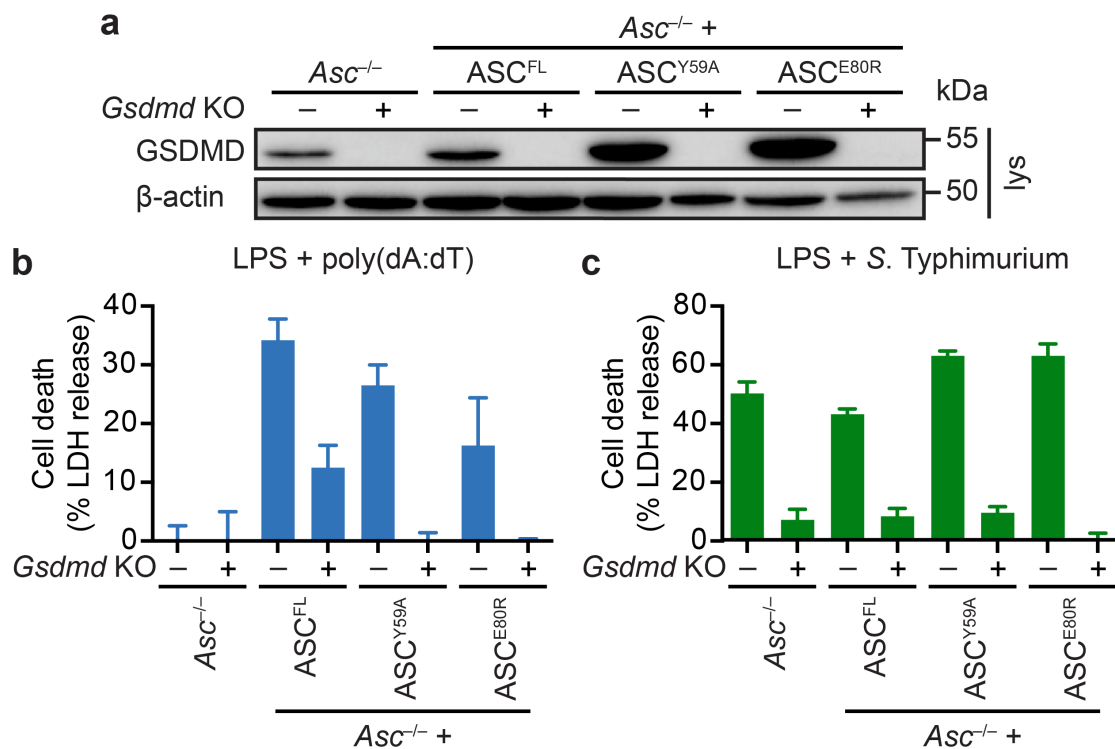


Figure 2.1: **Effect of *Gsdmd* deletion on pyroptosis.** (a) Western blot analysis for CRISPR-Cas9 mediated *Gsdmd* deletion in immortalized *Asc*^{-/-} BMDMs and immortalized *Asc*^{-/-} BMDMs expressing ASC^{FL}, ASC^{Y59A} or ASC^{E80R}. (b-c) Release of LDH from LPS-primed immortalized BMDMs from (a) after poly(dA:dT) transfection (1 µg/mL for 3 h, b) and *S. Typhimurium* infection (MOI 10 for 1h, c). Graphs show means and s.d. from quadruplicate wells. Data are representative of three independent experiments.

Western blotting confirmed that the CRISPR-Cas9 *Gsdmd* knock-out was successful in all cell lines (**Fig. 2.1a**). To assess the effect of *Gsdmd* ablation on PYD-containing

inflammasomes, cells were transfected with poly(dA:dT) for 3 h to activate AIM2. The results showed that gasdermin-D was responsible for the cell death observed in both, absence and presence of ASC oligomerization (**Fig. 2.1b**). As *S. Typhimurium* dependent NLRC4 activation proceeds also in absence of ASC, I also tested the effect of *Gsdmd* deficiency on NLRC4-dependent cell death. The results indicated that gasdermin-D was not only responsible for cell death upon activation of PYD-containing receptors, but also CARD-containing receptors (**Fig. 2.1c**) as deletion of *Gsdmd* in absence of *Asc* abrogated cell death. Consistently, gasdermin-D was also required for NLRC4-dependent pyroptosis in absence of ASC oligomerization (**Fig. 2.1**).

Collectively, these results suggested that the cell death observed in cells expressing ASC mutants that were no longer able to oligomerize and form specks (Y59A or E80R) was not only dependent on caspase-1 (see research article II³²²) but also on gasdermin-D. Furthermore, they implied that NLRC4-dependent, ASC-independent pyroptosis was relying on gasdermin-D as well.

2.3 Small-molecule inhibitor screen for ASC speck formation

Introduction

Even though aberrant inflammasome activation was implied in a variety of diseases, current treatment options are limited and target mostly IL-1 β signaling^{172,178}. For some diseases like rheumatoid arthritis or CAPS the IL-1 β targeting drugs anakinra, rilonacept and canakinumab are approved for clinical use^{178,179,181}. These drugs significantly ameliorate disease outcome but there are some disadvantages. The first is the high price ranging from 20'000 US\$ up to 250'000 US\$ per patient per year^{41–43}. Additionally, some of these drugs need to be administered by a daily subcutaneous injection hampering patient compliance^{172,178,323}. Furthermore, an increased incidence of bacterial infections, mainly with *Streptococcus*, occurs in patients treated with anakinra³²⁴. For FMF on the other hand, colchicine is in use as a treatment since decades. Even though colchicine does not display the two main disadvantages of the IL-1 β targeting treatments as it can be administered orally and the price is considerably lower, it still has some disadvantages. First, it only exhibits a very narrow therapeutic window with possibly debilitating side effects and secondly some patients are unresponsive to colchicine. Furthermore, the mechanism by which it ameliorates symptoms in FMF patients is poorly understood^{229–233}. Therefore, the need for safe, easily administrable and affordable treatments for these diseases persists.

Additionally, more and more data accumulate indicating that aberrant NLRP3 inflammasome activation is involved in multiple inflammatory diseases like diabetes, Alzheimers disease or gout^{325–328}. Novel work even implied obesity-induced NLRC4-dependent IL-1 β in breast cancer progression³²⁹. Thus, small-molecule inhibitors of inflammasomes would provide an alternative to the established treatments. Recently, two small-molecule inhibitors of the NLRP3 inflammasome were described. Both, β -hydroxybutyrate and MCC950 selectively inhibit NLRP3 activation while they did not influence AIM2 or NLRC4 activation^{330,331}. Yet, whether any of the two compounds or derivatives thereof will ever be approved for clinical use in humans is not known.

Additional lead compounds would enhance the chance of bringing a new drug onto the markets. Small molecules could also help to further elucidate the mechanisms by which inflammasomes are regulated and, in the case of NLRP3, activated. Thus, we performed a screen for small molecule inhibitors of ASC speck formation in immortalized BMDMs and an *in vitro* screen for inhibitors of ASC^{PYD} oligomerization. The goal of the screen was to find compounds that specifically inhibit ASC oligomerization and

would therefore reduce IL-1 β secretion irrespective of the activated receptors.

Statement of contribution

The full screen was done in collaboration with Lorenzo Sborgi and Johanna Ude of the group of Prof. Sebastian Hiller at the Biozentrum and performed with the BSF (Biomolecular Screening Facility) at EPFL (Ecole Polytechnique Federale Lausanne). I set up the initial protocol and performed the laboratory part of the screen in immortalized BMDMs at the BSF while Fabien Kuttler of the BSF improved the protocol for the high throughput screen as well as established and performed the image acquisition and analysis. The *in vitro* screen was entirely done by Lorenzo Sborgi, Johanna Ude and the BSF team.

Materials and methods

The screening cell lines was an *Asc* deficient immortalized BMDM cell line constitutively expressing an ASC-mCherry fusion protein and being a functional (CRISPR) knock-out for *Casp1*. This cell line was generated during the work for research article II and published therein³²². As the read out for the screen was formation of ASC specks, a cell line expressing an ASC-mCherry fusion protein was chosen as this allowed skipping the time and cost intensive staining step for ASC. The deficiency in caspase-1 was chosen to enable an accumulation of cells with an ASC speck as these cells did not die and detach through pyroptosis efficiently providing a higher dynamic range. The cells were cultured in DMEM (Dulbecco's modified Eagle's medium, Sigma) supplemented with 10% FCS (fetal calf serum) and 10% 3T3-MCSF (macrophage colony-stimulating factor) supernatant at 37 °C with 5% CO₂. Compounds were distributed in 384-well plates in duplicates in DMSO (dimethyl sulfoxide) at a final concentration of 10 μ M. DMSO alone served as negative control while MCC950³³⁰ served as positive control for blocking NLRP3 dependent ASC specks. 10'000 cells/well were seeded in 40 μ L using the Multidrop Combo dispenser (Thermo). The next day, 10 μ L/well LPS O55:B5 in medium was dispensed to get a final concentration of 100 ng/uL followed by 10 sec shaking for a better distribution of the LPS. After 4 h, 10 μ L/well ATP (pH 7.0 in PBS [phosphate buffered saline]) was dispensed per well for a final concentration of 5 mM followed by 30 sec shaking. After 3.5 h, the cells were fixed with 4% PFA (final concentration, Sigma) and concomitantly stained with 2.5 μ g/mL Hoechst (final concentration) for 30 min at room temperature. Plates were washed three times with 1x PBS and im-

aged using an automated microscope (GE Healthcare) with a 10x objective, 2x binning and acquiring 4 images/well of both channels, ASC specks (red) and cell nuclei (blue). Image analysis was done using CellProfiler and the percentage of cells containing an ASC speck was calculated. In parallel, the reduction of absolute cell numbers served as measurement for the toxicity of the compounds.

Results and discussion

The first screen was done using the Prestwick Chemical Library (<http://www.prestwick-chemical.com/prestwick-chemical-library.html>). It consists of 1280 compounds which are all approved for human use by administrations. The relative small size (eight 384-well plates, including 32 wells per plate for the positive and 32 wells for the negative control) of the library allowed for a proof of concept of the screen and showed that hits can be found. The initial threshold to consider a compound as a hit was a relative reduction of speck formation by 25% compared with DMSO (negative control, 0% speck reduction) and MCC950 (positive control, 100% relative speck reduction). Using this, a total of 60 compounds were considered to be hits (**Fig. 2.2**). However, most of the hits were detected due to a strong reduction of cell numbers of more than 66.6%. Only 15 compounds diminished cell numbers by less than 33.3%. While many of the compounds have no existing links to inflammasomes, there are some hits which were previously described to inhibit the NLRP3 inflammasome.

Ebselen lead to a reduction of speck formation by approximately 30% in the screen. It acts as hydrogen peroxide scavenger and was shown to inhibit NLRP3 inflammasome dependent IL-1 β release^{153,332}. The strongest hit of the Prestwick Chemical Library was auranofin (**Fig. 2.2**). Auranofin is a thioredoxin reductase inhibitor, inhibits the NLRP3 pathway³³³ and it is used to treat rheumatoid arthritis, an inflammatory disease with a known involvement of the NLRP3 pathway^{334,335}. Additionally, multiple members of the glucocorticoid family (betamethasone, prednisolone, fluticasone, isoflupredone, lumethasone pivalate) were detected as hits. Glucocorticoids are regularly used to treat inflammatory conditions. They bind to the glucocorticoid receptor leading to pleiotropic anti-inflammatory effects. Amongst others, glucocorticoids inhibit NF- κ B signaling³³⁶. Blocking NF- κ B signaling prevents NLRP3 upregulation during the LPS-priming step^{134,135} thereby leading to the reduction of ASC specks observed with the glucocorticoid family members in this screen (**Fig. 2.2**).

Thus, our initial concerns about the effect of blocking NF- κ B signaling on speck formation were confirmed. This might be circumvented by using a cell line constitutively expressing NLRP3 thereby overcoming the necessary LPS priming step. A more sophisticated approach could use the inducible expression of constitutive active receptors. This would allow to use not only ATP as an NLRP3 trigger, but also using CAPS associated NLRP3 mutants and other receptor mutants like FMF associated Pyrin mutants or LRR deficient NLRC4, which were shown to be constitutively active²⁴¹. A problem with this approach could be the need for *de novo* protein expression for inflammasome activation opening up the possibility of finding other, inflammasome unrelated hits. This might be circumvented by using co-expression of the receptor with a fluorophore from the same promoter. All conditions where cells failed to induce fluorophore expression would be disregarded as these compounds would block protein expression and would therefore not be specific for inflammasome activation and speck formation.

In conclusion, the proof of concept screen was successful as known inhibitors were found and blocking NF- κ B signaling had an effect as well. So far, no new inhibitor was found to be equally effective as MCC950 and non-toxic, but additional libraries will be screened as well.

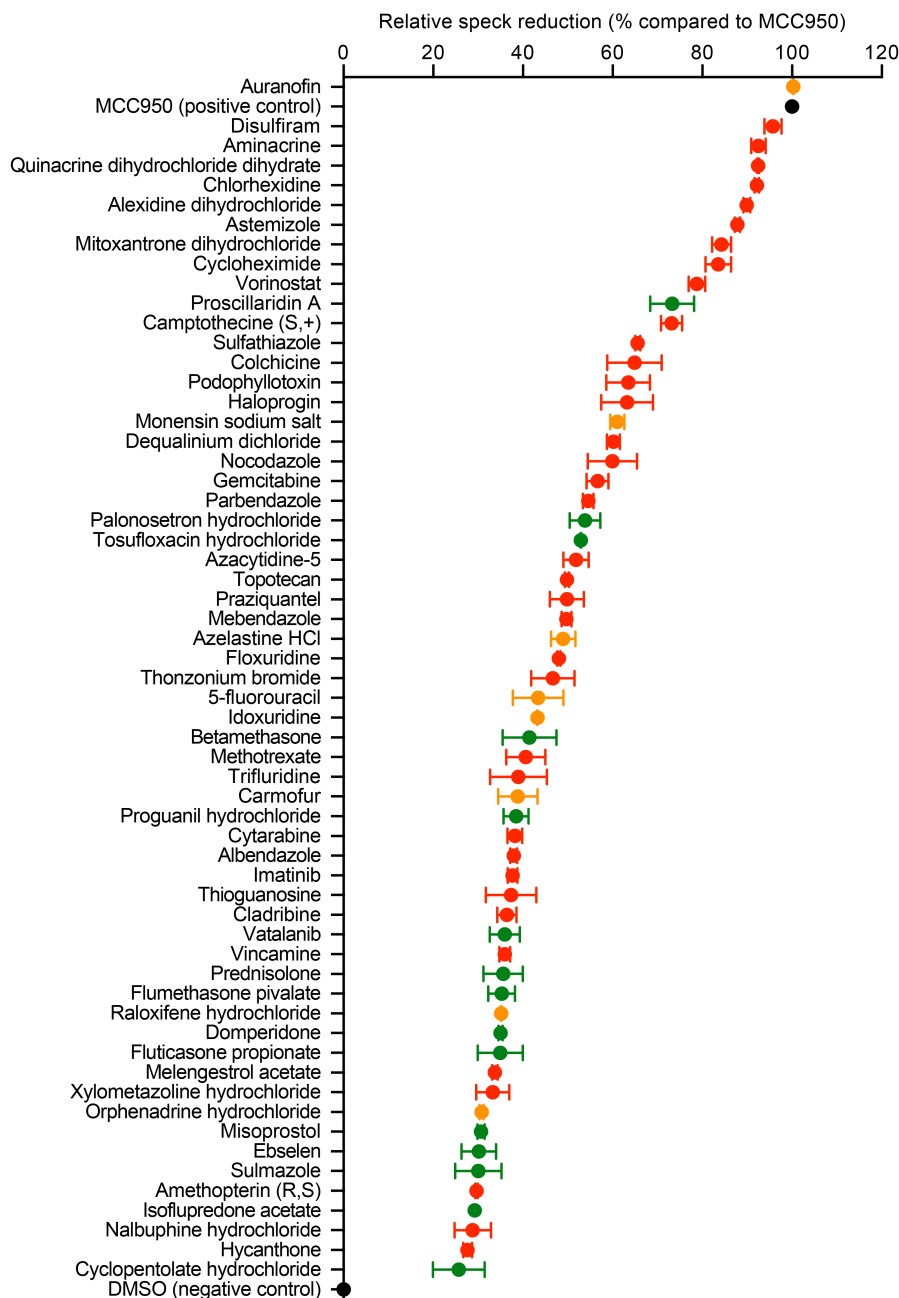


Figure 2.2: **Hits of the first screen with the Prestwick Chemical Library.** Relative reduction of speck numbers compared to the negative control DMSO (0%, black) and positive control MCC950 (100%, black). All compounds reducing the relative speck numbers by more than 25% were considered as hits. Colors correspond to the reduction of cell numbers by compounds, where green denotes $\leq 33.3\%$ reduction, orange 33.3%-66.6% reduction and red $\geq 66.6\%$ reduction. Data represent mean and s.d. of duplicate wells.

2.4 Generation and initial characterization of *Casp12* knock-out mice

Introduction

As outlined in the introduction (see above), caspase-12 is an inflammatory caspase closely related to caspase-1, murine caspase-11, human caspase-4 and human caspase-5. However, caspase-12 is comparably ill-characterized and conflicting reports regarding its role in inflammation and especially inflammasome signaling exist^{301,302,309–313}. Knock-out mice had previously been generated by disrupting the *Casp12* gene in 129SV mice embryonic stem cells, but were later shown to carry an inactivating passenger mutation in the neighboring *Casp11* gene, thus rendering them deficient in both caspases^{312,313}. Due to the conflicting reports of the physiological role of caspase-12, we set out to generate a new *Casp12* deficient mouse line employing the CRISPR-Cas9 system. The goal was to determine the role of murine caspase-12 in inflammasome signaling, elucidate its physiological role and hopefully shed light on the selective pressure driving the pseudogenization in humans.

Statement of contribution

The gRNA design and injection into murine embryos were done by Petr Broz and Pawel Pelczar of the Centre for Transgenic Models of the University Basel. I designed the breeding strategy, performed the sampling and sequencing of the offspring and performed the initial testing of BMDMs.

2.4.1 Materials and methods

Generation and genotyping of *Casp12* knock-out mice

gRNAs targeting exon 2 of the *Casp12* gene were designed using CRISPR Design (crispr.mit.edu) leading to the gRNA sequence (including PAM) atattatttttacagccaggagg. Injection of gRNAs and Cas9 protein into mouse embryos was done as described before³³⁷. Offspring were marked and samples taken for genotyping (toes) at an age of 10-12 days. DNA extraction was performed using the KAPA HotStart Mouse Genotyping Kit according to the manufacturers protocol (Kapa). Genotyping PCR was done with Q5

polymerase (NEB) according to the cycling protocol in **Tab. 2.1** using primers Oligo.482 (Casp12exon2FW2; aagccaggcagctagtttga) and Oligo.483 (Casp12exon2RV2; gggata-tggggaggtcagat), which were designed using Primer3 (<http://bioinfo.ut.ee/primer3-0.-4.0/338,339>) giving a fragment of 923 bp. The standard reaction contained 31 μL H_2O , 10 μL 5x Q5 polymerase buffer (NEB), 1 μL 10 mM dNTPs (Sigma), 2.5 μL of each primer (10 μM , Sigma), 1.5 μL DMSO (Sigma), 1 μL of the template and 0.5 μL Q5 polymerase (NEB). PCR samples were run on 1% agarose gels (Sigma), DNA was extracted from excised bands (Macherey-Nagel), and sequenced using Oligo.482 (Microsynth).

Table 2.1: *Casp12* genotyping PCR cycling program.

Step	Temp.	Time
Initialization	98°	2 min
Denaturation	98°	10 sec
Annealing	67°	20 min 35 x
Elongation	72°	23 sec
Final elongation	72°	2 min
Hold	4°	∞

Cell culture

BMDMs were cultured in DMEM (Sigma) supplemented with 10% FCS (Bioconcept), 20% 3T3-MCSF supernatant, penicillin/streptomycin (Bioconcept), non-essential amino acids (Bioconcept) and HEPES (4-(2-hydroxyethyl)-1-piperazineethanesulfonic acid, Bioconcept), and incubated at 37 °C with 5% CO_2 .

Inflammasome stimulation

Cells were seeded at 250'000 cells/mL in 96-well plates and primed with 100 ng/mL Pam3CSK4 (Invivogen) overnight. NLRP3 inflammasome activation was triggered by incubation with 20 μM nigericin (Invitrogen) for 60 min, the AIM2 inflammasome was triggered by transfection of 1 $\mu\text{g}/\text{mL}$ poly(dA:dT) (Invivogen) using 0.5 $\mu\text{L}/\text{well}$ Lipofectamine2000 (Invitrogen) in optiMEM (Gibco) for 2 h. The NLRC4 inflammasome was triggered by infection of the cells with *Salmonella enterica* serovar Typhimurium SL1344

at a multiplicity of infection of 10 for 60 min after a short centrifugation step (5 min, 1'000 rpm) to synchronize the infection. The non-canonical caspase-11 inflammasome was triggered by transfecting 200 ng LPS O111:B5 (Invivogen) per well using FuGene HD (Promega) according to the manufacturers instruction for 4 h.

Cell death and IL-1 β release measurements

IL-1 β release was measured by ELISA (enzyme-linked immunosorbent assay, eBio-sciences). Cell death was quantified by measuring LDH (lactate dehydrogenase) re-lease using the LDH Cytotoxicity detection kit (TaKaRa Clontech). To normalize for spontaneous cell lysis, the percentage of cell death was calculated as follows: [(LDH sample)-(LDH negative control)]/[(LDH positive control)-(LDH negative control)]x100.

2.4.2 Results and discussion

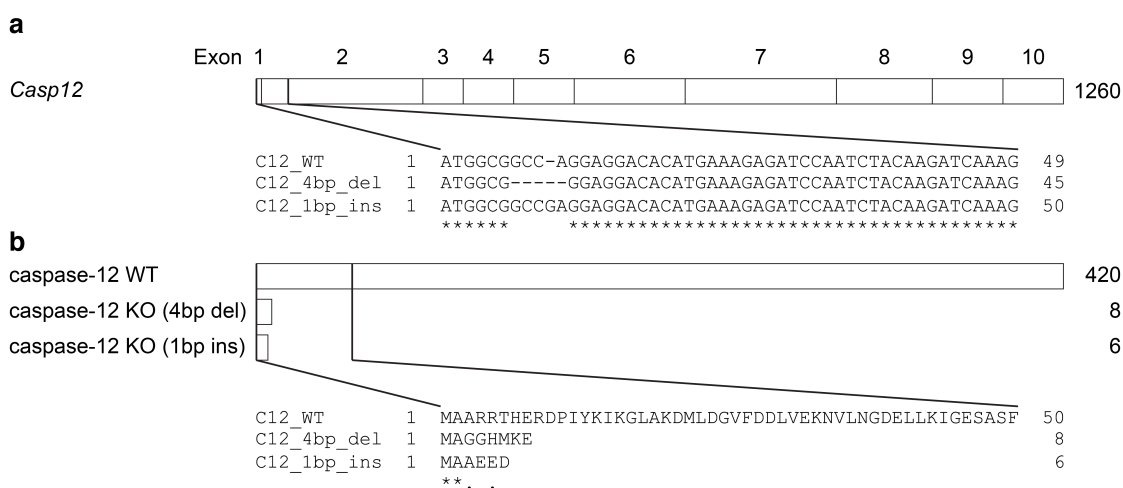


Figure 2.3: **Alignments of mutant *Casp12* alleles generated by CRISPR-Cas9.** (a) Exon structure of *Casp12* (1260 bp, drawn to scale) with the alignment of the section targeted by CRISPR-Cas9 of wild type *Casp12* and the two targeted knock-out alleles. (b) Schematic representation of the wild type caspase-12 protein (420 amino acids) and the two hypothetical caspase-12 KO proteins (8 and 6 amino acids, respectively) with the alignments of the respective amino acid sequences. Alignments performed using T-Coffee (<http://www.ebi.ac.uk/Tools/msa/tcoffee/>^{72,73,340}).

The gRNA and Cas9 protein injection into oocytes at the Center for Transgenic Mod-

els of the University of Basel (www.ctm-basel.ch) yielded two different animals with a targeted *Casp12* sequence. These animals were transferred to the breeding facility of the Biozentrum/Pharmazentrum and mated with wild type C57BL/6J mice. One of the animals had a 4 base pair deletion and the other a 1 base pair insertion in exon 2 of *Casp12* on one allele (**Fig. 2.3a**). Both mutations lead to a premature stop codon and a considerably shortened hypothetical transcript (**Fig. 2.3b**). Offspring of the first animals were further crossed in order to establish a homozygous knockout line harboring a 4 base pair deletion in exon 2.

To test the involvement of caspase-12 in inflammasome signaling, BMDMs were generated from *Casp12*^{+/+}, *Casp12*^{+/-} and *Casp12*^{-/-} animals and subjected to NLRP3, AIM2, NLRC4 as well as non-canonical caspase-11 activation. The results suggested that ablation of caspase-12 expression did influence neither canonical NLRP3 (**Fig. 2.4a**), AIM2 (**Fig. 2.4b**), NLRC4 (**Fig. 2.4c**) nor non-canonical caspase-11 (**Fig. 2.4d**) signaling, i.e. pyroptosis and IL-1 β release were unchanged compared to wild type cells. These preliminary findings are in accordance with a recent publication where the authors did not observe any difference in response to canonical inflammasome stimuli in BMDMs and only a small, but not significant, reduction in cytokine secretion upon LPS challenge or *Listeria monocytogenes* infection in *Casp12* deficient mice³¹³. However, bone marrow derived macrophages might not be the perfect model to study the role of caspase-12. Even though expression of caspase-12 can be induced up to 20 fold by LPS priming³¹³ other cell types might express higher levels of caspase-12, for example adipocytes or MEFs (mouse embryonic fibroblasts)^{311,312}. Also other phenotypes attributed to caspase-12, e.g. the role in ER-stress induced apoptosis^{300,307}, the involvement in resistance to *Plasmodium* or West Nile virus infections^{309,311} or the modulation of NOD and NF- κ B signaling^{309,310} require careful review since most studies have been done in either overexpression systems or *Casp11/Casp12*-double deficient mice. Furthermore, the role of caspase-12 during infections with *S. Typhimurium* or *F. novicida* *in vivo* remains to be investigated.

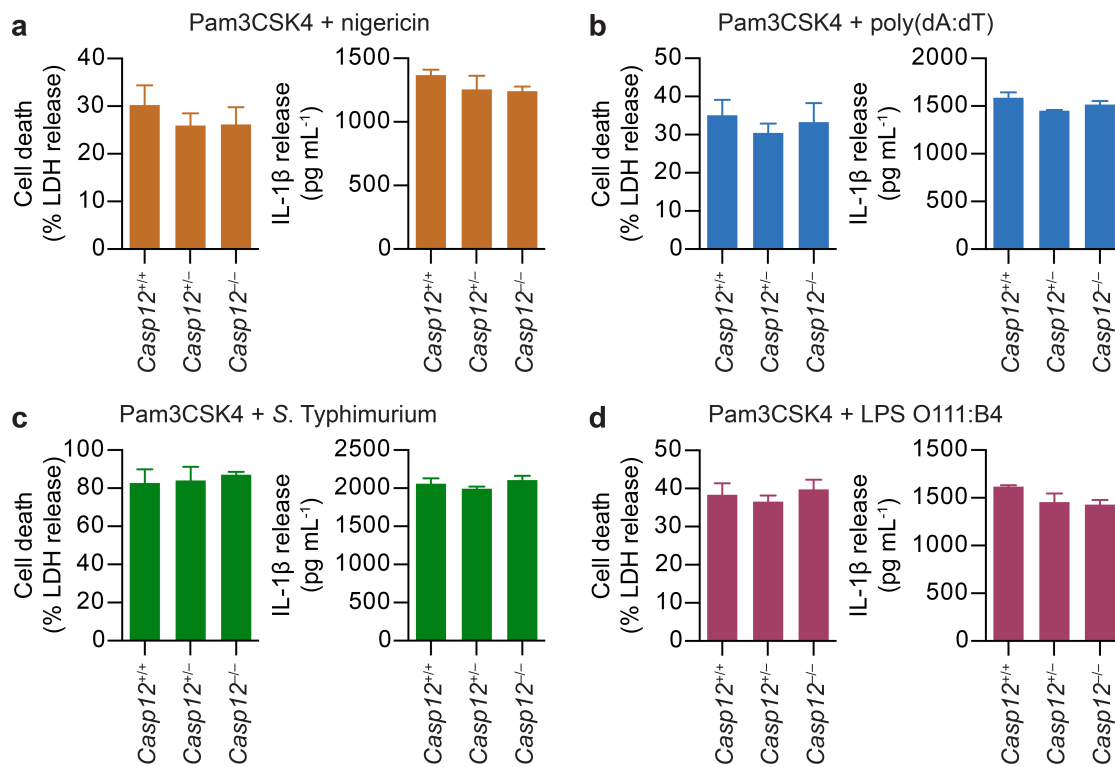


Figure 2.4: **Caspase-12 is not involved in canonical and non-canonical inflammasome signaling in murine BMDMs.** (a-d) Release of LDH (assessing cell death) and IL-1 β from Pam3CSK4 primed *Casp12*^{+/+}, *Casp12*^{+/-} and *Casp12*^{-/-} BMDMs 1 h after nigericin treatment (20 μ M, [a]), 2 h after poly(dA:dT) transfection (1 μ g/mL [b]), 1 h after infection with *S. Typhimurium* MOI 10 (c) or 4 h after transfection of LPS O111:B4 (1 μ g/mL [d]). Data are representative of two (a-c) or three (d) independent experiments. Graphs show the mean and s.d. from quadruplicate wells.

2.5 Generation of *Gsdmd* knock-out mice and involvement of gasdermin-D in IL-1 β secretion

Introduction

Recent publications^{30,31} showed that gasdermin-D plays a central role in pyroptosis downstream of active caspase-1 and that caspase-1 cleaves and activates gasdermin-D. The active gasdermin-D N-terminal fragment then forms a pore in the plasma membrane which is theoretically large enough to accommodate the secretion of IL-1 β and IL-18³¹⁷. However, there is no experimental evidence so far that gasdermin-D constitutes the pore through which mature IL-1 β or IL-18 is released. Therefore, we set out to create a *Gsdmd* deficient mouse line to further study the role and function of gasdermin-D and to elucidate whether it constitutes an IL-1 β permissive pore. As for *Casp12* (see above) the mouse line was generated using the CRISPR-Cas9 system at the Centre for Transgenic Models of the University of Basel.

Statement of contribution

The gRNA injection into murine embryos was done by Pawel Pelczar at the Centre for Transgenic Models of the University Basel. I designed the breeding strategy, performed the sampling and sequencing of the offspring and did the experiments presented here.

2.5.1 Materials and methods

Generation and genotyping of *Gsdmd* knock-out mice

gRNAs targeting exon 2 of the *Gsdmd* gene were designed as described³⁰ leading to gRNA sequence (including PAM) ggagaagggaaaatttctgg. Injection of the gRNAs and Cas9 protein into mouse embryos was done as described before³³⁷. Offspring were marked and samples taken for genotyping (toes) at an age of 10-12 days. DNA extraction was performed using the KAPA HotStart Mouse Genotyping Kit according to the manufacturer's protocol (Kapa). Genotyping PCR was done with Q5 polymerase (NEB) according to the cycling protocol in **Tab. 2.2** using primers Oligo.507 (GSDMD_ex2_fw2; gggtgtgagccaccgtctat) and Oligo.508 (GSDMD_ex_rv2; ctgtggagggactccattgt), which were designed using Primer3 (<http://bioinfo.ut.ee/primer3-0.4.0/>^{338,339}) giving a fragment of 768 bp. The standard reaction contained 31 μ L H₂O, 10 μ L 5x Q5 polymerase buffer (NEB), 1 μ L 10 mM dNTPs (Sigma), 2.5 μ L of each primer (10 μ M,

Sigma), 1.5 μ L DMSO (Sigma), 1 μ L of the template and 0.5 μ L Q5 polymerase (NEB). PCR samples were run on 1% agarose gels (Sigma), DNA was extracted from excised bands (Macherey-Nagel), and sequenced using Oligo.507 (Microsynth).

Table 2.2: *Gsdmd* genotyping PCR cycling program.

Step	Temp.	Time	
Initialization	98°	2 min	
Denaturation	98°	10 sec	
Annealing	68°	20 min	35 x
Elongation	72°	20 sec	
Final elongation	72°	2 min	
Hold	4°	∞	

Cell culture

BMDMs were differentiated in DMEM (Sigma) supplemented with 10% FCS (Bioconcept), 20% 3T3-MCSF supernatant, penicillin/streptomycin (Bioconcept), non-essential amino acids (Bioconcept) and HEPES (Bioconcept), and incubated at 37 °C with 5% CO₂. BMDCs (Bone marrow derived dendritic cells) were differentiated as described before³⁴¹. Red blood cells from the bone marrow were lysed with H₂O for 5 seconds before lysis was quenched with 10x PBS. The remaining cells were cultured in RPMI-1640 (Sigma) supplemented with 10% FCS (Bioconcept), HEPES (Bioconcept), penicillin/streptomycin (Bioconcept), 50 μ M β -mercaptoethanol (Sigma) and 20 ng/mL recombinant murine GM-CSF (granulocyte macrophage colony-stimulating factor, Peprotech), and incubated at 37 °C with 5% CO₂. The cells were fed with medium after 2 days and half the medium exchanged after 4 days. BMDCs were seeded after 6 or 8 days of differentiation.

Inflammasome stimulation

BMDMs were seeded at 250'000 cells/mL and BMDCs at 500'000 cells/mL in 96-well plates and primed with 100 ng/mL Pam3CSK4 (Invivogen) overnight. The NLRP3 inflammasome was triggered by incubation with 20 μ M nigericin (Invitrogen), the AIM2 inflammasome was triggered by transfection of 1 μ g/mL poly(dA:dT) (Invivogen) using 0.5 μ L/well Lipofectamine2000 (Invitrogen) in optiMEM (Gibco) for 1 h after a short cen-

trifugation (5 min, 1'000 rpm). The NLRC4 inflammasome was triggered by infection of the cells with *Salmonella enterica* serovar Typhimurium SL1344 at a multiplicity of infection of 10 for 60 min after a short centrifugation step (5 min, 1'000 rpm) to synchronize the infection process. The cytoprotectant glycine (Sigma) was added concomitantly to inflammasome stimulation at a final concentration of 5 mM. The NLRP3 pathway described by Underhill and colleagues¹⁵² was triggered by priming the BMDMs with 100 ng/mL LPS O55:B5 (Invivogen) for 3-4 h followed by treating the cells with 20 µg/mL peptidoglycan from *Staphylococcus aureus* (Sigma), *Bacillus subtilis* (Sigma) or *Streptomyces* sp. (Sigma) for 6 h after a short centrifugation (5 min, 1'000 rpm). Alternatively, *N*-acetylglucosamine (Roth) or sucrose (negative control, Sigma) were transfected using Lipofectamine2000 (Invitrogen) according to the manufacturers protocol using a final sugar concentration of 50 mM.

Cell death and IL-1 β release measurements

IL-1 β release was measured by ELISA (eBiosciences). Cell death was quantified by measuring LDH release using the LDH Cytotoxicity detection kit (TaKaRa Clontech). To normalize for spontaneous cell lysis, the percentage of cell death was calculated as follows: $[(\text{LDH sample}) - (\text{LDH negative control})] / [(\text{LDH positive control}) - (\text{LDH negative control})] \times 100$. Membrane permeabilization was quantified by incubating cells with 25 µg/mL PI (propidium iodide, Sigma) in HBSS (Hanks' balanced saline solution, Gibco) for 5 min on ice and measuring fluorescence emission at 617 nm (excitation at 530 nm). Cells lysed by one freeze-thaw cycle served as positive control. Wells without cells served as blank for the measurement. Percentage of PI positive cells was calculated as follows: $[(\text{treated cells} - \text{blank}) / (\text{positive control} - \text{blank})] \times 100$.

2.5.2 Results

The gRNA and Cas9 protein injection into oocytes at the Center for Transgenic Models of the University of Basel (www.ctm-basel.ch) yielded a single male animal with one WT allele and one targeted *Gsdmd* allele. This animal was transferred to the breeding facility of the Biozentrum/Pharmazentrum and mated with two wild type C57BL/6J females. The targeted *Gsdmd* allele had a 2 bp deletion in exon 2 (**Fig. 2.5a**). The mutation lead to a frame-shift resulting in a premature stop codon and thereby to a shortened hypothetical transcript (**Fig. 2.5b**). Offspring of this first animal were further crossed in order to establish a homozygous knockout line of *Gsdmd*. For functional analyses,

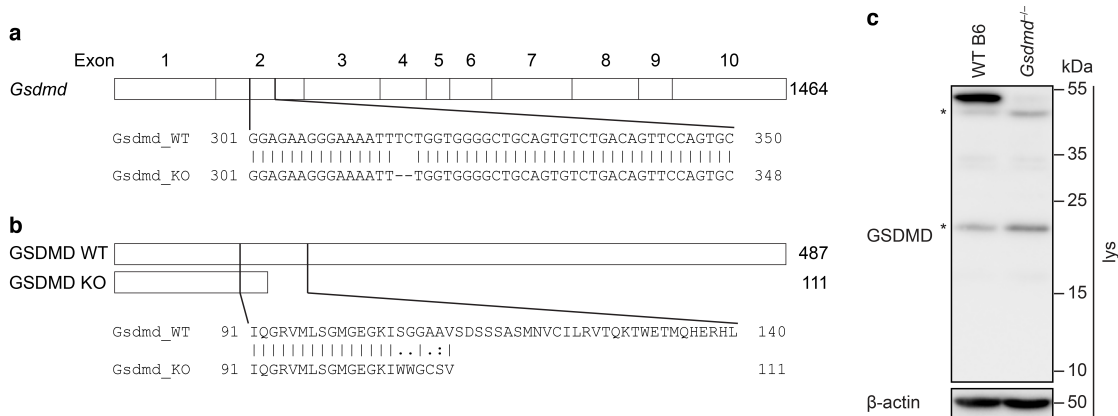


Figure 2.5: Comparison of wild type and *Gsdmd* knock out. (a) Exon structure of *Gsdmd* (1464 bp, drawn to scale) with alignment of the section targeted by the CRISPR-Cas9 of the *Gsdmd* knock-out allele with the *Gsdmd* wild type allele. (b) Schematic representation of the wild type gasdermin-D protein (487 amino acids) and the hypothetical gasdermin-D "knock-out" protein (111 amino acids, drawn to scale) with the alignment of the sections of wild type and "knock-out" gasdermin-D. (c) Western blot analysis of gasdermin-D expression in wild type and knock-out cells. Alignments performed using the EMBOSS (Nucleotide or Protein Alignment) Needle Tool (<http://www.ebi.ac.uk/Tools/psa/71-73>). Blot representative of three independent experiments. * denotes unspecific bands.

BMDMs were generated from homozygous knock-out animals. Western blotting confirmed successful ablation of gasdermin-D expression (**Fig. 2.5c**).

As expected^{30,31}, stimulation of the canonical inflammasome receptors AIM2 by poly(dA:dT) transfection (**Fig. 2.6a**), NLRC4 by *S. Typhimurium* infection (**Fig. 2.6b**) or NLRP3 by nigericin treatment (**Fig. 2.6c**) for short periods showed that gasdermin-D deficient cells were deficient in cell death induction (LDH release and PI uptake) and IL-1 β secretion, similar as caspase-1/-11 deficient cells.

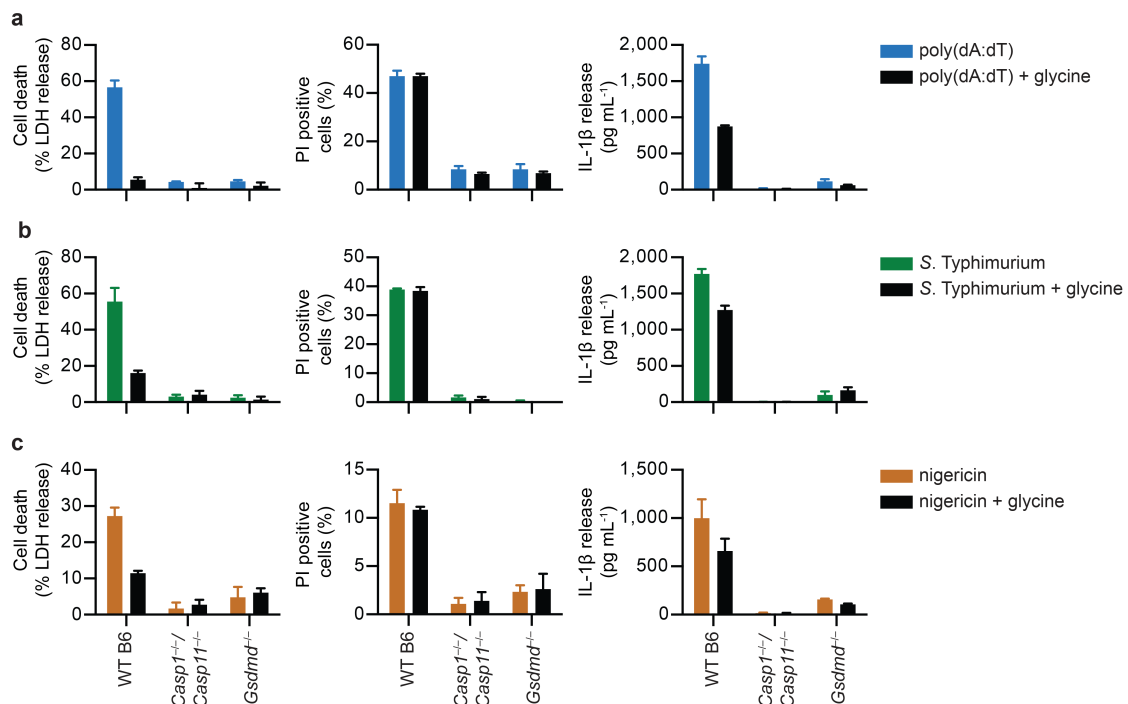


Figure 2.6: Canonical inflammasome activation in *Gsdmd*^{-/-} BMDMs. (a-c) Quantification of LDH release, PI uptake and IL-1 β release in presence or absence of glycine after stimulation of (a) AIM2 by poly(dA:dT) transfection (1 μ g/mL for 1 h), (b) NLRC4 by *S. Typhimurium* infection (MOI 10 for 1h), and (c) NLRP3 by treatment with nigericin (20 μ M for 1h). Graphs show means and s.d. from quadruplicate wells. Data are representative of three independent experiments.

The result showed that gasdermin-D was required not only for cell death, but also for cytokine release. The simplest explanation of this observation would be that lysis as a result of pyroptosis result in the unspecific release of the mature cytokine. On the other hand, IL-1 β release could also proceed through the gasdermin-D pore itself. To assess these possibilities, the cytoprotectant glycine was used³⁴². Glycine prevents

the cells from rupturing by preventing ion fluxes through non-specific leaks³⁴³. Indeed, extracellular glycine reduced the release of LDH considerably (**Fig. 2.6**) while it did not affect pore formation as PI incorporation was unaltered. Importantly, extracellular glycine reduced IL-1 β secretion only marginally. These results suggested that even though pyroptosis contributed to the release of IL-1 β , the largest part was released in a pyroptosis-independent manner, possibly through the gasdermin-D pore.

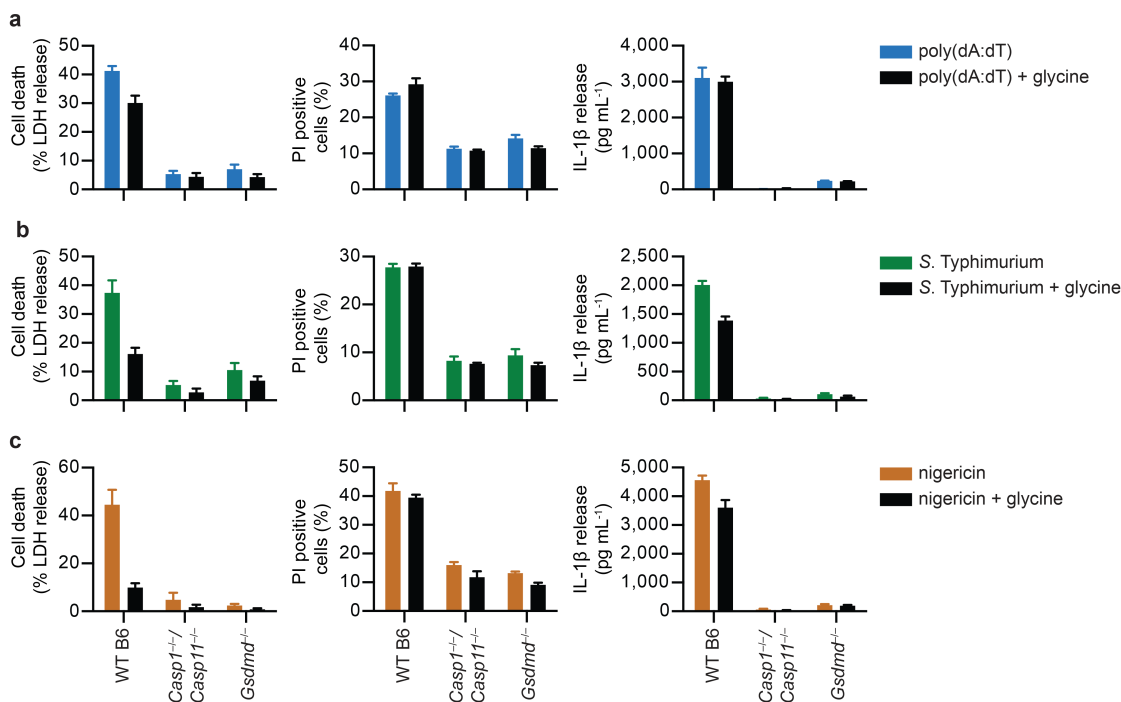


Figure 2.7: Canonical inflammasome activation in *Gsdmd*^{-/-} BMDCs. (a-c) Quantification of LDH release, PI uptake and IL-1 β release of bone marrow derived dendritic cells (BMDCs) in presence or absence of glycine after stimulation of (a) AIM2 by poly(dA:dT) transfection (1 μ g/mL for 1 h), (b) NLRP4 by *S. Typhimurium* infection (MOI 10 for 1h), and (c) NLRP3 by treatment with nigericin (20 μ M for 1h). Graphs show means and s.d. from quadruplicate wells. Data are representative of two independent experiments.

These observations can also be extended to bone marrow derived dendritic cells (BMDCs) (**Fig. 2.7**). Again, cell death, PI influx and IL-1 β release after stimulation of canonical inflammasome receptors were dependent on caspase-1/-11 and also largely dependent on gasdermin-D. Furthermore, blocking pyroptosis with glycine in wild type BMDCs did only partially reduce IL-1 β secretion while it strongly blocked LDH release, again suggesting a pyroptosis-independent IL-1 β release pathway in BMDCs.

To further substantiate the role of gasdermin-D in pyroptosis independent IL-1 β release, the involvement of gasdermin-D in the recently described atypical NLRP3 pathway was assessed¹⁵². Cytosolic N-acetylglucosamine derived from the peptidoglycan of gram-positive bacteria displaces hexokinase from the mitochondrial outer membrane leading to NLRP3 activation without the induction of pyroptosis¹⁵². Therefore, LPS primed WT B6, *Casp1*^{-/-}/*Casp11*^{-/-} and *Gsdmd*^{+/-} BMDMs were treated with peptidoglycan from different gram-positive bacteria, i.e. *Bacillus subtilis*, *Staphylococcus aureus* and *Streptomyces* sp. and the inflammasome signaling was analyzed (**Fig. 2.8a**). The response was not equal to all of the peptidoglycans and *S. aureus* peptidoglycan generally elicited the strongest response. LDH release levels as well as PI influx were generally low and the small responses detected were largely independent of caspase-1/caspase-11 or gasdermin-D. In comparison with published results¹⁵², the amounts of released IL-1 β were only small. Yet, it was clearly dependent on caspase-1/caspase-11 but independent of gasdermin-D. Very similar results were obtained if *N*-acetylglucosamine was transfected into BMDMs while transfection of sucrose did not elicit inflammasome activation (**Fig. 2.8b**). These results indicate that not gasdermin-D-dependent but other, lysis-independent, mechanisms are involved in IL-1 β release in this atypical NLRP3 inflammasome pathway. Possible, previously described, IL-1 β release mechanisms would be exosome shedding or microvesicular release of IL-1 β ³⁴⁴. Collectively, the results suggest that the generation of a *Gsdmd* deficient mouse line was successful and the cells derived thereof behave as expected. Furthermore, gasdermin-D seems to play a role in IL-1 β secretion beyond its role in pyroptosis. Yet, other gasdermin-D-independent IL-1 β release mechanism seem to exist.

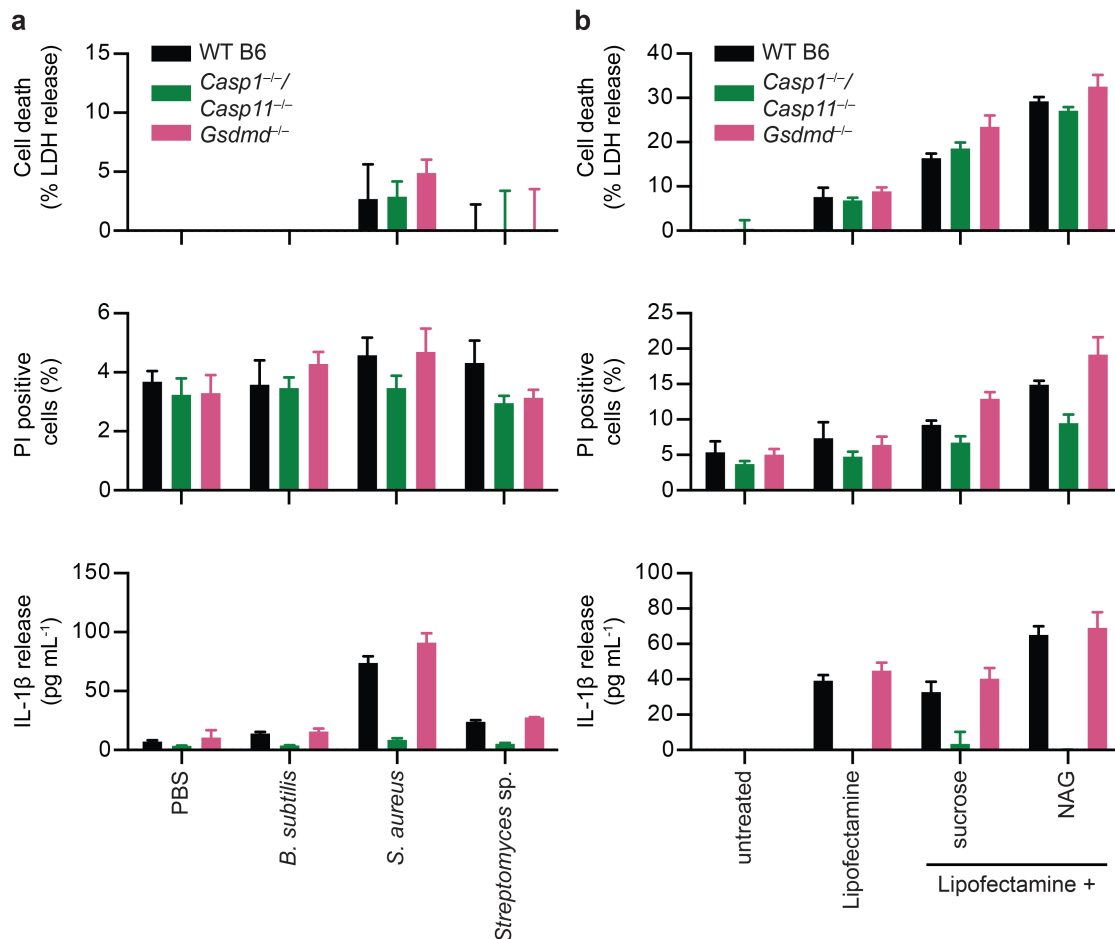


Figure 2.8: **Atypical NLRP3 inflammasome activation by PGN treatment or NAG transfection.** (a) Treatment of WT B6, *Casp1*^{-/-}/*Casp11*^{-/-} and *Gsdmd*^{-/-} BMDMs with peptidoglycans (PGN) from different gram-positive bacteria for 6 h. (b) Transfection of *N*-acetylglucosamine (NAG) or sucrose for 6 h with Lipofectamine2000. Graphs show means and s.d. of quadruplicate wells. Results are representative of two independent experiments.

3 Discussion and Outlook

Since the inception of the term inflammasome in 2002²⁸ immense advances were made regarding function, regulation and structure of inflammasomes^{23,24}. In parallel, it became more and more evident that inflammasomes, especially the NLRP3 inflammasome, do not only play pivotal roles in fighting infections but they are also important drivers of many non-communicable diseases like rheumatoid arthritis or gout^{345–347}. Still, many open questions regarding the underlying molecular mechanisms remain. In this work we elucidated the structure and signal transduction mechanism of the murine ASC speck, an important component of the inflammasome. Yet, most of the data presented in this thesis were already published and thus discussed in the respective articles (research article I and II^{321,322}). Therefore, in this section only further considerations regarding the results will be addressed.

How comparable is the structure of the ASC^{PYD} filament to other innate immunity-related filaments?

A common feature of proteins belonging to the death fold subfamilies is the ability to form higher order filaments and the structure has been solved for selected filaments of all subfamilies^{81,348–350}. However, not all filaments display the same architecture. While the human and murine ASC^{PYD} filaments are right-handed three-start helices^{81,321}, the short AIM2^{PYD} filaments and the caspase-1^{CARD} filaments are single-start helices^{100,194}. The AIM2^{PYD} filaments display a right-handed orientation and the caspase-1^{CARD} filaments display a left-handed orientation^{100,194}. The non-inflammasome filaments formed by the CARD of MAVS (mitochondrial anti-viral signaling), which is involved in antiviral signaling, or formed by the CARD of Bcl-10 (B-cell lymphoma 10), which is involved in NF- κ B signaling, display both a left-handed, single-stranded helical structure^{349,351}. A slightly different organization is presented by the tandem DEDs (death effector domain) of caspase-8 (caspase-8^{tDED}). Despite the low sequence conservation between the two caspase-8^{DEDs}, they take over quasi-equivalent roles in the filament. Even though always two subunits are covalently linked,

the parameters of the caspase-8^{tDED} filament are very similar to the ones of the ASC^{PYD} filament³⁵⁰.

Thus, even though the formation of helical filaments is a conserved feature of death fold domains, the proteins assemble in different conformations despite the similar tertiary structures of all death fold domains. As helical filaments are conserved, they must provide a clear evolutionary advantage. It has been suggested that filament formation serves to elicit a digital all-or-none signal amplification mechanism. This is in contrast to the gradual signal amplification by second messenger controlled mechanisms like the cGAS (cyclic GMP-AMP synthase) – cGAMP (cyclic guanosine monophosphate-adenosine monophosphate) – STING (stimulator of interferon genes) pathway^{352,353}. Filaments are assembled as soon as the stimulation reaches a certain threshold. This filament assembly then leads to signal amplification and the initiation of a downstream effect, for example caspase-1 activation in the case of ASC. Therefore, a small inflammatory stimulus could trigger an immense inflammatory reaction through filament-dependent signal amplification. The results from our structure-guided mutagenesis approach (research article II³²²) support this model.

Why is the ASC^{CARD} flexibly unfolded in the ASC filament structure?

The NMR structure determination of the ASC filament suggested that while the ASC^{PYD} forms the rigid filament backbone, the ASC^{CARD} is dynamically disordered on the outside of the filament (research article I³²¹). However, the structure of the monomeric, soluble ASC published by de Alba showed that only the linker is flexible but the ASC^{CARD} adopts, as the ASC^{PYD}, a defined tertiary structure⁷⁷. There are several possibilities why the ASC^{CARD} was not completely folded in the ASC filament in our structural analysis. First and foremost, the solution NMR spectra of monomeric ASC were recorded at an acidic pH in order to prevent ASC oligomerization⁷⁷ while we recorded the filament structure at a neutral pH. Thus, different pH could influence the structure of the ASC^{CARD}.

Alternatively, a partially folded ASC^{CARD} at a neutral pH might reflect the situation *in vivo*. In this scenario, the ASC^{CARD} would only adopt a fixed conformation upon binding of an interaction partner, i.e. another ASC^{CARD} or caspase-1^{CARD}. A completely different possibility would be that an only partially folded ASC^{CARD} reduces ASC^{CARD}/ASC^{CARD} interactions *in vivo* and thus keeps the ASC speck less dense (see below).

Lastly, the flexibly unfolded ASC^{CARD} in the ASC filament could constitute an *in vitro* artifact. The oligomerization conditions employed prior to structure determination might have been unfavorable for ASC^{CARD} folding and changing the conditions could support folding. Alternatively, a posttranslational modification might be required for proper ASC^{CARD} folding at neutral pH but not at acidic pH. Phosphorylation of human ASC^{CARD} Y146 (or Y144 in murine ASC) in a Syk and/or JNK dependent manner was shown to be important for speck formation after NLRP3 and AIM2 activation^{107–109}. This phosphorylation was absent *in vitro* as ASC was purified from *E. coli* for structure determination. A possibility to assess whether ASC^{CARD} phosphorylation is important for proper ASC^{CARD} folding would be the introduction of a phosphomimetic mutation in the ASC^{CARD}. Alternatively, ASC could be phosphorylated *in vitro* or purified from cells where this phosphorylation is taking place. Furthermore, the NMR structure determination could be done in presence of unlabeled caspase-1^{CARD} or ASC^{CARD} to check whether an interaction partner is required for complete ASC^{CARD} folding. The difficulty with the last approach is, however, the intrinsic propensity of CARDS to aggregate into filaments themselves^{86,100}. In any case, further experimental work is needed to clarify why the ASC^{CARD} is flexibly unfolded in the ASC filament *in vitro* and what the folding state of the ASC^{CARD} is *in vivo*.

How do CARD-containing receptors like NLRC4 initiate ASC speck formation?

The CARD-containing inflammasome receptors like NLRC4 or murine NLRP1b possess CARDS instead of PYDs as protein-protein interaction modules^{65,258}. Our results suggested that these receptors do not nucleate ASC^{PYD} filaments directly but rely on CARD/CARD interactions to recruit bridging ASC molecules which in turn nucleate ASC^{PYD} filaments (see Figure 7 of research article II³²²). Recently, Schmidt and colleagues also investigated this question but employed a different approach³⁵⁴. They expressed a fluorophore-tagged nanobody directed against the human ASC^{CARD} in the monocytic cell line THP-1. Their results show that the anti-ASC^{CARD} nanobody assembles along ASC filaments indicating that also in the case of NLRC4 activation ASC oligomerization is mediated via the ASC^{PYD}. Importantly, they also reached the conclusion that CARD-containing receptors require bridging or linking ASC molecules to nucleate ASC oligomerization. This process is functional even in the presence of the anti-ASC^{CARD} nanobody as only a few ASC molecules with free ASC^{CARDs} are required to interact with NLRC4 and initiate ASC^{PYD} filament formation³⁵⁴. Since they used a

human and we employed a murine system, the mechanism of ASC recruitment and filament initiation by CARD-containing receptors seems to be conserved.

An important question regarding speck initiation by CARD-containing receptors remains. One activated NAIP recruits 9-11 NLRC4 molecules together assembling a wheel-shaped complex with a 10-12 fold symmetry²⁴²⁻²⁴⁵. How is this 10-12 fold symmetry transformed into the three-start helix of the ASC^{PYD} filament?

One possibility would be that the NLRC4^{CARDs} recruit ASC^{CARDs} in an unstructured way thereby leading to a locally increased concentration of ASC^{PYDs} which auto-nucleate and form the filament. Another possibility is that only some of the NLRC4^{CARDs} take part in ASC recruitment. For example three or six NLRC4^{CARDs} would assemble into a disk- or filament-like structure to which ASC would be recruited via the ASC^{CARD}, initiating ASC^{PYD} filament formation. The third possibility would be that all NLRC4^{CARDs} participate in a short filament-like structure and ASC is recruited via its CARD to this short NLRC4^{CARD} filament. The observation that the presence of NLRC4^{CARDs} leads to an aggregation of two disk-like NAIP/NLRC4 structures²⁴⁴ suggests that NLRC4^{CARDs} are capable of interacting with each other, at least *in vitro*. Thus, it seems unlikely that only some NLRC4^{CARDs} are involved in ASC recruitment or that NLRC4^{CARDs} do not form any ordered superstructure favoring the third possibility. In any case, further experimental work is required. For example, one might reconstruct the NAIP/NLRC4 inflammasome *in vitro* in presence of full-length ASC, ASC^{CARD} only or ASC^{CARD} mutants that are not able to interact with themselves anymore but still with the NLRC4^{CARD}. Structure determination with these extended NAIP/NLRC4 complexes might shed light on the organization of the NLRC4^{CARD} in the receptor complex. Yet, again the propensity of CARDS and PYDs to auto-aggregate could impede such an approach.

Another open question is why both, CARD- and PYD-containing inflammasome receptors are present in the same organism? Evolutionary, the CARD seems to be older than the PYD as CARD-containing proteins along with DD (death domain)-containing proteins are present in *Drosophila melanogaster* and *Caenorhabditis elegans* while PYD- and DED-containing proteins appeared only later in zebrafish⁷⁴. Thus, the direct interaction between NLRC4 and caspase-1⁶⁵ seems to be evolutionary older than the interaction between PYD-containing receptors and ASC^{PYD}. This implies that PYD/PYD interactions in inflammasome signaling has evolved later and possibly surpassed CARD/CARD interactions for the largest part. This offers an explanation why more PYD-containing inflammasome receptors exist than CARD-containing receptors²⁴. The remaining CARD-containing receptors like NLRC4 might have survived due to a specific

selective advantage. It might be possible that the direct NLRC4/caspase-1 interaction, which only leads to pyroptosis but not cytokine maturation and release⁶⁴, provides a sufficient defense mechanism in some cases. Alternatively, distinct expression patterns of the different inflammasome components could be a reason for the retention of CARD-containing receptors. Some cell types might only express NLRC4 and caspase-1 but not NLRP3 or ASC. Thus, these cells would still be able to fight infections elicited by some bacteria but would not release IL-1 β and possibly confine the ensuing inflammation locally.

What are the advantages of an ASC speck compared to ASC filaments?

Our results presented in research article II³²² put forth a model in which the ASC speck is formed by ASC^{PYD} filaments, which are bound together by ASC^{CARDs}. Using the expression of the human anti-ASC^{CARD} nanobody, Schmidt and colleagues³⁵⁴ proposed the same model of how the ASC speck is built up. As they investigated the human and we investigated the murine system, the results suggest that the architecture of the ASC speck is conserved amongst mammals. Even in various fish species, the most distantly related animals expressing an ASC homologue, ASC is able to oligomerize into speck-like structures^{355–358}. Thus, it seems that speck formation is an intrinsic property of all ASC homologues.

But why did ASC evolve to form the dense specks and not just filaments? One possibility would be to increase the local concentration of caspase-1 more than what would be possible with filaments alone. But would that even be required? It was reported that the caspase-1^{CARD} is able to form filaments itself, at least *in vitro*, which would increase the local concentration of caspase-1 by itself^{81,100}. Additionally, it was shown that there is at least 3.5-fold more caspase-1 in the ASC speck than ASC itself⁸¹. Yet, the ASC speck is also formed in absence of caspase-1 that speck formation is an intrinsic property of ASC⁶⁴. Therefore, it seems that there would be more space for caspase-1^{CARD} filaments if ASC formed only filaments instead of specks and this could in turn lead to a more active caspase-1. Yet, there has to be an evolutionary reason why specks are favored over filaments.

So far it is not clear to what extent caspase-1^{CARD} filaments are formed in cells and whether ASC filaments would be more efficient in caspase-1 activation than the ASC speck itself. To test whether ASC speck formation is required for inflammasome signaling, a similar approach than we used for the ASC^{PYD} might be employed. Point muta-

tions in the ASC^{CARD} might be found which abrogate ASC^{CARD}/ASC^{CARD} interactions and thus ASC speck formation^{86,322}, yet these mutants would need to be able to interact with the caspase-1^{CARD} as efficiently as wild type. As neither the ASC^{CARD}/caspase-1^{CARD} nor the ASC^{CARD}/ASC^{CARD} interactions are characterized, finding these mutations using a direct approach might prove difficult. Alternatively, a screen-like approach with a library of ASC^{CARD} mutants could be used. An example would be a two-step yeast-2-hybrid approach screening for retained interaction with caspase-1^{CARD} but loss of interaction with wild type ASC^{CARD}.

An approach to determine the presence of caspase-1 filaments in cells might be the expression of catalytic inactive caspase-1, which is expected to be retained in the ASC speck. Additionally, the ASC speck could be rendered less dense by introducing low levels of ASC^{CARD} mutants that interfere with ASC crosslinking thus allowing better observation of the ASC speck architecture^{86,322}. This would allow the detection of caspase-1 filaments by immunofluorescence or even high resolution microscopy.

If the long caspase-1^{CARD} filaments^{81,100} were *in vitro* artifacts, the ASC speck would indeed be required to increase the local concentration of caspase-1 to enhance its auto-activation. But if the caspase-1^{CARD} filaments were found in cells at physiological caspase-1 levels, they would increase caspase-1 concentrations on their own. But why having a speck in the latter case? It could either enhance caspase-1 activation more or be a consequence from the architecture of ASC. Speck formation would have evolved in parallel to the ASC/caspase-1 interaction and if ASC formation speck was at least not disadvantageous, it would have been retained during evolution. Yet, the truth might also lie somewhere in between and in any case, the relevance for caspase-1^{CARD} filaments *in vivo* needs to be determined before this question might be answered.

How is the inflammasome regulated on the level of ASC speck formation?

Our hypothesis that the ASC oligomerization is only required for cytokine processing but not for pyroptosis (research article II³²²) opens up some interesting theoretical possibilities for cell-intrinsic inflammasome regulation. If any of the proposed post-translational modifications on ASC, e.g. phosphorylation of Y144 (or Y146 in human ASC), blocked only ASC^{CARD}/ASC^{CARD} interactions but left the interaction with caspase-1 mostly intact, this would only block cytokine release but not pyroptosis. While the effect of missing ASC Y144 phosphorylation on IL-1 β processing and release is well documented^{107,108,227}, its effect on NLRP3 or AIM2 dependent cell death is not yet reported.

This leaves the possibility that pyroptosis is not affected. Thus, it might be possible that Syk-dependent ASC Y144 phosphorylation by Pyk2 is only required for cytokine processing but not pyroptosis.

Besides posttranslational modifications, POPs (pyrin only proteins) and COPs (CARD only proteins) can regulate inflammasome signaling, specifically IL-1 β secretion^{115,116}. But the mode of action of these two protein families is controversially discussed. This controversy probably originated from the use of different model systems or different overexpression levels. POP1 was initially proposed to enhance IL-1 β secretion but was later shown to block both NLRP3 dependent IL-1 β release and pyroptosis by interacting with ASC^{PYD} and thus blocking NLRP3/ASC interaction. This prevents ASC speck formation, caspase-1 recruitment and activation^{122,124}. POP1 also blocks AIM2 and NLRC4 dependent IL-1 β release¹²⁴ but the effect on AIM2 or NLRC4 dependent pyroptosis was not reported. Even though it is likely that AIM2-dependent pyroptosis is blocked as well, it is possible that AIM2-dependent pyroptosis is unchanged if the AIM2/ASC interaction is not blocked by POP1. The same is probably true for NLRC4-dependent pyroptosis as it can progress even in absence of ASC⁶⁴. If pyroptosis is not affected, two different mechanisms could be envisioned. First, POP1 could integrate into the ASC^{PYD} filament without obstructing filament formation yet increasing the distance between ASC^{CARDs} rendering them unable or at least less efficient in caspase-1 recruitment and activation. Therefore, only low levels of caspase-1 would be active and unable to effectively mature cytokines. The second possibility would be that POP1 blocks ASC^{PYD} oligomerization and this is the mechanism by which caspase-1 recruitment and activation is blocked. High resolution microscopy could provide an answer to this question as in the first case ASC filaments should be observed but not in the latter. The literature concerning the role of COPs is even more complicated than for POPs^{115,116}. The short isoform of CARD16 was reported to interact with ASC and caspase-1 and to promote the formation of caspase-1 filaments and therefore IL-1 β maturation¹¹⁹. Yet, it remains unknown how CARD16 could integrate into caspase-1^{CARD} filaments and promote caspase-1 activation while not separating the catalytic domains of caspase-1 too far apart for proximity-induced autocatalytic activation. A possibility would be that the ASC^{CARD}/CARD16 and CARD16/caspase-1^{CARD} interactions are stronger than ASC^{CARD}/caspase-1^{CARD} interactions. Therefore, CARD16 could promote the association of caspase-1 with the ASC speck in an adaptor-like manner. This would suggest that CARD16 facilitates the formation of caspase-1 filaments leading to more active caspase-1 and thus higher levels of mature IL-1 β . Yet, the authors did not investigate

the effect of CARD16 on pyroptosis¹¹⁹ but based on our results, it might be expected that CARD16 does not change pyroptosis as the levels of pyroptosis are largely independent of the levels of caspase-1 activation.

CARD17, also known as INCA (inhibitory CARD), was reported to interact with caspase-1^{CARD} and block formation of caspase-1^{CARD} filaments by a capping mechanism efficiently blocking IL-1 β maturation after NLRP3 activation, at least when CARD17 is overexpressed¹⁰⁰. This is in agreement with our results that blocking caspase-1 auto-processing leads to reduced levels of IL-1 β maturation (research article II³²²). Once again, the effect of CARD17 overexpression on pyroptosis was not reported leaving the possibility that it is not affected by CARD17.

Thus, the discrepancy of the requirement of ASC speck formation for cytokine maturation and pyroptosis might be important for cell-intrinsic inflammasome regulation. Especially POPs and COPs have the potential to differentially regulate cytokine secretion and pyroptosis, at least in humans and related primates. In rodents, which lack COPs and POPs, this role might be taken over by the various known ASC isoforms whose functions are only poorly characterized so far^{130,131}. But also humans have different ASC isoforms¹³¹ and therefore inflammasome regulation by ASC isoforms might represent a more ancient regulatory mechanism compared to the evolutionary younger COPs and POPs.

Collectively, regulation of ASC speck formation, may it be organ, tissue or time specific, could provide the host with a possibility to mitigate the potentially debilitating outcomes of prolonged inflammasome activation. However, the effects on pyroptosis by the various cell-intrinsic mechanisms are only poorly studied and thus warrant further investigations.

How could the function of the ASC speck affect treatment of inflammatory diseases?

The pivotal role of the ASC speck for generation of bioactive IL-1 β and IL-18 puts it forth as a possible drug target. Blocking ASC speck formation but not the interaction between ASC and the receptor by a drug could be expected to block IL-1 β release but not pyroptosis. The advantage of such a drug would lie in the receptor independence. It could potentially be used in NLRP3 associated diseases like CAPS (cryopyrin-associated periodic syndrome), gout or rheumatoid arthritis but also Pypin-associated FMF (familial Mediterranean fever), NLRC4 associated MAS (macrophage activation syndrome)

and even AIM2 associated psoriasis^{172,173,187,214,215,253–255}. Furthermore, pyroptosis was shown to be the main inflammasome-mediated innate immune effector mechanism against some bacterial infections, e.g. *S. Typhimurium*⁵⁰. Therefore, even long term use of such a drug, as required for the treatment of autoinflammatory disorders, is not expected to be associated with an increased risk of infection with *S. Typhimurium* and similar bacteria. A drug that is currently used in rheumatoid arthritis and CAPS patients is the IL-1 receptor antagonist anakinra. Anakinra treatment was, however, shown to be associated with an increased risk of infections with gram-positive bacteria, especially GAS (group A streptococcus)³²⁴. A potential drug targeting ASC speck formation would also block IL-1 β signaling systemically. Thus it might increase the risk for GAS infections similar to anakinra treatment.

An alternative approach would aim at finding a drug that specifically targets the interaction between ASC and a single receptor, e.g. NLRP3 that was shown to be involved in multiple different inflammatory diseases^{325–328}. Such a drug would block both, cytokine release as well as pyroptosis after activation of a specific receptor. But it would not impair the function of any other inflammasome receptor leaving them capable of fighting infections. The disadvantage of such an approach would be that every receptor would need its specific inhibitor thus increasing cost and time for development of new and efficient therapies.

Does gasdermin-D form the pore through which IL-1 is released?

It was recently shown that gasdermin-D is the central executioner of canonical and non-canonical pyroptosis^{30,31}. The active N-terminal domain of gasdermin-D is able to insert itself into the plasma membrane and form a pore consisting of 16-24 monomers with a diameter of approximately 15 nm^{317–319}. Furthermore, in absence of gasdermin-D neither caspase-1 nor the biologically active IL-1 β and IL-18 are released from the cell^{30,31}. This was also confirmed by our experiments with *Gsdmd* deficient macrophages and dendritic cells. However, whether IL-1 β is released unspecifically by pyroptosis, i.e. during cell bursting, or specifically through the pore formed by gasdermin-D is not yet known. In favor of the latter speaks the fact that the pore formed by gasdermin-D is large enough to facilitate the crossing of IL-1 β and IL-18 with diameters of approximately 4.5 nm³¹⁷ but direct experimental evidence was missing so far.

We used the cytoprotectant glycine in the cell medium to prevent pyroptosis and thereby

pyroptosis-dependent IL-1 β release^{342,343}. Glycine did not diminish IL-1 β release but significantly decreased the levels of pyroptosis suggesting that IL-1 β release was independent of cell lysis. This was further substantiated by the fact that IL-1 β was released from vesicles through a gasdermin-D pore *in vitro* (Lorenzo Sborgi, personal communication) and that neutrophils, which did not show caspase-1 dependent pyroptosis, released IL-1 β in a gasdermin-D dependent manner (Etienne Meunier and Rosalie Heilig, personal communication). It is, however, clear that pyroptosis also lead to unspecific release of processed IL-1 β along with the cytosolic contents. Recently, an atypical NLRP3 pathway was described¹⁵². Cytosolic *N*-acetylglucosamine from gram-positive bacteria leads to dissociation of hexokinase from the mitochondria leading to activation of NLRP3. This pathway only leads to the release of IL-1 β but not pyroptosis¹⁵². Our results showed that IL-1 β release after atypical NLRP3 activation was independent of gasdermin-D clearly suggesting additional IL-1 β release mechanisms.

Collectively, our experimental evidence supports a model in which the gasdermin-D pore is able to facilitate IL-1 β and probably IL-18 secretion. However, direct experimental confirmation in cells is still missing. Furthermore, many open questions remain: How specific is the gasdermin-D pore and how is this specificity established? Does the gasdermin-D pore only release IL-1 β and IL-18, all IL-1 family cytokines, other cytokines or even everything below a certain size? Are pores formed by other gasdermin family members able to facilitate IL-1 β secretion? Is this process reversible? What are the signals and proteases activating and cleaving other gasdermin family members? Is the late, gasdermin-D independent cell death and IL-1 β release after activation of canonical inflammasomes described by Kayagaki and colleagues³⁰ dependent on another gasdermin pore? Why did multiple IL-1 β release mechanisms evolve and what is the purpose of them? And how important is IL-1 β release through the gasdermin-D pore *in vivo*?

Some of these questions might be easily addressed experimentally. The specificity of the gasdermin-D pore but also the ability of other gasdermins to release IL-1 β could be addressed in a liposome release assay *in vitro*. Additionally, the released cellular contents by the gasdermin-D pore could be assessed by Western blot or mass spectrometry. This should be done in presence and absence of glycine assessing the release via pores versus nonspecific lysis. Furthermore, the established *Gsdmd* deficient mouse line enables the elucidation of the role of gasdermin-D *in vivo* during bacterial infections.

What are the technical limitations of the approaches presented here and how could they be overcome?

We performed most of the experiments with a classical retroviral expression system in immortalized bone marrow derived macrophages using fluorescently labeled proteins. Thus, our model system offered an improvement over inflammasome reconstitution systems used in many previous studies^{79–81,85,86} as we only needed to manipulate the expression of a single component of the inflammasome while keeping all other proteins at physiological levels. Yet, there are shortcomings associated with every model system employed in biological sciences.

A first limitation comes from the fluorophore tag itself. Using fluorophore tags on ASC poses the risk of interfering with the native function of ASC and presented us some difficulties regarding degradation of the fluorophore tags. To circumvent this, small epitope-tags like HA (hemagglutinin) or V5 could reduce the risks of protein degradation and interference with protein function.

A second limitation comes from the retroviral expression system. Retroviral constructs integrate randomly and with multiple copies into the genome frequently leading to overexpression of the protein³⁵⁹. With the emergence of the CRISPR-Cas9 system it became feasible to introduce mutations or epitope-tags in the native locus thus leaving expression levels unchanged³⁶⁰. Currently, the efficiency of CRISPR-Cas9 mediated mutations is relatively low resulting in a time consuming process to set up and confirm mutated cell lines. The best approach to overcome classical retroviral expression systems would be a transgenic mouse model. However, setting up a mouse model requires even more time and is associated with high costs.

However, in a fast moving field time is always an issue and using a model system which can be set up relatively quick is advantageous. In any case, the model system chosen for our work proved to be efficient and reliable enough as a completely different approach corroborated parts of our results³⁵⁴.

4 Acknowledgments

The work on this PhD thesis was carried out in the lab of Prof. Dr. Petr Broz at the Biozentrum of the University of Basel, Switzerland.

First, I would like to thank my PhD advisor, Prof. Dr. Petr Broz for the opportunity to work on this exciting topic and his constant support, interesting discussions, his courage to take me as his first PhD student and the introduction to the field of innate immunity.

I am also grateful to our collaborators in structural biology, especially Prof. Dr. Sebastian Hiller, who was part of my PhD advisory committee and gave valuable input to the project, and Dr. Lorenzo Sborgi, without whose support my work would not have been possible. I am also thankful towards the people at the Biomolecular Screening Facility at EPFL, especially Dr. Fabien Kuttler for his help in setting up and performing the inflammasome inhibitor screen.

Furthermore, I thank Prof. Dr. Christoph Dehio for the discussions and input as a member of my PhD advisory committee.

I would like to thank Sebastian Rühl for his help with my first steps in the field of CRISPR and all other present and past members of the Broz Group, especially the initial Broz group members Dr. Etienne Meunier and Roland Dreier, but also Leonie Anton, Rosalie Heilig, Dr. José Vieira dos Santos, Kateryna Shkarina and Dr. Saori Yoshii for the great working environment, endless discussions and help whenever needed.

I also do want to mention the people who made working at the Biozentrum easier and let me focus on my research: Michaela Hanisch, Leonardo Faletti, Fatima Leite dos Reis, Marina Kuhn and Verena Heusner. Your support was always highly appreciated. Last but not least I would like to express my endless gratitude towards my family for their support through all the years and especially my girlfriend Kathrin for her support and understanding.

5 Bibliography

1. Shabbir, M. A. B. *et al.* Bacteria vs. bacteriophages: Parallel evolution of immune arsenals. *Frontiers in Microbiology* **7**, 1–8 (2016).
2. Flajnik, M. F. & Kasahara, M. Origin and evolution of the adaptive immune system: Genetic events and selective pressures. *Nature Reviews Genetics* **11**, 1–14 (2009).
3. Litman, G. W., Rast, J. P. & Fugmann, S. D. The origins of vertebrate adaptive immunity. *Nature Reviews Immunology* **10**, 543–53 (2010).
4. Boehm, T. Design principles of adaptive immune systems. *Nature Reviews Immunology* **11**, 307–317 (2011).
5. Buchmann, K. Evolution of innate immunity: Clues from invertebrates via fish to mammals. *Frontiers in Immunology* **5**, 1–8 (2014).
6. Irazoqui, J. E., Urbach, J. M. & Ausubel, F. M. Evolution of host innate defence: Insights from *Caenorhabditis elegans* and primitive invertebrates. *Nature Reviews Immunology* **10**, 47–58 (2010).
7. Kimbrell, D. A. & Beutler, B. The evolution and genetics of innate immunity. *Nature Reviews Genetics* **2**, 256–267 (2001).
8. Medzhitov, R. & Janeway, C. A. J. Innate immunity: The virtues of a nonclonal system of recognition. *Cell* **91**, 295–298 (1997).
9. Janeway, C. A. J. & Medzhitov, R. Innate immune recognition. *Annual Review of Immunology* **20**, 197–216 (2002).
10. Janeway, C. A. Approaching the asymptote? Evolution and revolution in immunology. *Cold Spring Harbour Symposium on Quantitative Biology* **54**, 1–13 (1989).
11. Brubaker, S. W., Bonham, K. S., Zanoni, I. & Kagan, J. C. *Innate immune pattern recognition: A cell biological perspective*. **1**, 257–90 (2015).
12. Takeuchi, O. & Akira, S. Pattern recognition receptors and inflammation. *Cell* **140**, 805–820 (2010).
13. Mogensen, T. H. Pathogen recognition and inflammatory signaling in innate immune defenses. *Clinical Microbiology Reviews* **22**, 240–273 (2009).
14. Sellge, G. & Kufer, T. A. PRR-signaling pathways: Learning from microbial tactics. *Seminars in Immunology* **27**, 75–84 (2015).
15. Land, W. G. The role of damage-associated molecular patterns in human diseases - Promoting inflammation and immunity. *Sultan Qaboos University Medical Journal* **15**, 9–21 (2015).

16. Schaefer, L. Complexity of danger: The diverse nature of damage-associated molecular patterns. *Journal of Biological Chemistry* **289**, 35237–35245 (2014).
17. Akira, S. & Takeda, K. Toll-like receptor signalling. *Nature Reviews Immunology* **4**, 499–511 (2004).
18. Beutler, B. A. TLRs and innate immunity. *Immunity* **113**, 1399–1407 (2009).
19. Jiménez-Dalmaroni, M. J., Gerswhin, M. E. & Adamopoulos, I. E. The critical role of toll-like receptors - From microbial recognition to autoimmunity: A comprehensive review. *Autoimmunity Reviews* **15**, 1–8 (2016).
20. Schlee, M. Master sensors of pathogenic RNA - RIG-I like receptors. *Immunobiology* **218**, 1322–1335 (2013).
21. Chen, G., Shaw, M. H., Kim, Y.-G. & Nuñez, G. NOD-like receptors: Role in innate immunity and inflammatory disease. *Annual Review of Pathology* **4**, 365–398 (2009).
22. Motta, V., Soares, F., Sun, T. & Philpott, D. J. NOD-like receptors: Versatile cytosolic sentinels. *Physiological Reviews* **95**, 149–178 (2014).
23. Von Moltke, J., Ayres, J. S., Kofoed, E. M., Chavarría-Smith, J. & Vance, R. E. Recognition of bacteria by inflammasomes. *Annual Review of Immunology*, 73–106 (2013).
24. Broz, P. & Dixit, V. M. Inflammasomes: Mechanism of assembly, regulation and signalling. *Nature Reviews Immunology* (2016).
25. Masumoto, J. *et al.* ASC, a novel 22-kDa protein, aggregates during apoptosis of human promyelocytic leukemia HL-60 cells. *Journal of Biological Chemistry* **274**, 33835–33838 (1999).
26. Hoss, F., Rodriguez-Alcazar, J. F. & Latz, E. Assembly and regulation of ASC specks. *Cellular and Molecular Life Sciences* (2016).
27. Thornberry, N. A. *et al.* A novel heterodimeric cysteine protease is required for interleukin-1 β processing in monocytes. *Nature* **356**, 768–774 (1992).
28. Martinon, F., Burns, K. & Tschopp, J. The inflammasome: a molecular platform triggering activation of inflammatory caspases and processing of proIL- β . *Molecular Cell* **10**, 417–26 (2002).
29. Fink, S. L. & Cookson, B. T. Apoptosis, pyroptosis, and necrosis: Mechanistic description of dead and dying eukaryotic cells. *Infection and Immunity* **73**, 1907–1916 (2005).
30. Kayagaki, N. *et al.* Caspase-11 cleaves gasdermin D for non-canonical inflammasome signaling. *Nature* **526**, 666–671 (2015).
31. Shi, J. *et al.* Cleavage of GSDMD by inflammatory caspases determines pyroptotic cell death. *Nature* **526**, 660–665 (2015).

32. Palomo, J., Dietrich, D., Martin, P., Palmer, G. & Gabay, C. The interleukin (IL)-1 cytokine family - Balance between agonists and antagonists in inflammatory diseases. *Cytokine* **76**, 25–37 (2015).
33. Dinarello, C. A., Renfer, L. & Wolff, S. M. Human leukocytic pyrogen: Purification and development of a radioimmunoassay. *Proceedings of the National Academy of Sciences of the United States of America* **74**, 4624–7 (1977).
34. Okamura, H. *et al.* Cloning of a new cytokine that induces IFN- γ production by T cells. *Nature* **378**, 88–91 (1995).
35. Dinarello, C. A. Immunological and inflammatory functions of the interleukin-1 family. *Annual Review of Immunology* **27**, 519–50 (2009).
36. Piccioli, P. & Rubartelli, A. The secretion of IL-1 β and options for release. *Seminars in Immunology*, 1–5 (2013).
37. Latz, E., Xiao, T. S. & Stutz, A. Activation and regulation of the inflammasomes. *Nature Reviews Immunology* **13**, 397–411 (2013).
38. Gurung, P. & Kanneganti, T. D. Novel roles for caspase-8 in IL-1 β and inflammasome regulation. *American Journal of Pathology* **185**, 17–25 (2015).
39. Keyel, P. A. How is inflammation initiated? Individual influences of IL-1, IL-18 and HMGB1. *Cytokine* **69**, 136–145 (2014).
40. Sims, J. E. & Smith, D. E. The IL-1 family: Regulators of immunity. *Nature Reviews Immunology* **10**, 89–102 (2010).
41. *Anakinra - DrugBank.ca* 2016.
42. Herper, M. *The world's most expensive drugs* 2010.
43. Kapur, S. & Bonk, M. E. Rilonacept (arcalyst), an interleukin-1 trap for the treatment of cryopyrin-associated periodic syndromes. *P & T* **34**, 138–41 (2009).
44. Boise, L. H. & Collins, C. M. *Salmonella*-induced cell death: Apoptosis, necrosis or programmed cell death? *Trends in Microbiology* **9**, 64–67 (2001).
45. Cookson, B. T. & Brennan, M. A. Pro-inflammatory programmed cell death. *Trends in Microbiology* **9**, 2001 (2001).
46. Lamkanfi, M. Emerging inflammasome effector mechanisms. *Nature Reviews Immunology* **11**, 213–20 (2011).
47. Jorgensen, I. & Miao, E. A. Pyroptotic cell death defends against intracellular pathogens. *Immunological Reviews* **265**, 130–142 (2015).
48. Chen, X. *et al.* Pyroptosis is driven by non-selective gasdermin-D pore and its morphology is different from MLKL channel-mediated necroptosis. *Cell Research*, 1–14 (2016).
49. LaRock, C. N. & Cookson, B. T. Burning down the house: Cellular actions during pyroptosis. *PLoS Pathogens* **9**, 1–3 (2013).

50. Miao, E. A. *et al.* Caspase-1-induced pyroptosis is an innate immune effector mechanism against intracellular bacteria. *Nature Immunology* **11**, 1136–1142 (2010).
51. Lamkanfi, M. *et al.* Inflammasome-dependent release of the alarmin HMGB1 in endotoxemia. *Journal of Immunology* **185**, 4385–4392 (2010).
52. Yang, H., Antoine, D. J., Andersson, U. & Tracey, K. J. The many faces of HMGB1: Molecular structure-functional activity in inflammation, apoptosis, and chemotaxis. *Journal of Leukocyte Biology* **93**, 865–73 (2013).
53. Doitsh, G. *et al.* Cell death by pyroptosis drives CD4 T-cell depletion in HIV-1 infection. *Nature* **505**, 509–14 (2014).
54. Fernandez, D. J. & Lamkanfi, M. Inflammatory caspases: Key regulators of inflammation and cell death. *Biological Chemistry* **396**, 193–203 (2015).
55. Sollberger, G., Strittmatter, G. E., Garstkiewicz, M., Sand, J. & Beer, H.-D. Caspase-1: The inflammasome and beyond. *Innate Immunity* **20**, 115–25 (2014).
56. Winkler, S. & Rösen-Wolff, A. Caspase-1: An integral regulator of innate immunity. *Seminars in Immunopathology* **37**, 419–427 (2015).
57. Black, R. A., Kronheim, S. R. & Sleath, P. R. Activation of interleukin-1 β by a co-induced protease. *FEBS Letters* **247**, 386–90 (1989).
58. Howard, A. D. *et al.* IL-1-converting enzyme requires aspartic acid residues for processing of the IL-1 β precursor at two distinct sites and does not cleave 31-kDa IL-1 α . *Journal of Immunology* **147**, 2964–2969 (1991).
59. Kostura, M. J. *et al.* Identification of a monocyte specific pre-interleukin 1beta convertase activity. *Proceedings of the National Academy of Sciences of the United States of America* **86**, 5227–5231 (1989).
60. Sleath, P. R., Hendrickson, R. C., Kronheim, S. R., March, C. J. & Black, R. A. Substrate specificity of the protease that processes human interleukin-1 β . *The Journal of Biological Chemistry* **265**, 14526–14528 (1990).
61. Agard, N. J., Maltby, D. & Wells, J. A. Inflammatory stimuli regulate caspase substrate profiles. *Molecular & Cellular Proteomics* **9**, 880–893 (2010).
62. Shao, W., Yeretssian, G., Doiron, K., Hussain, S. N. & Saleh, M. The caspase-1 digestome identifies the glycolysis pathway as a target during infection and septic shock. *Journal of Biological Chemistry* **282**, 36321–36329 (2007).
63. Denes, A, Lopez-Castejon, G & Brough, D. Caspase-1: Is IL-1 just the tip of the ICEberg? *Cell Death & Disease* **3**, e338 (2012).
64. Broz, P., von Moltke, J., Jones, J. W., Vance, R. E. & Monack, D. M. Differential requirement for Caspase-1 autoproteolysis in pathogen-induced cell death and cytokine processing. *Cell Host & Microbe* **8**, 471–483 (2010).
65. Poyet, J. L. *et al.* Identification of Ipaf, a human caspase-1-activating protein related to Apaf-1. *The Journal of Biological Chemistry* **276**, 28309–28313 (2001).

66. Broz, P. *et al.* Redundant roles for inflammasome receptors NLRP3 and NLRC4 in host defense against *Salmonella*. *The Journal of Experimental Medicine* **207**, 1745–1755 (2010).
67. Case, C. L., Shin, S. & Roy, C. R. Asc and Ipaf inflammasomes direct distinct pathways for caspase-1 activation in response to *Legionella pneumophila*. *Infection and Immunity* **77**, 1981–1991 (2009).
68. Mariathasan, S., Weiss, D. S., Dixit, V. M. & Monack, D. M. Innate immunity against *Francisella tularensis* is dependent on the ASC/caspase-1 axis. *The Journal of Experimental Medicine* **202**, 1043–9 (2005).
69. Masumoto, J., Taniguchi, S., Nakayama, K., Ayukawa, K. & Sagara, J. Murine ortholog of ASC, a CARD-containing protein, self-associates and exhibits restricted distribution in developing mouse embryos. *Experimental Cell Research* **262**, 128–133 (2001).
70. Masumoto, J. *et al.* Expression of apoptosis-associated speck-like protein containing a caspase recruitment domain, a pyrin N-terminal homology domain-containing protein, in normal human tissues. *Journal of Histochemistry & Cytochemistry* **49**, 1269–1275 (2001).
71. Rice, P., Longden, I. & Bleasby, A. EMBOSS: The European molecular biology open software suite. *Trends in Genetics* **16**, 276–277 (2000).
72. McWilliam, H. *et al.* Analysis tool web services from the EMBL-EBI. *Nucleic Acids Research* **41**, 597–600 (2013).
73. Li, W. *et al.* The EMBL-EBI bioinformatics web and programmatic tools framework. *Nucleic Acids Research* **43**, W580–4 (2015).
74. Kersse, K., Verspurten, J., Berghe, T. V. & Vandenabeele, P. The death-fold superfamily of homotypic interaction motifs. *Trends in Biochemical Sciences* **36**, 541–552 (2011).
75. Bertin, J. & DiStefano, P. S. The PYRIN domain: A novel motif found in apoptosis and inflammation proteins. *Cell Death & Differentiation* **7**, 1273–1274 (2000).
76. Liepinsh, E. *et al.* The death-domain fold of the ASC PYRIN domain, presenting a basis for PYRIN/PYRIN recognition. *Journal of Molecular Biology* **332**, 1155–1163 (2003).
77. De Alba, E. Structure and interdomain dynamics of apoptosis-associated speck-like protein containing a CARD (ASC). *The Journal of Biological Chemistry* **284**, 32932–41 (2009).
78. Masumoto, J., Taniguchi, S. & Sagara, J. Pyrin N-terminal homology domain- and caspase recruitment domain-dependent oligomerization of ASC. *Biochemical and Biophysical Research Communications* **280**, 652–655 (2001).
79. Moriya, M. *et al.* Role of charged and hydrophobic residues in the oligomerization of the PYRIN domain of ASC. *Biochemistry* **44**, 575–583 (2005).

80. Vajjhala, P. R., Mirams, R. E. & Hill, J. M. Multiple binding sites on the pyrin domain of ASC protein allow self-association and interaction with NLRP3 protein. *The Journal of Biological Chemistry* **287**, 41732–43 (2012).
81. Lu, A. *et al.* Unified polymerization mechanism for the assembly of ASC-dependent inflammasomes. *Cell* **156**, 1193–1206 (2014).
82. Oroz, J., Barrera-Vilarmau, S., Alfonso, C., Rivas, G. & de Alba, E. ASC pyrin domain self-associates and binds NLRP3 protein using equivalent binding interfaces. *Journal of Biological Chemistry* **291**, jbc.M116.741082 (2016).
83. Richards, N. *et al.* Interaction between pyrin and the apoptotic speck protein (ASC) modulates ASC-induced apoptosis. *The Journal of Biological Chemistry* **276**, 39320–39329 (2001).
84. Kersse, K., Lamkanfi, M., Bertrand, M. J. M., Vanden Berghe, T. & Vandenabeele, P. Interaction patches of procaspase-1 caspase recruitment domains (CARDs) are differently involved in procaspase-1 activation and receptor-interacting protein 2 (RIP2)-dependent nuclear factor κ B signaling. *The Journal of Biological Chemistry* **286**, 35874–82 (2011).
85. Sahillioglu, A. C., Sumbul, F., Ozoren, N. & Haliloglu, T. Structural and dynamics aspects of ASC speck assembly. *Structure* **22**, 1722–1734 (2014).
86. Proell, M., Gerlic, M., Mace, P. D., Reed, J. C. & Riedl, S. J. The CARD plays a critical role in ASC foci formation and inflammasome signalling. *The Biochemical Journal* **449**, 613–21 (2013).
87. Cai, X. *et al.* Prion-like polymerization underlies signal transduction in antiviral immune defense and inflammasome activation. *Cell* **156**, 1207–22 (2014).
88. Franklin, B. S. *et al.* The adaptor ASC has extracellular and 'prionoid' activities that propagate inflammation. *Nature Immunology* **15**, 727–737 (2014).
89. Baroja-Mazo, A. *et al.* The NLRP3 inflammasome is released as a particulate danger signal that amplifies the inflammatory response. *Nature Immunology* **15**, 738–748 (2014).
90. Manji, G. A. *et al.* PYPAF1, a PYRIN-containing Apaf1-like protein that assembles with ASC and regulates activation of NF- κ B. *The Journal of Biological Chemistry* **277**, 11570–11575 (2002).
91. Mariathasan, S. *et al.* Differential activation of the inflammasome by caspase-1 adaptors ASC and Ipaf. *Nature* **430**, 213–218 (2004).
92. McConnell, B. B., Vertino, P. M. & Tms, P. Activation of a caspase-9-mediated apoptotic pathway by subcellular redistribution of the novel caspase recruitment domain protein TMS1. *Cancer Research* **60**, 6243–6247 (2000).
93. Stehlik, C. *et al.* The PAAD/PYRIN-family protein ASC is a dual regulator of a conserved step in nuclear factor κ B activation pathways. *Journal of Experimental Medicine* **196**, 1605–1615 (2002).

94. Conway, K. E. *et al.* TMS1, a novel proapoptotic caspase recruitment domain protein, is a target of methylation-induced gene silencing in human breast cancers. *Cancer Research* **60**, 6236–6242 (2000).
95. Collard, R. L., Harya, N. S., Mozon, F. A., Maier, C. E. & O’Keefe, D. S. Methylation of the ASC gene promoter is associated with aggressive prostate cancer. *The Prostate* **66**, 687–695 (2006).
96. Das, P. M. *et al.* Methylation mediated silencing of TMS1/ASC gene in prostate cancer. *Molecular Cancer* **5**, 28 (2006).
97. Riojas, M. A. *et al.* Methylation-induced silencing of ASC/TMS1, a pro-apoptotic gene, is a late-stage event in colorectal cancer. *Cancer Biology & Therapy* **6**, 1710–1716 (2007).
98. Fernandes-Alnemri, T. *et al.* The pyroptosome: A supramolecular assembly of ASC dimers mediating inflammatory cell death via caspase-1 activation. *Cell Death & Differentiation* **14**, 1590–1604 (2007).
99. Cheng, J. *et al.* Kinetic properties of ASC protein aggregation in epithelial cells. *Journal of Cellular Physiology* **222**, 738–747 (2010).
100. Lu, A. *et al.* Molecular basis of caspase-1 polymerization and its inhibition by a new capping mechanism. *Nature Structural & Molecular Biology*, 1–12 (2016).
101. Suzuki, T. *et al.* Differential regulation of caspase-1 activation, pyroptosis, and autophagy via Ipaf and ASC in *Shigella*-infected macrophages. *PLoS Pathogens* **3**, e111 (2007).
102. De Jong, H. K. *et al.* Limited role for ASC and NLRP3 during in vivo Salmonella Typhimurium infection. *BMC Immunology* **15**, 30 (2014).
103. Elliott, E. I. & Sutterwala, F. S. Initiation and perpetuation of NLRP3 inflammasome activation and assembly. *Immunological Reviews* **265**, 35–52 (2015).
104. Bryan, N. B., Dorfleutner, A., Rojanasakul, Y. & Stehlik, C. Activation of inflammasomes requires intracellular redistribution of the apoptotic speck-like protein containing a caspase recruitment domain. *Journal of Immunology* **182**, 3173–82 (2009).
105. Martin, B. N. *et al.* IKK α negatively regulates ASC-dependent inflammasome activation. *Nature Communications* **5**, 4977 (2014).
106. Yang, J., Liu, Z. & Xiao, T. S. Post-translational regulation of inflammasomes. *Cellular & Molecular Immunology* **13**, 1–15 (2016).
107. Hara, H. *et al.* Phosphorylation of the adaptor ASC acts as a molecular switch that controls the formation of speck-like aggregates and inflammasome activity. *Nature Immunology* **14**, 1247–1255 (2013).
108. Lin, Y.-C. *et al.* Syk is involved in NLRP3 inflammasome-mediated caspase-1 activation through adaptor ASC phosphorylation and enhanced oligomerization. *Journal of Leukocyte Biology* **97**, 1–11 (2015).

109. Chung, I.-C. *et al.* Pyk2 activates the NLRP3 inflammasome by directly phosphorylating ASC and contributes to inflammasome-dependent peritonitis. *Scientific Reports* **6**, 36214 (2016).
110. Ito, M. *et al.* Bruton's tyrosine kinase is essential for NLRP3 inflammasome activation and contributes to ischaemic brain injury. *Nature Communications* **6**, 7360 (2015).
111. Gross, O. *et al.* Syk kinase signalling couples to the Nlrp3 inflammasome for anti-fungal host defence. *Nature* **459**, 433–436 (2009).
112. Rodgers, M. A. *et al.* The linear ubiquitin assembly complex (LUBAC) is essential for NLRP3 inflammasome activation. *The Journal of Experimental Medicine* (2014).
113. Shi, C.-S. *et al.* Activation of autophagy by inflammatory signals limits IL-1 β production by targeting ubiquitinated inflammasomes for destruction. *Nature Immunology* **13**, 255–263 (2012).
114. Guan, K. *et al.* MAVS promotes inflammasome activation by targeting ASC for K63-linked ubiquitination via the E3 ligase TRAF3. *The Journal of Immunology*, 1–11 (2015).
115. Dorfleutner, A., Chu, L. & Stehlik, C. Inhibiting the inflammasome: one domain at a time. *Immunological Reviews* **265**, 205–216 (2015).
116. Matusiak, M., Van Opendenbosch, N. & Lamkanfi, M. CARD- and pyrin-only proteins regulating inflammasome activation and immunity. *Immunological Reviews* **265**, 217–230 (2015).
117. Druilhe, A., Srinivasula, S. M., Razmara, M., Ahmad, M. & Alnemri, E. S. Regulation of IL-1 β generation by Pseudo-ICE and ICEBERG, two dominant negative caspase recruitment domain proteins. *Cell Death & Differentiation* **8**, 649–657 (2001).
118. Lee, S. H., Stehlik, C. & Reed, J. C. COP, a caspase recruitment domain-containing protein and inhibitor of caspase-1 activation processing. *Journal of Biological Chemistry* **276**, 34495–34500 (2001).
119. Karasawa, T. *et al.* Oligomerized CARD16 promotes caspase-1 assembly and IL-1 β processing. *FEBS Open Bio* **5**, 348–356 (2015).
120. Lamkanfi, M. *et al.* INCA, a novel human caspase recruitment domain protein that inhibits interleukin-1 β generation. *Journal of Biological Chemistry* **279**, 51729–51738 (2004).
121. Humke, E. W., Shriver, S. K., Starovasnik, M. A., Fairbrother, W. J. & Dixit, V. M. ICEBERG: A novel inhibitor of interleukin-1 β generation. *Cell* **103**, 99–111 (2000).
122. Stehlik, C. *et al.* The PAAD/PYRIN-only protein POP1/ASC2 is a modulator of ASC-mediated nuclear-factor-kappa B and pro-caspase-1 regulation. *The Biochemical Journal* **373**, 101–113 (2003).

123. Srimathi, T. *et al.* Mapping of POP1-binding site on pyrin domain of ASC. *The Journal of Biological Chemistry* **283**, 15390–8 (2008).
124. De Almeida, L. *et al.* The PYRIN domain-only protein POP1 inhibits inflammasome assembly and ameliorates inflammatory disease. *Immunity* **43**, 1–13 (2015).
125. Choi, J. Y. *et al.* Crystal structure of human POP1 and its distinct structural feature for PYD domain. *Biochemical and Biophysical Research Communications* **460**, 957–963 (2015).
126. Dorfleutner, A. *et al.* Cellular pyrin domain-only protein 2 is a candidate regulator of inflammasome activation. *Infection and Immunity* **75**, 1484–92 (2007).
127. Khare, S. *et al.* The PYRIN domainonly protein POP3 inhibits ALR inflammasomes and regulates responses to infection with DNA viruses. *Nature Immunology* (2014).
128. Dorfleutner, A. *et al.* A Shope Fibroma virus PYRIN-only protein modulates the host immune response. *Virus Genes* **35**, 685–694 (2007).
129. Johnston, J. B. *et al.* A poxvirus-encoded pyrin domain protein interacts with ASC-1 to inhibit host inflammatory and apoptotic responses to infection. *Immunity* **23**, 587–598 (2005).
130. Bryan, N. B. *et al.* Differential splicing of the apoptosis-associated speck like protein containing a caspase recruitment domain (ASC) regulates inflammasomes. *Journal of Inflammation* **7**, 23 (2010).
131. Matsushita, K. *et al.* A splice variant of ASC regulates IL-1 β release and aggregates differently from intact ASC. *Mediators of Inflammation* **2009**, 287387 (2009).
132. Agostini, L. *et al.* NALP3 forms an IL-1 β -processing inflammasome with increased activity in Muckle-Wells autoinflammatory disorder. *Immunity* **20**, 319–325 (2004).
133. Coll, R. C., O'Neill, L. A. J. & Schroder, K. Questions and controversies in innate immune research: What is the physiological role of NLRP3? *Cell Death Discovery* **2**, 16019 (2016).
134. Bauernfeind, F. G. *et al.* Cutting edge: NF- κ B activating pattern recognition and cytokine receptors license NLRP3 inflammasome activation by regulating NLRP3 expression. *The Journal of Immunology* **183**, 787–791 (2009).
135. Franchi, L., Eigenbrod, T. & Núñez, G. Cutting edge: TNF-alpha mediates sensitization to ATP and silica via the NLRP3 inflammasome in the absence of microbial stimulation. *Journal of Immunology* **183**, 792–6 (2009).
136. Juliana, C. *et al.* Non-transcriptional priming and deubiquitination regulate NLRP3 inflammasome activation. *Journal of Biological Chemistry* **287**, 36617–36622 (2012).

137. Py, B. F., Kim, M. S., Vakifahmetoglu-Norberg, H. & Yuan, J. Deubiquitination of NLRP3 by BRCC3 critically regulates inflammasome activity. *Molecular Cell* **49**, 331–338 (2013).
138. Lopez-Castejon, G. *et al.* Deubiquitinases regulate the activity of caspase-1 and interleukin-1 β secretion via assembly of the inflammasome. *Journal of Biological Chemistry* **288**, 2721–2733 (2013).
139. Horvath, G. L., Schrum, J. E., de Nardo, C. M. & Latz, E. Intracellular sensing of microbes and danger signals by the inflammasomes. *Immunological Reviews* **243**, 119–135 (2011).
140. Franchi, L., Muñoz-Planillo, R. & Núñez, G. Sensing and reacting to microbes through the inflammasomes. *Nature Immunology* **13**, 325–332 (2012).
141. Muñoz-Planillo, R. *et al.* K efflux is the common trigger of NLRP3 inflammasome activation by bacterial toxins and particulate matter. *Immunity* **38**, 1142–53 (2013).
142. Próchnicki, T., Mangan, M. S. & Latz, E. Recent insights into the molecular mechanisms of the NLRP3 inflammasome activation. *F1000Research* **5**, 1–15 (2016).
143. Perregaux, D & Gabel, C. A. Interleukin-1 β maturation and release in response to ATP and nigericin. *Journal of Biological Chemistry* **269**, 15195–15203 (1994).
144. Mariathasan, S. *et al.* Cryopyrin activates the inflammasome in response to toxins and ATP. *Nature* **440**, 228–232 (2006).
145. Alves, L. A. *et al.* The P2X7 receptor: Shifting from a low- to a high-conductance channel - An enigmatic phenomenon? *Biochimica et Biophysica Acta* **1838**, 2578–2587 (2014).
146. Pressman, B. C. Biological applications of ionophores. *Annual Review of Biochemistry* **45**, 501–530 (1976).
147. Allam, R. *et al.* Cutting edge: Cyclic polypeptide and aminoglycoside antibiotics trigger IL-1 β secretion by activating the NLRP3 inflammasome. *Journal of Immunology* **186**, 2714–2718 (2011).
148. Kelkar, D. A. & Chattopadhyay, A. The gramicidin ion channel: A model membrane protein. *Biochimica et Biophysica Acta* **1768**, 2011–2025 (2007).
149. Martinon, F., Pétrilli, V., Mayor, A., Tardivel, A. & Tschopp, J. Gout-associated uric acid crystals activate the NALP3 inflammasome. *Nature* **440**, 237–241 (2006).
150. Hornung, V. *et al.* Silica crystals and aluminum salts activate the NALP3 inflammasome through phagosomal destabilization. *Nature Immunology* **9**, 847–56 (2008).
151. Li, H., Willingham, S. B., Ting, J. P.-Y. & Re, F. Cutting edge: Inflammasome activation by alum and alum's adjuvant effect are mediated by NLRP3. *Journal of immunology* **181**, 17–21 (2008).

152. Wolf, A. J. *et al.* Hexokinase is an innate immune receptor for the detection of bacterial peptidoglycan. *Cell* **166**, 1–13 (2016).
153. Groß, C. J. *et al.* K⁺ efflux-independent NLRP3 inflammasome activation by small molecules targeting mitochondria. *Immunity*, 1–13 (2016).
154. He, Y., Hara, H. & Núñez, G. Mechanism and Regulation of NLRP3 Inflammasome Activation. *Trends in Biochemical Sciences*, 1–10 (2016).
155. Schmid-Burgk, J. L. *et al.* A genome-wide CRISPR (clustered regularly interspaced short palindromic repeats) screen identifies NEK7 as an essential component of NLRP3 inflammasome activation. *Journal of Biological Chemistry* **291**, 103–109 (2016).
156. Shi, H. *et al.* NLRP3 activation and mitosis are mutually exclusive events coordinated by NEK7, a new inflammasome component. *Nature Immunology* **17**, 1–12 (2015).
157. Chuang, Y.-T. *et al.* Tumor suppressor death-associated protein kinase is required for full IL-1 β production. *Blood* **117**, 960–970 (2011).
158. Ghonime, M. G. *et al.* Inflammasome priming by lipopolysaccharide is dependent upon ERK signaling and proteasome function. *Journal of Immunology* **192**, 3881–8 (2014).
159. Gong, Y.-N. *et al.* Chemical probing reveals insights into the signaling mechanism of inflammasome activation. *Cell Research* **20**, 1289–1305 (2010).
160. Saïd-Sadier, N., Padilla, E., Langsley, G. & Ojcius, D. M. *Aspergillus fumigatus* stimulates the NLRP3 inflammasome through a pathway requiring ROS production and the syk tyrosine kinase. *PLoS One* **5** (2010).
161. Tiemi Shio, M. *et al.* Malarial hemozoin activates the NLRP3 inflammasome through Lyn and Syk kinases. *PLoS Pathogens* **5** (2009).
162. Wong, K. W. & Jacobs, W. R. Critical role for NLRP3 in necrotic death triggered by *Mycobacterium tuberculosis*. *Cellular Microbiology* **13**, 1371–1384 (2011).
163. Han, S. H. *et al.* Lipopolysaccharide primes the NALP3 inflammasome by inhibiting its ubiquitination and degradation mediated by the SCF^{FBXL2} E3 ligase. *Journal of Biological Chemistry* **290**, 18124–18133 (2015).
164. Yan, Y. *et al.* Dopamine controls systemic inflammation through inhibition of NLRP3 inflammasome. *Cell* **160**, 62–73 (2015).
165. Bose, S. *et al.* ADP-Ribosylation of NLRP3 by *Mycoplasma pneumoniae* CARDS toxin regulates inflammasome activity. *mBio* **5**, 1–11 (2014).
166. Guarda, G. *et al.* Type I interferon inhibits interleukin-1 production and inflammasome activation. *Immunity* **34**, 213–223 (2011).
167. Hernandez-Cuellar, E. *et al.* Cutting edge: Nitric oxide inhibits the NLRP3 inflammasome. *The Journal of Immunology* **189**, 5113–5117 (2012).

168. Mao, K. *et al.* Nitric oxide suppresses NLRP3 inflammasome activation and protects against LPS-induced septic shock. *Cell Research* **23**, 201–12 (2013).
169. Mishra, B. B. *et al.* Nitric oxide controls the immunopathology of tuberculosis by inhibiting NLRP3 inflammasome-dependent processing of IL-1 β . *Nature Immunology* **14**, 52–60 (2013).
170. Yang, C.-S. *et al.* Small heterodimer partner interacts with NLRP3 and negatively regulates activation of the NLRP3 inflammasome. *Nature Communications* **6**, 6115 (2015).
171. Duncan, J. A. *et al.* Cryopyrin/NALP3 binds ATP/dATP, is an ATPase, and requires ATP binding to mediate inflammatory signaling. *Proceedings of the National Academy of Sciences of the United States of America* **104**, 8041–8046 (2007).
172. Federici, S., Caorsi, R. & Gattorno, M. The autoinflammatory diseases. *Swiss Medical Weekly* **142**, 1–17 (2012).
173. Ozaki, E., Campbell, M. & Doyle, S. L. Targeting the NLRP3 inflammasome in chronic inflammatory diseases: Current perspectives. *Journal of Inflammation Research* **8**, 15–27 (2015).
174. Aksentijevich, I. *et al.* De novo *CIAS1* mutations, cytokine activation, and evidence for genetic heterogeneity in patients with neonatal-onset multisystem inflammatory disease (NOMID): A new member of the expanding family of pyrin-associated autoinflammatory diseases. *Arthritis and Rheumatism* **46**, 3340–3348 (2002).
175. Feldmann, J. *et al.* Chronic infantile neurological cutaneous and articular syndrome is caused by mutations in *CIAS1*, a gene highly expressed in polymorphonuclear cells and chondrocytes. *American Journal of Human Genetics* **71**, 198–203 (2002).
176. Hoffman, H. M., Mueller, J. L., Broide, D. H., Wanderer, A. A. & Kolodner, R. D. Mutation of a new gene encoding a putative pyrin-like protein causes familial cold autoinflammatory syndrome and Muckle-Wells syndrome. *Nature Genetics* **29**, 301–305 (2001).
177. Hoffman, H. M., Wanderer, A. A. & Broide, D. H. Familial cold autoinflammatory syndrome: Phenotype and genotype of an autosomal dominant periodic fever. *Journal of Allergy and Clinical Immunology* **108**, 615–620 (2001).
178. Kuemmerle-Deschner, J. B. CAPS pathogenesis, presentation and treatment of an autoinflammatory disease. *Seminars in Immunopathology* **37**, 377–385 (2015).
179. Goldbach-Mansky, R. *et al.* Neonatal-onset multisystem inflammatory disease responsive to interleukin-1 β inhibition. *New England Journal of Medicine* **355**, 581–592 (2006).

180. Hawkins, P. N., Lachmann, H. J. & McDermott, M. F. Interleukin-1-receptor antagonist in the Muckle-Wells syndrome. *New England Journal of Medicine* **348**, 2583–2584 (2003).
181. Lachmann, H. J. *et al.* Use of canakinumab in the cryopyrin-associated periodic syndrome. *The New England Journal of Medicine* **360**, 2416–2425 (2009).
182. Duewell, P. *et al.* NLRP3 inflammasomes are required for atherogenesis and activated by cholesterol crystals. *Nature* **464**, 1357–1361 (2010).
183. Halle, A. *et al.* The NALP3 inflammasome is involved in the innate immune response to amyloid-beta. *Nature Immunology* **9**, 857–865 (2008).
184. Masters, S. L. *et al.* Activation of the NLRP3 inflammasome by islet amyloid polypeptide provides a mechanism for enhanced IL-1 β in type 2 diabetes. *Nature Immunology* **11**, 897–904 (2010).
185. Vitale, A., Cantarini, L., Rigante, D., Bardelli, M. & Galeazzi, M. Anakinra treatment in patients with gout and type 2 diabetes. *Clinical Rheumatology* **34**, 981–984 (2015).
186. Deyoung, K. L. *et al.* Cloning a novel member of the human interferon-inducible gene family associated with control of tumorigenicity in a model of human melanoma. *Oncogene* **15**, 453–458 (1997).
187. Man, S. M., Karki, R. & Kanneganti, T. D. AIM2 inflammasome in infection, cancer, and autoimmunity: Role in DNA sensing, inflammation, and innate immunity. *European Journal of Immunology* **46**, 269–280 (2016).
188. Muruve, D. A. *et al.* The inflammasome recognizes cytosolic microbial and host DNA and triggers an innate immune response. *Nature* **452**, 103–107 (2008).
189. Bürckstümmer, T. *et al.* An orthogonal proteomic-genomic screen identifies AIM2 as a cytoplasmic DNA sensor for the inflammasome. *Nature Immunology* **10**, 266–72 (2009).
190. Fernandes-Alnemri, T., Yu, J.-W., Datta, P., Wu, J. & Alnemri, E. S. AIM2 activates the inflammasome and cell death in response to cytoplasmic DNA. *Nature* **458**, 509–13 (2009).
191. Hornung, V. *et al.* AIM2 recognizes cytosolic dsDNA and forms a caspase-1-activating inflammasome with ASC. *Nature* **458**, 514–8 (2009).
192. Roberts, T. L. *et al.* HIN-200 proteins regulate caspase activation in response to foreign cytoplasmic DNA. *Science* **323**, 1057–1060 (2009).
193. Jin, T. *et al.* Structures of the HIN domain: DNA complexes reveal ligand binding and activation mechanisms of the AIM2 inflammasome and IFI16 receptor. *Immunity* **36**, 561–571 (2012).
194. Lu, A. *et al.* Plasticity in PYD assembly revealed by cryo-EM structure of the PYD filament of AIM2. *Cell Discovery* **1**, 15013 (2015).

195. Jin, T., Perry, A., Smith, P., Jiang, J. & Xiao, T. S. Structure of the absent in melanoma 2 (AIM2) pyrin domain provides insights into the mechanisms of AIM2 autoinhibition and inflammasome assembly. *Journal of Biological Chemistry* **288**, 13225–13235 (2013).
196. Belhocine, K. & Monack, D. M. Francisella infection triggers activation of the AIM2 inflammasome in murine dendritic cells. *Cellular Microbiology* **14**, 71–80 (2012).
197. Fernandes-Alnemri, T. *et al.* The AIM2 inflammasome is critical for innate immunity to Francisella tularensis. *Nature Immunology* **11**, 385–393 (2010).
198. Jones, J. W. *et al.* Absent in melanoma 2 is required for innate immune recognition of Francisella tularensis. *Proceedings of the National Academy of Sciences of the United States of America* **107**, 9771–9776 (2010).
199. Man, S. M. & Kanneganti, T.-D. Regulation of inflammasome activity. *Immunological Reviews* **265**, 6–21 (2015).
200. Meunier, E. *et al.* Guanylate-binding proteins promote activation of the AIM2 inflammasome during infection with Francisella novicida. *Nature Immunology* **16**, 476–84 (2015).
201. Rathinam, V. A. K. *et al.* The AIM2 inflammasome is essential for host defense against cytosolic bacteria and DNA viruses. *Nature Immunology* **11**, 395–402 (2010).
202. Saiga, H. *et al.* The recombinant BCG $\Delta ureC::hly$ vaccine targets the AIM2 inflammasome to induce autophagy and inflammation. *The Journal of Infectious Diseases* **211**, 1831–41 (2015).
203. Wassermann, R. *et al.* Mycobacterium tuberculosis differentially activates cGAS- and inflammasome-dependent intracellular immune responses through ESX-1. *Cell Host & Microbe* **17**, 799–810 (2015).
204. Kim, S. *et al.* Listeria monocytogenes is sensed by the NLRP3 and AIM2 inflammasome. *European Journal of Immunology* **40**, 1545–1551 (2010).
205. Warren, S. E. *et al.* Cutting edge: Cytosolic bacterial DNA activates the inflammasome via Aim2. *Journal of Immunology* **185**, 818–821 (2010).
206. Wu, J., Fernandes-Alnemri, T. & Alnemri, E. S. Involvement of the AIM2, NLRP3, and NLRP3 inflammasomes in caspase-1 activation by Listeria monocytogenes. *Journal of Clinical Immunology* **30**, 693–702 (2010).
207. Gomes, M. T. R. *et al.* Critical role of ASC inflammasomes and bacterial type IV secretion system in caspase-1 activation and host innate resistance to Brucella abortus infection. *Journal of Immunology* **190**, 3629–38 (2013).
208. Saiga, H. *et al.* Critical role of AIM2 in Mycobacterium tuberculosis infection. *International Immunology* **24**, 637–644 (2012).
209. Hanamsagar, R., Aldrich, A. & Kielian, T. Critical role for the AIM2 inflammasome during acute CNS bacterial infection. *Journal of Neurochemistry* **129**, 704–711 (2014).

210. Reinholz, M. *et al.* HPV16 activates the AIM2 inflammasome in keratinocytes. *Archives of Dermatological Research* **305**, 723–732 (2013).
211. Zhen, J. *et al.* AIM2 mediates inflammation-associated renal damage in Hepatitis B Virus-associated glomerulonephritis by regulating caspase-1, IL-1 β , and IL-18. *Mediators of Inflammation* **2014** (2014).
212. Ru, H. *et al.* Structural basis for termination of AIM2-mediated signaling by p202. *Cell research* **23**, 855–8 (2013).
213. Yin, Q. *et al.* Molecular mechanism for p202-mediated specific inhibition of AIM2 inflammasome activation. *Cell Reports* **4**, 327–339 (2013).
214. French FMF Consortium. A Candidate gene for familial Mediterranean fever. *Nature Genetics* **15**, 57–61 (1997).
215. International FMF Consortium. Ancient missense mutations in a new member of the RoRet gene family are likely to cause familial Mediterranean fever. *Cell* **90**, 797–807 (1997).
216. Manukyan, G. & Aminov, R. Update on pyrin functions and mechanisms of familial mediterranean fever. *Frontiers in Microbiology* **7**, 1–8 (2016).
217. D’Cruz, A. A., Babon, J. J., Norton, R. S., Nicola, N. A. & Nicholson, S. E. Structure and function of the SPRY/B30.2 domain proteins involved in innate immunity. *Protein Science* **22**, 1–10 (2013).
218. Chae, J. J. *et al.* The B30.2 domain of pyrin, the familial Mediterranean fever protein, interacts directly with caspase-1 to modulate IL-1 β production. *Proceedings of the National Academy of Sciences of the United States of America* **103**, 9982–9987 (2006).
219. Chae, J. J. *et al.* Targeted disruption of pyrin, the FMF protein, causes heightened sensitivity to endotoxin and a defect in macrophage apoptosis. *Molecular Cell* **11**, 591–604 (2003).
220. Papin, S. *et al.* The SPRY domain of Pyrin, mutated in familial Mediterranean fever patients, interacts with inflammasome components and inhibits proIL-1 β processing. *Cell Death & Differentiation* **14**, 1457–1466 (2007).
221. Yu, J.-W. *et al.* Cryopyrin and pyrin activate caspase-1, but not NF- κ B, via ASC oligomerization. *Cell Death & Differentiation* **13**, 236–249 (2006).
222. Chae, J. J. *et al.* Gain-of-function Pyrin mutations induce NLRP3 protein-independent interleukin-1 β activation and severe autoinflammation in mice. *Immunity* **34**, 755–768 (2011).
223. Xu, H. *et al.* Innate immune sensing of bacterial modifications of Rho GTPases by the Pyrin inflammasome. *Nature* **513**, 237–41 (2014).
224. Hall, A. Rho GTPases and the actin cytoskeleton. *Science* **279**, 509–14 (1998).
225. Aktories, K. Bacterial protein toxins that modify host regulatory GTPases. *Nature Reviews Microbiology* **9**, 487–498 (2011).

226. Gao, W., Yang, J., Liu, W., Wang, Y. & Shao, F. Site-specific phosphorylation and microtubule dynamics control Pyrin inflammasome activation. *Proceedings of the National Academy of Sciences of the United States of America* **113**, E4857–66 (2016).
227. Chung, L. K. *et al.* The *Yersinia* virulence factor YopM hijacks host kinases to inhibit type III effector-triggered activation of the Pyrin inflammasome. *Cell Host & Microbe* **20**, 1–11 (2016).
228. Kimura, T. *et al.* TRIM-mediated precision autophagy targets cytoplasmic regulators of innate immunity. *Journal of Cell Biology* **210**, 973–989 (2015).
229. Aybal Kutlugün, A. *et al.* AA type renal amyloidosis secondary to FMF: A long-term follow-up in two patients. *Renal Failure* **32**, 1230–2 (2010).
230. Bakkaloglu, A. Familial Mediterranean fever. *Pediatric Nephrology* **18**, 853–859 (2003).
231. Goldfinger, S. E. Colchicine for familial Mediterranean fever. *New England Journal of Medicine*, 1302 (1972).
232. Özkaya, N. & Yalçinkaya, F. Colchicine treatment in children with familial Mediterranean fever. *Clinical Rheumatology* **22**, 314–317 (2003).
233. Stanton, R. A., Gernert, K. M., Nettles, J. H. & Aneja, R. Drugs that target dynamic microtubules: A new molecular perspective. *Medicinal Research Reviews* **31**, 443–481–1327 (2011).
234. Franchi, L. *et al.* Cytosolic flagellin requires Ipaf for activation of caspase-1 and interleukin 1 β in *Salmonella*-infected macrophages. *Nature Immunology* **7**, 576–582 (2006).
235. Miao, E. A. *et al.* Cytoplasmic flagellin activates caspase-1 and secretion of interleukin 1 β via Ipaf. *Nature Immunology* **7**, 569–575 (2006).
236. Miao, E. A. *et al.* Innate immune detection of the type III secretion apparatus through the NLRC4 inflammasome. *Proceedings of the National Academy of Sciences of the United States of America* **107**, 3076–80 (2010).
237. Kofoed, E. M. & Vance, R. E. Innate immune recognition of bacterial ligands by NAIPs determines inflammasome specificity. *Nature* **477**, 592–5 (2011).
238. Zhao, Y. *et al.* The NLRC4 inflammasome receptors for bacterial flagellin and type III secretion apparatus. *Nature* **477**, 596–600 (2011).
239. Tenthorey, J. L., Kofoed, E. M., Daugherty, M. D., Malik, H. S. & Vance, R. E. Molecular basis for specific recognition of bacterial ligands by NAIP/NLRC4 inflammasomes. *Molecular Cell* **54**, 1–13 (2014).
240. Kortmann, J., Brubaker, S. W. & Monack, D. M. Cutting edge: Inflammasome activation in primary human macrophages is dependent on flagellin. *The Journal of Immunology* **195**, 815–9 (2015).

241. Hu, Z. *et al.* Crystal structure of NLRC4 reveals its autoinhibition mechanism. *Science* **341**, 172–5 (2013).
242. Diebold, C. A., Halff, E. F., Koster, A. J., Huizinga, E. G. & Koning, R. I. Cryo-electron tomography of the NAIP5/NLRC4 inflammasome: Implications for NLR activation. *Structure* **23**, 2349–2357 (2015).
243. Halff, E. F. *et al.* Formation and structure of a NAIP5-NLRC4 inflammasome induced by direct interactions with conserved N- and C-terminal regions of flagellin. *Journal of Biological Chemistry* **287**, 38460–38472 (2012).
244. Hu, Z. *et al.* Structural and biochemical basis for induced self-propagation of NLRC4. *Science* **350**, 1–11 (2015).
245. Zhang, L. *et al.* Cryo-EM structure of the activated NAIP2- NLRC4 inflammasome reveals nucleated polymerization. *Science* **4**, 12–14 (2015).
246. Matusiak, M. *et al.* Flagellin-induced NLRC4 phosphorylation primes the inflammasome for activation by NAIP5. *Proceedings of the National Academy of Sciences of the United States of America* **112**, 1541–1546 (2015).
247. Qu, Y. *et al.* Phosphorylation of NLRC4 is critical for inflammasome activation. *Nature* **490**, 539–42 (2012).
248. Geddes, B. J. *et al.* Human CARD12 is a novel CED4/Apaf-1 family member that induces apoptosis. *Biochemical and Biophysical Research Communications* **284**, 77–82 (2001).
249. Amer, A. *et al.* Regulation of *Legionella* phagosome maturation and infection through flagellin and host Ipaf. *Journal of Biological Chemistry* **281**, 35217–35223 (2006).
250. Cai, S., Batra, S., Wakamatsu, N., Pacher, P. & Jeyaseelan, S. NLRC4 inflammasome-mediated production of IL-1 β modulates mucosal immunity in the lung against gram-negative bacterial infection. *Journal of Immunology* **188**, 5623–35 (2012).
251. Carvalho, F. A. *et al.* Cytosolic flagellin receptor NLRC4 protects mice against mucosal and systemic challenges. *Mucosal Immunology* **5**, 288–98 (2012).
252. Pereira, M. S. F. *et al.* Activation of NLRC4 by flagellated bacteria triggers caspase-1-dependent and -independent responses to restrict *Legionella pneumophila* replication in macrophages and *in vivo*. *Journal of Immunology* **187**, 6447–55 (2011).
253. Canna, S. W. *et al.* An activating NLRC4 inflammasome mutation causes autoinflammation with recurrent macrophage activation syndrome. *Nature Genetics* **46**, 1140–6 (2014).
254. Kitamura, A., Sasaki, Y., Abe, T. & Kano, H. An inherited mutation in NLRC4 causes autoinflammation in human and mice. *Journal of Experimental Medicine* **211**, 2385–2396 (2014).

255. Romberg, N. *et al.* Mutation of NLRC4 causes a syndrome of enterocolitis and autoinflammation. *Nature Genetics* **46**, 1135–9 (2014).
256. Hiller, S. *et al.* NMR structure of the apoptosis- and inflammation-related NALP1 pyrin domain. *Structure* **11**, 1199–1205 (2003).
257. Hlaing, T. *et al.* Molecular cloning and characterization of DEFCAP-L and -S, two isoforms of a novel member of the mammalian Ced-4 family of apoptosis proteins. *Journal of Biological Chemistry* **276**, 9230–9238 (2001).
258. Boyden, E. D. & Deitrich, W. F. *Nalp1b* controls mouse macrophage susceptibility to anthrax lethal toxin. *Nature Genetics* **38**, 240–244 (2006).
259. Levinsohn, J. L. *et al.* Anthrax lethal factor cleavage of Nlrp1 is required for activation of the inflammasome. *PLoS Pathogens* **8** (2012).
260. Moayeri, M. & Leppla, S. H. Cellular and systemic effects of anthrax lethal toxin and edema toxin. *Molecular Aspects of Medicine* **30**, 439–455 (2009).
261. Hellmich, K. A. *et al.* Anthrax lethal factor cleaves mouse Nlrp1b in both toxin-sensitive and toxin-resistant macrophages. *PLoS One* **7**, 1–5 (2012).
262. Frew, B. C., Joag, V. R. & Mogridge, J. Proteolytic processing of Nlrp1b is required for inflammasome activity. *PLoS Pathogens* **8** (2012).
263. Zhong, F. L. *et al.* Germline NLRP1 mutations cause skin inflammatory and cancer susceptibility syndromes via inflammasome activation. *Cell* **167**, 187–202.e17 (2016).
264. Elinav, E. *et al.* NLRP6 inflammasome regulates colonic microbial ecology and risk for colitis. *Cell* **145**, 745–757 (2011).
265. Grenier, J. M. *et al.* Functional screening of five PYPAF family members identifies PYPAF5 as a novel regulator of NF- κ B and caspase-1. *FEBS Letters* **530**, 73–78 (2002).
266. Levy, M. *et al.* Microbiota-modulated metabolites shape the intestinal microenvironment by regulating NLRP6 inflammasome signaling. *Cell* **163**, 1428–1443 (2015).
267. Wlodarska, M. *et al.* NLRP6 inflammasome orchestrates the colonic host-microbial interface by regulating goblet cell mucus secretion. *Cell* **156**, 1045–1059 (2014).
268. Wang, P. *et al.* Nlrp6 regulates intestinal antiviral innate immunity. *Science* **350**, 826–830 (2015).
269. Sellin, M. E., Maslowski, K. M., Maloy, K. J. & Hardt, W. D. Inflammasomes of the intestinal epithelium. *Trends in Immunology* **36**, 442–450 (2015).
270. Pinheiro, A. S. *et al.* Three-dimensional structure of the NLRP7 pyrin domain insight into pyrin-pyrin-mediated effector domain signaling in innate immunity. *Journal of Biological Chemistry* **285**, 27402–27410 (2010).

271. Khare, S. *et al.* An NLRP7-containing inflammasome mediates recognition of microbial lipopeptides in human macrophages. *Immunity* **36**, 464–476 (2012).
272. Zhou, Y. *et al.* Virulent *Mycobacterium bovis* Beijing strain activates the NLRP7 inflammasome in THP-1 macrophages. *PLoS One* **11**, 1–13 (2016).
273. Radian, A. D., Khare, S., Chu, L. H., Dorfleutner, A. & Stehlik, C. ATP binding by NLRP7 is required for inflammasome activation in response to bacterial lipopeptides. *Molecular Immunology* **67**, 294–302 (2015).
274. Wang, L. *et al.* PYPAF7, a novel PYRIN-containing Apaf1-like protein that regulates activation of NF- κ B and caspase-1-dependent cytokine processing. *The Journal of Biological Chemistry* **277**, 29874–80 (2002).
275. Lich, J. D. *et al.* Monarch-1 suppresses non-canonical NF- κ B activation and p52-dependent chemokine expression in monocytes. *The Journal of Immunology* **178**, 1256–1260 (2007).
276. Ye, Z. *et al.* ATP binding by monarch-1/NLRP12 is critical for its inhibitory function. *Molecular and Cellular Biology* **28**, 1841–50 (2008).
277. Arthur, J. C. *et al.* Cutting edge: NLRP12 controls dendritic and myeloid cell migration to affect contact hypersensitivity. *Journal of Immunology* **185**, 4515–9 (2010).
278. Ataide, M. A. *et al.* Malaria-induced NLRP12/NLRP3-dependent caspase-1 activation mediates inflammation and hypersensitivity to bacterial superinfection. *PLoS Pathogens* **10**, e1003885 (2014).
279. Vladimer, G. I. *et al.* The NLRP12 inflammasome recognizes *Yersinia pestis*. *Immunity* **37**, 96–107 (2012).
280. Borghini, S *et al.* Clinical presentation and pathogenesis of cold-induced autoinflammatory disease in a family with recurrence of an NLRP12 mutation. *Arthritis and Rheumatism* **63**, 830–9 (2011).
281. Jeru, I. *et al.* Mutations in NALP12 cause hereditary periodic fever syndromes. *Proceedings of the National Academy of Sciences of the United States of America* **105**, 1614–1619 (2008).
282. J eru, I. *et al.* Identification and functional consequences of a recurrent NLRP12 missense mutation in periodic fever syndromes. *Arthritis and Rheumatism* **63**, 1459–64 (2011).
283. J eru, I. *et al.* Role of interleukin-1 β in NLRP12-associated autoinflammatory disorders and resistance to anti-interleukin-1 therapy. *Arthritis and Rheumatism* **63**, 2142–8 (2011).
284. Storek, K. M., Gertszovf, N. A., Ohlson, M. B. & Monack, D. M. cGAS and Ifi204 Cooperate To Produce Type I IFNs in Response to Francisella Infection. *The Journal of Immunology* **194**, 3236–3245 (2015).
285. Unterholzner, L. *et al.* IFI16 is an innate immune sensor for intracellular DNA. *Nature Immunology* **11**, 997–1004 (2010).

286. Kerur, N. *et al.* IFI16 acts as a nuclear pathogen sensor to induce the inflammasome in response to Kaposi Sarcoma-associated herpesvirus infection. *Cell Host & Microbe* **9**, 363–375 (2011).
287. Monroe, K. M. *et al.* IFI16 is an innate immune sensor for intracellular DNA. *Science* (2013).
288. Xiao, T. S. The nucleic acid-sensing inflammasomes. *Immunological Reviews* **265**, 103–111 (2015).
289. Li, P. *et al.* Mice deficient in IL-1 β -converting enzyme are defective in production of mature IL-1 β and resistant to endotoxic shock. *Cell* **80**, 401–411 (1995).
290. Wang, S. *et al.* Murine caspase-11, an ICE-interacting protease, is essential for the activation of ICE. *Cell* **92**, 501–9 (1998).
291. Kayagaki, N. *et al.* Non-canonical inflammasome activation targets caspase-11. *Nature* **479**, 117–21 (2011).
292. Schotte, P. *et al.* Cathepsin B-mediated activation of the proinflammatory caspase-11. *Biochemical and Biophysical Research Communications* **251**, 379–387 (1998).
293. Kayagaki, N. *et al.* Noncanonical inflammasome activation by intracellular LPS independent of TLR4. *Science* **130**, 1246–1249 (2013).
294. Rühl, S. & Broz, P. Caspase-11 activates a canonical NLRP3 inflammasome by promoting K⁺ efflux. *European Journal of Immunology* **45**, 2927–36 (2015).
295. Hagar, J. A., Powell, D. A., Aachoui, Y., Ernst, R. K. & Miao, E. A. Cytoplasmic LPS activates caspase-11: Implications in TLR4-independent endotoxic shock. *Science* **341**, 1250–1253 (2013).
296. Shi, J. *et al.* Inflammatory caspases are innate immune receptors for intracellular LPS. *Nature* (2014).
297. Aachoui, Y. *et al.* Caspase-11 protects against bacteria that escape the vacuole. *Science* (2013).
298. Broz, P. *et al.* Caspase-11 increases susceptibility to *Salmonella* infection in the absence of caspase-1. *Nature* **490**, 288–91 (2012).
299. Van De Craen, M. *et al.* Characterization of seven murine caspase family members. *FEBS Letters* **403**, 61–69 (1997).
300. Nakagawa, T. *et al.* Caspase-12 mediates endoplasmic-reticulum-specific apoptosis and cytotoxicity by amyloid-beta. *Nature* **403**, 98–103 (2000).
301. Saleh, M. *et al.* Differential modulation of endotoxin responsiveness by human caspase-12 polymorphisms. *Nature* **429**, 75–79 (2004).
302. Ferwerda, B. *et al.* Caspase-12 and the inflammatory response to *Yersinia pestis*. *PLoS One* **4** (2009).
303. Xue, Y. *et al.* Spread of an inactive form of caspase-12 in humans is due to recent positive selection. *American Journal of Human Genetics* **78**, 659–670 (2006).

304. Wang, X., Grus, W. E. & Zhang, J. Gene losses during human origins. *PLoS Biology* **4**, 0366–0377 (2006).
305. O'Brien, T. R. *et al.* HCV infection clearance with functional or non-functional caspase-12. *Scandinavian Journal of Gastroenterology* **42**, 416–417 (2007).
306. Roy, S. *et al.* Confinement of caspase-12 proteolytic activity to autoprocessing. *Proceedings of the National Academy of Sciences of the United States of America* **105**, 4133–4133 (2008).
307. Yoneda, T. *et al.* Activation of caspase-12, an endoplasmic reticulum (ER) resident caspase, through tumor necrosis factor receptor-associated factor 2-dependent mechanism in response to the ER stress. *Journal of Biological Chemistry* **276**, 13935–13940 (2001).
308. Saleh, M. *et al.* Enhanced bacterial clearance and sepsis resistance in caspase-12-deficient mice. *Nature* **440**, 1064–1068 (2006).
309. Labbe, K. *et al.* Caspase-12 dampens the immune response to malaria independently of the inflammasome by targeting NF- κ B signaling. *The Journal of Immunology* **185**, 5495–5502 (2010).
310. LeBlanc, P. M. *et al.* Caspase-12 modulates NOD signaling and regulates antimicrobial peptide production and mucosal immunity. *Cell Host & Microbe* **3**, 146–157 (2008).
311. Wang, P. *et al.* Caspase-12 controls West Nile virus infection via the viral RNA receptor RIG-I. *Nature Immunology* **11**, 912–9 (2010).
312. Skeldon, A. M. *et al.* Caspase-12, but not caspase-11, inhibits obesity and insulin resistance. *Journal of Immunology* **196**, 437–47 (2016).
313. Vande Walle, L. *et al.* Does caspase-12 suppress inflammasome activation? *Nature* **534**, E1–E4 (2016).
314. He, W.-T. *et al.* Gasdermin D is an executor of pyroptosis and required for interleukin-1 β secretion. *Cell Research* **25**, 1285–1298 (2015).
315. Tamura, M. *et al.* Members of a novel gene family, Gsdm, are expressed exclusively in the epithelium of the skin and gastrointestinal tract in a highly tissue-specific manner. *Genomics* **89**, 618–629 (2007).
316. Saeki *et al.* Gasdermin (Gsdm) localizing to mouse chromosome 11 is predominantly expressed in upper gastrointestinal tract but significantly suppressed in human gastric cancer cells. *Mammalian Genome* **11**, 718–724 (2000).
317. Ding, J. *et al.* Pore-forming activity and structural autoinhibition of the gasdermin family. *Nature* **535**, 111–6 (2016).
318. Sborgi, L. *et al.* GSDMD pore formation in the plasma membrane constitutes the mechanism of pyroptotic cell death. *The EMBO Journal*, 1–13 (2016).

319. Liu, X. *et al.* Inflammasome-activated gasdermin D causes pyroptosis by forming membrane pores. *Nature* **535**, 153–158 (2016).
320. Aglietti, R. A. *et al.* GsdmD p30 elicited by caspase-11 during pyroptosis forms pores in membranes. *Proceedings of the National Academy of Sciences of the United States of America*, 201607769 (2016).
321. Sborgi, L. *et al.* Structure and assembly of the mouse ASC inflammasome by combined NMR spectroscopy and cryo-electron microscopy. *Proceedings of the National Academy of Sciences of the United States of America* **112**, 13237–13242 (2015).
322. Dick, M. S., Sborgi, L., Rühl, S., Hiller, S. & Broz, P. ASC filament formation serves as a signal amplification mechanism for inflammasomes. *Nature Communications* **7**, 1–12 (2016).
323. Dinarello, C. A., Simon, A. & van der Meer, J. W. M. Treating inflammation by blocking interleukin-1 in a broad spectrum of diseases. *Nature Reviews Drug Discovery* **11**, 633–652 (2012).
324. LaRock, C. N. *et al.* IL-1 β is an innate immune sensor of microbial proteolysis. *Science Immunology* **1**, 1–8 (2016).
325. Dixit, V. D. Nlrp3 inflammasome activation in type 2 diabetes: Is it clinically relevant? *Diabetes* **62**, 22–24 (2013).
326. Haneklaus, M. & O’Neill, L. A. J. NLRP3 at the interface of metabolism and inflammation. *Immunological Reviews* **265**, 53–62 (2015).
327. Kingsbury, S. R., Conaghan, P. G. & McDermott, M. F. The role of the NLRP3 inflammasome in gout. *Journal of Inflammation Research* **4**, 39–49 (2011).
328. Saco, T., Parthasarathy, P. T., Cho, Y., Lockey, R. F. & Kolliputi, N. Inflammasome: a new trigger of Alzheimer’s disease. *Frontiers in Aging Neuroscience* (2014).
329. Kolb, R. *et al.* Obesity-associated NLRC4 inflammasome activation drives breast cancer progression. *Nature Communications* **7**, 1–12 (2016).
330. Coll, R. C. *et al.* A small-molecule inhibitor of the NLRP3 inflammasome for the treatment of inflammatory diseases. *Nature Medicine* **21**, 248–55 (2015).
331. Youm, Y.-H. *et al.* The ketone metabolite β -hydroxybutyrate blocks NLRP3 inflammasome-mediated inflammatory disease. *Nature Medicine* **21**, 263–269 (2015).
332. Jabaut, J., Ather, J. L., Taracanova, A., Poynter, M. E. & Ckless, K. Mitochondria-targeted drugs enhance Nlrp3 inflammasome-dependent IL-1 β secretion in association with alterations in cellular redox and energy status. *Free Radical Biology and Medicine* **60**, 233–245 (2013).
333. Isakov, E., Weisman-Shomer, P. & Benhar, M. Suppression of the pro-inflammatory NLRP3/interleukin-1 β pathway in macrophages by the thioredoxin reductase inhibitor auranofin. *Biochimica et Biophysica Acta* **1840**, 3153–3161 (2014).

334. Vande Walle, L. *et al.* Negative regulation of the NLRP3 inflammasome by A20 protects against arthritis. *Nature* **512**, 69–73 (2014).
335. Wang, G. *et al.* Endoplasmic reticulum stress mediates the anti-inflammatory effect of ethyl pyruvate in endothelial cells. *PLoS One* **9**, 1–16 (2014).
336. Rhen, T. & Cidlowski, J. A. Antiinflammatory action of glucocorticoids - New mechanisms for old drugs. *The New England Journal of Medicine* **353**, 1711–1723 (2005).
337. Hermann, M., Cermak, T., Voytas, D. F. & Pelczar, P. Mouse genome engineering using designer nucleases. *Journal of Visualized Experiments* **2**, 1–11 (2014).
338. Koressaar, T. & Remm, M. Enhancements and modifications of primer design program Primer3. *Bioinformatics* **23**, 1289–1291 (2007).
339. Untergasser, A. *et al.* Primer3 - new capabilities and interfaces. *Nucleic Acids Research* **40**, 1–12 (2012).
340. Notredame, C., Higgins, D. G. & Heringa, J. T-Coffee: A novel method for fast and accurate multiple sequence alignment. *Journal of Molecular Biology* **302**, 205–17 (2000).
341. Gross, O. Measuring the Inflammasome. *Methods in Molecular Biology* **844**, 199–222 (2012).
342. Fink, S. L. & Cookson, B. T. Caspase-1-dependent pore formation during pyroptosis leads to osmotic lysis of infected host macrophages. *Cellular Microbiology* **8**, 1812–1825 (2006).
343. Frank, A. & Rauen, U. Protection by glycine against hypoxic injury of rat hepatocytes: Inhibition of ion fluxes through nonspecific leaks. *Journal of Hepatology* **32**, 56–66 (2000).
344. Lopez-Castejon, G. & Brough, D. Understanding the mechanism of IL-1 β secretion. *Cytokine and Growth Factor Reviews* **22**, 189–195 (2011).
345. Hoffman, H. M. & Broderick, L. The role of the inflammasome in patients with autoinflammatory diseases. *The Journal of Allergy and Clinical Immunology* **139**, 3–14 (2016).
346. Dalbeth, N., Merriman, T. R. & Stamp, L. K. Gout. *The Lancet* **6736**, 1–14 (2016).
347. Zhong, Z., Sanchez-Lopez, E. & Karin, M. Autophagy, NLRP3 inflammasome and auto-inflammatory / immune diseases. *Clinical and Experimental Rheumatology* **34**, 12–16 (2016).
348. Lin, S.-C., Lo, Y.-C. & Wu, H. Helical assembly in the MyD88-IRAK4-IRAK2 complex in TLR/IL-1R signalling. *Nature* **465**, 885–890 (2010).
349. Qiao, Q. *et al.* Structural architecture of the CARMA1/Bcl10/MALT1 signalosome: Nucleation-induced filamentous assembly. *Molecular Cell* **51**, 766–779 (2013).

350. Fu, T.-M. *et al.* Cryo-EM structure of caspase-8 tandem DED filament reveals assembly and regulation mechanisms of the death-inducing signaling complex. *Molecular Cell* **64**, 236–250 (2016).
351. Wu, B. *et al.* Molecular imprinting as a signal-activation mechanism of the viral RNA sensor RIG-I. *Molecular Cell* **55**, 511–523 (2014).
352. Kagan, J. C., Magupalli, V. G. & Wu, H. SMOCs: Supramolecular organizing centres that control innate immunity. *Nature Reviews Immunology* **14**, 821–826 (2014).
353. Chen, Q., Sun, L. & Chen, Z. J. Regulation and function of the cGAS–STING pathway of cytosolic DNA sensing. *Nature Immunology* **17**, 1142–1149 (2016).
354. Schmidt, F. I. *et al.* A single domain antibody fragment that recognizes the adaptor ASC defines the role of ASC domains in inflammasome assembly. *The Journal of Experimental Medicine* **213**, 771–90 (2016).
355. Xie, J. & Belosevic, M. Functional characterization of apoptosis-associated speck-like protein (ASC) of the goldfish (*Carassius auratus* L.) *Developmental & Comparative Immunology* **65**, 201–210 (2016).
356. Masumoto, J. *et al.* Caspy, a zebrafish caspase, activated by ASC oligomerization is required for pharyngeal arch development. *Journal of Biological Chemistry* **278**, 4268–4276 (2003).
357. Li, S. *et al.* Cloning and characterization of apoptosis-associated speck-like protein containing a CARD domain (ASC) gene from Japanese flounder *Paralichthys olivaceus*. *Fish and Shellfish Immunology* **54**, 294–301 (2016).
358. Sun, Y. *et al.* Molecular cloning and expression analysis of the ASC gene from mandarin fish and its regulation of NF- κ B activation. *Developmental & Comparative Immunology* **32**, 391–9 (2008).
359. Kurian, K. M., Watson, C. J. & Wyllie, A. H. Retroviral Vectors. *Molecular Pathology* **53**, 173–176 (2000).
360. Hsu, P. D., Lander, E. S. & Zhang, F. Development and applications of CRISPR-Cas9 for genome engineering. *Cell* **157**, 1262–1278 (2014).
361. Meunier, E. *et al.* Caspase-11 activation requires lysis of pathogen-containing vacuoles by IFN-induced GTPases. *Nature* **509**, 366–370 (2014).

6 Appendix

6.1 Research article III

Caspase-11 activation requires lysis of pathogen-containing vacuoles by IFN-induced GTPases

E. Meunier, **M. S. Dick***, R. F. Dreier*, N. Schürmann, D. Kenzelmann Broz, S. Warming, M. Roose-Girma, D. Bumann, N. Kayagaki, K. Takeda, M. Yamamoto and P. Broz.

* denotes equal contribution.

Nature

2014 May 15; 509(7500):366-790. doi: 10.1038/nature13157.³⁶¹

Statement of contribution

I performed multiple control experiments including infections with *Burkholderia* and Western blots. Furthermore, I assessed the possibility that GBPs can directly kill bacteria by expressing them in *E. coli*, generating results that were not included in the final manuscript. I was further involved in the discussion of the results and writing of the manuscript.

LETTER

doi:10.1038/nature13157

Caspase-11 activation requires lysis of pathogen-containing vacuoles by IFN- γ -induced GTPasesEtienne Meunier¹, Mathias S. Dick^{1*}, Roland F. Dreier^{1*}, Nura Schürmann¹, Daniela Kenzelmann Broz², Søren Warming³, Merone Roose-Girma³, Dirk Bumann¹, Nobuhiko Kayagaki³, Kiyoshi Takeda⁴, Masahiro Yamamoto⁴ & Petr Broz¹

Lipopolysaccharide from Gram-negative bacteria is sensed in the host cell cytoplasm by a non-canonical inflammasome pathway that ultimately results in caspase-11 activation and cell death^{1–3}. In mouse macrophages, activation of this pathway requires the production of type-I interferons^{4,5}, indicating that interferon-induced genes have a critical role in initiating this pathway. Here we report that a cluster of small interferon-inducible GTPases, the so-called guanylate-binding proteins, is required for the full activity of the non-canonical caspase-11 inflammasome during infections with vacuolar Gram-negative bacteria. We show that guanylate-binding proteins are recruited to intracellular bacterial pathogens and are necessary to induce the lysis of the pathogen-containing vacuole. Lysis of the vacuole releases bacteria into the cytosol, thus allowing the detection of their lipopolysaccharide by a yet unknown lipopolysaccharide sensor. Moreover, recognition of the lysed vacuole by the danger sensor galectin-8 initiates the uptake of bacteria into autophagosomes, which results in a reduction of caspase-11 activation. These results indicate that host-mediated lysis of pathogen-containing vacuoles is an essential immune function and is necessary for efficient recognition of pathogens by inflammasome complexes in the cytosol.

Previous studies have reported that induction of caspase-11-dependent cell death by Gram-negative bacteria requires Trif-dependent production of type-I interferons (type-I-IFNs)^{4,5} (Extended Data Fig. 1a). Type-I-IFN production is however not required for pro-caspase-11 induction^{4,6,7} and is dispensable for caspase-11 activation by transfected lipopolysaccharide (LPS; Extended Data Fig. 1b)². This indicates that interferon-stimulated genes (ISGs) play a major role in activating caspase-11 in response to intracellular bacteria. To investigate which ISGs were involved in activating caspase-11, we used proteomics-based expression analysis to identify proteins that were highly induced following *Salmonella* infection. Among the most strongly upregulated proteins were interferon-induced GTPases, such as the large 65–67 kDa guanylate-binding proteins (GBPs) and small 47 kDa immunity-related GTPases (IRGs) (data not shown). These proteins function in cell-autonomous immunity, that is, mechanisms that allow host cells to kill pathogens or restrict their replication, and have even been associated with the activation of inflammasomes^{8–10}.

Mice have 11 GBPs, which are highly homologous and are clustered in two genomic loci on chromosomes 3 and 5, respectively^{8,11}. Recently, GBPs on chromosome 3 have been shown to restrict the replication of *Toxoplasma gondii* in peritoneal macrophages and mice¹¹. We therefore infected bone-marrow-derived macrophages (BMDMs) from *Gbp^{chr3}* KO mice, which lack GBP1, 2, 3, 5 and 7 (Extended Data Fig. 2a–e), and wild-type littermates with a number of Gram-negative vacuolar pathogens that trigger caspase-11 activation (data not shown)^{14,5} and determined the activity of the non-canonical inflammasome pathway at 16 h post-infection (Fig. 1a, b). Macrophages from *Gbp^{chr3}* KO mice showed a significant reduction of cell death (as measured by lactate dehydrogenase (LDH) release) and IL-1 β secretion when infected with wild-type *Salmonella typhimurium*, a type three secretion system (T3SS)-deficient

mutant of *S. typhimurium* (Δ SP1-2), *Vibrio cholerae*, *Enterobacter cloacae* or *Citrobacter koseri* (Fig. 1a), and this was independent of LPS or polyinosinic:polycytidylic acid (poly(I:C)) priming (Extended Data Fig. 2f, g). *Gbp^{chr3}*-deficiency also reduced secretion of caspase-1 p20 subunit, caspase-11 and mature IL-1 β , IL-18 and IL-1 α (Fig. 1b). Because interferons induce GBP expression (Extended Data Fig. 2b, c)³, we investigated whether IFN- γ treatment would accelerate LDH release in response to *Salmonella* infection. IFN- γ -treated wild-type BMDMs released LDH as soon as 4 h after infection, whereas *Gbp^{chr3}* KO BMDMs failed to release LDH at early time points even after IFN- γ priming (Fig. 1c), indicating that GBP induction was required for activity of the non-canonical inflammasome pathway.

We next explored whether GBPs play a role in the activation of canonical inflammasomes. LPS-primed wild-type and *Gbp^{chr3}*-deficient macrophages released comparable levels of LDH and mature IL-1 β when infected with logarithmic phase *S. typhimurium*, which exclusively engage the NLR4 inflammasome via the SPI-1 T3SS (Fig. 1d)¹². Similarly, *Gbp^{chr3}*-deficiency did not affect AIM2 inflammasome activation upon poly (deoxyadenylic-deoxythymidylic acid (poly(dA:dT)) transfection (Fig. 1d). Although GBP5 had been previously linked to NLRP3 activation⁹, we did not observe a defect in NLRP3 activation in *Gbp^{chr3}* KO mice (Fig. 1d), possibly owing to different modes of pre-stimulation. These data indicate that GBPs are dispensable for canonical inflammasome activity, but are required for the activation of the non-canonical inflammasome pathway.

To investigate whether GBPs directly mediated the detection of intracellular LPS, we engaged the non-canonical inflammasome by transfecting macrophages with different types of ultra-pure LPS (Fig. 1e). Cytoplasmic LPS triggered LDH release and IL-1 β secretion to a similar extent in both wild-type and *Gbp^{chr3}*-deficient BMDMs, indicating that GBPs were required upstream of LPS sensing and only during bacterial infection. We next investigated if GBPs were required for immune detection of vacuolar or cytosolic bacteria by infecting BMDMs with *ΔsifA S. typhimurium* and *Burkholderia thailandensis*, which rapidly enter the cytosol and activate caspase-11 (ref. 13). Unprimed *Gbp^{chr3}* KO and wild-type BMDMs responded comparably to these bacteria (Extended Data Fig. 3a–c). Because GBPs might affect this response when pre-induced, we also infected IFN- γ -primed BMDMs with *ΔsifA S. typhimurium* (Extended Data Fig. 3d). IFN- γ -priming indeed resulted in a small difference between wild-type and *Gbp^{chr3}* KO BMDMs after infection with *ΔsifA Salmonella*, yet not to the extent seen with wild-type *Salmonella* (Fig. 1c), indicating that GBPs mainly participate in the activation of the non-canonical inflammasome by vacuolar bacteria.

Finally, to investigate which GBP controls caspase-11 activation, all 11 murine *Gbps* were individually knocked down in BMDMs and the cells were infected with flagellin-deficient *Salmonella*, which activate the non-canonical inflammasome but not NLR4 (Extended Data Fig. 4a and Supplementary Information)⁴. Only knockdown of *Gbp2* resulted in reduced LDH release and IL-1 β secretion (Extended Data Fig. 4b–d).

¹Focal Area Infection Biology, Biozentrum, University of Basel, CH-4056 Basel, Switzerland. ²Department Biomedicine, University of Basel, CH-4056 Basel, Switzerland. ³Genentech Inc., South San Francisco, California 94080, USA. ⁴Department of Microbiology and Immunology, Osaka University, Yamadaoka, Suita, Osaka 565-0871, Japan.

*These authors contributed equally to this work.

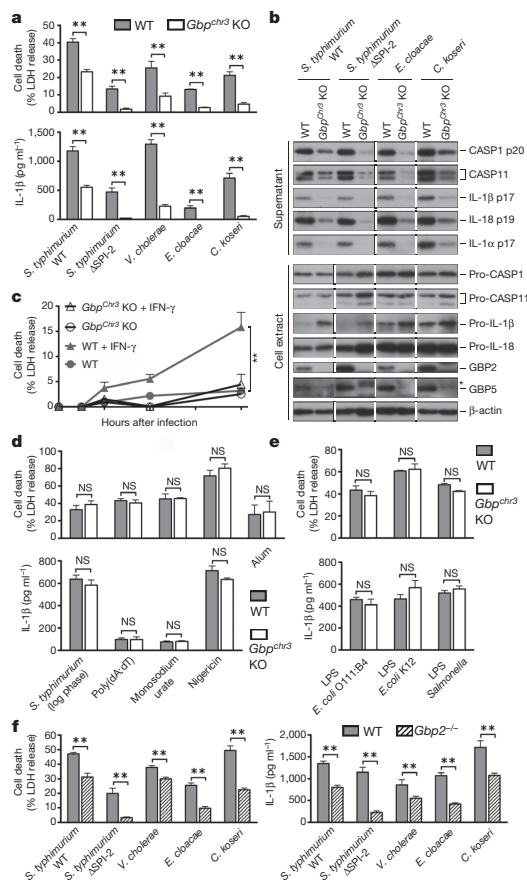


Figure 1 | Caspase-11 activation by intracellular bacterial pathogens requires GBPs. **a, b.** LDH release, IL-1 β secretion (**a**) and immunoblots for caspase-1, caspase-11, IL-1 β , IL-18 and IL-1 α (**b**) from unprimed BMDMs infected for 16 h with the indicated bacteria (grown to stationary phase). **c.** Time course measuring LDH release from unprimed or IFN- γ -primed BMDMs infected with *S. typhimurium*. **d, e.** LDH release and IL-1 β secretion from primed BMDMs infected with SPI-1-expressing logarithmic phase *S. typhimurium*, treated with monosodium urate, alum and nigericin or transfected with poly(dA:dT) and LPS. **f.** LDH release and IL-1 β secretion from unprimed wild-type and *Gbp2*^{-/-} BMDMs infected for 16 h with the indicated bacteria (grown to stationary phase). Graphs show mean and s.d. of quadruplicate wells and data are representative of two (**b**) and three (**a, c–f**) independent experiments. *Crossreactive band; ** $p < 0.01$; NS, not significant (two-tailed *t*-test).

To validate these data we obtained BMDMs from *Gbp2*^{-/-} mice and wild-type littermates¹⁴ and infected them with vacuolar Gram-negative bacteria. As expected, we observed reduced levels of cell death, cytokine secretion and caspase release in *Gbp2*^{-/-} BMDMs, indicating attenuated activation of the non-canonical inflammasome (Fig. 1f and Extended Data Fig. 4e), whereas direct LPS sensing or the activation of canonical inflammasomes was not affected (Extended Data Fig. 4f, g). In contrast, *Gbp5*-deficiency did not have any effect on canonical and non-canonical inflammasome activation (Extended Data Fig. 5). Nevertheless, *Gbp2*-deficiency did not reduce caspase-11 activation as markedly as *Gbpchr3*-deficiency, indicating that whereas caspase-11 activation mainly requires GBP2, other GBPs might also be partially involved.

Reduced numbers of intracellular bacteria could account for low levels of caspase-11 activation in *Gbpchr3*- and *Gbp2*-deficient macrophages. However, a comparison of wild-type and *Gbpchr3* KO BMDMs showed that *Gbpchr3*-deficiency resulted in significantly higher numbers of total and live *Salmonella* per cell (Fig. 2a), consistent with higher colony forming units numbers in *Gbpchr3* KO BMDMs (Extended Data Fig. 6). In addition, fluorescence-activated cell sorting (FACS)-based analysis of dead (mCherry-negative, FITC⁺) and live (mCherry-positive, FITC⁺) *Salmonella* at 16 h post-infection found significantly fewer dead bacteria (~20%) in *GBPchr3* KO and *Gbp2*^{-/-} BMDMs when compared to wild-type BMDMs (>30%) (Fig. 2b). Importantly, bacterial killing in *Casp11*^{-/-} BMDMs was comparable to wild-type BMDMs, indicating that the control of bacterial replication was directly linked to GBP function and not to the activation of the non-canonical inflammasome (Fig. 2b). In conclusion, we show that GBPs control bacterial replication on a cell-autonomous level, which is consistent with a previous report that GBP1 partially restricts *Mycobacterium bovis* and *Listeria monocytogenes* replication¹⁰.

Restricting bacterial replication has been proposed to require the association of GBPs with pathogen-containing vacuoles and the recruitment of antimicrobial factors⁸. We therefore investigated whether GBPs targeted intracellular Gram-negative bacteria. Indeed, GBP2 could be detected on intracellular bacteria within hours after infection (Fig. 2c). Very little GBP-positive bacteria were detected in *Stat1*^{-/-} BMDMs, which do not respond to type-I- and type-II-IFNs and largely failed to induce GBP expression (data not shown). Remarkably, GBP-positive *Salmonella* seemed to have lost mCherry expression (Fig. 2c), indicating that these bacteria were dead. To determine whether GBPs are recruited to dead bacteria we infected BMDMs with *Salmonella* killed by heat, paraformaldehyde or 70% ethanol treatment, yet only live *Salmonella* acquired GBP staining and activated the inflammasome (Fig. 2d). To examine this mechanism *in vivo*, we immunostained spleen tissue sections of mice infected with *Salmonella* for GBPs. Indeed, GBPs could also be found associated with approximately 20% of bacteria *in vivo*, and a significantly higher proportion of these bacteria were dead, based on the loss of mCherry expression (Fig. 2e–g). Furthermore, treatment with IFN- γ -neutralizing antibodies reduced the percentage of GBP-positive bacteria (Fig. 2f), consistent with reports that IFN- γ controls *Salmonella* replication *in vivo*^{15,16}. Taken together, these results indicated that GBPs either kill bacteria directly or control an antimicrobial effector pathway, and raised the interesting possibility that GBP-mediated killing of bacteria might result in the release of LPS and caspase-11 activation^{2,3}.

To identify the antimicrobial effector pathway that is controlled by GBPs we first examined the role of free radicals⁸. Although GBP7 was reported to be required for reactive oxygen species (ROS) production and to interact with the phagosome oxidase complex¹⁰, we did not find any role for ROS or NO production in caspase-11 activation (Extended Data Fig. 7). Furthermore, GBPs were also proposed to recruit components of the autophagy machinery to pathogen-containing vacuoles (PCVs), possibly resulting in bacterial killing within autophagosomes^{8,10}. Indeed, many GBP-positive *S. typhimurium*, *E. cloacae* and *C. koseri* co-stained for the commonly used autophagy marker LC3 (Fig. 3a and Extended Data Fig. 8a). Recruitment of LC3 to intracellular *Salmonella* was partially GBP-dependent, because we found significantly lower numbers of LC3-positive *Salmonella* in *Gbpchr3* KO compared to wild-type macrophages (Fig. 3b, c). Therefore, we speculated that autophagy-mediated killing might result in the release of LPS from bacteria and caspase-11 activation. Unexpectedly, however, pharmacological inhibition of autophagy with 3-methyladenine (3-MA) resulted in significantly higher levels of LDH release, IL-1 β secretion and caspase-1/caspase-11 activation in macrophages infected with *S. typhimurium*, *E. cloacae* or *C. koseri* (Fig. 3d, e), indicating increased activation of the non-canonical inflammasome. Consistently, cell death was still caspase-11-dependent because *Casp11*^{-/-} BMDMs did not release LDH when treated with 3-MA and infected with Gram-negative bacteria (Fig. 3f). Direct activation of caspase-11 by LPS transfection was independent of

RESEARCH LETTER

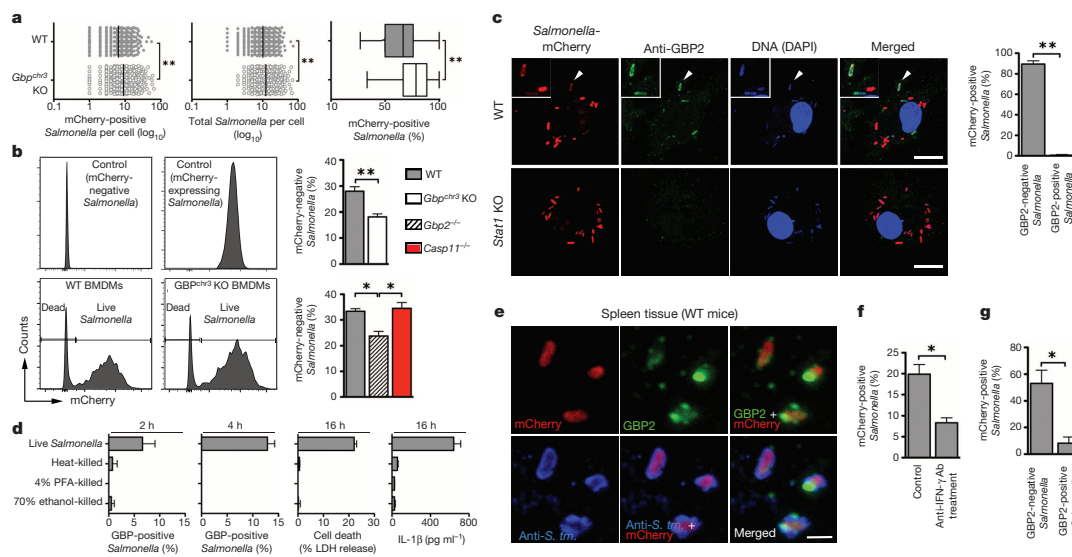


Figure 2 | GBPs control bacterial replication. **a, b**, Quantification of live (mCherry-positive) and dead (mCherry-negative) *S. typhimurium* per cell by immunofluorescence (**a**) or as percent of total by flow-cytometry (**b**) in unprimed BMDMs at 16 h post-infection. **c**, Immunostaining for GBP2 and quantification of live and dead *Salmonella* at 4 h post-infection. Arrowheads, bacteria shown in insets. **d**, Quantification of GBP-positive bacteria, LDH release and IL-1 β secretion at indicated time points from BMDMs infected with *Salmonella*, live or killed by different means. **e**, Immunohistochemistry for

GBP2 and *Salmonella* on spleen tissue from *Salmonella* (mCherry-positive)-infected mice (representative of $n = 3$ per group). *S. tm.*, *S. typhimurium*. **f, g**, Quantification of GBP-positive *Salmonella* in anti-IFN- γ -treated or control animals (**f**) and live and dead bacteria among GBP2-negative/-positive *Salmonella* (**g**) ($n = 3$ per group). Scale bars, 10 μm (**c**), 1 μm (**e**). Graphs show mean and 5–95 percentile (box plots) or s.d. of technical triplicates, and data are representative of three independent experiments. * $P < 0.05$, ** $P < 0.01$ (two-tailed *t*-test).

autophagy (Fig. 3g), indicating that autophagy only counteracts non-canonical inflammasome activation during bacterial infections. To further confirm our data, we infected *Atg5*^{-/-} BMDMs with *S. typhimurium* and we also observed significantly higher levels of non-canonical inflammasome activation compared to wild-type BMDMs (Fig. 3h, i). Taken together, these results indicated that, although GBPs promoted the uptake of bacteria into autophagosomes, autophagy actually counteracted caspase-11 activation. Thus, GBP-dependent LPS detection occurs before bacteria are targeted to autophagosomes.

A possible explanation could be that autophagy sequesters bacteria that had escaped from the vacuole, and thus prevents further LPS release into the cytosol. Recently, the cytosolic danger receptor galectin-8 was reported to function as a marker for lysed vacuoles. Galectin-8 binds β -galactosides, which are normally found on the inner leaflet of the vacuolar membrane and get exposed to the cytosol upon vacuolar lysis¹⁷. Indeed, quantification of galectin-8-positive *Salmonella* showed that significantly fewer bacteria were targeted by galectin-8 in *Gbp*^{chr3} KO BMDMs than in wild-type macrophages (Fig. 4a). Because galectin-8 colocalized with GBP- and LC3-positive *Salmonella* (Fig. 4b, c), we speculated that GBPs promote LC3 recruitment through galectin-8. Consistently, we found lower levels of galectin-8-positive *Salmonella* among LC3-positive *Salmonella* in *Gbp*^{chr3} KO compared to wild-type BMDMs (Fig. 4d). Galectin-8 interacts with the autophagy adaptor protein NDP52, which in humans contains binding sites for galectin-8, ubiquitin and LC3¹⁸. In line with a role for NDP52 in linking galectin-8 to LC3, murine NDP52 colocalized with galectin-8 on intracellular *Salmonella* (Extended Data Fig. 8b). Targeting of *Salmonella* to autophagosomes might also involve other autophagy cargo adaptors, because p62 was associated with the majority of LC3-positive bacteria, yet this was independent of GBPs (Extended Data Fig. 8c, d). Altogether, these results suggested that GBPs might promote the lysis of vacuoles or help to recruit galectin-8 to lysed vacuoles.

To confirm a direct role of GBPs in vacuolar lysis, we adapted a phagosome integrity assay based on differential permeabilization with digitonin (Extended Data Fig. 9). Comparing wild-type and *Gbp*^{chr3} KO BMDMs, we found significantly lower numbers of cytosolic (FITC⁺) *S. typhimurium* in *Gbp*^{chr3}-deficient cells (Fig. 4e, f). Similarly, *Gbp2*^{-/-} BMDMs also harboured fewer cytosolic *S. typhimurium* compared to BMDMs from wild-type littermates (Fig. 4g). In contrast, we did not find a defect in cytosolic localization between wild-type and *Gbp*^{chr3} KO BMDMs infected with the specialized cytosolic pathogen *Shigella flexneri*, which uses its T3SS to destabilize the phagosome and escape into the cytoplasm (Fig. 4h)¹⁹. Although we cannot exclude that GBPs might also be involved in the recruitment or assembly of the non-canonical inflammasome, these results indicate that GBPs, in particular GBP2, directly promote the destruction of vacuoles.

In conclusion, our data demonstrate that host-induced destruction of PCVs or phagosomes is an essential immune function and assures recognition of vacuolar bacteria by cytosolic innate immune sensors (Extended Data Fig. 10). Additional studies are required to determine how GBPs distinguish 'self' and 'non-self' membranes and by which mechanism phagosomes are lysed. In mice, this might involve the IRGM proteins that can act as GDI (guanine nucleotide dissociation inhibitor) and inhibit IRG and GBP activity. Absence of IRGMs results in mislocalization of both IRGs and GBPs and even in degradation of lipid droplets^{20–22}, supporting a model in which IRGM proteins would protect 'self'-vacuoles from being targeted by host IRGs and GBPs²³. Because both commensals and pathogens activate caspase-11 (ref. 1), it can be assumed that GBPs are not specific towards pathogens but are a general innate immune response against bacteria trapped in the phagosomes of macrophages. Finally, given the important role of LPS-induced caspase-11 activation in septic shock^{1–3}, pharmaceutical targeting of the above-described pathways might be used to modulate inflammation during bacterial sepsis.

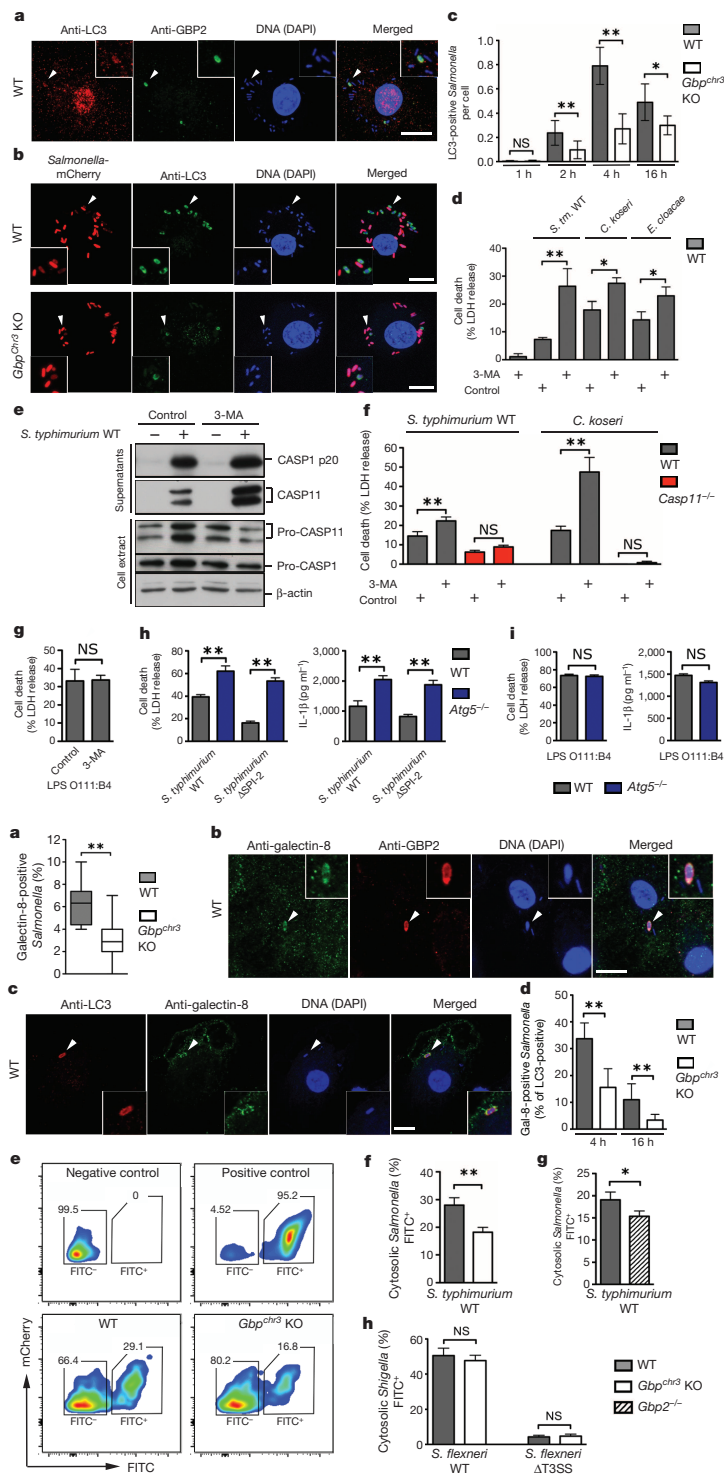


Figure 3 | Autophagy reduces caspase-11 activation. **a, b**, Unprimed BMDMs infected with *S. typhimurium* for 4 h and immunostained for LC3 and GBP2. Arrowheads, bacteria shown in insets. Scale bars, 10 μm . **c**, Quantification of results from **b**. **d–g**, LDH release and immunoblots for caspase-1 and caspase-11 from BMDMs infected for 16 h or transfected with LPS in presence or absence of 3-methyladenine (3-MA). **h, i**, LDH release and IL-1 β secretion from BMDMs infected for 16 h or transfected with LPS. Graphs show mean and s.d. of quadruplicate wells and data are representative of two (**e, i**) and three (**a–d, f–h**) independent experiments. * $P < 0.05$, ** $P < 0.01$; NS, not significant (two-tailed *t*-test).

Figure 4 | GBP-mediated lysis of the PCV releases *Salmonella* into the cytosol. **a**, Quantification of galectin-8-positive *Salmonella* in unprimed BMDMs at 4 h post-infection. **b, c**, Unprimed BMDMs infected with *S. typhimurium* for 4 h and immunostained for galectin-8, GBP2 and LC3. Arrowheads, bacteria shown in insets. Scale bars, 10 μm . **d**, Quantification of galectin-8/LC3-double-positive *Salmonella* at indicated time points post-infection. **e–h**, Quantification of cytosolic and vacuolar bacteria by flow cytometry in BMDMs infected with mCherry-positive *S. typhimurium* (**e–g**) or *S. flexneri* (**h**, wild-type or ΔT3SS) for 4 h. Graphs show mean and s.d. or 5–95 percentile (Box plots) of technical triplicates. Data are representative of 2 (**g, h**), 3 (**a–d**) and 4 (**e, f**) independent experiments. * $P < 0.05$, ** $P < 0.01$ (two-tailed *t*-test).

RESEARCH LETTER

METHODS SUMMARY

BMDMs were cultured and seeded for infections as described previously⁴. Priming was done overnight with PAM3CSK4 (1 µg ml⁻¹), LPS O111:B4 (0.1 µg ml⁻¹), murine IFN-β or murine IFN-γ (1 unit per µl). *S. typhimurium*, *S. flexneri*, *V. cholerae*, *E. cloacae*, *C. koseri* and *B. thailandensis* were grown overnight in LB or TSB medium at 37 °C with aeration. Bacteria were diluted in fresh pre-warmed macrophage medium and added to the macrophages at a multiplicity of infection (m.o.i.) of 100:1 for measurements of caspase-11 and caspase-1 activity or 10:1 for all other assays. For assaying NLR4 activation, *Salmonella* were subcultured for 4 h to induce SPI-1 T3SS expression before infection (m.o.i. 20:1). *S. flexneri* were subcultured for 3 h to induce T3SS expression before infection (m.o.i. 30:1). When required, apocynin, L-NG-nitroarginine methyl ester (L-NAME), 3-methyladenine or vehicle controls were added 30 min before infection. Plates were centrifuged for 15 min at 500g to synchronize the infection and placed at 37 °C for 1 h. Next, 100 µg ml⁻¹ gentamycin was added to kill extracellular bacteria. After 1 h incubation, the cells were washed once with DMEM and given fresh macrophage medium containing 10 µg ml⁻¹ gentamicin for the remainder of the infection. Transfection with poly(dA:dT) or MSU, alum or nigericin treatment was done as described previously² or as indicated. All animal experiments were approved and performed according to local guidelines. Female BALB/c mice (10–14 weeks old) were infected intravenously with *Salmonella* (1,000 c.f.u.) and euthanized 4–5 days later. For antibody injections, mice received on day 3 two intraperitoneal injections of 200 µl PBS containing 0.2 mg anti-IFN-γ monoclonal or 0.2 mg rat IgG1, κ isotype control antibody.

Online Content Any additional Methods, Extended Data display items and Source Data are available in the online version of the paper; references unique to these sections appear only in the online paper.

Received 31 October 2013; accepted 14 February 2014.

Published online 16 April 2014.

- Kayagaki, N. *et al.* Non-canonical inflammasome activation targets caspase-11. *Nature* **479**, 117–121 (2011).
- Kayagaki, N. *et al.* Noncanonical inflammasome activation by intracellular LPS independent of TLR4. *Science* **341**, 1246–1249 (2013).
- Hagar, J. A., Powell, D. A., Aachoui, Y., Ernst, R. K. & Miao, E. A. Cytoplasmic LPS activates caspase-11: implications in TLR4-independent endotoxemic shock. *Science* **341**, 1250–1253 (2013).
- Broz, P. *et al.* Caspase-11 increases susceptibility to *Salmonella* infection in the absence of caspase-1. *Nature* **490**, 288–291 (2012).
- Rathinam, V. A. *et al.* TRIF licenses caspase-11-dependent NLRP3 inflammasome activation by Gram-negative bacteria. *Cell* **150**, 606–619 (2012).
- Case, C. L. *et al.* Caspase-11 stimulates rapid flagellin-independent pyroptosis in response to *Legionella pneumophila*. *Proc. Natl Acad. Sci. USA* **110**, 1851–1856 (2013).
- Casson, C. N. *et al.* Caspase-11 activation in response to bacterial secretion systems that access the host cytosol. *PLoS Pathog.* **9**, e1003400 (2013).
- MacMicking, J. D. Interferon-inducible effector mechanisms in cell-autonomous immunity. *Nature Rev. Immunol.* **12**, 367–382 (2012).

- Shenoy, A. R. *et al.* GBP5 promotes NLRP3 inflammasome assembly and immunity in mammals. *Science* **336**, 481–485 (2012).
- Kirn, B. H. *et al.* A family of IFN-gamma-inducible 65-kD GTPases protects against bacterial infection. *Science* **332**, 717–721 (2011).
- Yamamoto, M. *et al.* A cluster of interferon-gamma-inducible p65 GTPases plays a critical role in host defense against *Toxoplasma gondii*. *Immunity* **37**, 302–313 (2012).
- Broz, P. *et al.* Redundant roles for inflammasome receptors NLRP3 and NLRC4 in host defense against *Salmonella*. *J. Exp. Med.* **207**, 1745–1755 (2010).
- Aachoui, Y. *et al.* Caspase-11 protects against bacteria that escape the vacuole. *Science* **339**, 975–978 (2013).
- Degrandi, D. *et al.* Murine guanylate binding protein 2 (mGBP2) controls *Toxoplasma gondii* replication. *Proc. Natl Acad. Sci. USA* **110**, 294–299 (2013).
- VanCott, J. L. *et al.* Regulation of host immune responses by modification of *Salmonella* virulence genes. *Nature Med.* **4**, 1247–1252 (1998).
- Burton, N. A. *et al.* Disparate impact of oxidative host defenses determines the fate of *Salmonella* during systemic infection in mice. *Cell Host Microbe* **15**, 72–83 (2014).
- Thurston, T. L., Wandel, M. P., von Muhlinen, N., Foeglein, A. & Randow, F. Galectin 8 targets damaged vesicles for autophagy to defend cells against bacterial invasion. *Nature* **482**, 414–418 (2012).
- Deretic, V., Saitoh, T. & Akira, S. Autophagy in infection, inflammation and immunity. *Nature Rev. Immunol.* **13**, 722–737 (2013).
- Paetzold, S., Lourido, S., Raupach, B. & Zychlinsky, A. *Shigella flexneri* phagosomal escape is independent of invasion. *Infect. Immun.* **75**, 4826–4830 (2007).
- Hunn, J. P. *et al.* Regulatory interactions between IRG resistance GTPases in the cellular response to *Toxoplasma gondii*. *EMBO J.* **27**, 2495–2509 (2008).
- Traver, M. K. *et al.* Immunity-related GTPase M (IRGM) proteins influence the localization of guanylate-binding protein 2 (GBP2) by modulating macroautophagy. *J. Biol. Chem.* **286**, 30471–30480 (2011).
- Haldar, A. K. *et al.* IRG and GBP host resistance factors target aberrant, “non-self” vacuoles characterized by the missing of “self” IRGM proteins. *PLoS Pathog.* **9**, e1003414 (2013).
- Coers, J. Self and non-self discrimination of intracellular membranes by the innate immune system. *PLoS Pathog.* **9**, e1003538 (2013).

Supplementary Information is available in the online version of the paper.

Acknowledgements We thank N. Mizushima and S. Virgin for Atg5-deficient BMDMs, K. Pfeiffer for Gbp2-deficient BMDMs, J. Frey for *B. thailandensis*, the Biozentrum Proteomics and Imaging Core Facilities for technical assistance, K. Anderson, T. Soukup, R. Schwingendorf, J. C. Cox, V. M. Dixit for reagents and N. Perronich for discussions. This work was supported by an SNSF Professorship PP00P3_139120/1, University of Basel project grant ID2153162 to P.B. and a Marie Heim-Voegtlin Fellowship 145516 to D.K.B.

Author Contributions E.M. and P.B. designed the study and wrote the manuscript. E.M., R.F.D., M.S.D., N.S. and P.B. performed the experiments and analysed data; D.K.B., D.B., S.W., M.R.-G., N.K., M.Y. and K.T. contributed reagents.

Author Information Reprints and permissions information is available at www.nature.com/reprints. The authors declare no competing financial interests. Readers are welcome to comment on the online version of the paper. Correspondence and requests for materials should be addressed to P.B. (petr.broz@unibas.ch).

METHODS

Bacterial strains and plasmids. *Salmonella enterica* serovar Typhimurium (S. typhimurium) SL1344 and congenic mutants were published before¹². Other bacterial strains used were *Shigella flexneri*, *Vibrio cholerae*, *Enterobacter cloacae*, *Citrobacter koseri* and *Burkholderia thailandensis* ATCC700388.

Mice. *Gbp*^{chr3} KO, *Gbp2*^{-/-}, *Atg5*^{fl/fl}-Lyz-Cre, *Cybb*^{-/-} (gp91^{phox}), *Casp1*^{-/-}/*Casp11*^{-/-} (a.k.a caspase-1 knockout), *Casp11*^{-/-} and *Casp1*^{-/-} (*Casp1*^{-/-}/*Casp11*^{fl/fl}) mice have been previously described^{1,11,14,24,25}. Mice were bred in the animal facilities of the University of Basel, Genentech Inc., Heinrich-Heine-University Dusseldorf or the University of Osaka. Generation of mice with *Gbp5* KO alleles by zinc finger nuclease (ZFN) technology. A ZFN pair was obtained from Sigma-Aldrich (SAGE Labs). The ZFN pair recognizes a sequence in mouse *Gbp5* exon 2 (cut site is underlined): 5'-TGCCATCACACAGCCAGTGGTGGTGGTAGCCATTGTGGGT-3'. ZFN mRNA and a donor plasmid harbouring a 10-bp deletion in *Gbp5* exon 2 was co-microinjected into C57BL/6N zygotes using established procedures. One male founder carrying the 10-bp deletion was obtained by homologous recombination (10-bp deletion is underlined): 5'-TGCCATCACACAGCCAGTGGTGGTGGTAGCCATTGTGGGT-3. This founder was bred with C57BL/6N females to generate heterozygous progeny for subsequent intercrossing. Two founders (a male and a female) carrying identical 1-bp deletions were obtained by non-homologous end-joining (deleted bp is underlined): 5'-TGCCATCACACAGCCAGTGGTGGTGGTAGCCATTGTGGGT-3. These two founders were intercrossed to directly generate homozygous progeny. Both the 10-bp (designated KO line 1) and 1 bp (designated KO line 2) deletions lead to frameshifts and premature stop codons in *Gbp5* exon 2.

Animal infection. All animal experiments were approved (license 2239, Kantonales Veterinäramt Basel-Stadt) and performed according to local guidelines (Tierschutz-Verordnung, Basel-Stadt) and the Swiss animal protection law (Tierschutz-Gesetz). Female BALB/c mice (10–14 weeks old) were infected intravenously with mCherry-positive *Salmonella* (1,000 c.f.u.) and euthanized 4–5 days later. For antibody injections, mice ($n = 3$ per group) received on day 3 two intraperitoneal injections of 200 μ l PBS containing 0.2 mg anti-IFN- γ monoclonal antibody (Clone XMG1.2, BioLegend) or 0.2 mg rat IgG1, κ isotype control antibody (clone RTK2071, BioLegend). No randomization or blinding was performed.

Cell culture and infections. BMDMs were differentiated in DMEM (Invitrogen) with 10% v/v FCS (Thermo Fisher Scientific), 10% MCSF (L929 cell supernatant), 10 mM HEPES (Invitrogen), and nonessential amino acids (Invitrogen). 1 day before infection, macrophages were seeded into 6-, 24-, or 96-well plates at a density of 1.25×10^6 , 2.5×10^5 , or 5×10^4 per well. If required macrophages were pre-stimulated with PAM3CSK4, LPS O111:B4 (InvivoGen), mIFN- β or mIFN- γ (eBioscience). For infections with *S. typhimurium*, *V. cholerae*, *E. cloacae*, *C. koseri* and *B. thailandensis*, bacteria were grown overnight in LB or TSB at 37 °C with aeration. The bacteria were diluted in fresh pre-warmed macrophage medium and added to the macrophages at a multiplicity of infection (m.o.i.) of 100:1 for measurements of caspase-11 and caspase-1 activity or 10:1 for all other assays. For assaying *Salmonella*-induced NLR4 activation, *Salmonella* were subcultured for 4 h before infection to induce SPI-1 T3SS and flagellin expression. *S. flexneri* were cultured overnight in TSB medium and subcultured for 3 h before infection to induce T3SS expression. IFN- γ -primed BMDMs (to induce GBP expression) were infected with m.o.i. of 30:1 with *S. flexneri* for FACS analysis. When required, chemical reagents, Apocynin (Sigma Aldrich, 100 μ M), L-NG-nitroarginine methyl ester (L-NAME; Sigma Aldrich, 100 μ M) and 3-methyladenine (Sigma Aldrich, 5 mM) were added 30 min before infection. The plates were centrifuged for 15 min at 500 g to ensure comparable adhesion of the bacteria to the cells and placed at 37 °C for 60 min. Next, 100 μ g ml⁻¹ gentamycin (Invitrogen) was added to kill extracellular bacteria. After a 60-min incubation, the cells were washed once with DMEM and given fresh macrophage medium containing 10 μ g ml⁻¹ gentamycin for the remainder of the infection. For infections with killed bacteria, *Salmonella* were grown as above. Shortly before the infection, bacteria were left untreated or incubated for 30 min at 95 °C, in 4% paraformaldehyde or in 70% ethanol. Following the treatment, bacteria were washed with PBS and prepared for infections as outlined above. The effectiveness of the killing procedures was verified by plating serial dilutions. Transfection with poly(dA:dT) or treatment with MSU, alum or nigericin was done as described previously² or as indicated.

siRNA knockdown. Gene knockdown was done using GenMute (SigmaGen) and siRNA pools (siGenome, Dharmacon). Briefly, wild-type BMDMs were seeded into 24-, or 96-well plates at a density of 1.5×10^6 or 3×10^5 per well. siRNA complexes were prepared at 25 nM siRNA in 1 \times GenMute Buffer according to the manufacturer's instructions for forward knockdowns. siRNA complexes were mixed with BMDM medium and added onto the cells. BMDMs were infected with *S. typhimurium* at an m.o.i. of 100:1 after 56 h of knockdown and analysed for inflammatory activation as outlined below. siRNA pools included: *Casp11* (that is, *Casp4*) (M-042432-01), *Gbp1* (M-040198-01), *Gbp2* (M-040199-00), *Gbp3* (M-063076-01),

Gbp4 (M-047506-01), *Gbp5* (M-054703-01), *Gbp6* (M-041286-01), *Gbp7* (M-061204-01), *Gbp8* (M-059726-01), *Gbp9* (M-052281-01), *Gbp10* (M-073912-00), *Gbp11* (M-079932-00) and NT (non-targeting) pool 2 (D-001206-14). See Supplementary information for sequences.

LPS transfection. Macrophages were seeded as described above. Cells were pre-stimulated with 10 μ g ml⁻¹ of PAM3CSK4 for 4 h in Opti-MEM and transfected for 16 h with ultrapure LPS *E. coli* O111:B4, ultrapure LPS *E. coli* K12 or ultrapure LPS *Salmonella minnesota* (InvivoGen) in complex with FuGeneHD (Promega) as described previously⁷.

Cytokine and LDH release measurement. IL-1 β and tumour necrosis factor (TNF)- α was measured by ELISA (eBioscience). LDH was measured using LDH Cytotoxicity Detection Kit (Clontech). To normalize for spontaneous lysis, the percentage of LDH release was calculated as follows: (LDH infected – LDH uninfected)/(LDH total lysis – LDH uninfected)*100.

Western blotting. Western blotting was done as described before⁴. Antibodies used were rat anti-mouse caspase-1 antibody (1:1,000; 4B4; Genentech), rat anti-mouse caspase-11 (1:500; 17D9; Sigma), rabbit anti-IL-1 α (1:1,000; ab109555; Abcam), rabbit anti-IL-18 (1:500; 5180R; Biovision), goat anti-mouse IL-1 β antibody (1:500; AF-401-NA; R&D Systems) and rabbit anti-GBP2 and rabbit anti-GBP5 (1:1,000; 11854-1-AP/13220-1-AP; Proteintech). Cell lysates were probed with anti- β -actin antibody (Sigma) at 1:2,000.

Statistical analysis. Statistical data analysis was done using Prism 5.0a (GraphPad Software, Inc.). To evaluate the differences between two groups (cell death, cytokine release, FACS, CFU and immunofluorescence-based counts) the two-tailed *t*-test was used. In figures NS indicates 'not significant', *P* values are given in figure legends.

Immunofluorescence. Macrophages were seeded on glass coverslips and infected as described above. At the desired time points cells were washed 3 \times with PBS and fixed with 4% paraformaldehyde for 15 min at 37 °C. Following fixation coverslips were washed and the fixative was quenched with 0.1 M glycine for 10 min at room temperature. Coverslips were stained with primary antibodies at 4 °C for 16 h, washed 4 \times with PBS, incubated for 1 h with appropriate secondary antibodies at room temperature (1:500, AlexaFluor, Invitrogen), washed 4 \times with PBS and mounted on glass slides with Vectashield containing 4',6-diamidino-2-phenylindole (DAPI) (Vector Labs). Antibodies used were rabbit anti-LC3 (1:1,000; NB600-1384, Novus), mouse anti-LC3 (1:100, 2G6, NanoTools), guinea-pig anti-p62 (1:100, GP62-C, Progen), goat anti-*Salmonella* (1:500, CSA-1 and CSA-1-FITC, KPL), mouse anti-galectin-8 (1:1,000, G5671, Sigma), goat anti-galectin-8 (1:100, AF1305, R&D), rabbit anti-Optineurin (1:100, ab23666, Abcam), rabbit anti-NDP52 (1:100, D01, Abnova), anti-PDI (1:100, ADI-SPA-890, Enzo Lifesciences), anti-Calnexin (1:100, ADI-SPA-860-D, Enzo Lifesciences), goat anti-GBP1-5 (1:100, sc-166960, Santa Cruz Biotech), rabbit anti-GBP2 and rabbit anti-GBP5 (1:100; 11854-1-AP/13220-1-AP; Proteintech). Coverslips were imaged on a Zeiss LSM700 or a Leica SP8 at $\times 63$ magnification. Colocalization studies were performed as blinded experiments, with in general a minimum count of 100 bacteria per coverslip and performed in triplicate. Immunofluorescence based counts of live (mCherry⁺/FITC⁺) and dead (mCherry⁻/FITC⁺) bacteria were done as blinded experiment on *z* stacks taken from 15 random fields in three biological replicates, with a total of approximately 10,000 bacteria counted.

Immunohistochemistry. Cryosections were blocked in 1% blocking reagent (Invitrogen) and 2% mouse serum (Invitrogen) in TBST (0.05% Tween in 1 \times TBS pH 7.4), and stained with primary and secondary antibodies (goat anti-CSA1; 1:500; 01-91-99-MG; KPL and anti-GBP2; 1:100; 11854-1-AP; Proteintech). Secondary antibodies included Santa Cruz Biotech sc-362245 and Molecular Probes A21206, A21445 and A21469.

ROS assay. Measurement of oxygen-dependent respiratory burst of BMDMs was performed by chemiluminescence in the presence of 5-amino-2,3-dihydro-1,4-phthalazinedione (luminol, Sigma Aldrich, 66 μ M) using a thermostatically (37 °C) controlled luminometer. Both oxygen and nitrogen species were detected (O₂⁻, ONOO⁻, OH[•]). Chemiluminescence generation was monitored every minute for 1 h after IFN- γ (100 U ml⁻¹) and/or *Salmonella* challenge and expressed as counts per minute.

NO assay. Nitrite production was measured by the Griess assay as previously described²⁶. Briefly, in 96-well plates, BMDMs were infected as described above in presence or absence of IFN- γ or IL-1 β for 16 h. Supernatants were mixed 1:1 with 2.5% phosphoric acid solution containing 1% sulfanilamide and 0.1% naphthylethylenediamine. After 30 min incubation at room temperature, the nitrite concentration was determined by measuring absorbance at 550 nm. Sodium nitrite (Sigma) was used as a standard to determine nitrite concentrations in the cell-free medium.

Digitonin assay. For flow-cytometry-based quantification of cytoplasmic and vacuolar bacteria, macrophages were infected with mCherry⁺ *S. typhimurium* or mCherry⁺ *S. flexneri* as described above. At the desired time point, cells were washed 3 \times with KHM buffer (110 mM potassium acetate, 20 mM HEPES, 2 mM MgCl₂,

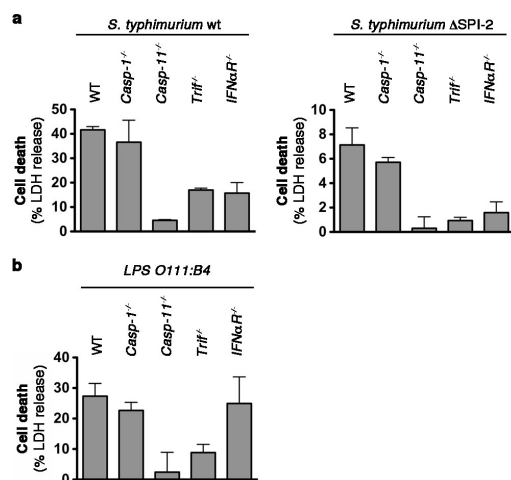
RESEARCH LETTER

pH 7.3) and incubated for 1 min in KHM buffer with $150 \mu\text{g ml}^{-1}$ digitonin (Sigma). Cells were immediately washed $2\times$ with KHM buffer and then stained for 12 min with anti-*Salmonella*-FITC (1:500, CSA-1, KPL) or anti-*Shigella* (1:100, BP1064, Acris) in KHM buffer with 2% BSA. Secondary antibodies used for *S. flexneri* staining were: anti-Rabbit-488 (1:500, Invitrogen). Cells were washed $3\times$ with PBS and lysed in PBS with 0.1% Triton-X (Sigma) and analysed on a FACS-Canto-II. Controls were included in every assay and are described in (Extended Data Fig. 9).

Live/dead analysis by FACS. Infection of macrophages was performed using mCherry⁺ bacteria as described above. At 16 h post-infection cells were washed and lysed with PBS solution containing 0.1% Triton X-100 (Sigma Aldrich) to release intracellular bacteria. *Salmonella* were counterstained using an anti-*Salmonella* antibody (CSA-1, KPL) and analysed using a FACS Canto-II for fluorescence intensities

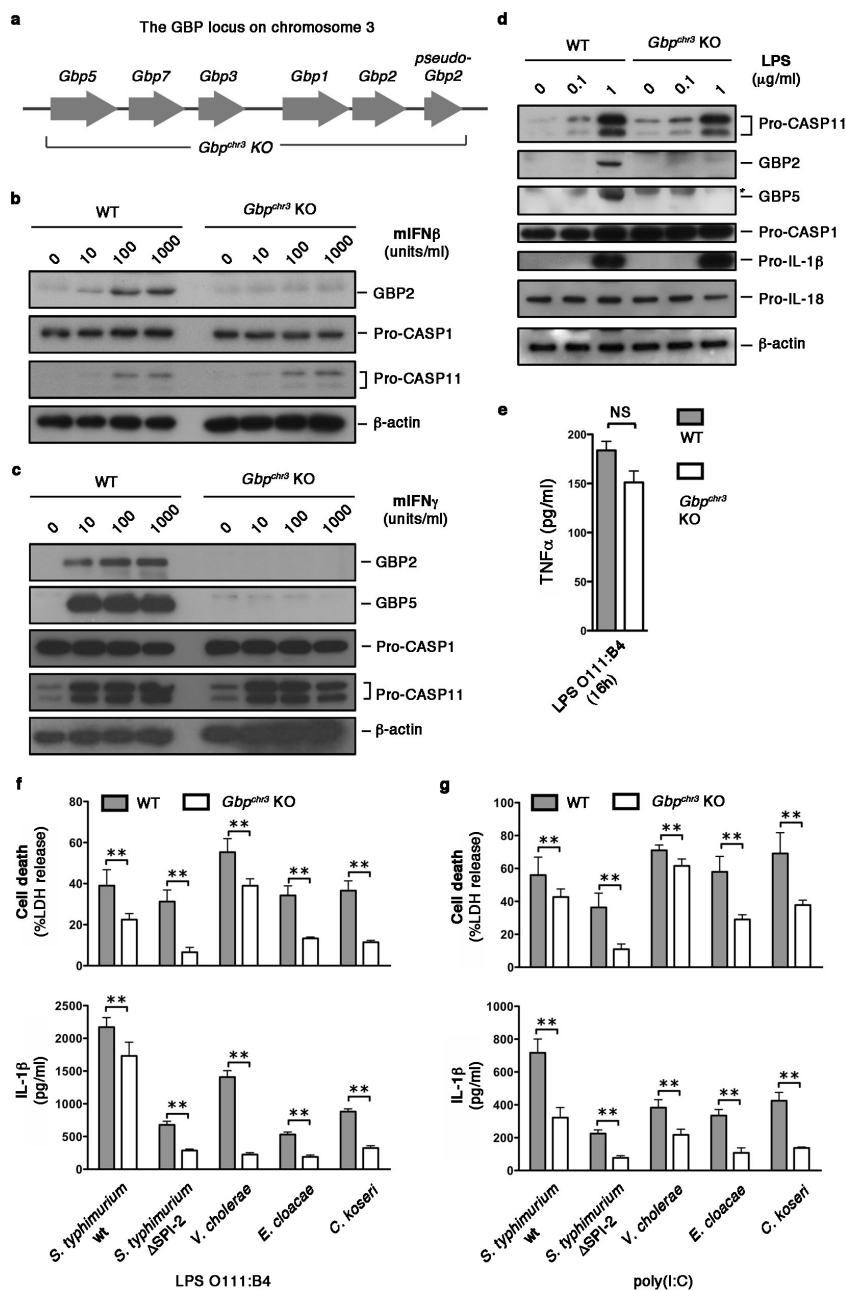
in FL-1 and FL-2 channels. Data were analysed with FlowJo 10.0.6 software. The gate was set for the bacterial population based on the FSC/SSC and the anti-*Salmonella* staining (CSA-1-FITC, KPL). Controls included live mCherry-expressing and mCherry-negative *Salmonella* stained with anti-*Salmonella* antibodies (CSA-1, KPL).

24. Mariathasan, S. *et al.* Differential activation of the inflammasome by caspase-1 adaptors ASC and Ipaf. *Nature* **430**, 213–218 (2004).
25. Zhao, Z. *et al.* Autophagosome-independent essential function for the autophagy protein Atg5 in cellular immunity to intracellular pathogens. *Cell Host Microbe* **4**, 458–469 (2008).
26. Lima-Junior, D. S. *et al.* Inflammasome-derived IL-1 β production induces nitric oxide-mediated resistance to *Leishmania*. *Nature Med.* **19**, 909–915 (2013).



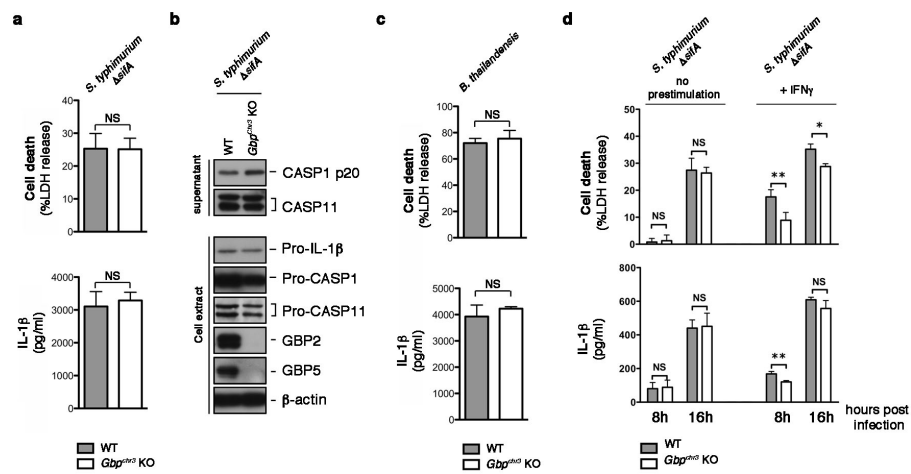
Extended Data Figure 1 | Type-I-interferon signalling is required to induce caspase-11-dependent cell death in response to bacterial infection, but not in response to LPS transfection. a, LDH release from unprimed BMDMs infected for 16 h with wild-type (WT) *S. typhimurium* or Δ SPI-2 *S. typhimurium* grown to stationary phase. b, LDH release from primed BMDMs transfected with LPS O111:B4. Graphs show the mean and s.d. of quadruplicate wells and are representative of three independent experiments.

RESEARCH LETTER



Extended Data Figure 2 | BMDMs from *Gbp^{chr3}* KO mice have normal responses to priming stimuli, but fail to activate the non-canonical inflammasome during bacterial infections. a, Schematic representation of the GBP locus on murine chromosome 3. The extent of the deletion in *Gbp^{chr3}* KO mice is indicated. b–d, Induction of pro-caspase-11, GBP2 and GBP5 expression in lysates of wild-type and *Gbp^{chr3}* KO BMDMs stimulated for 16 h with the indicated amounts of murine IFN- β , murine IFN- γ or LPS O111:B4. e, TNF- α release from BMDMs stimulated for 16 h with LPS O111:B4. f, g, LDH

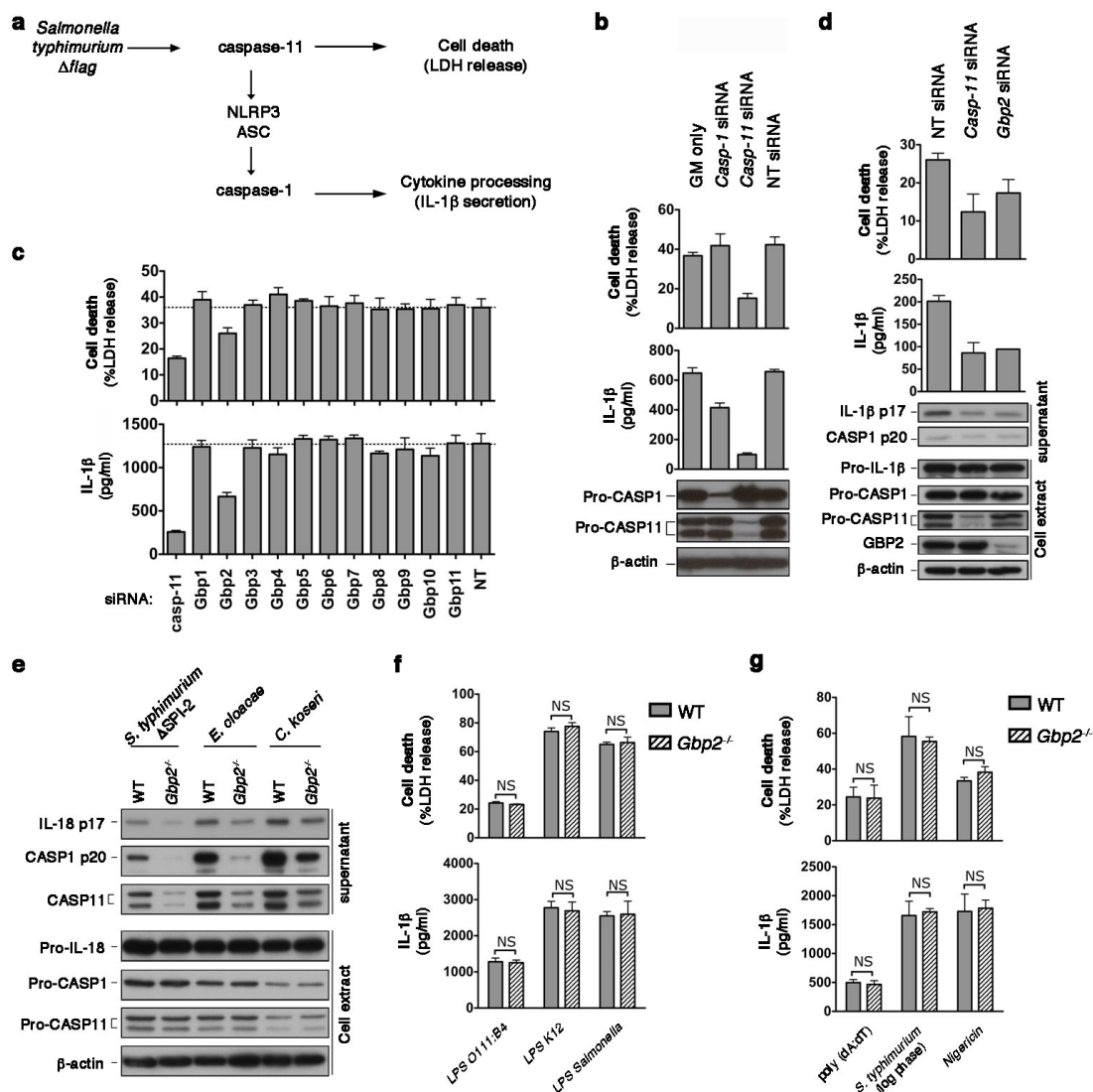
release and IL-1 β secretion from wild-type and *Gbp^{chr3}* KO BMDMs infected for 16 h with wild-type (WT) *S. typhimurium*, Δ SPI-2 *S. typhimurium*, *V. cholerae*, *E. cloacae* or *C. koseri* grown to stationary phase. Cells were primed overnight with LPS (f) or poly(I:C) (g). *Indicates background band. Graphs show the mean and s.d. of quadruplicate wells and data are representative of two independent experiments. ** $P < 0.01$, NS, not significant (two-tailed *t*-test).



Extended Data Figure 3 | GBPs assist the detection of bacteria that escape into the cytosol only in primed macrophages. a–c, LDH release, IL-1 β secretion and immunoblots for processed caspase-1 and caspase-11 released from unprimed BMDMs infected for 8–16 h with *AsifA S. typhimurium* or *B. thailandensis* grown to stationary phase. d, LDH release and IL-1 β secretion

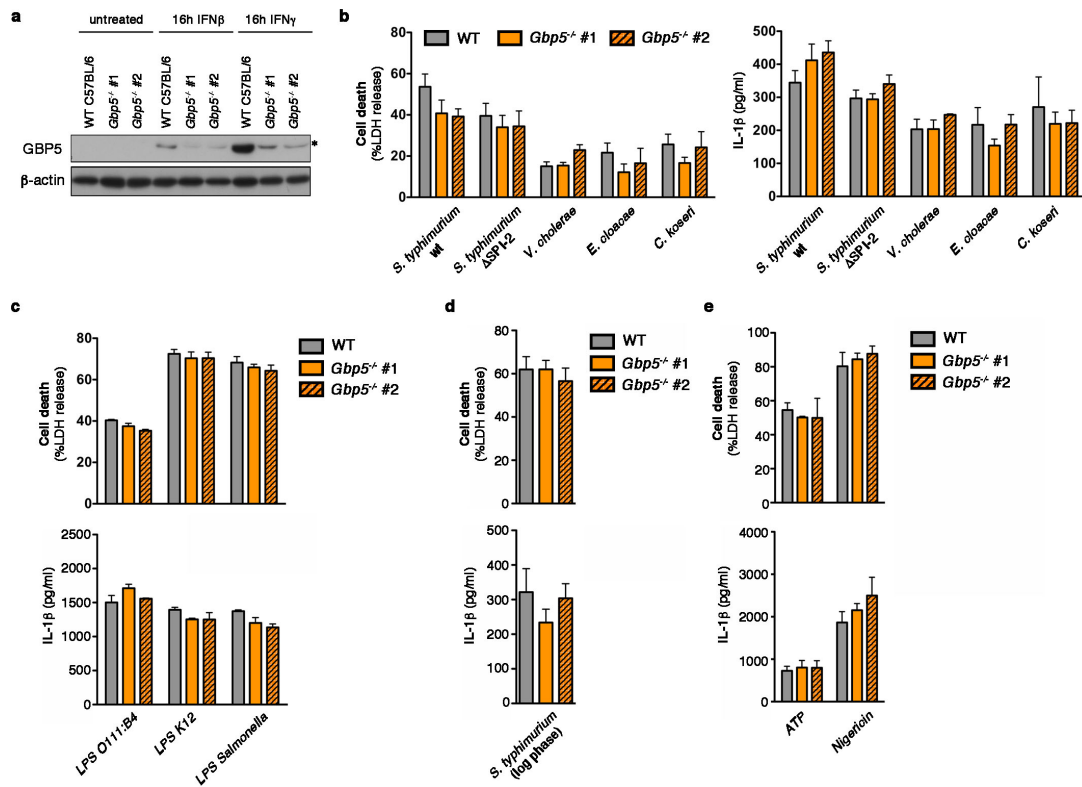
from unprimed or IFN- γ -primed BMDMs infected for 16 h with *AsifA S. typhimurium* grown to stationary phase. Ext, extract; SN, supernatant. Graphs show the mean and s.d. of quadruplicate wells and data are representative of two independent experiments. * $P < 0.05$; ** $P < 0.01$; NS, not significant (two-tailed *t*-test).

RESEARCH LETTER



Extended Data Figure 4 | Murine GBP2 controls non-canonical inflammasome activation during *Salmonella* infection, but is dispensable for direct LPS sensing and canonical inflammasomes. **a**, Schematic drawing of the inflammasome pathways activated by flagellin-deficient *Salmonella*. **b–d**, LDH release, IL-1 β secretion and immunoblots for processed caspase-1 and processed IL-1 β released from unprimed BMDMs infected for 17 h with Δ flag *S. typhimurium* grown to stationary phase. BMDMs were treated with the indicated siRNA for 56 h before infection. **e**, Immunoblots for processed caspase-1, IL-18 and caspase-11 released from unprimed BMDMs infected for

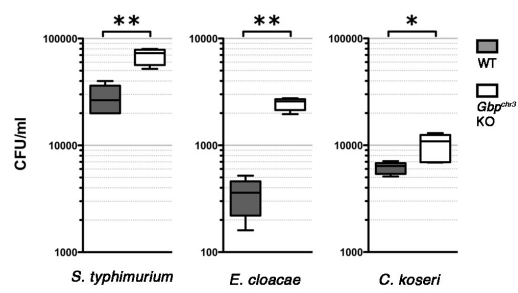
16 h with Δ SP1-2 *S. typhimurium*, *E. cloacae* or *C. koseri* grown to stationary phase. **f**, **g**, LDH release and IL-1 β secretion from primed wild-type and *Gbp2*^{-/-} BMDMs transfected with the indicated types of LPS for 16 h, treated with nigericin for 1 h, infected with SPI-1 T3SS expressing logarithmic phase wild-type *S. typhimurium* for 1 h, or transfected with poly(dA:dT) for 6 h. Cells were primed with PAM3CSK4 in **f** or LPS **g**. Graphs show the mean and s.d. of quadruplicate wells and data are representative of two (**e**) and three (**b–d**, **f**, **g**) independent experiments. NT, non-targeting siRNA; GM, GenMute transfection reagent; NS, not significant (two-tailed *t*-test).



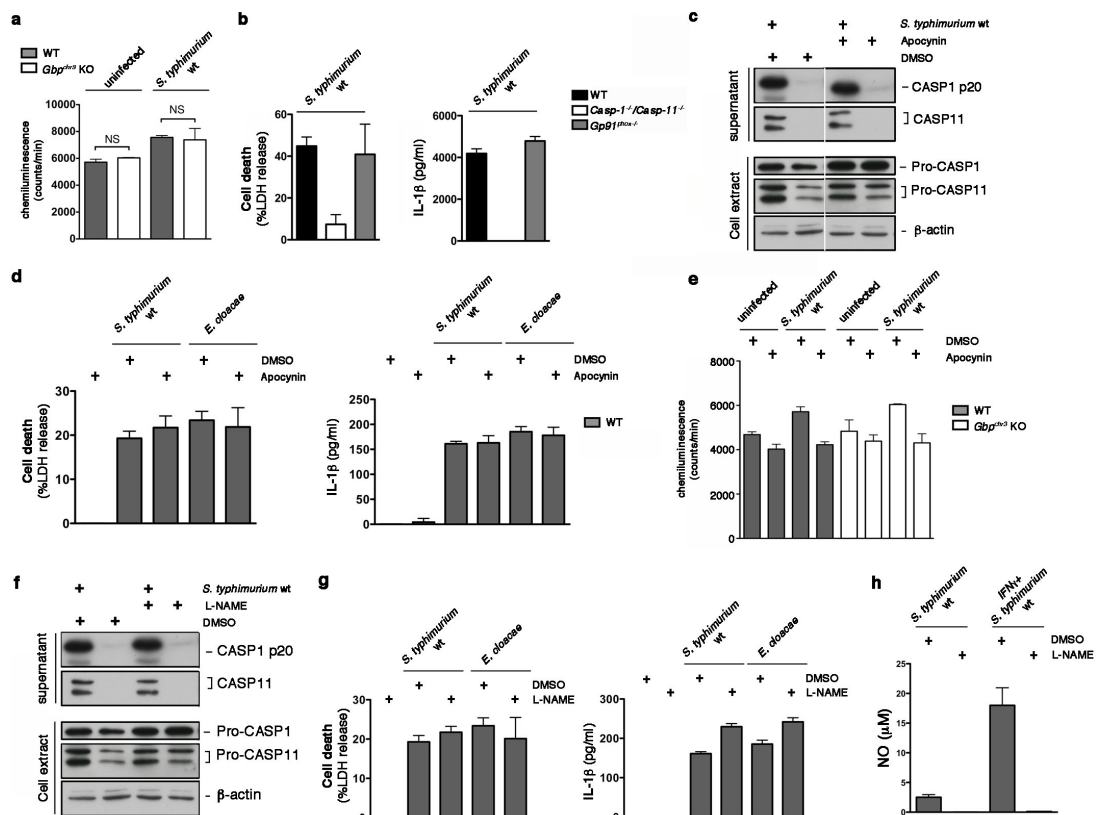
Extended Data Figure 5 | Normal activation of non-canonical and canonical inflammasomes in *Gbp5*^{-/-} BMDMs. a, Expression of GBP5 in wild-type and two lines of *Gbp5*^{-/-} BMDMs (1 and 2). *Indicates a cross-reactive band. b–e, LDH release and IL-1 β secretion from BMDMs infected for 16 h with wild-type (WT) *S. typhimurium*, Δ SPI-2 *S. typhimurium*, *V. cholerae*, *E. cloacae* or *C. koseri* grown to stationary phase (b), transfected

with the indicated LPS for 16 h (c) infected for 1 h with SPI-1 T3SS expressing logarithmic phase wild-type *S. typhimurium* (d), or treated with 5 mM ATP or 20 mM nigericin for 4 h (e). Cells were left unprimed (b) or primed with PAM3CSK4 in (c) or LPS (d, e). Graphs show the mean and s.d. of triplicate or quadruplicate wells and data are representative of three independent experiments.

RESEARCH LETTER



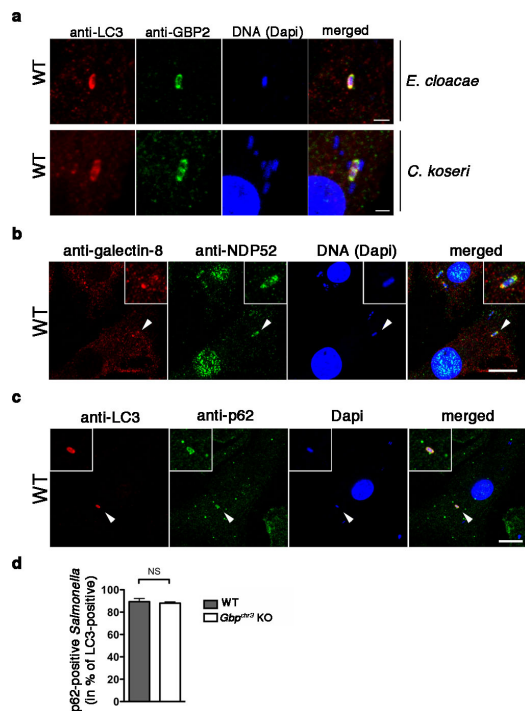
Extended Data Figure 6 | GBPs control bacterial replication. c.f.u.s at 16 h post-infection in wild-type and *Gbp^{chr3}* KO BMDMs infected with the indicated bacterial strains. Experiments are representative of two independent experiments.



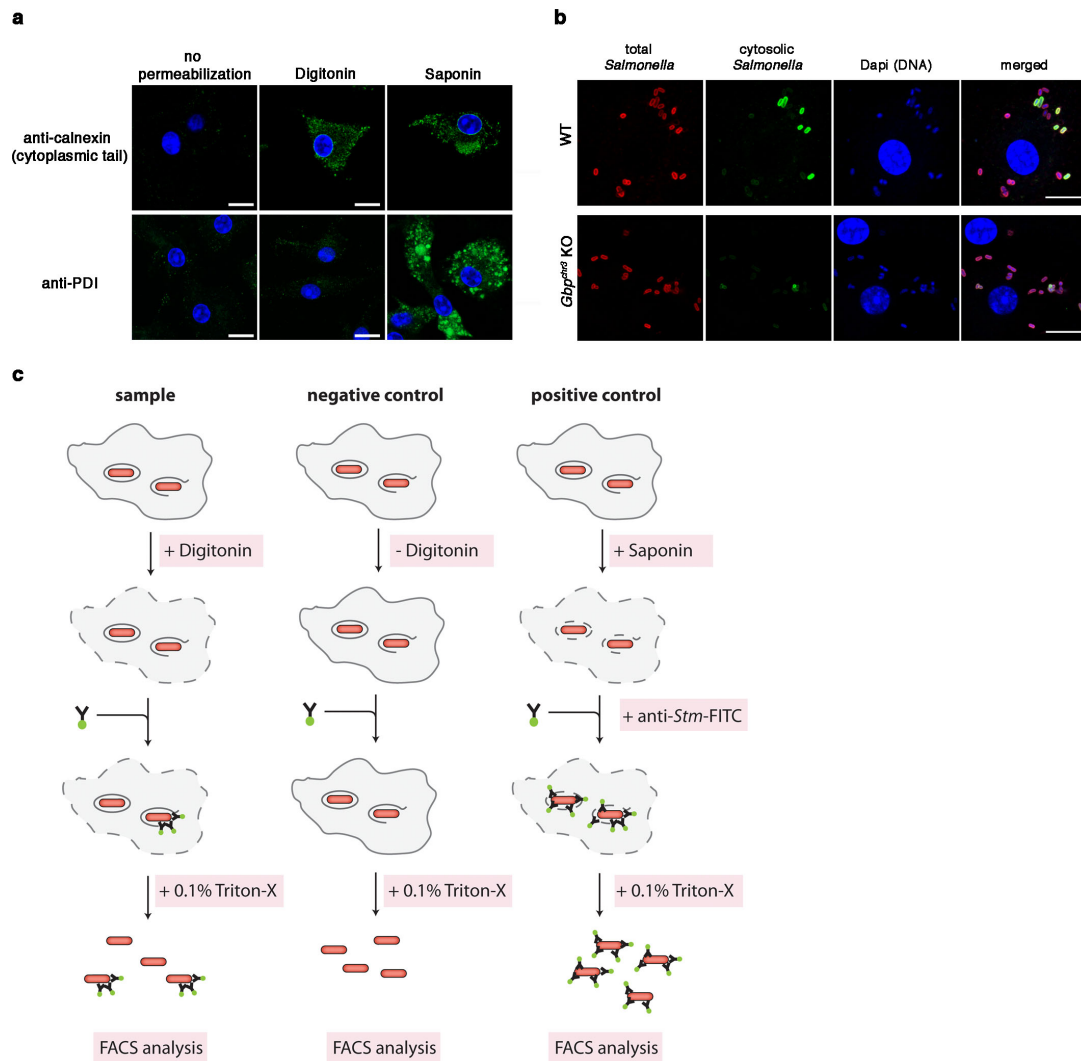
Extended Data Figure 7 | Inhibition of ROS and NO production does not affect non-canonical inflammasome activation. **a, b**, ROS levels, LDH release and IL-1 β secretion in unprimed BMDMs left uninfected or infected for 16 h with wild-type *S. typhimurium* grown to stationary phase. **c–e**, LDH release, IL-1 β secretion, ROS levels and immunoblots for processed caspase-1 and caspase-11 released from unprimed BMDMs infected for 16 h with wild-type (WT) *S. typhimurium* or *E. cloacae* grown to stationary phase in the presence of the ROS inhibitor (apocynin) or a vehicle control (DMSO). **f, g**, LDH release, IL-1 β secretion and immunoblots for processed caspase-1 and

caspase-11 released from unprimed BMDMs infected for 16 h with wild-type *S. typhimurium* or *E. cloacae* grown to stationary phase in the presence of the iNOS inhibitor (L-NAME) or a vehicle control (DMSO). **h**, NO release from unprimed or IFN- γ -primed BMDMs infected for 16 h with *S. typhimurium* in presence of the iNOS inhibitor (L-NAME) or a vehicle control (DMSO). Ext, extract; SN, supernatant. Graphs show the mean and s.d. of quadruplicate wells and data are representative of two (**a–c, e–g**) and three (**d, h**) independent experiments. NS, not significant (two-tailed *t*-test).

RESEARCH LETTER



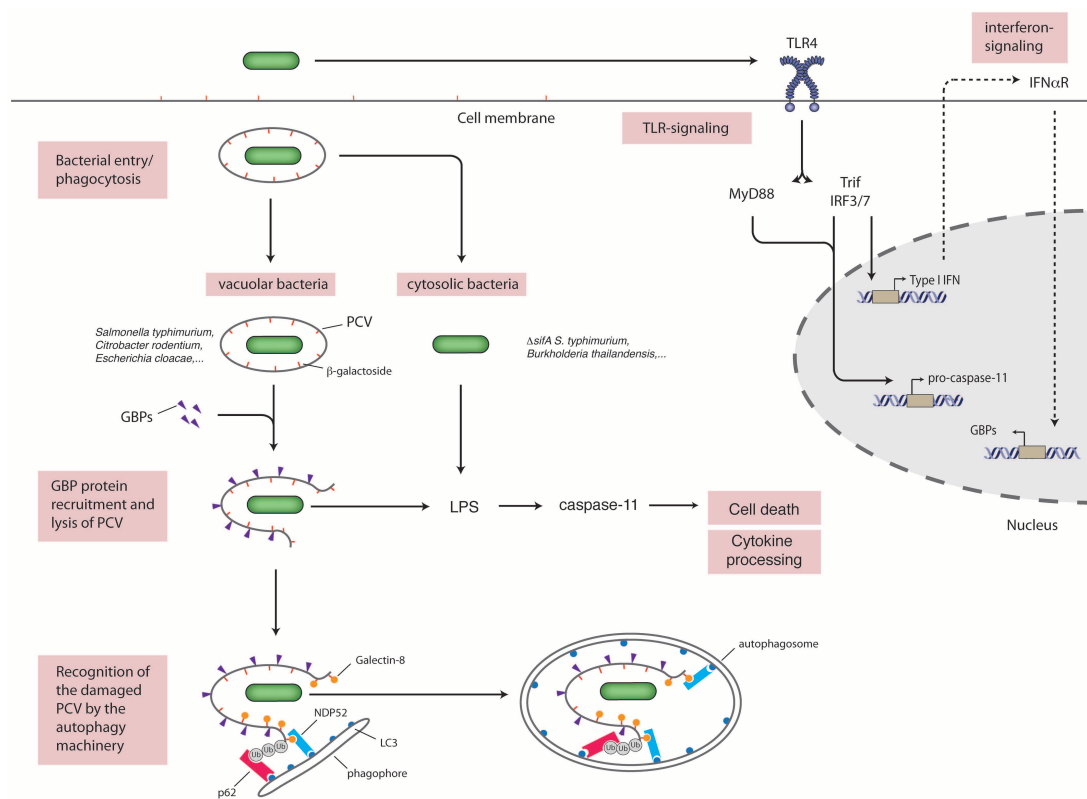
Extended Data Figure 8 | Colocalization of GBPs and autophagy proteins on intracellular bacteria. **a**, Colocalization of LC3 with GBPs in unprimed wild-type BMDMs infected with *E. cloacae* or *C. koseri* for 4 h and stained for LC3, GBP2 and DNA. **b**, Colocalization of galectin-8 and NDP52 in unprimed wild-type BMDMs infected with wild-type *S. typhimurium* for 4 h and stained for galectin-8, NDP52 and DNA. **c**, Colocalization of p62 and LC3 in unprimed wild-type BMDMs infected with wild-type *S. typhimurium* for 4 h and stained for LC3, p62 and DNA. **d**, Quantification of p62 and LC3 co-staining in wild-type and *Gbp^{tr3}* KO BMDMs at 4 h post-infection with *Salmonella*. Arrowheads indicate region shown in insets. Scale bars, 1 μ m (**a**) and 10 μ m (**b**, **c**). Graph shows the mean and s.d. of triplicate counts and images and graph are representative of at least two independent experiments. NS, not significant (two-tailed *t*-test).



Extended Data Figure 9 | Digitonin-based quantification of cytoplasmic bacteria. **a**, Immunostaining for calnexin and PDI (protein disulphide isomerase) in wild-type BMDMs left untreated or permeabilized with digitonin or saponin. **b**, Differentially permeabilized macrophages stained for cytosolic

and vacuolar *Salmonella* at 4 h post-infection. **c**, Schematic representation of FACS-based analysis of cytosolic and vacuolar bacterial populations of *Salmonella*. Scale bars, 10 μ m.

RESEARCH LETTER



Extended Data Figure 10 | Model for the role of GBPs and autophagy in caspase-11 activation. The pathogen-containing vacuole of vacuolar bacterial pathogens is recognized by interferon-induced GBPs in an unknown manner. GBPs promote the lysis of the PCV either directly or indirectly, resulting in the release of the bacteria into the cytosol and activation of caspase-11 by bacterial LPS. β -galactosides of the lysed vacuole serve as danger signals upon

exposure to the cytosol and are recognized by galectin-8 leading to the recruitment of the autophagy machinery. p62 participates in this process by recognizing ubiquitin-chains on the vacuole or the bacterium. Uptake of the bacterium and the lysed vacuole into autophagosomes reduces caspase-11 activation by removing the source of LPS from the cytosol.

SUPPLEMENTARY INFORMATION

doi:10.1038/nature13157

Dharmacon Pool Catalog Number	Dharmacon Duplex Catalog Number	Gene Symbol	Gene Accession	GINumber	Sequence
M-042432-01	D-042432-01	Casp4	NM_007609	157951737	GUGCAACAAUCAUUUGAAA
M-042432-01	D-042432-02	Casp4	NM_007609	157951737	GCUAAUGUCUCAUGGCACA
M-042432-01	D-042432-03	Casp4	NM_007609	157951737	GAUGUGCUACAGUAUGAUA
M-042432-01	D-042432-04	Casp4	NM_007609	157951737	CGAAAGGCUCUUUCAUAU
M-040198-01	D-040198-01	GBP1	NM_010259	134031981	GCAACUACGUCAAGAGAUA
M-040198-01	D-040198-02	GBP1	NM_010259	134031981	GGAAAGACUUCUCAAGCAA
M-040198-01	D-040198-03	GBP1	NM_010259	134031981	GAUCAUGCACCAUACUUUA
M-040198-01	D-040198-04	GBP1	NM_010259	134031981	CAACUCAGCUAACUUUGUG
M-040199-00	D-040199-01	GBP2	NM_010260	6753949	UGAAGAAGCUGACUGAGAA
M-040199-00	D-040199-02	GBP2	NM_010260	6753949	GAAGUGCACUAUACUCUGA
M-040199-00	D-040199-03	GBP2	NM_010260	6753949	GGAGCUGUGUGGAAUUUU
M-040199-00	D-040199-04	GBP2	NM_010260	6753949	GGAGCUAACUGAUUUUAUC
M-063076-01	D-063076-01	Gbp3	NM_018734	134053870	GAACGAAGCAGCAUCUAUU
M-063076-01	D-063076-02	Gbp3	NM_018734	134053870	GGACUUUGGUGCAGACCUA
M-063076-01	D-063076-03	Gbp3	NM_018734	134053870	GGCCAUUGUUGUUUAUAU
M-063076-01	D-063076-04	Gbp3	NM_018734	134053870	CACAAGCGACAAACGUUUA
M-047506-01	D-047506-01	Gbp4	NM_008620	126157520	GGACAUAAACAUAAGGAAA
M-047506-01	D-047506-02	Gbp4	NM_008620	126157520	CCAAUUGGAUCCUACGUUU
M-047506-01	D-047506-03	Gbp4	NM_008620	126157520	GAUAUAAGACACAAGCUGA
M-047506-01	D-047506-04	Gbp4	NM_008620	126157520	GGAAUUGCGUCGAGAGAUC
M-054703-01	D-054703-01	GBP5	NM_153564	91064875	CGCAGGAGUUCUAUCAUA
M-054703-01	D-054703-02	GBP5	NM_153564	91064875	UGACUGUGUUUAUAGCUAA
M-054703-01	D-054703-03	GBP5	NM_153564	91064875	ACUCAGAUUUUGCACUAG
M-054703-01	D-054703-04	GBP5	NM_153564	91064875	GCGAGAGGCCAUAGAAAUC
M-041286-01	D-041286-02	Mpa2l	NM_194336	170650636	AAGAAACACUGAUCGAAUU
M-041286-01	D-041286-04	Mpa2l	NM_194336	170650636	GGGACAGAAUACACGGCUUU
M-041286-01	D-041286-05	Mpa2l	NM_194336	170650636	GGAAUUAUAGGAGAGAAC
M-041286-01	D-041286-06	Mpa2l	NM_194336	170650636	GCACAUAUACAGUCAGGUUA
M-061204-01	D-061204-01	Gbp6	NM_001083312	134032013	AAGAAUAGUCUAUUGGGUG
M-061204-01	D-061204-02	Gbp6	NM_001083312	134032013	CGACCUACGUGGAUGCUAU
M-061204-01	D-061204-03	Gbp6	NM_001083312	134032013	GGACUAUACCGUACGGGAA
M-061204-01	D-061204-04	Gbp6	NM_001083312	134032013	GACGUGCCGUGUUUAGAGA
M-059726-01	D-059726-01	5830443L24RIK	NM_029509	115292436	CACCAAAUCCUGAUGGAAU
M-059726-01	D-059726-03	5830443L24RIK	NM_029509	115292436	GUGACAACCUAUGUAGAUG
M-059726-01	D-059726-17	5830443L24RIK	NM_029509	115292436	AUUAUAGUGAGGCGGAAA
M-059726-01	D-059726-18	5830443L24RIK	NM_029509	115292436	ACGGAGAGAUACAGCAACU
M-052281-01	D-052281-01	BC057170	NM_172777	118129953	UAGAGAGACUGGAACAUAA
M-052281-01	D-052281-02	BC057170	NM_172777	118129953	GAGGAAGGAUUUACGAACA
M-052281-01	D-052281-03	BC057170	NM_172777	118129953	GAUCUUCGCCCUAAGUGUG
M-052281-01	D-052281-04	BC057170	NM_172777	118129953	AAACAUUGGUCCAUUCUG
M-073912-00	D-073912-09	Gbp10	NM_001039646	116812913	CCAUAUAGUGUAAAAGACACA
M-073912-00	D-073912-10	Gbp10	NM_001039646	116812913	GGAAUUAUAGGAGAGAAC
M-073912-00	D-073912-11	Gbp10	NM_001039646	116812913	GCUGAUCCAGGUGACAAA
M-073912-00	D-073912-12	Gbp10	NM_001039646	116812913	AGAAACACUGAUCGAAUUA
M-079932-00	D-079932-13	EG634650	NM_001039647	88900482	UGUAAAGAGACCUUGCUUUA
M-079932-00	D-079932-14	EG634650	NM_001039647	88900482	GGAAUUAUAAAGUGAGAAG
M-079932-00	D-079932-15	EG634650	NM_001039647	88900482	GAAGAGAGAUCAUCGACU
M-079932-00	D-079932-16	EG634650	NM_001039647	88900482	GCUAUAAGAAGAAAGCGUA

Supplementary information 1: Sequences of siRNA duplexes

WWW.NATURE.COM/NATURE | 1

6.2 Research article IV

Guanylate-binding proteins promote activation of the AIM2 inflammasome during infection with *Francisella novicida*

E. Meunier*, P. Wallet*, R. F. Dreier, S. Costanzo, L. Anton, S. Rühl, S. Dussurgey, **M. S. Dick**, A. Kistner, M. Rigard, D. Degrandi, K. Pfeffer, M. Yamamoto, T. Henry and P. Broz.

* denotes equal contribution.

Nature Immunology

2015 May 16; 16(5):467-84. doi: 10.1038/ni.3119.²⁰⁰

Statement of contribution

I performed several Western blots and was involved in the discussion of the results.

Guanylate-binding proteins promote activation of the AIM2 inflammasome during infection with *Francisella novicida*

Etienne Meunier^{1,6}, Pierre Wallet^{2,6}, Roland F Dreier¹, Stéphanie Costanzo², Leonie Anton¹, Sebastian Rühl¹, Sébastien Dussurgey³, Mathias S Dick¹, Anne Kistner¹, Mélanie Rigard², Daniel Degrandi⁴, Klaus Pfeffer⁴, Masahiro Yamamoto⁵, Thomas Henry² & Petr Broz¹

The AIM2 inflammasome detects double-stranded DNA in the cytosol and induces caspase-1-dependent pyroptosis as well as release of the inflammatory cytokines interleukin 1 β (IL-1 β) and IL-18. AIM2 is critical for host defense against DNA viruses and bacteria that replicate in the cytosol, such as *Francisella tularensis* subspecies *novicida* (*F. novicida*). The activation of AIM2 by *F. novicida* requires bacteriolysis, yet whether this process is accidental or is a host-driven immunological mechanism has remained unclear. By screening nearly 500 interferon-stimulated genes (ISGs) through the use of small interfering RNA (siRNA), we identified guanylate-binding proteins GBP2 and GBP5 as key activators of AIM2 during infection with *F. novicida*. We confirmed their prominent role *in vitro* and in a mouse model of tularemia. Mechanistically, these two GBPs targeted cytosolic *F. novicida* and promoted bacteriolysis. Thus, in addition to their role in host defense against vacuolar pathogens, GBPs also facilitate the presentation of ligands by directly attacking cytosolic bacteria.

The innate immune system detects invading pathogens through membrane-bound and cytosolic pattern-recognition receptors, which recognize microbe- and damage-associated molecular patterns and induce conserved signaling pathways. Nucleic acids and their derivatives are detected by RIG-I-like receptors, cGAS, DAI and RNA polymerases, which results in the induction of type I interferons via the signaling molecule STING and the kinase TBK1 (refs. 1–3). Cytosolic microbial and host DNA also induces inflammasome formation through AIM2, a member of the PYHIN family of receptors^{4–7}. AIM2 binds double-stranded DNA through its HIN-200 domain⁸ and recruits the inflammasome adaptor ASC. ASC rapidly oligomerizes to form a macromolecular inflammasome complex known as an ‘ASC speck’, which activates caspase-1. Active caspase-1 promotes the maturation and release of the pro-inflammatory cytokines interleukin 1 β (IL-1 β) and IL-18. In addition, it induces pyroptosis, a lytic form of cell death that restricts pathogen replication. The AIM2 inflammasome mediates the recognition of DNA viruses as well as that of various Gram-negative and Gram-positive cytosolic bacteria, such as *Listeria monocytogenes*, *Legionella pneumophila*, *Mycobacterium* species and *Francisella tularensis* subspecies *novicida* (*F. novicida*)^{8–14}. Notably, several studies have shown that activation of AIM2 by these bacteria requires bacteriolysis and the subsequent release of bacterial chromosomal DNA into the cytosol^{10,12,15}.

However, whether the bacteriolysis is accidental or is an active, host-directed mechanism has remained unclear.

The activation of AIM2 via the transfection of synthetic DNA or during infection with a DNA virus is independent of signaling via Toll-like receptors or interferons^{9,13,16}. In contrast, the activation of AIM2 during infection with *F. novicida* requires the production of type I interferons, which are induced as a result of the recognition of an as-yet-undefined *F. novicida*-derived nucleic acid ligand in the cytosol^{9,10,17–20}. Consistent with that, the activation of AIM2 inflammasomes in *F. novicida*-infected cells requires signaling through STING and the transcription factor IRF3 (refs. 9,10,17). It has been speculated that interferon signaling is necessary to increase cellular AIM2 for the detection of *F. novicida* DNA⁹, yet interferon-mediated induction of AIM2 is contested, and even small amounts of transfected DNA efficiently trigger activation of AIM2 in an interferon-independent manner⁹. Therefore, it is likely that one or several interferon-inducible factor(s) is (are) required for efficient activation of AIM2 during bacterial infection.

Type I and type II interferons are potent cytokines that exert anti-microbial effects through the induction of a broad transcriptional program involving ~2,000 genes, the so-called ‘interferon-stimulated genes’ (ISGs), many of which remain uncharacterized.

¹Focal Area Infection Biology, Biozentrum, University of Basel, Basel, Switzerland. ²Centre International de Recherche en Infectiologie, Inserm U1111, CNRS UMR 5308, Université Claude Bernard Lyon-1, Ecole Normale Supérieure, Lyon, France. ³Structure Fédérative de Recherche Biosciences, UMS344/US8, Inserm, CNRS, Université Claude Bernard Lyon-1, Ecole Normale Supérieure, Lyon, France. ⁴Institute of Medical Microbiology and Hospital Hygiene, Heinrich-Heine-University Duesseldorf, Duesseldorf, Germany. ⁵Department of Microbiology and Immunology, Osaka University, Osaka, Japan. ⁶These authors contributed equally to this work. Correspondence should be addressed to T.H. (thomas.henry@inserm.fr) or P.B. (petr.broz@unibas.ch).

Received 11 November 2014; accepted 6 February 2015; published online 16 March 2015; doi:10.1038/ni.3119

Prominent among the products of these ISGs are several families of interferon-inducible GTPases, such as the 47-kilodalton immunity-related GTPases and the 65- to 73-kilodalton guanylate-binding proteins (GBPs)^{21,22}. GBPs are conserved among vertebrates, with 11 GBPs in mice and 7 in humans, and exert anti-microbial effects on intracellular bacteria and protozoa²³. GBP1 and GBP7 restrict *Mycobacterium bovis* bacillus Calmette-Guérin and *L. monocytogenes* by recruiting anti-microbial effectors to the pathogen-containing vacuole (PCV)²⁴. Several GBPs are recruited onto the *Toxoplasma* parasitophorous vacuole²⁵, and most are also required for restricting the replication of *Toxoplasma gondii*^{23,26–28}. In addition, GBPs encoded by genes on mouse chromosome 3 promote recognition of the vacuolar, Gram-negative bacterium *Salmonella typhimurium* by the innate immune system by destabilizing its PCV, which leads to egress of the bacteria into the cytosol and subsequent detection of its lipopolysaccharide (LPS) by the caspase-11 inflammasome²⁹. In this study we found that GBPs encoded by genes on mouse chromosome 3 were a key factor for the activation of AIM2 during infection with *F. novicida*. In particular, GBP2 and GBP5 controlled the activation of AIM2 by targeting cytosolic *F. novicida* and inducing lysis of these bacteria by an as-yet-uncharacterized mechanism. We demonstrated that GBP-deficient mice were unable to control infection with *F. novicida* *in vivo*. Together our data reveal a function for GBPs during microbial infection, in that GBPs promoted bacteriolysis in the cytosol and the exposure of bacterial DNA to cytosolic sensors of the innate immune system.

RESULTS

AIM2 activation during *F. novicida* infection requires interferons

F. novicida is a facultative intracellular Gram-negative bacterium that avoids phagosomal degradation in phagocytes by escaping into the cytosol, a process that requires the *Francisella* pathogenicity island (FPI). After escaping from the phagosome, *F. novicida* replicates in

the cytosol but also triggers AIM2-dependent activation of caspase-1 (refs. 10,13). Infection of mouse bone marrow-derived macrophages (BMDMs) with wild-type *F. novicida* resulted in cell death (pyroptosis; measured by the release of lactate dehydrogenase (LDH)) and the release of IL-1 β dependent on AIM2, ASC and caspase-1, while a mutant lacking the FPI (Δ FPI) did not activate the inflammasome (Fig. 1a). STING is linked to the activation of AIM2 during infection with *F. novicida*^{10,12}. Macrophages deficient in STING (via the 'goldenticket' (Gt) *N*-ethyl-*N*-nitrosourea-induced nonfunctional mutation of alleles encoding *Tmem173* (called 'Sting^{Gt/Gt}' here)) had considerable attenuation of their ability to induce expression of type I interferons and activation of the AIM2 inflammasome upon infection with *F. novicida*⁵ (Fig. 1b and Supplementary Fig. 1a). Inconsistent with a role for type I interferons in activation of the AIM2 inflammasome^{17,19}, macrophages from mice deficient in *Ifnar1*, which encodes the receptor for interferon- α (IFN- α) and IFN- β (IFNAR1), or *Stat1*, which encodes the transcription factor STAT1, displayed significantly less pyroptosis and release of IL-1 β when infected with *F. novicida* than did their wild-type counterparts (Fig. 1c). To further confirm that activation of AIM2 during infection with *F. novicida* depended on signaling via type I interferons, we assessed whether exogenous interferons were able to restore inflammasome activation in STING-deficient BMDMs. As expected, IFN- β restored cell death and the release of cytokines in *Sting*^{Gt/Gt} BMDMs (Fig. 1d). The addition of IFN- γ restored cell death and the release of cytokines in both *Sting*^{Gt/Gt} BMDMs and *Ifnar1*^{-/-} BMDMs (Fig. 1d), which indicated a requirement for a general interferon signature.

The induction of *Aim2* mRNA could explain the considerable dependence on type I interferons and signaling via STAT1 during infection with *F. novicida*¹⁰. However, activation of the AIM2 inflammasome by transfection of DNA or infection with DNA viruses is independent of interferon signaling^{9,13,16}. In accordance with those reports, induction of cell death by transfection of the synthetic

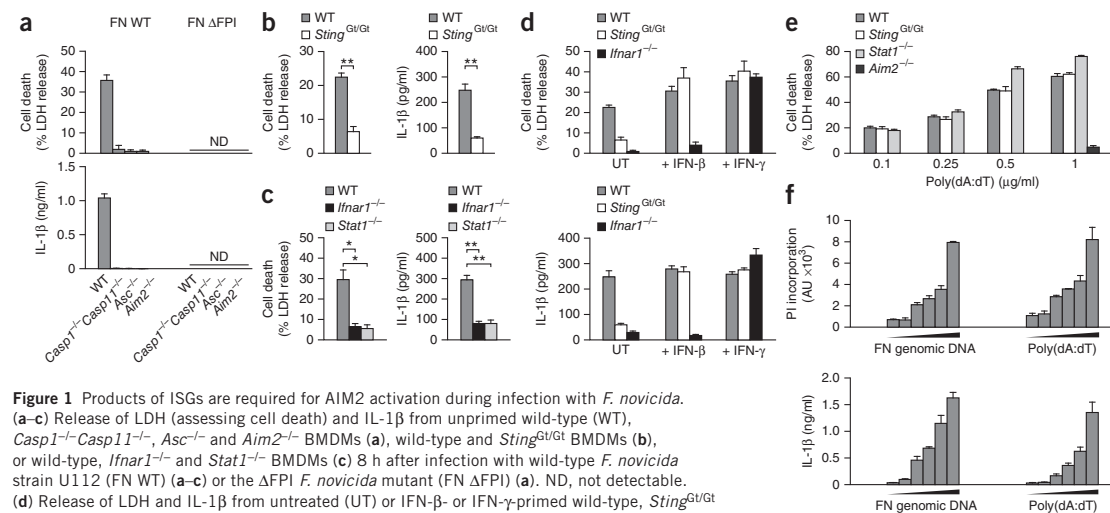


Figure 1 Products of ISGs are required for AIM2 activation during infection with *F. novicida*. (a–c) Release of LDH (assessing cell death) and IL-1 β from unprimed wild-type (WT), *Casp1*^{-/-}*Casp11*^{-/-}, *Asc*^{-/-} and *Aim2*^{-/-} BMDMs (a), wild-type and *Sting*^{Gt/Gt} BMDMs (b), or wild-type, *Ifnar1*^{-/-} and *Stat1*^{-/-} BMDMs (c) 8 h after infection with wild-type *F. novicida* strain U112 (FN WT) (a–c) or the Δ FPI *F. novicida* mutant (FN Δ FPI) (a). ND, not detectable. (d) Release of LDH and IL-1 β from untreated (UT) or IFN- β - or IFN- γ -primed wild-type, *Sting*^{Gt/Gt} and *Ifnar1*^{-/-} BMDMs 8 h after infection with wild-type *F. novicida* U112. (e) Release of LDH from wild-type, *Sting*^{Gt/Gt}, *Stat1*^{-/-} and *Aim2*^{-/-} BMDMs transfected with increasing concentrations of poly(dA:dT) (horizontal axis). (f) Incorporation of propidium iodide (PI) (assessing cell death) and release of IL-1 β by wild-type BMDMs primed with Pam₃CSK₄ and then transfected with increasing concentrations (wedges) of purified *F. novicida* (FN) genomic DNA or poly(dA:dT) (0, 20, 100, 250, 500 and 1000 ng/ml), assessed 1 h after transfection. **P* < 0.01 and ***P* < 0.001 (two-tailed unpaired *t*-test). Data are representative of three (a,c,e) or two (b,d,f) independent experiments (mean and s.d. of quadruplicate wells).

ARTICLES

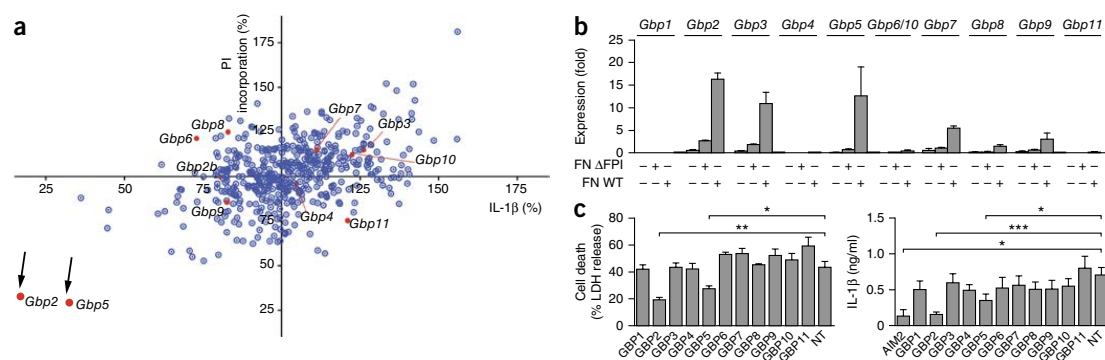


Figure 2 Screening by RNA-mediated interference identifies members of the GBP family as activators of AIM2. (a) Screening results for wild-type BMDMs treated with siRNA targeting various genes (red, genes encoding members of the GBP family; black arrows, *Gbp2* and *Gbp5*), presented as incorporation of propidium iodide and release of IL-1 β , normalized to the average values obtained with all siRNA (set as 100%) and to the values obtained with *Aim2*-specific siRNA (set as 0%). (b) Expression of mRNA from various GBP-encoding genes (top) in wild-type BMDMs left uninfected (–) or infected (+) with wild-type *F. novicida* strain U112 or the Δ FPI mutant, assessed 8 h after infection. (c) Release of LDH and IL-1 β from unprimed wild-type BMDMs pretreated with nontargeting control siRNA (NT) or with siRNA targeting genes encoding various GBPs (horizontal axis) 48 h before infection with wild-type *F. novicida* strain U112, assessed 8 h after infection. * $P < 0.05$, ** $P < 0.01$ and *** $P < 0.001$ (two-tailed unpaired *t*-test). Data are representative of one experiment (a) or two (b) or three (c, LDH) independent experiments or are pooled from six independent experiments (c, IL-1 β) (mean and s.d. of quadruplicate wells in b,c).

B-form double-stranded DNA poly(dA:dT) at a concentration of 1 μ g/ml required AIM2 but was completely independent of STING and STAT1 (Fig. 1e). The transfection of large amounts of DNA might overload the system and render it independent of interferon signaling. To rule out this possibility, we ‘titrated down’ the amount of transfected DNA. The activation of AIM2 remained interferon independent even upon the transfection of small quantities of DNA (Fig. 1e). These results indicated that basal AIM2 was sufficient to initiate inflammasome activation^{9,13}. Indeed, we observed only weak induction of *Aim2* mRNA following infection with *F. novicida* (Supplementary Fig. 1b).

Finally, we confirmed that *F. novicida* genomic DNA was as stimulatory as synthetic DNA by transfecting increasing amounts of each into macrophages that had been primed with the synthetic lipopeptide Pam₃CSK₄ to induce expression of pro-IL-1 β . Both types of DNA triggered similar cell death and release of IL-1 β (Fig. 1f), which excluded the possibility that *F. novicida* DNA had properties that allowed it to evade recognition by AIM2. Together these results indicated that one (or several) IFN- β - or IFN- γ -inducible gene(s) was (were) needed to activate AIM2 specifically during bacterial infection.

Identification of the GBP family by genetic screening

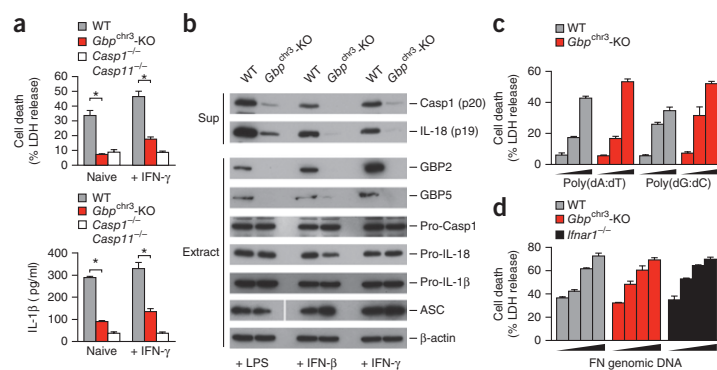
To identify ISGs encoding products involved in *F. novicida*-mediated activation of the AIM2 inflammasome, we screened BMDMs by RNA-mediated interference with small interfering RNA (siRNA). We selected 443 genes with at least twofold higher expression in *F. novicida*-infected wild-type macrophages than in *F. novicida*-infected *Ifnar1*^{–/–} macrophages¹⁷ and selected 40 additional genes on the basis of published reports^{9,10,17,18} (data not shown and Supplementary Table 1). At 48 h after transfection of siRNA specific for those genes, we infected macrophages with *F. novicida* and monitored inflammasome activation by measuring the release of IL-1 β and incorporation of propidium iodide (as a measure of cell death). Knockdown of most of the 483 genes did not substantially affect the release of IL-1 β or cell death (Fig. 2a). In contrast, knockdown of *Gbp2* or *Gbp5* resulted in much less *F. novicida*-mediated release of IL-1 β

and macrophage death than that of cells treated with nontargeting siRNA, while knockdown of other GBP-encoding genes showed no comparable effect (Fig. 2a). *Gbp2* and *Gbp5* had the highest expression among the GBP-encoding genes in macrophages and were substantially and specifically induced upon infection with wild-type *F. novicida* in a STING- and IFNAR-dependent manner but independently of Toll-like receptor 2 and MyD88 (Fig. 2b and Supplementary Fig. 1c–e). We confirmed by RT-PCR the efficiency of siRNA-mediated knockdown of GBP-encoding genes expressed during infection with *F. novicida* (Supplementary Fig. 2a). We next confirmed the screening results by knocking down all 11 mouse GBP-encoding genes individually and measuring cell death and IL-1 β release (Fig. 2c). Knockdown of *Gbp2* and *Gbp5* specifically decreased the *F. novicida*-mediated release of IL-1 β and cell death, as assessed by two different techniques (Fig. 2c and Supplementary Fig. 2b). In conclusion, our screening approach identified GBP2 and GBP5 as two possible ISG products that controlled the activation of AIM2 during infection with *F. novicida*.

AIM2 activation requires GBP-encoding genes on chromosome 3

To confirm our screening data, we obtained macrophages from wild-type mice, mice deficient in both caspase-1 and caspase-11 (*Casp1*^{–/–}*Casp11*^{–/–}; called ‘*Casp1*^{–/–}*Casp11*^{–/–}’ here) or mice that lack the locus on chromosome 3 encoding GBP1, GBP2, GBP3, GBP5 and GBP7 (called ‘*Gbp*^{chr3}’ here)²³ and infected naive or primed macrophages with *F. novicida*. Consistent with defective activation of the AIM2 inflammasome, *Gbp*^{chr3}-deficient BMDMs displayed a significant reduction in cell death and cytokine release and had a diminished abundance of processed caspase-1 p20 compared with that of their wild-type counterparts, even though their expression of pro-caspase-1, ASC and AIM2 protein was similar to that of wild-type cells (Fig. 3a,b and Supplementary Fig. 3a). Measuring the incorporation of propidium iodide in real time following infection showed that *Gbp*^{chr3}-deficient BMDMs died with delayed kinetics compared with that of wild-type cells and similar to that of *Ifnar1*^{–/–} BMDMs (Supplementary Fig. 3b). To determine if GBPs encoded by genes on

Figure 3 Macrophages from *Gbp^{chr3}*-deficient mice have deficient activation of AIM2 in response to *F. novicida*. (a) Release of LDH and IL-1 β from naive or IFN- γ -primed wild-type, *Gbp^{chr3}*-deficient (*Gbp^{chr3}*-KO) and *Casp1^{-/-}Casp11^{-/-}* BMDMs 8 h after infection with wild-type *F. novicida* strain U112. (b) Immunoblot analysis of cleaved caspase-1 (p20) and IL-18 (p19) in culture supernatants (Sup), and of GBP2, GBP5, pro-caspase-1 (Pro-Casp1), pro-IL-18, pro-IL-1 β , ASC and β -actin (loading control) in extracts (Extract), of wild-type and *Gbp^{chr3}*-deficient BMDMs primed with LPS, IFN- β or IFN- γ (below blots) and then infected with wild-type *F. novicida* strain U112, assessed 8 h after infection. (c) Release of LDH from wild-type and *Gbp^{chr3}*-deficient BMDMs 8 h after transfection of increasing concentrations (wedges) of poly(dA:dT) or poly(dG:dC) (0.25, 0.5 or 1 μ g/ml). (d) Release of LDH from wild-type, *Gbp^{chr3}*-KO and *Ifnar1^{-/-}* BMDMs 8 h after transfection of increasing concentrations (wedges) of *F. novicida* genomic DNA (0.1, 0.25, 0.5 or 1 μ g/ml). * $P < 0.001$ (two-tailed unpaired *t*-test). Data are representative of six (a) three (b,c) or two (d) independent experiments (mean and s.d. of quadruplicate wells in a,c,d).



chromosome 3 were directly involved in the activation of AIM2, we engaged AIM2 by transfecting synthetic DNA into unprimed wild-type and *Gbp^{chr3}*-deficient macrophages. Cytosolic DNA triggered LDH release to a similar extent in both groups of cells, even when the amount of transfected DNA was 'titrated down' (Fig. 3c). Wild-type, *Gbp^{chr3}*-deficient and *Ifnar1^{-/-}* cells also responded similarly to the transfection of purified *F. novicida* genomic DNA (Fig. 3d). Thus, GBPs were not required in the context of DNA transfection, which suggested that they functioned upstream of AIM2-mediated DNA detection.

GBP2 and GBP5 direct parallel pathways of AIM2 activation

Since our screening data suggested that mainly GBP2 and GBP5 were required for the activation of AIM2 (Fig. 2a), we infected BMDMs from wild-type, *Casp1^{-/-}Casp11^{-/-}*, *Gbp^{chr3}*-deficient, *Gbp2^{-/-}* or *Gbp5^{-/-}* mice with *F. novicida* and measured activation of the AIM2 inflammasome. *Gbp2^{-/-}* BMDMs displayed less death and cytokine release than did wild-type BMDMs (Fig. 4a,b). Similarly, *Gbp5^{-/-}* BMDMs also displayed attenuated inflammasome activation when

infected with *F. novicida* relative to that of their wild-type counterparts (Fig. 4a,b). Deficiency in *Gbp2* or *Gbp5* did not affect cell death in response to DNA transfection, even when we used very small amounts of DNA (Fig. 4c). To determine if expression of GBP2 or GBP5 could restore activation of the AIM2 inflammasome in *Ifnar1^{-/-}* cells, we retrovirally transduced macrophages with constructs expressing GBP2 or GBP5 or with an empty vector (control) and infected them with *F. novicida*. Such ectopic expression was not able to complement the deficiency in inflammasome activation (Supplementary Fig. 4a–c), which suggested that other products of ISGs might be required for the function of GBP2 and GBP5, in line with data showing that the interferon response²⁵.

Single deficiency in *Gbp2* or *Gbp5* did not reduce the activation of AIM2 during infection with *F. novicida* as much as *Gbp^{chr3}* deficiency did (Fig. 4a,b), which suggested that GBP2 and GBP5 promoted activation of AIM2 through independent pathways. To investigate whether GBP2 and GBP5 acted sequentially or in parallel, we knocked down *Gbp2* expression in wild-type, *Gbp2^{-/-}* and *Gbp5^{-/-}* BMDMs (control

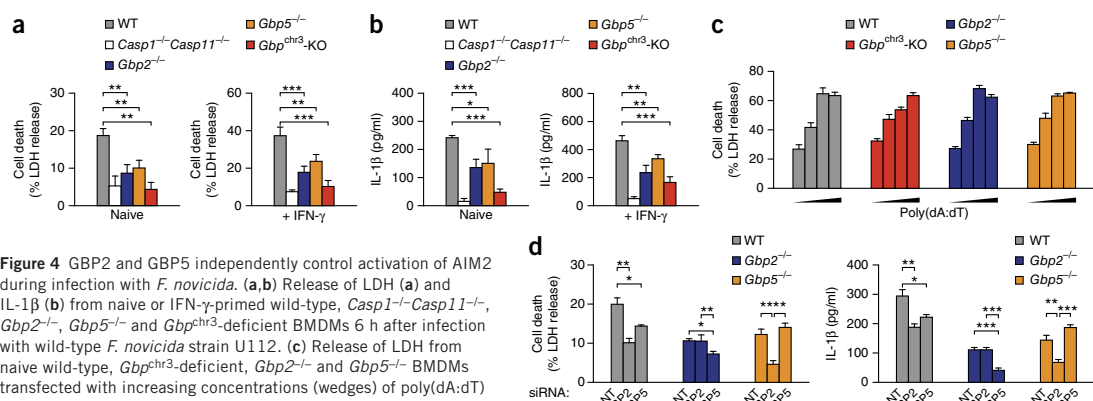


Figure 4 GBP2 and GBP5 independently control activation of AIM2 during infection with *F. novicida*. (a,b) Release of LDH (a) and IL-1 β (b) from naive or IFN- γ -primed wild-type, *Casp1^{-/-}Casp11^{-/-}*, *Gbp2^{-/-}*, *Gbp5^{-/-}* and *Gbp^{chr3}*-deficient BMDMs 6 h after infection with wild-type *F. novicida* strain U112. (c) Release of LDH from naive wild-type, *Gbp^{chr3}*-deficient, *Gbp2^{-/-}* and *Gbp5^{-/-}* BMDMs transfected with increasing concentrations (wedges) of poly(dA:dT) (0.1, 0.25, 0.5 or 1 μ g/ml). (d) Release of LDH and IL-1 β from naive wild-type, *Gbp2^{-/-}* and *Gbp5^{-/-}* BMDMs treated with nontargeting control siRNA or siRNA specific for the gene encoding GBP2 or GBP5 (horizontal axis), then, 22 h later, infected with wild-type *F. novicida* U112, assessed 8 h after infection. * $P < 0.05$, ** $P < 0.01$ and **** $P < 0.001$ (two-tailed unpaired *t*-test). Data are representative of four (a,b), three (c) or two (d) independent experiments (mean and s.d. of quadruplicate wells).

ARTICLES

of siRNA knockdown efficacy, **Supplementary Fig. 4d**) and measured inflammasome activation after infection with *F. novicida*. Knockdown of *Gbp2* reduced cell death and release of IL-1 β in wild-type BMDMs but not in *Gbp2*-deficient BMDMs (**Fig. 4d**). Treatment with *Gbp2*-specific siRNA also significantly reduced inflammasome activation in *Gbp5*^{-/-} BMDMs (**Fig. 4d**), which demonstrated that in *Gbp5*-deficient cells, GBP2 was still active and was able to promote activation of AIM2. Consistent with that, knockdown of *Gbp5* reduced activation of the inflammasome in both wild-type BMDMs and *Gbp2*^{-/-} BMDMs (**Fig. 4d**). In conclusion, our data suggested that the interferon-inducible GTPases GBP2 and GBP5 controlled non-redundant, parallel pathways that promoted activation of AIM2 during infection with *F. novicida*.

Escape of *F. novicida* from phagosomes is GBP independent

Since cytosolic localization of *F. novicida* is required for the activation of AIM2 and since GBPs promote the destabilization of phagosomes and/or pathogen-containing vacuoles of protozoan parasites or bacteria^{23,27,29}, we speculated that GBPs might facilitate the escape of *F. novicida* from phagosomes. We used a phagosome-protection assay^{29,30} based on selective permeabilization of the plasma membrane with digitonin to assay the escape of *F. novicida* from phagosomes. As reported before³⁰, we observed that 90–95% of wild-type *F. novicida* escaped from phagosomes within a few hours of infection, but this frequency was similar for wild-type BMDMs and *Gbp*^{chr3}-deficient BMDMs at various time points after infection (**Fig. 5a**). In contrast, Δ FPI *F. novicida* remained in the phagosome (data not shown).

F. novicida is naturally resistant to β -lactam antibiotics and secrete the β -lactamase FTN₁₀₇₂. Taking advantage of this, we developed an alternative assay to detect cytosolic bacteria based on cleavage of the FRET (Förster resonance energy transfer) reporter probe CCF4 by FTN₁₀₇₂, which leads to a loss of FRET activity^{31,32} (**Supplementary Fig. 5**). We preloaded wild-type, *Gbp2*^{-/-} and *Gbp*^{chr3}-deficient BMDMs with CCF4-AM, the membrane-permeable form of the reporter, and subsequently infected the cells with wild-type *F. novicida*, an FTN₁₀₇₂-deficient strain (the β -lactamase mutant Δ bla) or the Δ FPI mutant. We observed no difference among wild-type, *Gbp2*^{-/-} or *Gbp*^{chr3}-deficient BMDMs in terms of FRET activity after infection with wild-type *F. novicida* (**Fig. 5b** and **Supplementary Fig. 5**). The Δ FPI and Δ bla mutant strains did not produce any significant FRET signals, similar to the signaling of uninfected macrophages (**Supplementary Fig. 5**). Thus, we concluded that GBPs did not control the activation of AIM2 by promoting the escape of *F. novicida* from phagosomes but that they were active after *F. novicida* reached the cytosol. This was consistent with our data showing that in unprimed cells, *F. novicida*-induced expression of GBP-encoding mRNA was dependent on the FPI and on the escape from phagosomes (**Fig. 2b**) and that cytosolic recognition was required for interferon induction (**Supplementary Fig. 1a**).

GBPs promote cytosolic lysis of *F. novicida*

To identify the mechanism by which GBPs controlled the activation of AIM2 during infection with *F. novicida*, we investigated the subcellular localization of GBPs in infected cells. GBPs are known to co-localize with vacuolar pathogens such as *S. typhimurium*, *M. bovis* bacillus Calmette-Guérin and *T. gondii*, consistent with the ability of GBPs to recruit anti-microbial effector mechanisms to the pathogen and to destabilize PCVs^{24,27,29}. We observed that both GBP2 and GBP5 were targeted to intracellular *F. novicida* (**Fig. 6a**). Closer examination of GBP-positive *F. novicida* revealed that GBPs localized to different spots close to or onto the surface of the bacterium (data not shown). However, it was unclear if GBPs targeted the bacterium directly or

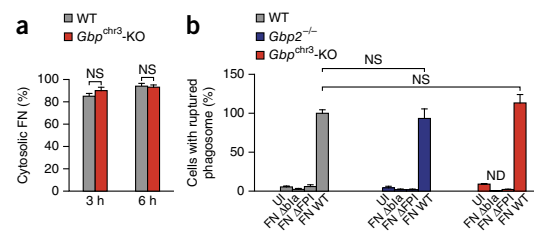


Figure 5 The escape of *F. novicida* from phagosomes is GBP independent. **(a)** Frequency of cytosolic *F. novicida* (FN) among total bacteria at 3 h and 6 h after infection of wild-type and *Gbp*^{chr3}-deficient BMDMs with wild-type *F. novicida* strain U112, assessed by phagosome-protection assay. **(b)** Quantification of cells with ruptured phagosomes at 16 h after infection of wild-type, *Gbp2*^{-/-} and *Gbp*^{chr3}-deficient BMDMs with wild-type *F. novicida* U112, the β -lactamase-deficient mutant Δ bla or the Δ FPI mutant or in uninfected cells (UI), assessed with the β -lactamase-cleavable FRET probe CCF4 and presented relative to that of wild-type cells infected with wild-type *F. novicida*. NS, not significant (two-tailed unpaired *t*-test). Data are pooled from four independent experiments with 300 bacteria counted in each **(a)**; mean and s.d.) or three independent experiments with 1.5×10^5 cells counted three times in each **(b)**; mean and s.d.).

targeted remnants of the host membrane (i.e., lysed phagosomes) or another closely associated membrane compartment.

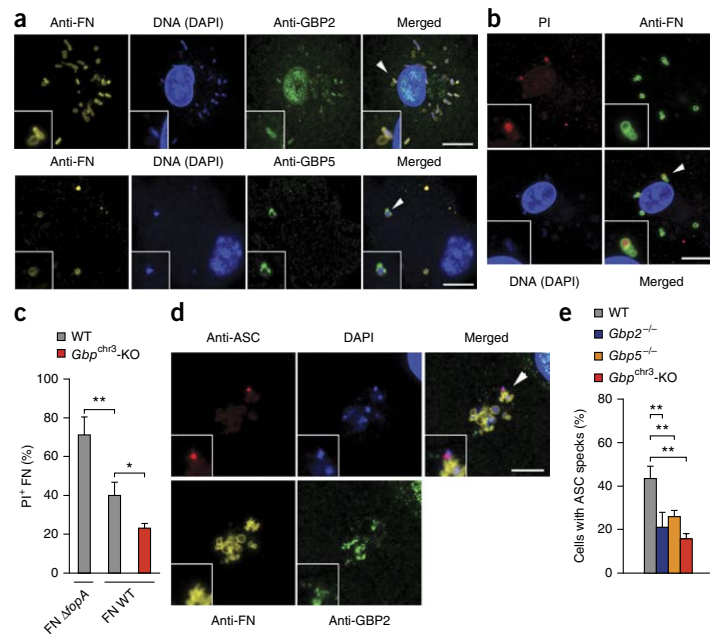
Since the irregular shape of GBP-positive bacteria suggested that they were lysed, we next determined if wild-type and *Gbp*^{chr3}-deficient cells differed in the abundance of lysed intracellular *F. novicida*. Viable and lysed intracellular bacteria can be quantified on the basis of propidium iodide staining, since intact bacteria remain protected from the influx of propidium iodide³³ (**Fig. 6b**). We tested the assay by quantifying lysed bacteria in wild-type BMDMs infected with wild-type *F. novicida* or an *F. novicida* mutant in which the gene encoding the outer membrane protein FopA is deleted (Δ fopA) and thus it has lower membrane stability that results in increased intracellular lysis and hyperactivation of the AIM2 inflammasome¹⁵. We detected significantly larger amounts of propidium iodide-positive Δ fopA *F. novicida* than wild-type *F. novicida* (**Fig. 6c**), which confirmed the validity of our assay. We next compared the frequency of lysed bacteria in wild-type and *Gbp*^{chr3}-deficient macrophages. The *Gbp*^{chr3}-deficient BMDMs had a significantly lower frequency of lysed bacteria (positive for staining with antibodies to *F. novicida* and propidium iodide) (23% on average) than the wild-type BMDMs had (40% on average) (**Fig. 6c**).

The macromolecular inflammasome complex known as the ‘ASC speck’ assembles on genomic DNA released from lysed cytosolic *F. novicida*¹⁰. Immunofluorescence analysis revealed mostly irregularly shaped *F. novicida* in the vicinity of ASC specks (**Fig. 6d**). These bacteria released DNA and were often also positive for GBP staining (**Fig. 6d** and **Supplementary Fig. 6**). Consistent with that, the number of ASC speck-containing cells was significantly lower in GBP-deficient (*Gbp2*^{-/-}, *Gbp5*^{-/-} or *Gbp*^{chr3}-deficient) BMDMs than in wild-type BMDMs (**Fig. 6e**). In conclusion, these findings indicated that GBPs associated with cytosolic *F. novicida* and, by an as-yet-undefined mechanism, induced lysis of the bacterium, which resulted in DNA release and detection by the cytosolic DNA sensor AIM2, followed by oligomerization of ASC.

GBPs control *F. novicida* replication

Inflammasome-induced cell death (pyroptosis) restricts intracellular bacteria by removing their replicative niche and reexposing

Figure 6 GBPs promote the activation of AIM2 by inducing bacteriolysis. (a) Immunostaining with antibody to *F. novicida* (anti-FN), antibody to GBP2 (anti-GBP2) and anti-GBP5, and staining with the DNA-binding dye DAPI, in IFN- γ -primed wild-type BMDMs 8 h after infection with wild-type *F. novicida*. (b) Microscopy of lysed (propidium iodide-positive) *F. novicida* in IFN- γ -primed wild-type BMDMs 8 h after infection with wild-type *F. novicida*. (c) Quantification of lysed (propidium iodide-positive) *F. novicida* (PI⁺ FN) in IFN- γ -primed wild-type and *Gbp*^{chr3}-deficient BMDMs 8 h after infection with wild-type *F. novicida* (FN WT) or the $\Delta fopA$ mutant (FN $\Delta fopA$). (d) Immunostaining of ASC, GBP2 and *F. novicida* in IFN- γ -primed wild-type BMDMs 8 h after infection with wild-type *F. novicida*. (e) Quantification of ASC speck formation in IFN- γ -primed wild-type, *Gbp2*^{-/-}, *Gbp5*^{-/-} and *Gbp*^{chr3}-deficient BMDMs 8 h after infection with wild-type *F. novicida*. Outlined areas (a,b,d) contain 2 \times enlargement of areas marked by arrowheads. Scale bars (a,b,d), 10 μ m. * P < 0.05 and ** P < 0.01 (two-tailed unpaired t -test). Data are representative of three independent experiments (a,b,d) or are pooled from three independent experiments with 300 bacteria in each (c) or cells (e) counted in each (mean and s.d.).



them to extracellular immunological mechanisms³⁴. Cell-autonomous immunity, on the other hand, relies on cell-intrinsic mechanisms to restrict bacterial growth without the need for killing the host cell²¹. To determine whether GBPs restricted *F. novicida* growth through cell-autonomous mechanisms or inflammasome-dependent mechanisms, we infected wild-type, *Aim2*^{-/-}, *Gbp*^{chr3}-deficient and *Ifnar1*^{-/-} BMDMs with wild-type *F. novicida* expressing green fluorescent protein (GFP) and used flow cytometry to quantify infected cells (more than two bacteria per cell, our specific fluorescence-detection threshold) among the live cell population. We observed a significantly higher percentage of live infected *Aim2*^{-/-},

Gbp^{chr3}-deficient and *Ifnar1*^{-/-} BMDMs than live infected wild-type BMDMs (Fig. 7a). This suggested that deficiency in *Ifnar1* or *Gbp*^{chr3}, similar to deficiency in *Aim2*, resulted in a reduction in inflammasome-mediated killing of host cells upon infection.

Cell-autonomous growth restriction is an interferon-induced mechanism that is at least partially independent of inflammasome-mediated cell death^{35,36}. Therefore, we next determined if *Gbp*^{chr3}-deficient BMDMs and *Ifnar1*-deficient BMDMs also had a defect in restricting intracellular bacterial replication. We infected macrophages with GFP⁺ *F. novicida* and quantified bacteria (per cell) by both automated microscopy in flow and microscopy at various

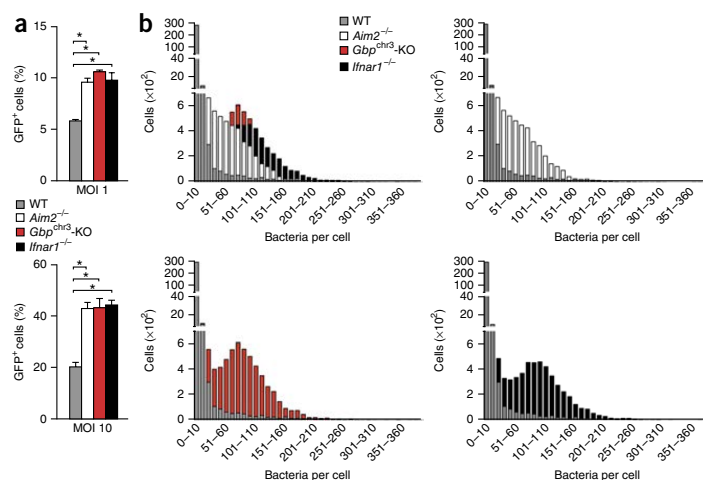
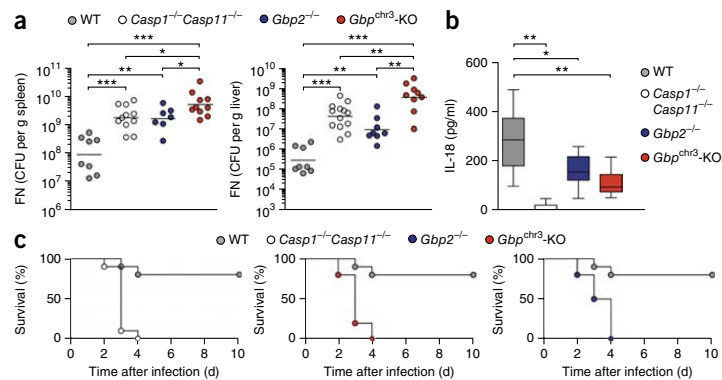


Figure 7 GBPs restrict the intracellular replication of *F. novicida*. (a) Flow cytometry-based quantification of infected (GFP⁺) cells among live wild-type, *Aim2*^{-/-}, *Gbp*^{chr3}-deficient and *Ifnar1*^{-/-} BMDMs 12 h after infection with GFP-expressing wild-type *F. novicida* at a multiplicity of infection (MOI) of 1 (top) or 10 (bottom). * P < 0.001 (two-tailed unpaired t -test). (b) Quantification of bacterial loads in single cells among wild-type, *Aim2*^{-/-}, *Gbp*^{chr3}-deficient and *Ifnar1*^{-/-} BMDMs 12 h after infection with GFP-expressing wild-type *F. novicida* at a multiplicity of infection of 10, assessed by high-resolution microscopy in flow and presented as a comparison of all four genotypes (top left) or a comparison of wild-type cells with each other genotype, with bacteria-per-cell values grouped by increments of 10 (horizontal axes). P < 0.0001, wild-type versus *Aim2*^{-/-}, wild-type versus *Gbp*^{chr3}-deficient, and wild-type versus *Ifnar1*^{-/-} (Kolmogorov-Smirnov test with Bonferroni correction). Data are representative of three independent experiments (a); mean and s.d. of triplicate wells) or are pooled from three independent experiments (b).

ARTICLES

Figure 8 GBPs control host defense against *F. novicida* in vivo. (a) Bacterial burden (as colony-forming units (CFU) of *F. novicida* (FN) per gram tissue) in the liver and spleen at day 2 after subcutaneous infection of wild-type, *Casp1^{-/-}Casp11^{-/-}*, *Gbp2^{-/-}* and *Gbp^{chr3}*-deficient mice with 5×10^3 wild-type *F. novicida*. Each symbol represents an individual mouse ($n = 8$ (wild-type), 10 (*Casp1^{-/-}Casp11^{-/-}*), 7 (*Gbp2^{-/-}*) and 10 (*Gbp^{chr3}*-deficient) (spleen), or $n = 8$ (wild-type), 13 (*Casp1^{-/-}Casp11^{-/-}*), 8 (*Gbp2^{-/-}*) and 9 (*Gbp^{chr3}*-deficient) (liver)); small horizontal lines indicate the mean. * $P < 0.05$, ** $P < 0.01$ and *** $P < 0.001$ (Mann-Whitney test). (b) IL-18 in serum obtained from wild-type mice ($n = 12$), *Casp1^{-/-}Casp11^{-/-}* mice ($n = 11$), *Gbp2^{-/-}* mice ($n = 12$) and *Gbp^{chr3}*-deficient mice ($n = 14$) 16 h after subcutaneous infection with 1.5×10^5 wild-type *F. novicida*. * $P < 0.01$ and ** $P < 0.001$ (Mann-Whitney test). (c) Survival of wild-type, *Casp1^{-/-}Casp11^{-/-}*, *Gbp2^{-/-}* and *Gbp^{chr3}*-deficient mice ($n = 10$ per genotype) after subcutaneous infection with 5×10^3 wild-type *F. novicida*. $P < 0.0001$, wild-type versus *Casp1^{-/-}Casp11^{-/-}* or wild-type versus *Gbp^{chr3}*-deficient, and $P = 0.0005$, wild-type versus *Gbp2^{-/-}* (log-rank (Mantel-Cox) test). Data are representative of two independent experiments (a,c) or are pooled from two individual experiments (b; with 10th–90th percentiles).



time points after infection. Wild-type macrophages efficiently controlled intracellular replication, but *Aim2^{-/-}* BMDMs contained large numbers of intracellular *F. novicida* (30 or more per cell) (Fig. 7b and Supplementary Fig. 7a,b), consistent with a loss of inflammasome-mediated killing of host cells. Bacterial loads were even higher in *Gbp^{chr3}*-deficient or *Ifnar1*-deficient BMDMs, with many cells containing up to 100 bacteria (Fig. 7b and Supplementary Fig. 7a,b). The production of reactive oxygen species and nitric oxide is a potent cell-intrinsic anti-microbial mechanism that can also be activated in an interferon-dependent manner. GBP7 has been shown to recruit subunits of the NADPH oxidase to intracellular *L. monocytogenes* and *M. bovis* bacillus Calmette-Guérin²⁴, and inducible nitric oxide synthase can restrict bacterial growth in a cell-intrinsic manner²¹. However, deficiency in these mechanisms achieved through the use of BMDMs deficient in both inducible nitric oxide synthase and Nox2 did not significantly alter bacteriolysis and inflammasome activation after infection with *F. novicida* ($P = 0.3081$, $P = 0.2786$ and $P = 0.0529$; Supplementary Fig. 8a,b). Overall, these data indicated that GBPs encoded by the locus on chromosome 3 participated in growth restriction in two ways: directly, by promoting the lysis of intracellular bacteria by an as-yet-unknown mechanism; and indirectly, by promoting the inflammasome-mediated killing of host cells, thereby removing the intracellular replicative niche of *F. novicida*.

GBPs control *F. novicida* replication in vivo

AIM2, ASC and caspase-1 control the replication of *F. novicida* in mice^{9,10,37}. Since GBPs are required for inflammasome activation *in vitro*, we investigated whether these proteins also have a physiological role in host defense. We infected age- and sex-matched wild-type, *Casp1^{-/-}Casp11^{-/-}*, *Gbp2^{-/-}* and *Gbp^{chr3}*-deficient mice subcutaneously with 5×10^3 colony-forming units of wild-type *F. novicida* strain U112 and measured the bacterial burden in the liver and spleen at 2 d after infection. As published before³⁷, *Casp1^{-/-}Casp11^{-/-}* mice displayed a significantly higher bacterial burden in the liver and spleen than that of wild-type mice (Fig. 8a). Similarly, *Gbp2^{-/-}* and *Gbp^{chr3}*-deficient mice showed higher bacterial counts than wild-type mice, similar to or even higher than those of *Casp1^{-/-}Casp11^{-/-}* mice (Fig. 8a). Consistent with diminished inflammasome activation *in vivo*, we detected a significantly lower serum concentration of IL-18 in *Casp1^{-/-}Casp11^{-/-}*, *Gbp2^{-/-}* and *Gbp^{chr3}*-deficient mice

than in wild-type mice (Fig. 8b). To further assess the effects of GBP deficiency *in vivo*, we analyzed survival. Within 4 d of infection, all *Casp1^{-/-}Casp11^{-/-}*, *Gbp2^{-/-}* and *Gbp^{chr3}*-deficient mice died, while most wild-type mice survived until the end of the experiment (day 10) (Fig. 8c). These results confirmed the relevance of our *in vitro* data and demonstrated that GBPs encoded by the locus on chromosome 3 were important for inflammasome activation and host defense against *F. novicida* *in vivo*.

DISCUSSION

Since the activation of AIM2 during infection with the cytosolic pathogen *F. novicida* required interferon signaling, we investigated the role of the products of ISGs in this process. Our results showed that the interferon-inducible GTPases GBP2 and GBP5 promoted *F. novicida*-mediated activation of the AIM2 inflammasome but were dispensable for the activation of AIM2 upon transfection of DNA. Members of the GBP family take part in interferon-induced cell-autonomous immunity and are known to induce disruption of the PCVs of vacuolar bacteria and parasites^{23,27,29}. However, the cytosolic localization of *F. novicida* was similar in wild-type and *Gbp^{chr3}*-deficient cells, which indicated that GBPs must have been involved later during infection, after the bacteria had entered the cytosol. This was consistent with results showing that the escape from phagosomes is an interferon-independent process³⁶ and that cytosolic localization of *F. novicida* is a prerequisite for interferon induction¹⁷. Since the activation of AIM2 during infection with *F. novicida* or *L. monocytogenes* is known to require cytosolic bacteriolysis^{12,15}, we investigated whether GBPs controlled the bacteriolysis and replication of *F. novicida* in the cytosol. Significantly fewer lysed and more overall *F. novicida* were present in cells deficient in GBP-encoding genes or *Ifnar1* than in wild-type cells, which indicated that GBPs were required for interferon-mediated cell-autonomous immunity to the pathogen. Furthermore, our results demonstrated that in addition to their known function in destabilizing PCVs, GBPs can also promote the lysis of cytosolic bacteria.

GBPs are also critical for the cytosolic recognition of LPS and for activation of the caspase-11 inflammasome pathway. In this context, they act by promoting the release of vacuolar *S. typhimurium* into the cytosol or by promoting activation of caspase-11 during infection with *L. pneumophila*^{29,38}. At present, no model fully explains how GBPs restrict pathogen growth during infection with microbes or protozoa

and at the same time control inflammasome signaling. It is, however, conceivable that the membrane-destabilizing activity of GBPs in combination with their bacteriolytic activity could not only result in the entry of bacteria into the cytosol but also release microbe-associated molecular patterns (for example, LPS and DNA) directly. Such a model might explain their effect on both the caspase-11 pathway³⁸ and the AIM2 pathway in response to cytosolic bacteria. Thus, bacteriolysis would also release *F. novicida* LPS into the cytosol. However, since *F. novicida* LPS is tetra-acylated, it does not trigger caspase-11 activation³⁹. Conversely, we would expect GBPs to lyse cytosolic *Salmonella* or *Legionella*, which would result in activation of AIM2. But in this case, activation of AIM2 is most probably masked by a high degree of caspase-11-dependent cell death and cytokine release.

GBP-mediated bacteriolysis might also be expected to release DNA and amplify the production of type I interferons via STING. Notably, what triggers initial STING signaling and the induction of GBP-encoding genes during infection with *F. novicida* is still undefined, but two possibilities exist. One is the direct activation of STING via a secreted bacterial cyclic nucleotide, analogous to infection with *L. monocytogenes*⁴⁰, and another is activation of the DNA sensor cGAS by *F. novicida* DNA and subsequent production of the cyclic dinucleotide cGAMP^{41,42}. Lysis of *F. novicida* within the phagosome followed by translocation of its DNA into the cytosol could trigger interferon production⁹. Alternatively, low levels of *F. novicida* extracellular DNA could reach the cytosol by sticking to the surface of the infecting bacteria, as suggested for infection with *M. tuberculosis*⁴³. Finally, small amounts of spontaneous bacteriolysis might occur in the host-cell cytosol. If DNA indeed triggers initial STING-mediated production of interferons, it remains to be shown why it is insufficient to trigger activation of AIM2. Additional experiments are needed to determine the relative DNA-binding affinities of cGAS and AIM2 and how their signaling hierarchy is controlled.

Our results have revealed an underappreciated, close connection between cell-autonomous immunity and recognition by the innate immune system. The attack of GBPs on PCVs or pathogens liberates microbe-associated molecular patterns and thus ensures subsequent immunological recognition of the pathogen, which explains the role of interferon signaling in the detection of bacterial DNA by AIM2 or LPS from vacuolar bacteria by the caspase-11 pathway^{9,10,13,44,45}. Additional questions remain, such as how GBP targeting is regulated and how GBPs act mechanistically. Ectopic expression of GBP2 or GBP5 did not 'rescue' the inflammasome deficiency of *Ifnar1*^{-/-} cells, which suggests that other products of ISGs are necessary for proper targeting and activity of GBPs^{24,25}. Indeed, members of the IRGM family, a subclass of the immunity-related GTPases, can act as guanine-dissociation inhibitors and control the targeting of both immunity-related GTPases and GBPs to pathogen-containing vacuoles, yet the molecular mechanism of this is still unclear^{46–49}. Additional biochemical studies are needed to define the mechanism of GBP targeting and action during bacterial infection and how this promotes the exposure of bacterial ligands to cytosolic recognition pathways.

METHODS

Methods and any associated references are available in the [online version of the paper](#).

Note: Any Supplementary Information and Source Data files are available in the [online version of the paper](#).

ACKNOWLEDGMENTS

We thank N. Gekara (Umea University) for *Sting*^{Gt/Gt} mice; M. Roth and S. Hofer for support with mouse experiments; D. Monack (Stanford University) for chicken

antibody to *F. novicida*; N. Kayagaki (Genentech) and V. Dixit (Genentech) for *Gbp5*^{-/-} and *Aim2*^{-/-} mice, rat antibody to ASC and rat antibody to caspase-1; L. Gallagher and C. Manoil (University of Washington) for plasmid pFFlp; O. Allatif for statistical analysis; the Imaging and FACS Core Facilities of the Biozentrum, University of Basel, for technical assistance; and the Plateau de Biologie Expérimentale de la Souris and the flow cytometry platform of SFR Biosciences Gerland-Lyon Sud. Supported by Swiss National Science Foundation (PP00P3_139120/1 to P.B.), the University of Basel (ID2153162 to P.B.), the European Research Council (311542 to T.H.) and the Délégation Générale de l'Armement (M.R.).

AUTHOR CONTRIBUTIONS

E.M., P.W., T.H. and P.B. conceived of the research; E.M., P.W., R.F.D., S.C., L.A., S.R., S.D., M.S.D., A.K., M.R., T.H. and P.B. performed experiments; D.D., K.P. and M.Y. provided reagents; and T.H. and P.B. wrote the manuscript.

COMPETING FINANCIAL INTERESTS

The authors declare no competing financial interests.

Reprints and permissions information is available online at <http://www.nature.com/reprints/index.html>.

- Paludan, S.R. & Bowie, A.G. Immune sensing of DNA. *Immunity* **38**, 870–880 (2013).
- Ishikawa, H., Ma, Z. & Barber, G.N. STING regulates intracellular DNA-mediated, type I interferon-dependent innate immunity. *Nature* **461**, 788–792 (2009).
- Sauer, J.D. *et al.* The *N*-ethyl-*N*-nitrosourea-induced Goldenticket mouse mutant reveals an essential function of Sting in the *in vivo* interferon response to *Listeria monocytogenes* and cyclic dinucleotides. *Infect. Immun.* **79**, 688–694 (2011).
- Hornung, V. *et al.* AIM2 recognizes cytosolic dsDNA and forms a caspase-1-activating inflammasome with ASC. *Nature* **458**, 514–518 (2009).
- Fernandes-Alnemri, T., Yu, J.W., Datta, P., Wu, J. & Alnemri, E.S. AIM2 activates the inflammasome and cell death in response to cytoplasmic DNA. *Nature* **458**, 509–513 (2009).
- Roberts, T.L. *et al.* HIN-200 proteins regulate caspase activation in response to foreign cytoplasmic DNA. *Science* **323**, 1057–1060 (2009).
- Bürckstümmer, T. *et al.* An orthogonal proteomic-genomic screen identifies AIM2 as a cytoplasmic DNA sensor for the inflammasome. *Nat. Immunol.* **10**, 266–272 (2009).
- Ge, J., Gong, Y.N., Xu, Y. & Shao, F. Preventing bacterial DNA release and absent in melanoma 2 inflammasome activation by a *Legionella* effector functioning in membrane trafficking. *Proc. Natl. Acad. Sci. USA* **109**, 6193–6198 (2012).
- Fernandes-Alnemri, T. *et al.* The AIM2 inflammasome is critical for innate immunity to *Francisella tularensis*. *Nat. Immunol.* **11**, 385–393 (2010).
- Jones, J.W. *et al.* Absent in melanoma 2 is required for innate immune recognition of *Francisella tularensis*. *Proc. Natl. Acad. Sci. USA* **107**, 9771–9776 (2010).
- Kim, S. *et al.* *Listeria monocytogenes* is sensed by the NLRP3 and AIM2 inflammasomes. *Eur. J. Immunol.* **40**, 1545–1551 (2010).
- Sauer, J.D. *et al.* *Listeria monocytogenes* triggers AIM2-mediated pyroptosis upon infrequent bacteriolysis in the macrophage cytosol. *Cell Host Microbe* **7**, 412–419 (2010).
- Rathinam, V.A. *et al.* The AIM2 inflammasome is essential for host defense against cytosolic bacteria and DNA viruses. *Nat. Immunol.* **11**, 395–402 (2010).
- Briken, V., Ahlbrand, S.E. & Shah, S. *Mycobacterium tuberculosis* and the host cell inflammasome: a complex relationship. *Front. Cell. Infect. Microbiol.* **3**, 62 (2013).
- Peng, K., Broz, P., Jones, J., Joubert, L.M. & Monack, D. Elevated AIM2-mediated pyroptosis triggered by hypercytotoxic *Francisella* mutant strains is attributed to increased intracellular bacteriolysis. *Cell. Microbiol.* **13**, 1586–1600 (2011).
- Muruve, D.A. *et al.* The inflammasome recognizes cytosolic microbial and host DNA and triggers an innate immune response. *Nature* **452**, 103–107 (2008).
- Henry, T., Brotcke, A., Weiss, D.S., Thompson, L.J. & Monack, D.M. Type I interferon signaling is required for activation of the inflammasome during *Francisella* infection. *J. Exp. Med.* **204**, 987–994 (2007).
- Cole, L.E. *et al.* Macrophage proinflammatory response to *Francisella tularensis* live vaccine strain requires coordination of multiple signaling pathways. *J. Immunol.* **180**, 6885–6891 (2008).
- Cole, L.E. *et al.* Toll-like receptor 2-mediated signaling requirements for *Francisella tularensis* live vaccine strain infection of murine macrophages. *Infect. Immun.* **75**, 4127–4137 (2007).
- Jones, J.W., Broz, P. & Monack, D.M. Innate immune recognition of *Francisella tularensis*: activation of type-I interferons and the inflammasome. *Front. Microbiol.* **2**, 16 (2011).
- Kim, B.H., Shenoy, A.R., Kumar, P., Bradfield, C.J. & MacMicking, J.D. IFN-inducible GTPases in host cell defense. *Cell Host Microbe* **12**, 432–444 (2012).
- Howard, J.C., Hunn, J.P. & Steinfeldt, T. The IRG protein-based resistance mechanism in mice and its relation to virulence in *Toxoplasma gondii*. *Curr. Opin. Microbiol.* **14**, 414–421 (2011).
- Yamamoto, M. *et al.* A cluster of interferon- γ -inducible p65 GTPases plays a critical role in host defense against *Toxoplasma gondii*. *Immunity* **37**, 302–313 (2012).

ARTICLES

24. Kim, B.H. *et al.* A family of IFN-gamma-inducible 65-kD GTPases protects against bacterial infection. *Science* **332**, 717–721 (2011).
25. Degrandi, D. *et al.* Extensive characterization of IFN-induced GTPases mGBP1 to mGBP10 involved in host defense. *J. Immunol.* **179**, 7729–7740 (2007).
26. Kresse, A. *et al.* Analyses of murine GBP homology clusters based on in silico, in vitro and in vivo studies. *BMC Genomics* **9**, 158 (2008).
27. Degrandi, D. *et al.* Murine guanylate binding protein 2 (mGBP2) controls *Toxoplasma gondii* replication. *Proc. Natl. Acad. Sci. USA* **110**, 294–299 (2013).
28. Kravets, E. *et al.* The GTPase activity of murine guanylate-binding protein 2 (mGBP2) controls the intracellular localization and recruitment to the parasitophorous vacuole of *Toxoplasma gondii*. *J. Biol. Chem.* **287**, 27452–27466 (2012).
29. Meunier, E. *et al.* Caspase-11 activation requires lysis of pathogen-containing vacuoles by IFN-induced GTPases. *Nature* **509**, 366–370 (2014).
30. Checron, C., Wehrly, T.D., Fischer, E.R., Hayes, S.F. & Celli, J. Autophagy-mediated reentry of *Francisella tularensis* into the endocytic compartment after cytoplasmic replication. *Proc. Natl. Acad. Sci. USA* **103**, 14578–14583 (2006).
31. Nothelfer, K., Dias Rodrigues, C., Bobard, A., Phalipon, A. & Enninga, J. Monitoring *Shigella flexneri* vacuolar escape by flow cytometry. *Virulence* **2**, 54–57 (2011).
32. Juruj, C. *et al.* Caspase-1 activity affects AIM2 speck formation/stability through a negative feedback loop. *Front. Cell. Infect. Microbiol.* **3**, 1–11 (2013).
33. Chong, A. *et al.* Cytosolic clearance of replication-deficient mutants reveals *Francisella tularensis* interactions with the autophagic pathway. *Autophagy* **8**, 1342–1356 (2012).
34. Miao, E.A. *et al.* Caspase-1-induced pyroptosis is an innate immune effector mechanism against intracellular bacteria. *Nat. Immunol.* **11**, 1136–1142 (2010).
35. Zhou, H. *et al.* Genome-wide RNAi screen in IFN- γ -treated human macrophages identifies genes mediating resistance to the intracellular pathogen *Francisella tularensis*. *PLoS ONE* **7**, e31752 (2012).
36. Edwards, J.A., Rockx-Brouwer, D., Nair, V. & Celli, J. Restricted cytosolic growth of *Francisella tularensis* subsp. *tularensis* by IFN- γ activation of macrophages. *Microbiology* **156**, 327–339 (2010).
37. Mariathasan, S., Weiss, D.S., Dixit, V.M. & Monack, D.M. Innate immunity against *Francisella tularensis* is dependent on the ASC/caspase-1 axis. *J. Exp. Med.* **202**, 1043–1049 (2005).
38. Pilla, D.M. *et al.* Guanylate binding proteins promote caspase-11-dependent pyroptosis in response to cytoplasmic LPS. *Proc. Natl. Acad. Sci. USA* **111**, 6046–6051 (2014).
39. Hagar, J.A., Powell, D.A., Aachoui, Y., Ernst, R.K. & Miao, E.A. Cytoplasmic LPS activates caspase-11: implications in TLR4-independent endotoxic shock. *Science* **341**, 1250–1253 (2013).
40. Woodward, J.J., Iavarone, A.T. & Portnoy, D.A. c-di-AMP secreted by intracellular *Listeria monocytogenes* activates a host type I interferon response. *Science* **328**, 1703–1705 (2010).
41. Sun, L., Wu, J., Du, F., Chen, X. & Chen, Z.J. Cyclic GMP-AMP synthase is a cytosolic DNA sensor that activates the type I interferon pathway. *Science* **339**, 786–791 (2013).
42. Li, X.D. *et al.* Pivotal roles of cGAS-cGAMP signaling in antiviral defense and immune adjuvant effects. *Science* **341**, 1390–1394 (2013).
43. Manzanillo, P.S., Shiloh, M.U., Portnoy, D.A. & Cox, J.S. *Mycobacterium tuberculosis* activates the DNA-dependent cytosolic surveillance pathway within macrophages. *Cell Host Microbe* **11**, 469–480 (2012).
44. Broz, P. *et al.* Caspase-11 increases susceptibility to Salmonella infection in the absence of caspase-1. *Nature* **490**, 288–291 (2012).
45. Rathinam, V.A. *et al.* TRIF licenses caspase-11-dependent NLRP3 inflammasome activation by gram-negative bacteria. *Cell* **150**, 606–619 (2012).
46. Martens, S. *et al.* Disruption of *Toxoplasma gondii* parasitophorous vacuoles by the mouse p47-resistance GTPases. *PLoS Pathog.* **1**, e24 (2005).
47. Howard, J.C., Hunn, J.P. & Steinfeldt, T. The IRG protein-based resistance mechanism in mice and its relation to virulence in *Toxoplasma gondii*. *Curr. Opin. Microbiol.* **14**, 414–421 (2011).
48. Bekpen, C. *et al.* The interferon-inducible p47 (IRG) GTPases in vertebrates: loss of the cell autonomous resistance mechanism in the human lineage. *Genome Biol.* **6**, R92 (2005).
49. Haldar, A.K. *et al.* IRG and GBP host resistance factors target aberrant, “non-self” vacuoles characterized by the missing of “self” IRGM proteins. *PLoS Pathog.* **9**, e1003414 (2013).

ONLINE METHODS

Bacterial strains and plasmids. *F. novicida* strain U112 and isogenic Δ FP1 mutants have been published¹⁰. Where applicable, strains were transformed with the plasmid pKK219-GFP (Supplementary Table 2). The β -lactamase mutant Δ *bla* was generated by PCR-mediated homologous recombination with a kanamycin selection cassette through use of the following primers (upper case indicates *F. novicida* sequence; lower case indicates the kanamycin-resistance cassette sequence): ForUpstream, GTCGAGTACGCTAATATAAAAATTCTAAAAA; RevUpstream, gcttatcgataccgtcgacctcGGGATTAATGATAAAGTTGTAACATAATATACGC; ForDownstream, gatcatgctcgcagctatgCAGCTTATAAATAAGCGGTACGCCAC; and RevDownstream, AAGACGGTGATGTACCATTGTCTATAG. The kanamycin-resistance cassette was removed by transformation of the mutant obtained with the thermosensitive plasmid pFFlp (provided by L. Gallagher and C. Manoil) encoding the recombinase Flp. Following loss of the plasmid, genomic deletion was verified by sequencing.

Mice. *Gbp*^{chr3}-deficient, *Gbp2*^{-/-}, *Gbp5*^{-/-}, *Nos2*^{-/-}, *Cybb*^{-/-}, *Casp1*^{-/-}, *Casp11*^{-/-} ('caspase-1-knockout'), *Asc*^{-/-}, *Aim2*^{-/-}, *Stat1*^{-/-}, *Ifnar1*^{-/-}, *Sting*^{G3/G4}, *Tlr2*^{-/-} and *Myd88*^{-/-} mice have been described^{3,10,23,27,29,44}. Mice were bred in the animal facilities of the University of Basel or at the Plateau De Biologie Expérimentale De La Souris.

Animal infection. All animal experiments were approved (license 2535, Kantonales Veterinäramt Basel-Stadt and ENS_2012_061) and were performed according to local guidelines (Tierschutz-Verordnung, Basel-Stadt and CECCAPP, Lyon) and the Swiss animal protection law (Tierschutz-Gesetz). Age- and sex-matched mice (8–10 weeks of age) were infected subcutaneously with 5×10^3 or 1.5×10^5 colony-forming units of stationary-phase wild-type *F. novicida* strain U112 in 50 μ l PBS. Mice were killed at the appropriate time point after infection. No randomization or 'blinding' of researchers to sample identity was used.

Cell culture and infection. BMDMs were differentiated in DMEM (Invitrogen) with 10% vol/vol FCS (Thermo Fisher Scientific), 10% MCSF (supernatants of L929 mouse fibroblasts), 10 mM HEPES (Invitrogen) and nonessential amino acids (Invitrogen). 1 d before infection, macrophages were seeded into 6-, 24- or 96-well plates at a density of 1.25×10^6 , 2.5×10^5 or 5×10^4 cells per well. Where required, macrophages were pre-stimulated with Pam₃CSK₄ (tripalmitoyl cysteinyl seryl tetralysine), LPS (from *Escherichia coli* strain O111:B4 (InvivoGen)), mouse IFN- β or mouse IFN- γ (eBioscience). For infection with *F. novicida*, bacteria were grown overnight at 37 °C with aeration in brain-heart-infusion medium or tryptic soy broth. The bacteria were added to the macrophages at a multiplicity of infection of 100 or the appropriate value. The plates were centrifuged for 15 min at 500g to ensure similar adhesion of the bacteria to the cells and were incubated for 120 min at 37 °C. Next, cells were washed and fresh medium with 10 μ g/ml gentamycin (Invitrogen) was added to kill extracellular bacteria, then plates were incubated for the desired length of time. Transfection with poly(dA:dT) or poly(dG:dC) was done as described²⁹ or as indicated in the figures and legends (Figs. 1 and 3).

siRNA-mediated knockdown. Genes were knocked down with GenMute (SignaGen Laboratories) and siRNA pools (siGenome; Dharmacon). Wild-type BMDMs were seeded into 24- or 96-well plates at a density of 1.5×10^5 or 3×10^4 cells per well. siRNA complexes were prepared at a concentration of 25 nM siRNA in GenMute Buffer according to the manufacturer's instructions for forward knockdown (SignaGen laboratories). siRNA complexes were mixed with BMDM medium (described above) and were added onto the cells. After 22–48 h of gene knockdown, BMDMs were infected with *F. novicida* at a multiplicity of infection of 100:1 and were analyzed for inflammasome activation as outlined below. siRNA pools targeted the following genes (numbers in parentheses indicate Dharmacon reference): *Aim2* (M-044968-01), *Casp11* (that is, *Casp4*) (M-042432-01), *Gbp1* (M-040198-01), *Gbp2* (M-040199-00), *Gbp3* (M-063076-01), *Gbp4* (M-047506-01), *Gbp5* (M-054703-01), *Gbp6* (M-041286-01), *Gbp7* (M-061204-01), *Gbp8* (M-059726-01), *Gbp9* (M-052281-01), *Gbp10* (M-073912-00), *Gbp11* (M-079932-00) and NT (non-targeting) pool 2 (D-001206-14).

siRNA screening. Knockdown of the 483 selected genes was performed as described above in the 36 central wells of 96-well plates; this included the nontargeting control siRNA and siRNA specific for *Asc* and *Aim2* on each plate. Macrophages were infected with *F. novicida* at a multiplicity of infection of 100:1 and, following a wash at 1 h after infection, cells were incubated with medium supplemented with propidium iodide at 5 μ g/ml. At 6 h after infection, the fluorescence of propidium iodide was determined on a plate reader (Tecan) and supernatants were collected for analysis of the release of IL-1 β by enzyme-linked immunosorbent assay (DuoSet; R&D Systems). The fluorescence of propidium iodide and concentration of IL-1 β in cells transfected with each siRNA were normalized to the average value of the full plate set, set as 100, and to the value obtained with *Aim2*-specific siRNA, set as 0, with the following calculation (for gene 'X'): normalized value obtained with X-specific siRNA = (value obtained with X-specific siRNA_X - value obtained with *Aim2*-specific siRNA) / (average value obtained with siRNA - value obtained with *Aim2*-specific siRNA). All the siRNA presenting variation of more than 50% in either one of the two parameters have been retested two or three times. Average normalized values are presented in the display items.

Ectopic expression of GBP2 and GBP5. Mouse *Gbp2* and *Gbp5* were cloned into the lentiviral plasmid TRIP iziE-SSV-GFP with the following primers and restriction enzymes (upper case indicates gene sequence; lower case indicates restriction site (underlined) and four bases flanking in the 5' direction): For_mGBP2_AvrII, attaccctaggGACATGGCCTCAGAGATCCACATG; Rev_mGBP2_EcoRV, aatagataTCAGAGTATAGTGCACCTCCAGACG; For_mGBP5_AvrII, aaatcctagGACATGGCCGCCAGAGATTCACATG; and Rev_mGBP5_HpaI, attgttaacTTAGCTTATAACACAGTCATGATGATGTCTAC. The production of lentiviruses in 293T human embryonic kidney cells and the transduction of primary BMDMs were performed by standard methods. IFNAR1-deficient macrophages were transduced after 8 d of differentiation by spin-inoculation (1,500g for 2 h at room temperature). Transduced macrophages were infected 48 h later. Transduction frequency was determined by flow cytometry based on GFP expression. Specific ectopic expression was checked by quantitative RT-PCR.

Cytokine and LDH release measurement. IL-1 β , IL-18 and tumor-necrosis factor were measured by enzyme-linked immunosorbent assay (eBioscience). LDH was measured with an LDH Cytotoxicity Detection Kit (Clontech). To normalize for spontaneous lysis, the percentage of LDH release was calculated as follows: (LDH infected - LDH uninfected) / (LDH total lysis - LDH uninfected) \times 100.

Immunoblot analysis. Immunoblot analysis was done as described²⁹. Antibodies used were rat anti-mouse caspase-1 (1:1,000 dilution; 4B4; Genentech), rabbit anti-IL-1 α (1:1,000 dilution; ab109555; Abcam), rabbit anti-IL-18 (1:500 dilution; 5180R; Biovision), goat anti-mouse IL-1 β (1:500 dilution; AF-401-NA; R&D Systems), rabbit anti-GBP2 (1:1,000 dilution; 11854-1-AP; Proteintech) and rabbit anti-GBP5 (1:1,000 dilution; 13220-1-AP; Proteintech). Cell lysates were probed with monoclonal anti- β -actin (1:2,000 dilution; AC-15; A1978; Sigma). Secondary antibodies were as follows (all conjugated to horseradish peroxidase and all at a dilution of 1:3,000): goat anti-rat (NA935V; GE Healthcare), goat anti-rabbit (G21234; Invitrogen), rabbit anti-goat (811620; Invitrogen) and rabbit anti-mouse (816720; Invitrogen).

Real-time PCR. Primers used for mRNA quantification are in Supplementary Table 3. Experiments were performed with an iCycler (Bio-Rad) and SYBR green (Applied Biosystems) with standard protocols.

Statistical analysis. Prism 5.0a software (GraphPad Software) was used for statistical analysis of data. For evaluation of the differences between two groups (cell death, cytokine release, flow cytometry, colony-forming units and immunofluorescence-based counts), a two-tailed *t*-test was used. The Kolmogorov-Smirnov test was used for comparison of the cell distribution as determined by ImageStream microscopy in flow. *P* values were adjusted for multiple comparisons with the Bonferroni correction approach. Animal experiments were evaluated with the Mann-Whitney or log-rank Cox-Mantel test.

Immunofluorescence. Macrophages were seeded on glass coverslips and were infected as described above. At the desired time points, cells were washed three times with PBS and were fixed for 15 min at 37 °C with 4% paraformaldehyde. Following fixation, coverslips were washed, and the fixative was quenched for 10 min at room temperature with 0.1 M glycine. Coverslips were stained for 16 h at 4 °C with primary antibodies (identified below), then were washed with PBS and then incubated for 1 h at room temperature with the appropriate Alexa Fluor–conjugated secondary antibodies (identified below) (1:500 dilution; Invitrogen), then were washed with PBS and mounted on glass slides with Vectashield containing DAPI (6-diamidino-2-phenylindole; Vector Labs). Antibodies used were chicken anti-*F. novicida* (1:1,000 dilution; a gift from D. Monack), rat anti-ASC (1:1,000 dilution; Genentech), rabbit anti-GBP2 (1:100 dilution; 11854-1-AP; Proteintech) and rabbit anti-GBP5 (1:100 dilution; 13220-1-AP; Proteintech). Secondary antibodies used were as follows (all at a dilution of 1:500 and all from Life Technologies): goat anti-rat coupled to Alexa Fluor 488 (A11006), Alexa Fluor 568 (A11077) or Alexa Fluor 633 (A21094); goat anti-chicken coupled to Alexa Fluor 488 (A11008) or Alexa Fluor 568 (A10042); and goat anti-rabbit coupled to Alexa Fluor 488 (A11032), Alexa Fluor 568 (A11047) or Alexa Fluor 633 (A21103). Coverslips were imaged on a Zeiss LSM700 or a Leica SP8 at a magnification of $\times 63$ and vacuolar versus cytosolic bacteria, total intracellular bacteria or ASC specks were quantified as described in the figure legends.

Phagosome protection assay. For quantification of cytoplasmic and vacuolar bacteria, macrophages were infected with GFP⁺ *F. novicida* as described above. At the desired time point, cells were washed with KHM buffer (110 mM potassium acetate, 20 mM HEPES and 2 mM MgCl₂, pH 7.3), followed by incubation for 1 min in KHM buffer with 50 μ g/ml digitonin (Sigma). Cells were immediately washed three times with KHM buffer and then were stained for 12 min with Texas Red–coupled chicken antibody to *F. novicida* (identified above) in KHM buffer with 2% BSA. Cells were washed with PBS, then were fixed and analyzed by microscopy. Controls were included in every assay as described²⁹.

Intracellular viability measurement. For measurement of the intracellular lysis of *F. novicida*, we adapted a published propidium iodide–staining method³³. Infected BMDMs were incubated for 12 min at 37 °C with Alexa Fluor 488–conjugated mouse antibody to *F. novicida* (identified above) and 2.6 μ M propidium iodide (Sigma) in KHM buffer (described above) for labeling of accessible cytosolic bacteria and compromised bacteria, respectively, in permeabilized cells. Cells were fixed and imaged as described above.

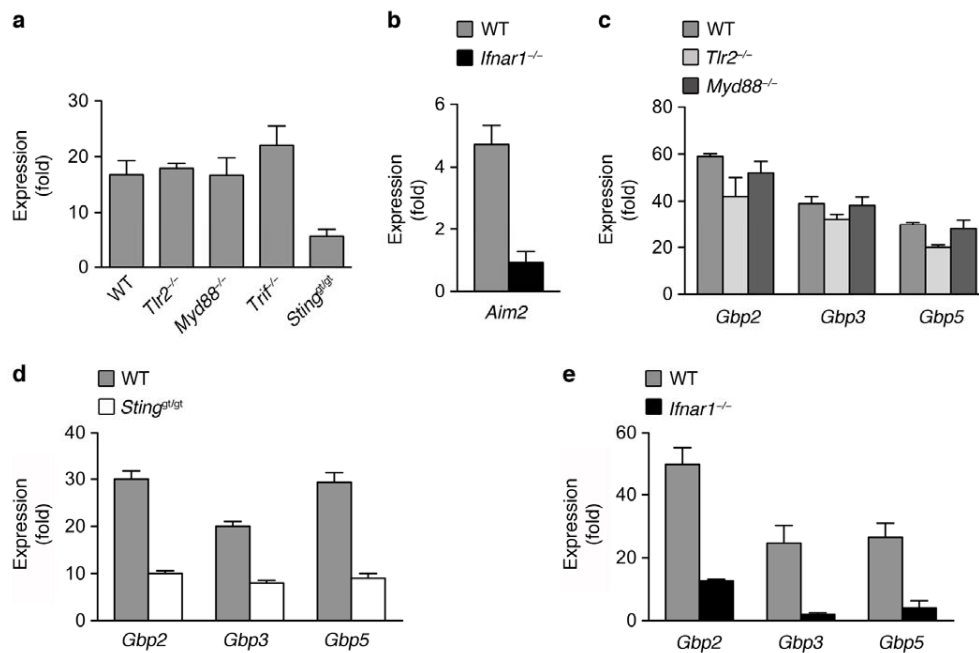
CCF4 measurements. Quantification of escape from vacuoles with the β -lactamase–CCF4 assay was performed following manufacturer's instructions

(Life Technologies). Macrophages seeded onto non-treated plates were infected for 1 h as described above, washed and then incubated for 1 h at room temperature in CCF4 in the presence of 2.5 mM probenidicid (Sigma). Live (propidium iodide–negative) cells were used for quantification of cells containing cytosolic *F. novicida*, with excitation at 405 nm and detection at 450 nm (cleaved CCF4) or 510 nm (intact CCF4).

Flow cytometry. For assessment of bacterial replication by flow cytometry, macrophages seeded onto untreated plates were infected as described above with GFP-expressing *F. novicida* strains. At 8 h after infection, cells were lifted with trypsin and were immediately analyzed by flow cytometry on a FACSCanto II cytometer (BD Biosciences). Dead cells were excluded on the basis of staining with propidium iodide.

ImageStream flow cytometry. Macrophages infected with GFP-expressing bacteria were fixed in 4% PFA and were analyzed on an ImageStream X Mark II (Amnis; EMD-Millipore) with Inspire software, with the extended depth-of-field function activated to increase the accuracy of spot counts. Images of single cells were analyzed with Ideas software (Amnis; EMD-Millipore) with the following steps (each step being confirmed by visualization of at least 20 single cells). Doublets and debris were excluded by morphological parameters (aspect ratio and area in the brightfield channel). Defocused images were eliminated by the Gradient RMS function of the brightfield function. For spot counts and definition of the mean fluorescence of single bacterium, the specific GFP fluorescence signal was defined by application of a mask combining an intensity threshold and a spot to cell background ratio (peak) function. Automatic spot counts were performed with the mask described above. Cells containing a single spot (either a single bacterium or a tight cluster of several bacteria) were gated. The area of the specific signal was analyzed in single cells on the gated population. For the exclusion of bacterial clusters and quantification of the fluorescence of single bacterium, the mean fluorescence intensity was calculated on the GFP⁺ signal covering an area of $1 \pm 0.5 \mu\text{m}^2$ in 1,599 cells.

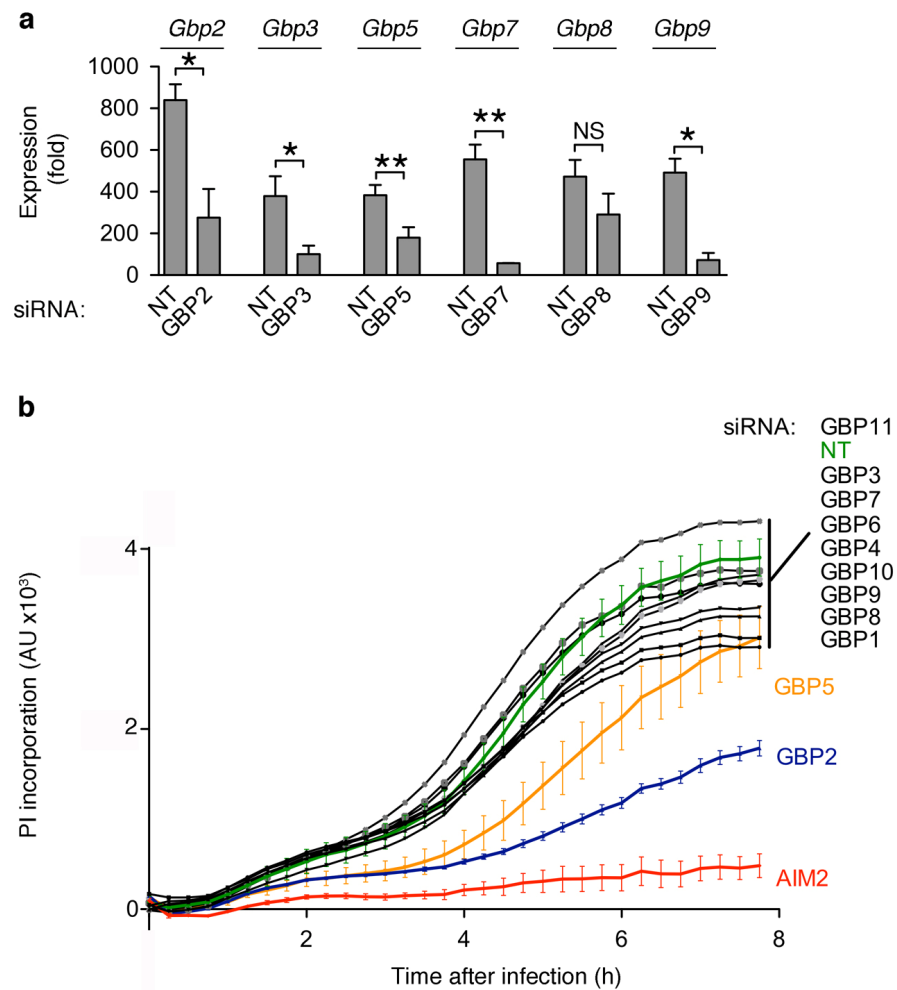
Bacteria in single cells were quantified by the automatic spot count function or their numbers were calculated based on the fluorescence of single bacterium. The quantification was identical for cells containing fewer than seven bacteria ($R^2 > 0.99$). For higher intracellular burden, the spot-count function largely underestimated the number of bacteria per cell due to the difficulty to discriminate bacterial cluster. We thus relied on the specific fluorescence of the bacteria within the cells as defined by the mask described above and the calculated fluorescence value of single intracellular bacterium to quantify bacteria per cell. The mask was applied to at least 10,000 images of single cells per sample to extract the specific fluorescence of the intracellular bacteria in single cells.



Supplementary Figure 1

Induction of *Ifnb*, *Aim2* or *Gbp* mRNA in dependence of STING and IFNAR signaling.

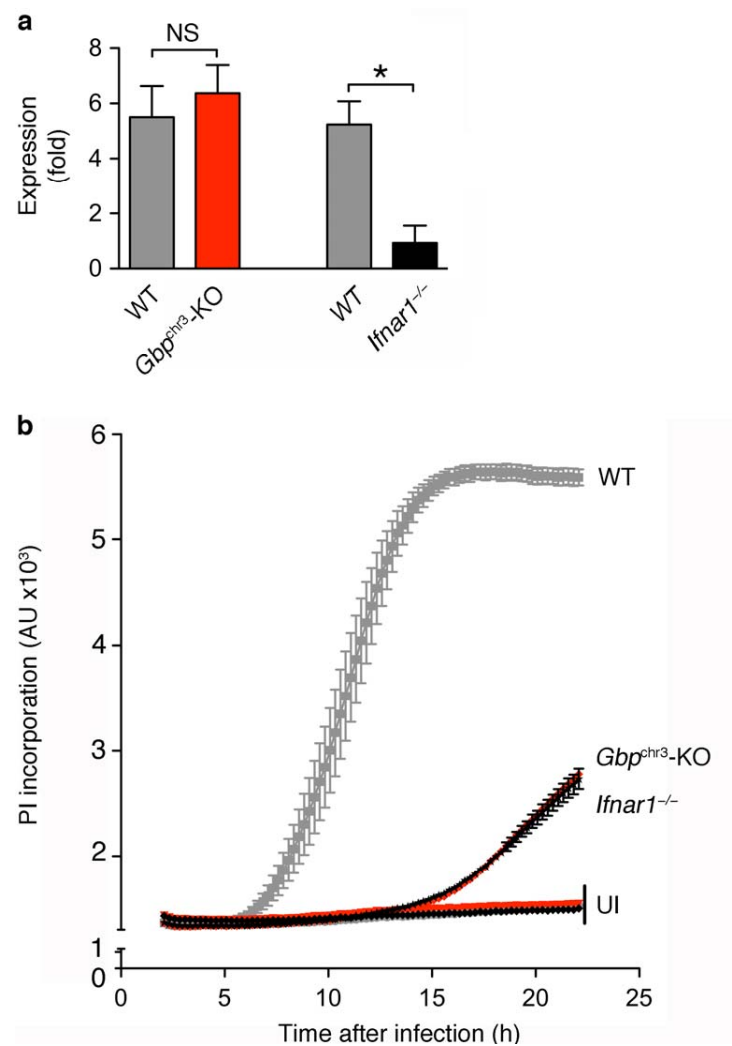
(a) Induction of *Ifnb* expression from unprimed wild-type (WT), *Tlr2*^{-/-}, *Myd88*^{-/-}, *Trif*^{-/-} and *Sting*^{st/st} bone-marrow derived macrophages (BMDMs) following infection with wild-type *F. novicida* U112 for 6 h. (b–e) Induction of *Gbp2*, *Gbp3*, *Gbp5* or *Aim2* expression from unprimed wild-type, *Tlr2*^{-/-}, *Myd88*^{-/-}, *Ifnar1*^{-/-} and *Sting*^{st/st} BMDMs following infection with wild-type *F. novicida* U112 for 6 h. Graphs show mean and s.d. of quadruplicate assays and data are representative of two (b–d) or three (a) independent experiments.



Supplementary Figure 2

Gbp knockdown efficiency and real-time cell death after knock-down of Gbps.

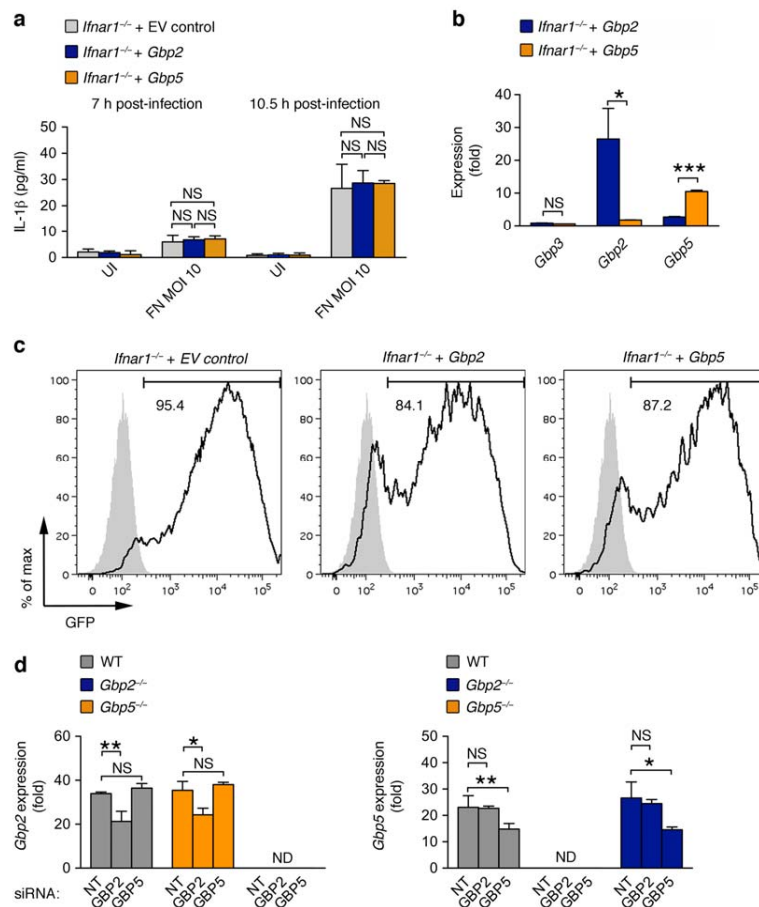
(a) Induction of the expression of individual *Gbps* from LPS/ $\text{IFN}\gamma$ -primed wild-type BMDMs treated with Non-Targeting (NT) or the indicated gene-specific siRNA for 22 h. Graph shows mean and s.d. of quadruplicate wells. *Gbp1*, *4*, *6/10*, *11* were not tested due to their low expression (see Fig. 2b). (b) Cell death as measured by propidium iodide (PI) influx in real-time in unprimed wild-type BMDMs infected with wild-type *F. novicida* U112. BMDMs were treated with Non-Targeting (NT) or indicated gene-specific siRNA for 48 h before infection. Graphs show mean and s.d. of triplicate assays and data are representative of three independent experiments. *, $p < 0.05$; **, $p < 0.01$; NS, not significant (two-tailed unpaired t-test).



Supplementary Figure 3

***Aim2* induction and real-time cell death assay in *Gbp*-deficient and *Ifnar1*-deficient cells.**

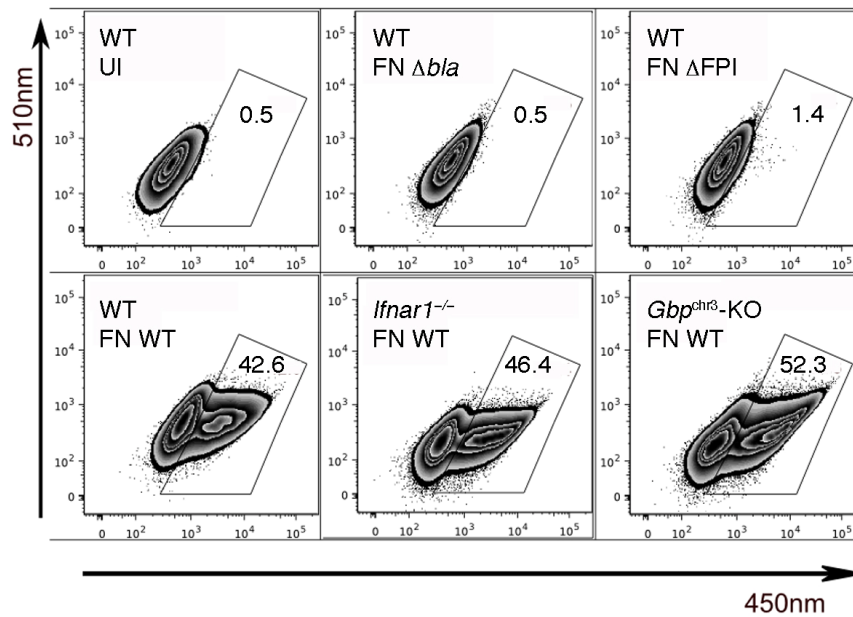
(a) Induction of *Aim2* expression from unprimed wild-type, *Gbp^{chr3}*-deleted and *Ifnar1^{-/-}* BMDMs infected with wild-type *F. novicida* U112 for 6 h. *, $p < 0.01$; NS, not significant (two-tailed unpaired t-test). (b) Cell death as measured by propidium iodide influx in real-time in unprimed wild-type, *Gbp^{chr3}*-deleted and *Ifnar1^{-/-}* BMDMs left uninfected (UI) or infected with wild-type *F. novicida* U112. Graphs show mean and s.d. of triplicate assays and data are representative of two (a) and three (b) independent experiments.



Supplementary Figure 4

Ectopic expression of GBPs in *Ifnar1*^{-/-} cells and efficiency of *Gbp2* and *Gbp5* knockdown.

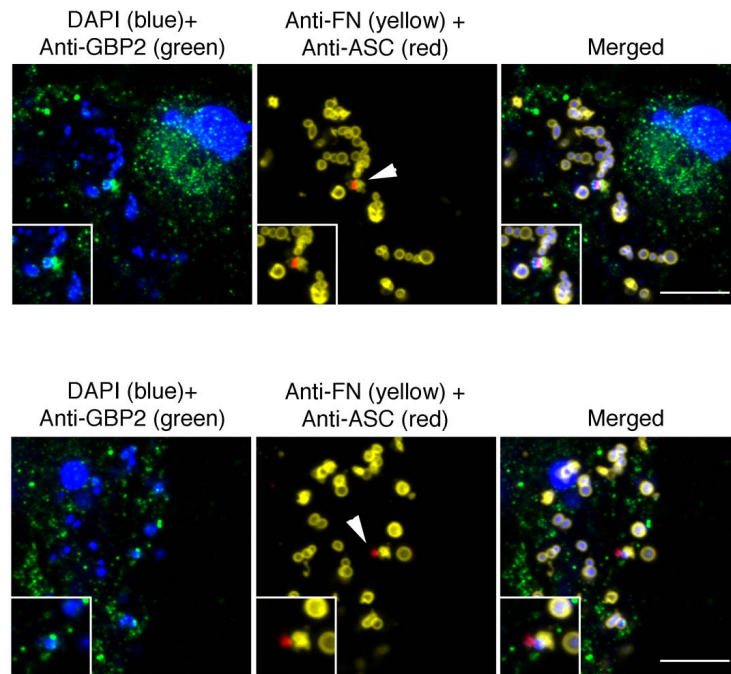
(a–c) Ectopic expression of GBP2 or GBP5 do not complement type-I-IFN receptor deficiency. *Ifnar1*^{-/-} macrophages were transduced with lentivirus encoding either GFP only (EV = empty vector) and GFP-GBP2 and GFP-GBP5. 48 h post transduction, macrophages were infected with *F. novicida* at the indicated MOI. IL-1 β concentration in the supernatant was determined at 7 h and 10.5 h post infection (a). Specific ectopic expression was verified by quantifying the *Gbp3* (control), *Gbp2* and *Gbp5* transcript levels. Results are expressed as fold induction relative to the transcript level in *Ifnar1*^{-/-} macrophages transduced with empty vector control (b). Graphs show mean and s.d. of triplicate assays. The percentage of transduced cells was determined by flow cytometry based on GFP expression (c). (d) RT-PCR for *Gbp2* and *Gbp5* expression from unprimed wild-type, *Gbp2*^{-/-} and *Gbp5*^{-/-} BMDMs treated with Non-Targeting or the indicated gene-specific siRNA for 22 h and infected for 8 h with wild-type *F. novicida* U112. Graphs show mean and s.d. of quadruplicate assays and data are representative of independent two experiments. *, p<0.05; **, p<0.01; NS, not significant (two-tailed unpaired t-test). ND, not detected.



Supplementary Figure 5

Phagosomal rupture assay using the CCF4/ β -lactamase system.

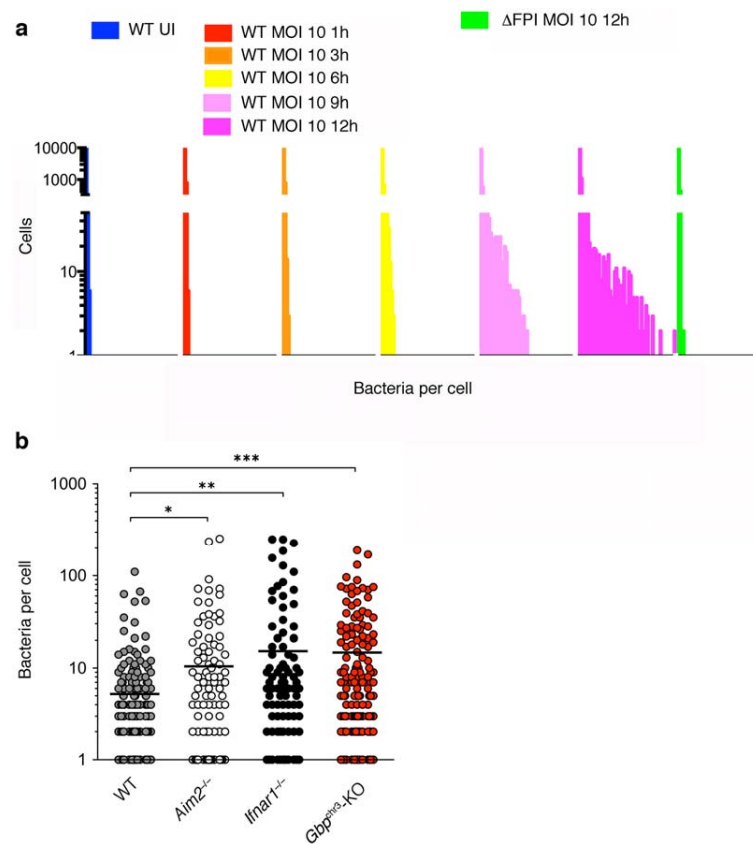
Wild-type, $lfnar1^{-/-}$ and $Gbp^{chr3-KO}$ BMDMs were primed for 16 h with IFN- β (500 units/ml), infected for 1 h with wild-type *F. novicida* (FN) U112, a β -lactamase-deficient mutant (Δbla) or a ΔFPI mutant and loaded with CCF4-AM for 1 h before analysis by flow cytometry. Phagosomal rupture is associated with β -lactamase (encoded by FTN_1072) release into the cytosol and cleavage of the CCF4 substrate (maximum emission at 520 nm) into a product which emits with a maximum of fluorescence at 447 nm. FACS plots show pooled data from three independent samples and representative of three independent experiments. Live cells (propidium iodide negative) are shown.



Supplementary Figure 6

GBPs co-localize with irregularly shaped bacteria next to ASC specks.

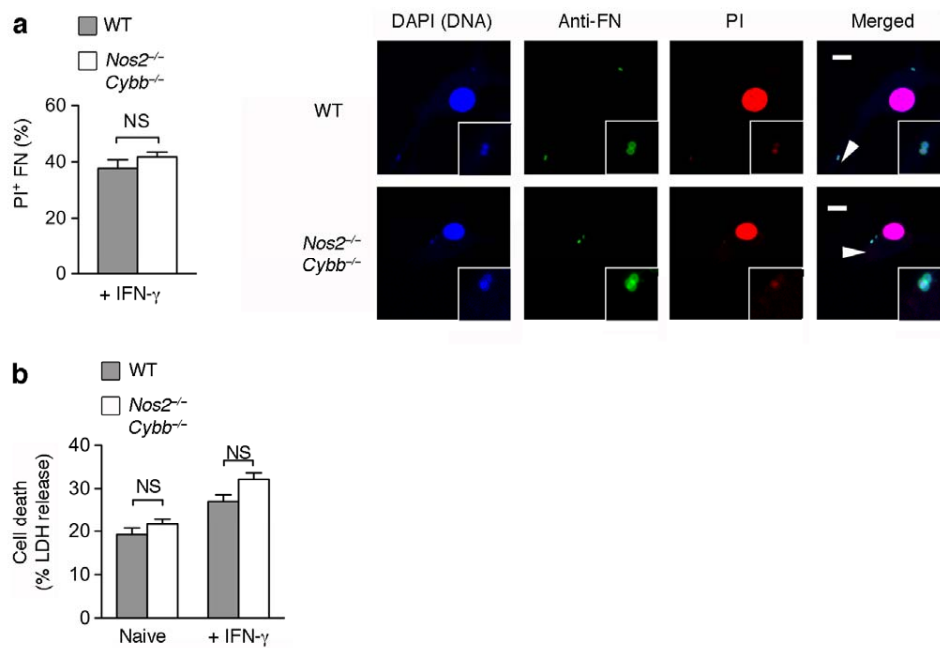
Wild-type BMDMs infected with wild-type *F. novicida* for 8 h, stained for DNA (DAPI), GBP2, *F. novicida* and ASC. Scale bars: 10 μ m. Data are representative of three independent experiments.



Supplementary Figure 7

Analysis of bacterial replication in infected macrophages.

(a) Quantification of bacterial loads in single cells by high-resolution microscopy in flow over time. Wild-type BMDMs were left uninfected or infected with GFP⁻-wild-type *F. novicida* or a Δ FPI mutant at an MOI of 10 for 0-12 h, fixed and analyzed by ImageStreamTM microscopy in flow. Each bar corresponds to the number of cells with the indicated numbers of bacteria per cell grouped by increments of 5... Wild-type UI vs. wild-type MOI 10 3h $p > 0.9999$, wild-type UI vs. wild-type MOI 10 6h $p > 0.9999$, wild-type UI vs. wild-type MOI 10 9h $p < 0.0001$, wild-type UI vs. wild-type MOI 10 12h $p < 0.0001$, wild-type MOI 10 12h vs. Δ FPI MOI 10 12h $p < 0.0001$ Kolmogorov-Smirnov test with Bonferroni correction). (b) Quantification of bacterial loads as determined by microscopy. Wild-type, *Aim2*^{-/-}, *Gbp*^{-/-}-deleted and *Ifnar1*^{-/-} BMDMs were infected with GFP⁻-wild-type *F. novicida* at an MOI of 10 for 16 h, fixed and analyzed by confocal microscopy. Graph show pooled data from 2 independent experiments ($n > 1000$ bacteria counted). *, $p < 0.05$; **, $p < 0.01$; ***, $p < 0.001$ (two-tailed unpaired t-test).



Supplementary Figure 8

Bacteriolysis and cell death during *F. novicida* infection are independent of ROS or NO production.

(a) Quantification of lysed (propidium iodide⁺ *F. novicida*) in IFN- γ -primed wild-type and *Nos2*^{-/-}/*Cybb*^{-/-} BMDMs infected for 8 h with wild-type *F. novicida*. Imaging of lysed (propidium iodide⁺) *F. novicida* in IFN- γ -primed wild-type and *Nos2*^{-/-}/*Cybb*^{-/-} BMDMs infected for 8 h with wild-type *F. novicida*. Arrowheads indicate region in insets. Scale bars 10 μ m. (b) LDH release from naïve or IFN- γ -primed wild-type and *Nos2*^{-/-}/*Cybb*^{-/-} BMDMs infected for 8 h with wild-type *F. novicida* U112. Graphs show mean and s.d. of quadruplicate wells and data are representative of three independent experiments. NS, not significant (two-tailed unpaired t-test).

Supplementary Table 2 Bacterial strains and plasmid used in this study.

Name	Parental strain	Characteristic
wild-type <i>F. novicida</i> U112	-	-
Δ FPI	wild-type <i>F. novicida</i> U112	Δ FTN_1309-1325::Kan
Δ bla	wild-type <i>F. novicida</i> U112	Δ FTN_1072
Δ fopA	wild-type <i>F. novicida</i> U112	fopA::T20
pKK219-GFP	-	GFP expressing plasmid

Supplementary Table 3 | Primers used for qRT-PCR. Target gene, sequence and size of amplicon are indicated.

Target gene	Forward primer	Reverse primer	Amplicon (bp)
mGBP1	aataagctggctggaaagca	tgtgtgagactgcacagtgg	60
mGBP2	accagctgcactatgtgacg	tcagaagtgcgggttttcc	172
mGBP3	gtctggagaacgcagtgaca	gtgctccatgaagacagcaa	182
mGBP4	gagcagctcatcaaagacca	ttcctcacggaagtcttttg	72
mGBP5	ccagagtaaagcgaacaag	gtgcaactcttgcttctcc	158
mGBP6/10	tggagcagctgcattatgtc	gcattctgggtttgcacct	228
mGBP7	aacagcatgagcaccatcaa	gaagtggactttgccctgat	89
mGBP8	tgctatgaccaaccacaaa	ccttggctgagactgcaca	227
mGBP9	tgtgcagtctcagaccaagg	aagcacacttagggcgaaga	154
mGBP11	agcaactgagaaggaagctga	caaggagagcctttgttct	99
m β -actin	gtggatcagcaagcaggagt	agggtgtaaaacgcagctca	96